

UC Santa Cruz

UC Santa Cruz Electronic Theses and Dissertations

Title

Magnetoelastic Dynamics in Nanomagnetic Metamaterials

Permalink

<https://escholarship.org/uc/item/5mj818rc>

Author

Berk, Cassidy Russell

Publication Date

2019

Copyright Information

This work is made available under the terms of a Creative Commons Attribution License, available at <https://creativecommons.org/licenses/by/4.0/>

Peer reviewed|Thesis/dissertation

UNIVERSITY OF CALIFORNIA
SANTA CRUZ

**MAGNETOELASTIC DYNAMICS IN NANOMAGNETIC
METAMATERIALS**

A dissertation submitted in partial satisfaction
of the requirements for the degree of

DOCTOR OF PHILOSOPHY

In

ELECTRICAL ENGINEERING

by

Cassidy R. Berk

June 2019

The Dissertation of Cassidy Berk is approved:

Professor Holger Schmidt, chair

Professor Nobuhiko Kobayashi

Professor Michael Isaacson

Lori Kletzer
Vice Provost and Dean of Graduate Studies

Copyright © by

Cassidy R. Berk

2019

Table of Contents

CHAPTER 1: INFORMATION AND CIVILIZATION.....	1
1.1 Early Information Technology	1
1.2 Neolithic Information Technology.....	3
1.3 Industrial Information Storage	7
1.4 Magnetic Recording	8
1.4.1 Superparamagnetic Effect	9
1.4.2 Giant Magnetoresistance	11
1.4.3 Bit Patterned Media.....	12
1.4.4 Heat Assisted Magnetic Recording	14
1.4.5 All-Optical Switching	15
1.4.6 Fundamental Questions and Other Technological Applications	17
1.5 Contemporary Information Technology	19
1.6 Metamaterials	20
1.7 Problem Statement and Chapters	20
CHAPTER 2: MICROSCOPIC MAGNETISM.....	23
2.1 Single electron.....	23
2.2 Electron and Nucleus	26
2.2.1 Angular Momentum and Magnetic Moments	26
2.2.2 Hydrogen-Like Atoms and Atomic Orbitals	28
2.3 Multi-Electron Atoms	31
2.3.1 Hartree-Fock Approximation and Slater Determinant	31
2.3.2 LS-Coupling	33
2.3.3 Spin-Orbit Coupling	35
2.3.4 Hund's Rules	37
2.4 Multiple Atoms	40
2.4.1 Crystal Field	40

2.4.2 Quenching of Orbital Angular Momentum	43
2.4.3 Hubbard Model	45
2.4.4 Exchange Interaction	47
2.4.5 Heisenberg Approximation	49
CHAPTER 3: MACROSCOPIC MAGNETISM (MICROMAGNETICS)	51
3.1 Magnetization Vector	51
3.2 Free Energy	53
3.2.1 Zeeman Energy	54
3.2.2 Exchange Energy	55
3.2.3 Bilinear Exchange Energy	58
3.2.4 Demagnetization Field and Shape Anisotropy Energy	58
3.2.5 Magnetocrystalline Anisotropy Energy	65
3.2.6 Magnetostriction	67
3.3 Dynamics	71
3.4 Free Energy Resonance	74
CHAPTER 4: EXPERIMENTAL SETUP AND THEORY	78
4.1 Introduction	78
4.2 Stroboscopic Measurements	79
4.3 The Pump Excitation	82
4.3.1 Three Temperature Model	83
4.3.2 Thermal Anisotropy Pulse	85
4.4 The Probe Detection	87
4.4.1 Gyrotropic Media	87
4.4.2 Normal Modes	91
4.4.3 Faraday Effect	94
4.4.4 Magneto-Optic Kerr Effect	97
4.5 Detection	101
4.5.1 Crossed Polarizer	101

4.5.2 Balanced Photodiodes	104
4.6 TR-MOKE Experiment.....	108
4.6.1 Beam Paths	108
4.6.2 Excitation Geometry Considerations	110
4.6.3 Time Domain Analysis.....	112
4.6.4 Discrete Fourier Transform Linewidth	114
CHAPTER 5: ALL-OPTICAL MEASUREMENT OF INTERLAYER EXCHANGE COUPLING IN FE/PT/FEPT THIN FILMS	117
5.1 Introduction	117
5.2 Film Properties	118
5.3 Acoustic and Optic Modes	119
5.4 Single Film Resonance –Kittel Formula	121
5.4.1 Single Film TR-MOKE Measurements.....	123
5.5 Multilayer Film Resonance	125
5.5.1 Multilayer TR-MOKE Measurements	127
5.6 OOMMF Simulations	132
5.7 Conclusion	134
CHAPTER 6: MULTI-PULSE METHOD FOR SELECTIVE CONTROL OF MAGNETIZATION PRECESSIONS IN MAGNETIC MULTILAYERS	135
6.1 Introduction	135
6.2 Double-Pump Configuration.....	136
6.3 Demonstration on Single Layer	138
6.4 Demonstration on Multilayer Structure	141
6.5 Representation in the Complex Plane	145
6.6 Spin Pumping and Damping	147
6.7 Conclusion	154
CHAPTER 7: MAGNETO-ELASTIC DYNAMICS DUE TO SURFACE ACOUSTIC WAVES IN NANOMAGNETIC ARRAYS	155
7.1 Introduction	155

7.2 Intrinsic vs. Extrinsic Damping.....	157
7.2.1 Elliot-Yafet (Spin-Flip) Scattering.....	157
7.2.2 Extrinsic Mechanisms	159
7.2.3 Pump Probe Alignment	162
7.3 Damping in Nanomagnet Arrays Using TR-MOKE.....	163
7.3.1 Magnetoelastic Coupling in Arrays.....	164
7.3.2 Effect of Array Geometry on SAW Influence.....	168
7.3.3 Effect of Array Geometry on Damping.....	176
7.2.4 Measurement of Damping using SAW Pinning Width	178
7.4 Conclusion	184
CHAPTER 8: STRONGLY COUPLED MAGNON-PHONON DYNAMICS IN A SINGLE NANOMAGNET.....	186
8.1 Introduction	186
8.2 Coupled Resonances and Avoided Crossings	188
8.3 Analytical Derivation	189
8.2.1 2D Elastic Dynamics	191
8.2.2 Magnetic Dynamics.....	193
8.2.3 Coupled Dynamics	196
8.4 Magnon-Phonon Anti-Crossings.....	201
8.4.1 Tuning the Coupling into the Strong Coupling Regime	208
8.4.2 Loss Rates and Cooperativity.....	211
8.5 Conclusion	217
CHAPTER 9: FUTURE OF INFORMATION TECHNOLOGY AND SUMMARY	219
REFERENCES	224

Table of Figures

Figure 1.1: Cave art of lions hunting bison from the Chauvet-Pont d'Arc cave in France. The oldest drawings in this cave date back roughly 30,000 years. Taken from [1].	2
Figure 1.2: Jiahu symbols found inscribed on a Tortoise shell in Henan, China. The markings date back to 6600 BC. Taken from [3].	4
Figure 1.3: Instructions of Shuruppak. Early example of literature written in cuneiform on a clay tablet around 2500 BC. Taken from [4].	5
Figure 1.4: (a) Example of bits (red or blue) written into a granular magnetic material. A bit consists of a region composed of multiple magnetic grains all oriented in the same direction. Taken from [12]. (b) Energy barrier separating two different magnetic states. When this barrier becomes comparable to the thermal energy in the room kBT , the bits become less stable.	9
Figure 1.5: (a) Example of longitudinal recording and (b) perpendicular recording. Perpendicular recording offers the benefit of increased storage areal densities.	11
Figure 1.6: (a) When the magnetization of two layers are oriented in the same direction, current flows through the system more easily—the structure has a low resistance. (b) When the magnetizations of the layers are anti-parallel there is more spin scattering resulting in a higher resistance.	12
Figure 1.7: Schematic showing the difference between conventional granular media and patterned magnetic media. Taken from [12].	13
Figure 1.8: (a) Example of the write process in HAMR. Initially the bit is stored in a state which is too hard to switch (high coercivity). Application of a laser heats the magnetic material resulting in a decrease of the coercivity so that the bit can be affected by the magnetic field from the write coil. As the magnetic material cools it assumes its original stable state. (b) Schematic of HAMR write head. Taken from [12].	15

Figure 1.9: (a) Experimental demonstration of all-optical switching (AOS) on a GdFeCo thin film. The different contrasts of the film are obtained using a Kerr microscope and represent the magnetization orientation. Right handed circularly polarized light $\sigma +$ only affects the magnetization oriented in one direction while left handed circularly polarized light $\sigma -$ affects the magnetization oriented in the other direction. (b) Schematic showing how AOS could be used to write bits. Taken from [19]...... 16

Figure 1.10: (a) Illustration of the timescales of magnetic processes and some potential technologies which could be impacted. Taken from [24]. (b) Magnons have many data processing applications. In some instances magnonics may replace electronics. However, realistically they will be implemented into existing technologies which will require mechanisms for converting between spin and charge. Taken from [26]...... 18

Figure 2.1: The electron is a wavelike particle with an intrinsic property known as spin. The name spin comes from the similarity to angular momentum. However, the exact nature of what causes spin is debated..... 23

Figure 2.2: Relationship between the total spin angular momentum and the projections onto the z-axis. 25

Figure 2.3: Vector diagram showing the relationship between the angular momentum, l , of the electron, which arises due to the circulating electron mass, m_e , and the magnetic dipole, μ_l resulting from the circulating current, i 26

Figure 2.4: Atomic orbitals. Each row of orbitals is a successive electron shell characterized by quantum number n . The columns separate the different electron orbitals or subshells (s, p and d) which are specified by their orbital quantum number l . The different spatial configurations of the subshells are further specified by their magnetic quantum number m_l . The spatial designation of each orbital is shown below its magnetic quantum number. 30

Figure 2.5: Vector diagram demonstrating the difference between LS-coupling and jj-coupling. (a) When electron-electron coulombic interaction is larger than the spin orbit interaction ($V_{ee} > V_{so}$) the sum of the electrons' orbital moments is coupled to the sum of their spins. (b) If $V_{ee} < V_{so}$ then the individual electron's orbital moment is coupled to its spin moment and then the total J is found by summing up the individual j 's from the different electrons. 35

Figure 2.6: Diagram showing symmetric and anti-symmetric wavefunctions and their probability amplitudes. The anti-symmetric wavefunction has a probability of zero at the origin which makes it a lower energy state from a coulombic potential point of view. Taken from [36]. 39

Figure 2.7: (a) Position of atom (red dot) in cubic crystalline environment surrounded by negative point charges. (b) The d -orbitals that point in the direction of the point charges have a higher energy and form e_g doublet group. (c) The orbitals that do not point directly at the negative point charges form the t_{2g} triplet group and have a lower energy. Taken from [39]. 42

Figure 2.8: Probability amplitude of wavefunctions demonstrating (a) No quenching of the orbital moment. The wavefunction is complex, made up of a superposition of wavefunctions with the same m_l . (b) Partial quenching of the orbital momentum. In this case the spin-orbit interaction still has some effect so as to mix the two real wavefunctions with the same m_l . (c) Total quenching of the orbital momentum. The effect from the crystal field causes xy to be the ground state. This is a real eigenfunction and therefore has zero expectation value for L_z . Taken from [39]. 44

Figure 3.1: At lower temperatures all of the dipoles are aligned due to the exchange interaction and the magnetization vector which is the net dipole moment per unit volume is large. As the temperature increases, thermal energy excites the spins so that they are no longer perfectly aligned with one another. This causes the magnitude of the magnetization vector to decrease. The temperature at which the net magnetic moment is zero is known as the Curie Temperature. 52

Figure 3.2: Free energy landscape (a) only considering the exchange energy causes all the spins to be aligned but with no preferential direction. All directions are energetically equivalent. (b) Applying an external field along the z -direction will deform the free energy surface creating an energy minimum. The direction of the magnetization vector is normal to the surface at the minimum (along the z -direction). 54

Figure 3.3: Magnetization vectors for different spins, m_i and m_j separated by a distance Δr 55

Figure 3.4: Exchange constant terms for different crystallographic structures. 57

Figure 3.5: Field generated by a magnetic dipole which tends to align neighboring dipoles along the field lines. The field strength depends inversely on the distance, but it also depends on the mutual orientation between the dipoles which can cause alignment in different directions. 59

Figure 3.6: Diagram showing the different regions used to derive the demagnetization energy. The total dipole field \mathbf{H}_{dip} is obtained by subtracting from the internal demagnetization field \mathbf{H}_d the field \mathbf{H}_R which is the field within a sphere of radius R and then adding the individual dipole interactions within the sphere, $h_{i,r < R}$. The summation within the sphere depends on the relative positions of the dipoles and can be absorbed into the magnetocrystalline anisotropy. Furthermore, if the magnetization is homogeneous within the sphere, then \mathbf{H}_R can be attributed solely to the surface charge which is given by the equation for the volume of a sphere. This term is constant and can be neglected. \mathbf{H}_d can also be decomposed into surface and volume terms, and if the magnetization is homogeneous within the magnetic body then \mathbf{H}_d arises solely due to the surface contribution, which leads to the concept of shape anisotropy. Taken from [45]. 60

Figure 3.7: Coordinate systems and free energy landscapes for (a) uniaxial anisotropy given by equation (3.34) with $K_0 = 0$ and $K_1 < 0$. (b) $K_0 = 0$ and $K_1 > 0$ (similar to hcp Co) (c) Magnetocrystalline anisotropy energy landscape for cubic crystal with $K_0 = 1$ and $K_1 = 1$ (similar to bcc Fe) (d) $K_0 = 1$ and $K_1 = -1$ (similar to fcc Ni). 67

Figure 3.8: (a) Landau-Lifshitz (LL) equation dictates the magnetization vector's rotation around the effective field, H_{eff} . (b) The Landau-Lifshitz-Gilbert (LLG) equation models the precession of the magnetization while including a phenomenological damping term, α in the direction $\mathbf{M} \times \frac{d\mathbf{M}}{dt}$ 73

Figure 3.9: The Magnetization precession can be mapped to the $\{1, 2, 3\}$ coordinate system defined by the direction of the magnetization vector and the plane of the cone due to the precession of \mathbf{M} . \mathbf{m}_3 is along the direction of \mathbf{M} at equilibrium (3), \mathbf{m}_2 is parallel to the xy plane (2) and \mathbf{m}_1 is orthogonal to \mathbf{m}_2 and \mathbf{m}_3 (1) 74

Figure 4.1: Illustration of the concept behind the stroboscopic pump-probe method. The pump ($\lambda_{pump} = 400$ nm) pulses are separated by Δt_{pump} which for a repetition rate of 76MHz is 13ns. By the time each new pump pulse arrives, the system has fully relaxed back to equilibrium. At time t_1 each probe ($\lambda_{probe} = 400$ nm) pulse (which

has the same repetition rate as the pump pulses) is separated from a corresponding pump pulse. Since the magnetization follows the same dynamical path upon excitation, the probe pulse for a given pump-probe separation reads the same magnetic state. The data for each time step is an average of the signal from all the probe pulses. In order to read a later state of the magnetic evolution and acquire the next data point t_2 , the path length of the probe pulse is increased which results in the probe pulse being delayed by Δt 80

Figure 4.2: (a) Schematic showing the interaction between the electron, lattice and spin subsystems and (b) an example of the time evolution of the different subsystems governed by the rate equations (4.1) – (4.3). The red line corresponds to the excitation laser pulse. The subscripts e , l , and s correspond to the electron, lattice and spin systems, respectively. The evolution of the spin system is shown for a metal (blue dotted line) and a dielectric (blue dashed line). Taken from [68]. 84

Figure 4.3: Schematic demonstrating how the influence of a thermal pulse acts as an excitation mechanism for the precession of the magnetization. (a) Initially the magnetization (\mathbf{M}) is at rest, oriented along the equilibrium direction of the effective field (solid black arrow, \mathbf{H}_{eff}). (b) Upon irradiation from an ultrashort laser pulse ($t = 0$), the elevated temperature causes the value of M_S to decrease. This changes the direction of the effective field and causes the magnetization to precess around the new effective field direction, \mathbf{H}'_{eff} . (c) After a short time ($t = t_{eq}$) the system has cooled and the magnetization has regained the original value of M_S . However it is no longer aligned along the initial effective field direction, \mathbf{H}_{eff} . Therefore, it again begins to precess around the new (original) equilibrium direction..... 85

Figure 4.4: (a) Electrons oscillate around their equilibrium positions as they interact with an electromagnetic field. Due to their orientation in a helical structure their motion will cause a time varying B -field along the direction of electromagnetic wave propagation. This induces an extra polarization of the electrons in the medium. (b) For the case of a plasma in an external B -field, the motion of the electrons due to the electromagnetic wave causes an additional Lorentz force on the electrons. This induces an extra polarization of the electrons..... 89

Figure 4.5: The normal modes in gyrotropic media are (a) Left (LHC) and (b) right handed circular polarization (RHC). (c) When RHC and LHC have the same amplitude and phase their sum results in linear polarization along the y -direction. (d) If there is a phase offset between the RHC and LHC modes then the resultant linear

polarization is rotated. **(e)** If the amplitudes of the RHC and LHC modes are different then the summed wave is elliptically polarized. 94

Figure 4.6: When linearly polarized light enters an optically active medium, it splits into two circularly polarized modes. Because the medium has different refractive indices, the two modes propagate at different speeds and a phase difference is introduced between the modes as it propagates through the medium. This leads to a rotation of the polarization. Additionally, the two modes have different attenuation coefficients so that the relative amplitudes are different after propagating through the medium. This introduces ellipticity to the light. The light that emerges is thus elliptically polarized with the major axis of the ellipse rotated. 96

Figure 4.7: Schematic showing the different Kerr effect layouts. **(a)** In the Polar configuration the z -component, m_z , of the magnetization is responsible for affecting the light. The incident light can come at an angle or normal to the sample surface. **(b)** The longitudinal configuration is sensitive to the in-plane component of the magnetization that is parallel to the plane of incidence, m_y . The incident light must come at an angle in order to be affected, therefore it is necessary to be careful to separate any possible polar effects. **(c)** In the Transverse configuration the magnetization that is perpendicular to the plane of incidence is responsible for affecting the light. Unlike the previous two configurations which affect the angle and ellipticity of the light, this configuration only affects the reflectivity. 99

Figure 4.8: Schematic of the crossed polarizer configuration discussed in text. Light is sent through a polarizer (**L**) oriented at 90° with respect to the plane of incidence so that the light is s -polarized. After light is reflected off the sample (**R**) the polarization is rotated (θ_K) and it becomes slightly elliptic due to the Kerr effect. The light then passes through another polarizer (**L**) oriented at 0° with respect to the plane of incidence. The light that passes through the second polarizer is proportional to the Kerr rotation due to the reflection. The intensity is detected by a photodiode (**PD**). 104

Figure 4.9: Schematic of the balanced polarizer configuration discussed in text. Light is sent through a polarizer (**L**) oriented at 90° with respect to the plane of incidence so that the light is s -polarized. After light is reflected off the sample (**R**) the Kerr effect causes the polarization to be rotated (θ_K) and become slightly elliptic. The light then passes through a polarizing beam splitter (**PBS**) oriented at 45° with respect to the plane of incidence. This splits the light into two even components so that the difference signal is “balanced”. Dynamic changes in the difference (-) of the signal from the two photodiodes (**PD**) give information on the magnetic system and

changes in the sum (+) of the signal from the photodiodes give information on the non-magnetic system. 107

Figure 4.10: Schematic illustration of the experimental setup described in the text. Beam Splitter (BS); Delay Stage (DS); Linear Polarizer ($L(\alpha_p)$); Dichroic Filter (DF); Charge Coupled Device camera (CCD); Witec Microscope (WM); Permanent Magnets (PM); Second Harmonic Generator (SHG); Mechanical Chopper Wheel (MCW); Color Filter (CF); Polarizing Beam Splitter (PBS); Balanced Photodiodes (BPD) 110

Figure 4.11: Precessional and excitation characteristics for a thin film with an in-plane easy axis. **(a)** If the magnetization is oriented normal to the surface by application of a strong external magnetic field, then the precession will be in the xy plane and will contribute no z -component. Therefore, there will be no detected signal in a polar Kerr configuration. **(b)** If the magnetization is oriented along the easy axis, then the pump pulse will heat up the magnetization which will cause the magnitude of the magnetization vector to decrease. However, there will be no subsequent precession because the effective field direction will not change. **(c)** If the magnetization is canted with respect to the easy axis, then the pump pulse will perturb the system so that the magnetization precesses and there will also be a component of the precession along the z -direction so that it will be detectable in the polar Kerr configuration. 111

Figure 4.12: **(a)** Raw TR-MOKE signal from a thin Ni film with $H = 5kOe$ and $\theta_H = 30^\circ$. At $t = 0$ the pump pulse excites the system. This causes the sample to heat up and demagnetize which is represented as a rapid change in the signal. On a slower time scale the magnetization precesses around the effective field. There is still some residual heat in the system which is represented as a slowly decaying backdrop to the oscillation. (red line) **(b)** By subtracting the slowly decaying backdrop from the raw signal the pure dynamical motion given by the LLG equation is left. **(c)** Using an Fast Fourier Transform (FFT) algorithm we can transform the time signal into the frequency domain..... 113

Figure 4.13: **(a)** The decaying oscillation of a Ni film ($H=6 kOe$) **(b)** Fitting the DFT spectra from (a) to a Lorentzian gives $FWHM = 2.8 \pm 0.14$ GHz. **(c)** Demonstration of the effect of the broadening due to the finite scan length. The Conv data points are obtained by convolving a Lorentzian associated with the intrinsic loss with a Sinc function associated with the finite time duration. Fitting the convolved signal gives

$FWHM = 2.89$ GHz. **(d)** DFT spectra and fit to a Lorentzian after using a Hamming window to the data in (a), showing a smaller but non-negligible broadening. 116

Figure 5.1: Schematic of the multilayer structure studied in this chapter. 117

Figure 5.2: **(a)** The Fe and Pt atoms are randomly distributed in the A1 phase. **(b)** The L10 phase is characterized by a very high magnetocrystalline anisotropy. The Fe and Pt atoms occupy successive planes in the crystal..... 118

Figure 5.3: The exchange coupled modes consist of **(a)** an Acoustic Mode in which the two coupled magnetization vectors oscillate in-phase with one another, and **(b)** an Optic mode in which the magnetization vectors oscillate out-of-phase with one another. The sign of J_1 dictates which mode has the lower energy. 119

Figure 5.4: FMR spectra demonstrating the resonance fields of Ferromagnetic and Anti-ferromagnetically coupled films. The solid line is the uncoupled case. The dashed and the dotted lines are the coupled cases, with the dotted line corresponding to a coupling twice that of the dashed line. Care should be taken when comparing results from TR-MOKE and FMR experiments. In FMR with a fixed frequency, the external field is varied through resonance so that the position of the higher energy mode occurs at a lower applied field. In TR-MOKE the field is held fixed and the frequencies measured simultaneously so that the higher energy mode has a higher frequency at that applied field. Taken from [92]. 121

Figure 5.5: **a)** Experimental geometry for single film measurements (Fe or FePt) **b)** Fits of equation (5.8) (lines) to experimental data (symbols) at three angles over a range of applied fields for **(b)** single Fe film and **(c)** single FePt film. Taken from [86]. 124

Figure 5.6: Fits of equation (5.11) (lines) to experimental data (symbols) at three angles over a range of applied fields for **(a)** Fe / Pt($x = 0$ nm) / FePt **(b)** Fe / Pt ($x = 0.5$ nm) / FePt **(c)** Fe / Pt ($x = 1.0$ nm) / FePt and **(d)** Fe / Pt ($x = 1.5$ nm) / FePt **(e)** Experimental geometry of multilayer measurements. Taken from [86]. 127

Figure 5.7: **(a)** Fourier transforms of TR-MOKE time traces for the trilayers with different Pt spacer layer thickness at $\theta_H = 30^\circ$ and $H_a = 4$ kOe. The solid red arrow is a guide to mode 1 and the dashed blue arrow a guide to mode 2. **(b)** Mode frequencies vs. Pt thickness for $H_a = 4$ kOe. **(c)** Fourier amplitudes of the modes at different Pt thickness. Taken from [86]. 128

Figure 5.8: (a) Effective magnetization of the two layers. The dotted line is the strongly coupled M_{eff}^* where the two films can be treated as having a single effective magnetization. (b) Extracted interlayer exchange constant vs. Pt thickness. (c) Optic mode amplitude and $1/J_1$ normalized to Pt = 1.5 nm values vs. Pt thickness. Taken from [86]. 130

Figure 5.9: Simulation (lines) on top of experimental Fourier maps normalized at each Ha. The small Fourier amplitude of the optic mode is difficult to see in the Fourier map so it has been highlighted in the (a) Fe / Pt(0.5 nm) / FePt film and the (b) Fe / Pt(1.0 nm) / FePt film. (c) The experimental Fourier map of the strongly coupled Fe/FePt film with simulation (line) using the modified magnetic parameters M_{eff}^* and γ^* . Taken from [86]. 132

Figure 6.1: Schematic of the double pump experimental setup discussed in the text. Beam Splitter (BS); Neutral Density Filter (ND); Mirror 1 (M1); Mirror 2 (M2); Distance between BS and M1 (d_1); Distance between BS and M2 (d_2); Pump 1 power (P_1); Pump 2 power (P_2); Time delay between pump pulses (Δtp)..... 136

Figure 6.2: (a) Representation of the magnetization vector as a phasor in the complex plane. The black arrow is the precession of the magnetization due to the initial pulse. If the second pulse is timed such that the position of the magnetization vector is $e^{i\theta} = -1$ or π out of phase with respect to $t = 0$, the precession can be quenched (solid red). If the second pulse arrives when the magnetization vector is $e^{i\theta} = 1$ or back in phase with respect to the 1st pulse, the precession can be enhanced (dotted green). (b) The real part of the phasor can be used to visualize the time dependence of the control. Each arrow indicates a different time $t^{(m)}$ discretized by successive values of m . (c) TR-MOKE time and frequency domain signals of the dynamics from a single pulse on a Ni thin film (30nm). (d) By tuning the arrival time of the 2nd pulse, the magnetic precession can be quenched or (e) enhanced. Taken From [117]. 139

Figure 6.3: (a) Phasor and time domain signals of a 10nm Fe film for different pump power ratios (P_2/P_1).. (b) Fast Fourier Transform (FFT) of the time domain signals corresponding to the different ratios. (c) The reason the ratio is less than unity is that as the magnetization precesses it spirals closer and closer to the equilibrium position in the center of the circle. The quenching is shown for the case where $m = 3$. Taken From [116]. 141

Figure 6.4: (a) Schematic of the magnetic multilayer structure. (b) Attempting to quench the FePt resonance (R1) gives discrete values of the location of the Fe resonance (R2) in time $t_1^{(m)}$ which can be mapped onto the complex plane. The arrows show a symmetric path of the position of R2 for successive m traced out in the complex plane starting with the black dashed arrow at $m = 1$. (c) Real component of the phasors for the Fe(10nm) / Pt(5nm) / FePt(10nm) multilayer. (d) Fourier transform and phasor diagram of the stack subjected to only one pulse displaying two resonances corresponding to the different magnetic layers. (e) Fourier transform and phasor diagram demonstrating the quenching of the FePt layer and (f) the Fe layer. Taken From [116]. 143

Figure 6.5: Chord length in the complex plane as a function of the frequency ratio of two resonances. Assuming R1 is being quenched ($\theta_1 = 2m - 1\pi$), the insets show the location and direction of R2 for increasing m at ratio intervals of 0.1. For $f_2/f_1 = 1$ both resonances will be quenched for all m and when $f_2/f_1 = 2$, R2 will always be enhanced. More complex symmetries are possible depending on the ratio, but this example shows how the chord length and the path symmetry depend on the ratio and how by tuning the frequency ratio different locations of R2 can be obtained for different values of m . Taken From [116]. 146

Figure 6.6: Spin pumping induced damping ($\alpha - \alpha_0$) for Py films of varying thicknesses for different adjacent non-magnetic materials. The additional damping due to spin pumping depends on the thickness of the Py layer as well as on the adjacent material. Pt and Pd have short spin relaxation times and act as strong spin sinks causing a larger effect on the damping than Ta. Cu has a long spin relaxation time and has virtually no effect on the damping. Taken from [120]. 149

Figure 6.8: Quenched and Unquenched damping for the Fe(2nm) / Cu (5nm) / Fe (10nm) multilayer. Quenched refers to the case where the other layer has been shut off. For example, red quenched means that the 10nm Fe layer has been shut off so only 2nm Fe is precessing. 153

Figure 7.1: Schematic of different scattering processes between electrons (blue solid arrows) and phonons (red dotted arrows). 157

Figure 7.2: (a) In the presence of a weak magnetic field the distribution of local anisotropy fields causes slightly different effective fields in each region (visualized by different directions of the magnetization vectors within different regions). This causes the different regions to precess at different frequencies which causes the

damping to appear to be larger. **(b)** When the applied field is sufficiently strong, the local variation of the anisotropy field is negligible (arrows all same direction) and all the regions precess at the same frequency. **(c)** This effect can be seen in the α_{eff} vs. H_a graph. At low fields the damping is higher until it approaches a saturation point at high fields which is approximately the intrinsic Gilbert damping..... 160

Figure 7.3: **(a)** Schematic of inhomogeneous excitation due to similarity in the sizes of the pump (blue) and probe (red) pulses. The different amplitudes of the excited region cause a spin wave with non zero k to form and cause an increase in the damping of the system. **(b)** When the pump is large, the effects of disorder are reduced and with a smaller probe pulse, the area that is being probed is more homogeneous. 162

Figure 7.4: **(a)** Non-magnetic Al periodic nanostructures of size d with pitch, p . Taken from [149]. **(b)** After irradiation of a femtosecond pump pulse the elastic dynamics of a structure with $d = 200$ nm displays a $1/p$ dependence on the array pitch (Type II modes). The Type I modes are independent of the pitch and are due to the vibration of the elements themselves (depend on d). Taken from [149]. **(c)** A strain pulse is launched in the Al film which travels through the GaAs Substrate to the (Ga,Mn)As magnetic film where the dynamics are detected by the probe pulse. Taken from [148]. **(d)** The strain pulse initiates magnetic dynamics due to the magneto-elastic interaction in the magnetic film. A combination of these two effects occur in nanomagnetic arrays. Taken from [147]. 164

Figure 7.5: **(a)** SEM image of a periodic Ni array of 156 nm wide squares with a pitch of 330nm. The colors indicate the wavelength and direction of the different SAW modes. **(b)** 2D Spatial Fourier transform of the periodic array from (a). The geometric arrangement of the elements cause discrete points in the spatial Fourier transform which correspond to the different SAWs. **(c)** Magnetic and **(d)** non-magnetic (elastic) H_a vs. Frequency dynamics. The non-magnetic spectra shows field independent frequencies corresponding to the SAWs. In the magnetic spectra (c) there is a magnetic mode that changes with H_a . However, as it passes through the SAW frequencies it is pinned and enhanced. 167

Figure 7.6: **(a)** SEM images of the periodic array (top) and the random aperiodic pattern (bottom). **(b)** 2D Spatial Fourier Transforms of the patterns. The dashed line in the Random 2D Fourier Transform corresponds to the k -vector with the largest average Fourier amplitude, and the solid lines to the limits of SAW influence as defined in the text. **(c)** Average radial Fourier amplitude as a function of k -vector

magnitude (k_r). The periodic array displays discrete k-vectors while the randomized pattern has a continuous spread in k-vectors. The dashed line is a Gaussian fit to this distribution and the solid line the e^{-1} cutoff. The arrow is the maximum average radial Fourier amplitude. Taken from [156]. 170

Figure 7.7: (a) Measured TR-MOKE Fourier spectra of the periodic array. The non-magnetic channel displays well-defined field-independent SAW resonances. The magnetic response is pinned at these SAW frequencies. Dotted black line is the simulated Kittel mode. (b) In the randomized array, the non-magnetic channel shows a drastically reduced signal from the SAWs, indicating that their dominant influence has been suppressed. In the magnetic channel the intrinsic Kittel mode has been restored. There is still slight driving of the magnetization from SAWs at 9.6 GHz and 12.7 GHz. Dotted black line is the simulated Kittel mode. Taken from [155]. 172

Figure 7.8: Side-by-side comparison of absolute Fourier spectra at different applied fields for (a) periodic and (b) randomized array. The periodic spectra are dominated by field-independent modes at the SAW frequencies (dashed lines), while the randomized array shows a dominant, strongly field-dependent peak at the Kittel resonance (red arrows). At 4.5 kOe, the absolute Fourier amplitude of the restored Kittel mode is $\sim 2\times$ larger than the amplitude at that frequency in the periodic array. Taken from [155]. 175

Figure 7.9: (a) Example of random array TR-MOKE time trace ($H = 6$ kOe) and fit to Eqn. (2) ($R^2=0.88$); (b) Effective damping of the Kittel mode or dominant mode in the periodic array along with 95% confidence intervals of the fit. (c) The effective damping in the random pattern shows a restoration of the intrinsic relaxation with high confidence especially at higher fields. In the intermediate region there is still some driving due to weaker radial SAWs. Taken from [155]. 177

Figure 7.10: Magnetic channel Fourier amplitude spectra measured on the (a) Ni and (b) Co arrays with comparison to non-magnetic reflectivity channel. Time sections of $t = 1500\text{--}2500$ ps were analyzed. The dashed white lines indicate the SAW frequencies analyzed. (c-d) Normalized complex Fourier amplitude of the magnetic signal traced at f_{SAW} , after phase adjustment and scaling with the nonmagnetic signal. The circles and squares represent the real and imaginary parts, respectively. The solid and the dashed lines are the fits with the Lorentzian shape. The obtained pinning width ΔH_p , pinning width error and Gilbert damping parameter estimated with Eq. (6) are also displayed. (e) α_{eff} displays effects due to inhomogeneous broadening and approaches the value of a film measured at 6 kOe (straight lines). 183

Figure 8.1: (a) In the $\{x,y,z\}$ coordinate system, the x and y directions are defined by the edges of the nanomagnet and the z-direction is the surface normal. The external field H is applied at $\theta_H = 60^\circ$ with respect to the surface normal. This cants the magnetization vector M_s out of the plane to an angle θ_M with respect to the surface normal and to an in-plane angle, φ_M from the x-axis. The phononic modes k are characterized by their mode indices and their in-plane angle, φ_k . φ_{mp} is the in-plane angle between M_s and k . (b) The magnetization precession can be mapped to the $\{1,2,3\}$ coordinate system defined by the direction of the magnetization vector and the plane of the cone due to the precession of M_s . m_3 is along the direction of M_s at equilibrium, m_2 lies in the film plane and m_1 is orthogonal to m_2 and m_3 190

Figure 8.2: (a) DFT spectra from TR-MOKE measurement at 3.6 kOe of the non-magnetic signal. The time trace is shown in the inset. These frequencies do not change with applied field. Although the (2,1) mode is hard to see in this scan due to its much smaller amplitude compared to the other modes, its presence is verified by observing the full colormap of the magnetic signal. (b) Fit of the phononic modes to equation (8.7). 193

Figure 8.3: (a) DFT spectra of the magnetic channel from TR-MOKE measurements at 1 kOe – 6kOe (left to right) for $\theta_H = 30^\circ, 45^\circ$ and 60° (b) Fits of the magnetic resonances to equation (8.14) at $\theta_H = 30^\circ, 45^\circ$ and 60° over a range of applied field strengths. 196

Figure 8.4: Angular dependences of the various trigonometric terms (8.19-8.23) governing the coupling given by equations 8.17 and 8.18. 199

Figure 8.5: Example of solution to the magnon-phonon part of equation (8.26). When $\omega_c = 0$, the two solutions are attributed to the phononic and magnonic resonances. If $\omega_c \neq 0$, then the two systems are coupled, and close to the region where the magnon and phonon modes are degenerate the modes split and the two solutions have both magnon and phonon character. 201

Figure 8.6: (a) Scanning electron microscope image of 330nm x 330nm x 30nm Ni nanomagnet. (b) When the pump pulse (400nm) irradiates the sample, the deposited heat causes the element to thermally expand, which causes the element to vibrate at eigenfrequencies determined by the geometry and material properties. Additionally, the heat perturbs the magnetization causing the spins to precess around the effective field. Due to magnetostriction, the spin and phonon systems are coupled to one another. A probe pulse (800nm) which is delayed in time monitors the dynamics

following excitation. (c) Fourier amplitude spectra normalized for each field bin of the magnetic and (d) the non-magnetic detection channels. The arrows and dotted lines are indicators of the phononic eigenfrequencies. The positions of these frequencies match in the magnetic and non-magnetic spectra..... 202

Figure 8.7: (a) Different vibrational modes measured in arrays of 200nm Al nanomagnets. Type II modes (red outline) depend on the pitch of the arrays and Type I are the intrinsic vibrations of the elements themselves and are independent of the pitch. Taken from [194]. (b) The crossings in periodic arrays (SEM in inset) discussed in chapter 7 are due to type II modes (c) whereas the crossings in an isolated nanomagnet (SEM in inset) discussed in this chapter are due to type I modes. (d) The coupling for Type II modes is more akin to a forced oscillation since the elastic energy is dominated by the SAW vibrations (red arrow). (e) With type I modes the coupling is more direct, occurring within the element itself..... 205

Figure 8.8: Close-ups of the Fourier amplitude spectra exhibiting anti-crossings for the (a) (1,1) and (b) (2,0) modes. The amplitudes are normalized within each figure. Next to each colormap are the Fourier spectra obtained from the TR-MOKE time trace for the range of applied fields selected by the dotted gray box in the colormap. The two peaks are indicated by the red arrows. The inset in (a) is the boxed region Fourier transformed over a longer time length to display the two modes more clearly. (c) Simultaneous fits of equation (8.26) to the frequencies of the (1,1) and (d) (2,0) modes. The error in the frequencies is the FFT resolution obtained from the time duration of each frequency component in the signal. (e) Mode splitting energy of the (1,1) and (2,0) crossings..... 206

Figure 8.9: (a) Normalized H vs. φ_{mp} plot of the weighted angular coupling term ($\omega_1 C_2 + \omega_2 C_1$). (b) Due to the experimental geometry, only certain out of plane angles of the magnetization θM were accessible for the range of applied fields employed in the experiment. (c) The calculated frequency splitting as a function of φ_{mp} (dotted line in fig 8.9a) as well as the minimum frequency splitting taken from the data. The y-error was calculated from the FFT resolution. For the x-error a resolution of $\pm 10^\circ$ was assumed for the in-plane positioning of the nanomagnet. (d) The experimental configuration and the measured spectra with fits to equation (8.26) when the magnetization is oriented along the edge of the square so that it is parallel with the (2,0) phononic mode and (e) after rotating the nanoelement so that $\varphi_{mp} = 45^\circ$. The spectrum shows an increase in the splitting of the two modes and the fit matches the rotation within $\pm 10^\circ$ 210

Table 8.1: Coupling, Loss rates and cooperativities for the different crossings..... 214

Figure 8.11: Cooperativities of the 3 crossings. The first two are within the intermediate coupling regime while the 3rd is in the strong coupling regime. The DFT spectra at the crossover points are shown next to the colormaps. 215

Table 8.2: Coupling and loss rates for the different crossings extracted from the time domain fits and from the DFT spectra (all values in GHz)..... 216

Figure 8.12: Crossover points and peakfit data for **(a)** the (1,1) crossover, **(b)** the (2,0) crossover at 0° and **(c)** the (2,0) crossover at 45° . **(d)** The FWHM of the peaks and the mode splitting for the different crossings..... 217

Abstract

Magnetoelastic Dynamics in Nanomagnetic Metamaterials

Cassidy Berk

5000 years ago cuneiform was imprinted on clay tablets in order to store information in Mesopotamia. The necessity to store information was due to the increasing complexity of civilizations which evolved after the Neolithic revolution. Today magnetic materials are used in order to imprint 0's and 1's into the spins of electrons. Again, this level of technological prowess is a reflection of our growing complexity as a civilization. Currently, we are in the throes of an information revolution, where individuals, businesses and governments alike store every possible bit of data obtainable. The demands of processing this data faster as well as addressing the massive amount of energy required to store it is going to be a major technological challenge of the ensuing decades. Being one of the dominant means of storing information, it is necessary to explore different methods of manipulating the spins in magnetic structures. Utilizing ultrafast laser pulses enables us to probe the magnetic system at unprecedentedly fast timescales and using the material's elastic degree of freedom may enable more energy efficient control of the spins. At the very least a more thorough understanding of magnetoelastic interactions in condensed matter systems is important from a fundamental perspective.

In this thesis, Time Resolved Magneto-Optical Kerr Effect (TR-MOKE) Spectroscopy is used to characterize magnetic materials. This technique is used to

measure the interlayer exchange coupling in magnetic multilayer structures. Additionally, a novel all-optical method to selectively manipulate spin dynamics in magnetic multilayers is introduced.

Next, the magnetoelastic coupling in nanomagnetic arrays is presented. The array acts as a metamaterial due to the dependence of the elastic and magnetic dynamics on the array geometry. Furthermore, the dynamics are modelled as a forced harmonic oscillator, where the elastic waves act as the driving term. Finally, the magnetoelastic coupling in an individual nanomagnet is explored, and is modeled as a pair of coupled harmonic oscillators. The hybridization between elastic and magnetic oscillations is observed for the first time, and the angular dependence between the relevant elastic and magnetic vectors is used to tune the system into the strong coupling regime.

Acknowledgements

It is interesting to reflect on my mindset as I entered graduate school and began the undertaking of this PhD. Fresh to California, bright eyed and full of hope, I had a full two years of undergraduate research under my belt and was ready to tackle the problems of magnetism (whatever that was). The plan was to start at the ground floor and address the issues in magnetism arising at the level of quantum electrodynamics and work my way up from there.

I knew research would be challenging, but I did not know the extent of the psychological effects that the scientific process has on a fresh researcher—most notably the failure, and the sense of perpetually wandering around in the dark, lost and feeling personally to blame. However, I was also unaware of the sheer joy of discovery that occurs after spending time lost, and how much perspective occurs at the end of the process. I feel extremely fortunate and grateful to have had this experience and am conscious of all of those who helped me throughout:

First off, my advisor Holger Schmidt who supported me from beginning to end. His meticulous ability to pick out relevant information and his solid reliance on quantitative proof has rubbed off on me and without a doubt made me a better scientist.

Second, my parents, Lon Berk and Linda Wetzel and my sister Norah Berk who offered their ear and words of wisdom whenever I needed them.

Third, the *Applied Optics Group*. I have enjoyed everyone who I have had the opportunity to work with. However I must make some special shoutouts. Yu Yahagi,

who mentored me as I first started on this endeavor, and taught me that most problems can be solved through patience and Mike Jaris, my magnetic brother in arms.

Lastly, I must give a special thanks to The Knutzens who provided me with a hilarious and creative outlet during these years.

“Magnetism, you recall from physics class, is a powerful force that causes certain items to be attracted to refrigerators”

—Dave Barry

CHAPTER 1: INFORMATION AND CIVILIZATION

“In the beginning the earth was a bare plain. All was dark. There was no life, no death. The sun, the moon, and the stars slept beneath the earth. All the eternal ancestors slept there, too, until at last they woke themselves out of their own eternity and broke through to the surface.”

-Australian Aboriginal Origin Story

1.1 Early Information Technology

One of the most defining and powerful characteristics of Homo sapiens is their ability to pass on information. While today we take our ability to send an email, calculate driving directions, or save a document for granted, achieving this level of information processing and storage was a gradual process. The first information storage mechanism was the human brain. While the brain's information processing ability is remarkable, we are all aware of the limitations when it comes to memory. The information tends to become corrupted for a multitude of reasons. Personal biases, injury, stress, and age all contribute to the corruption of data. Despite these limitations, in early societies it was the means of storing information. Furthermore, the information was transferred from generation to generation through oral traditions. Ancient orators had a remarkable ability to recount long epics. They worked around

the brain's data corruption issues through the use of mnemonic techniques such as repetitive rhythmic storytelling. In this way concepts of personal history, rule of law and religion (often all intertwined into an overall worldview) could be maintained throughout generations. Information transfer in the way of oral traditions enabled different cultures to form. Additionally, passing on information was vital as a matter of survival. For example, by passing on information regarding seasonal changes early humans were better able to prepare for and live through a harsh winter. Information on what food was edible, what plants make good medicines and improved hunting tactics could also be passed down through the ages.



Figure 1.1: Cave art of lions hunting bison from the Chauvet-Pont d'Arc cave in France. The oldest drawings in this cave date back roughly 30,000 years. Taken from [1].

Additionally, lessons of morality were interwoven into these oral traditions. Developing a moral code enabled humans to cooperate more effectively, enhancing their likelihood of survival. At some point art as a visual aid was incorporated into the story telling. Of all the senses, vision is the most dominant in human beings—the majority of information concerning the environment is obtained through sight. Art as a visual aid to storytelling evoked more imagination in the listeners and enabled a more effective transfer of information. There are examples of cave art found around the world dating back as far as 40,000 years ago. Some of the most preserved cave art can be found in the Chauvet-Pont d’Arc Cave in southeast France. [1] (Fig. 1.1)

1.2 Neolithic Information Technology

Sometime around 12,000 years ago Homo sapiens began settling down into farming communities. This change is known as the Neolithic revolution and marked the beginning of more settled societies. As humans settled down, they began to amass things that they were not able to hold on to as nomadic hunter gatherers. The concept of personal possessions began to form. During the rise of these communities, symbols inscribed on various media began to appear. The oldest of these symbols are the Jiahu symbols inscribed on a tortoise shell found in China which date back 8500 years. (Fig. 1.2) [2] The exact meaning of the symbols is debated by scholars and may never be known. However, the act of inscribing information in the form of symbols onto a permanent medium is a non-trivial development in the information storage ability of Homo sapiens.



Figure 1.2: Jiahu symbols found inscribed on a Tortoise shell in Henan, China. The markings date back to 6600 BC. Taken from [3].

Additionally, farming in these societies provided stability by providing more food which in turn allowed communities to grow. With larger communities, people began to assume different roles within society and more complex social and political systems began to form. More complex societies meant more information was necessary to hold them together. For example, feeding more people became a collective effort which meant information on food yield and reserves needed to be kept track of. Taxes and systems of currency formed around the more complex social and political arrangements. Keeping track of all of this information quickly became too complex for a single person or even group of people relying on memory or abstract symbols inscribed on tortoise shells. As societies became more complex symbols evolved into an actual writing system. Cuneiform is considered the first writing system and emerged in Mesopotamia around 3200 BC. The wedge-like symbols were designed in order to directly convey information in Sumerian. Many of

the tablets were administrative and bureaucratic in origin which reflected the information needs of these increasingly complex societies. However, some have more humanitarian historical interest. The Instructions of Shuruppak are an example of one of the earliest forms of literature which was used in order to convey ideas of morality. (Fig. 1.3) [4]

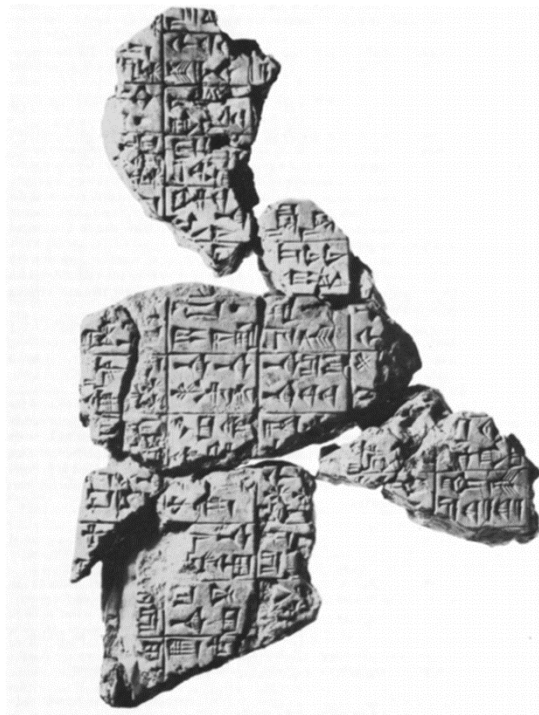


Figure 1.3: Instructions of Shuruppak. Early example of literature written in cuneiform on a clay tablet around 2500 BC. Taken from [4].

It must have been quite difficult being an administrator in ancient Sumer, sorting through clay tablets in an attempt to find a record. The problem was certainly

understood by the ancients and soon a solution was found. Papyrus scrolls were developed. The scrolls could be rolled up so that many more scrolls could be stored in the same area as a clay tablet—increasing the information storage density. Writing on papyrus was much easier than imprinting markings in clay. Additionally, sorting through sheets of papyrus was easier than moving around large clay tablets making data retrieval easier. The only downside was that the scrolls were less durable than clay tablets.

Another development of information technology was the use of alphabets which mapped phonemes to a particular symbol. The spoken word was then able to be directly stored onto a medium, either clay tablet or papyrus. This reduced the complexity of necessitating multiple symbols in order to represent various concepts. The Phoenician alphabet is the earliest alphabet and was spread throughout the Mediterranean world by Phoenician traders. It derived from Egyptian hieroglyphs and from it derived Greek and Latin. Many modern writing systems can therefore be directly linked to the Phoenician alphabet. [5]

Major developments of information storage technology remained relatively stagnant for many years until the advent of the printing press in 1451 by Johannes Gutenberg. This occurred at the beginning of the age of European exploration, when European ships circled the globe in search of riches and adventure as well as in an attempt to spread Christianity. The printing press enabled exciting accounts of these voyages to be spread throughout the populations of Europe which lead to an increase in literacy among the middle classes. [6] Additionally, it allowed scientists to more effectively

share their discoveries with one another since scientific texts were more easily mass produced, which brought about the scientific revolution and the enlightenment. The remarkable change in the availability and communicability of information due to the printing press was a driving factor contributing to the industrial revolution.

1.3 Industrial Information Storage

Once again information technology was drastically altered by another monumental change in human civilization—the industrial revolution. Typically traced to the development of the steam engine by Thomas Newcomen in 1712 [7] the industrial revolution marked the beginning of industrialized society as well as ushering in unprecedented developments in science and technology. Machines began to assist every aspect of human life. As societies industrialized and became more complex, improvements to information technology followed. In 1725 the punch card was invented by Joseph Marie Jacquard as a means for representing digital data and controlling a loom. [8] In 1832 Semen Korsakov conceived of a machine to use punch cards to store and retrieve information. [9] The industrial revolution also ushered in the age of electricity. Through the work of Andre-Marie Ampere, Charles-Augustin de Coulomb, Michael Faraday and James Clerk Maxwell, humanity learned of the intimate connection between electricity and magnetism. It wasn't long before information technology was affected by this newly discovered relationship. Magnetic materials which are the topic of this thesis became a dominant medium for the storage of information.

1.4 Magnetic Recording

The first magnetic recording was demonstrated by Valdemar Poulsen in 1898 who recorded a human voice on a ferromagnetic wire. [10] In 1928 magnetic tape was invented in Germany. The tape consisted of Fe_2O_3 coated on a strip of paper. [11] Along with the development of the ring shape taped head in 1933 and AC biasing the quality of audio recording vastly improved. [11] In 1951 tape was used to record digital data at a density of 256 bits/in². The bits are physically represented as the magnetization orientation of a collection of grains. (Fig. 1.4 a) Improvements to the bits/in² metric are a perpetual drive of the storage industry. In 1956 the first magnetic hard disk drive (HDD) was developed by IBM. Known as RAMAC and operating at 2000 bits/in², this HDD was intended to be used on main frame computers. Today, HDDs are standard on all personal computers and have storage (areal) densities of 10¹² bits/in² (1 TB/in²). [11] HDDs consist of a disk with a magnetic material as the storage medium, a head which can both write and read the data, a motor, and circuitry for signal processing, and motor feedback and control. [12] The write head is a tiny electromagnet.

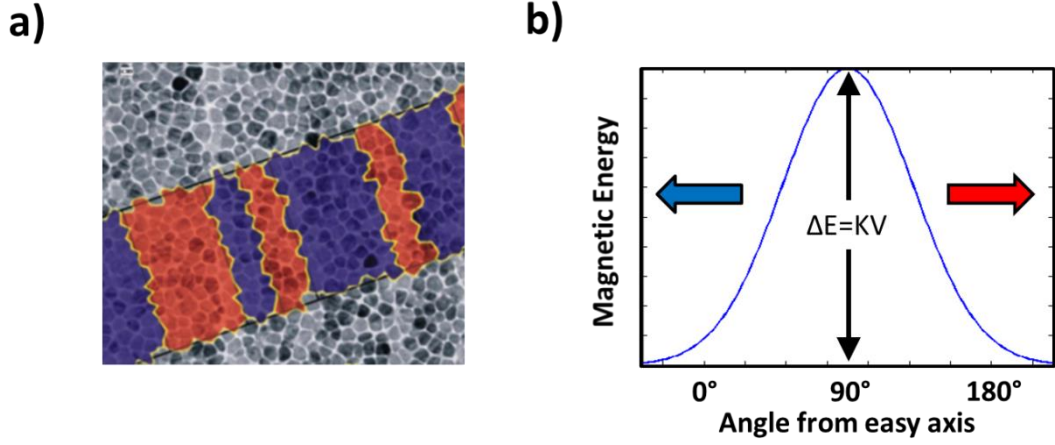


Figure 1.4: (a) Example of bits (red or blue) written into a granular magnetic material. A bit consists of a region composed of multiple magnetic grains all oriented in the same direction. Taken from [12]. (b) Energy barrier separating two different magnetic states. When this barrier becomes comparable to the thermal energy in the room ($k_B T$), the bits become less stable.

1.4.1 Superparamagnetic Effect

As HDD areal densities increase and the sizes of bits decrease, fundamental limits become an issue. One limit is due to the superparamagnetic effect. In small nanoparticles the direction of the magnetization can flip due to the thermal energy of the room (~ 300 K). (Fig. 1.4 b) The time between successive flips is given by the Neel relaxation time [13]

$$\tau_N = \tau_0 e^{\left(\frac{KV}{k_B T}\right)} \quad (1.1)$$

Where τ_0 is a characteristic time related to the material, K is the anisotropy constant, V is the volume, k_B is the Boltzmann constant, and T is the temperature. Therefore, as dimensions decrease, the anisotropy must increase in order to maintain stability. Increased anisotropy requires more energy to write the bits which is limited by the accessible magnetic fields of write heads. Therefore, there is a tradeoff between size, stability and energy consumption. The industry standard for HDD stability is $\tau_N = 10$ years which translates to $\frac{KV}{k_B T} > 60$. [12]

Achieving storage densities of this magnitude has been a continual process of improving all aspects of the device. Some examples are utilizing perpendicularly magnetized materials rather than materials that are magnetized in the plane (longitudinal). (Fig. 1.5) Advantages to perpendicular recording media are that the superparamagnetic limit is different, allowing the dimensions of the grains to be scaled down. Additionally, it is possible to use amorphous materials with no grains at all in which bits are stable at even smaller sizes. [14]

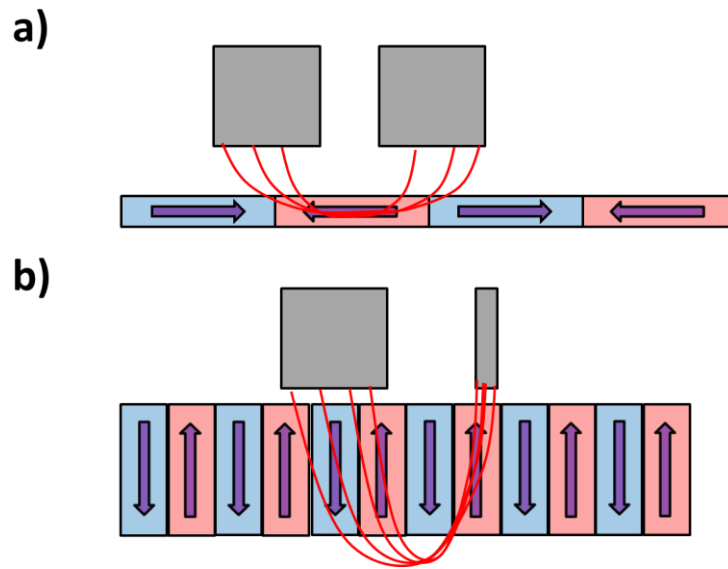


Figure 1.5: (a) Example of longitudinal recording and (b) perpendicular recording. Perpendicular recording offers the benefit of increased storage areal densities.

1.4.2 Giant Magnetoresistance

Another major achievement in increasing areal densities came from improvements in the read head due to the giant magnetoresistance Effect (GMR). GMR was discovered in 1988 [15] and commercialized by IBM in the 1990's [16]. GMR is a change in the resistance due to the mutual orientation of two magnetic thin films separated by a spacer layer. If the two magnetizations are oriented in the same direction the resistance is low, if they are oriented in opposite directions the resistance is high. (Fig. 1.6) This effect improved the SNR of the readout process and allowed smaller elements to be detected.

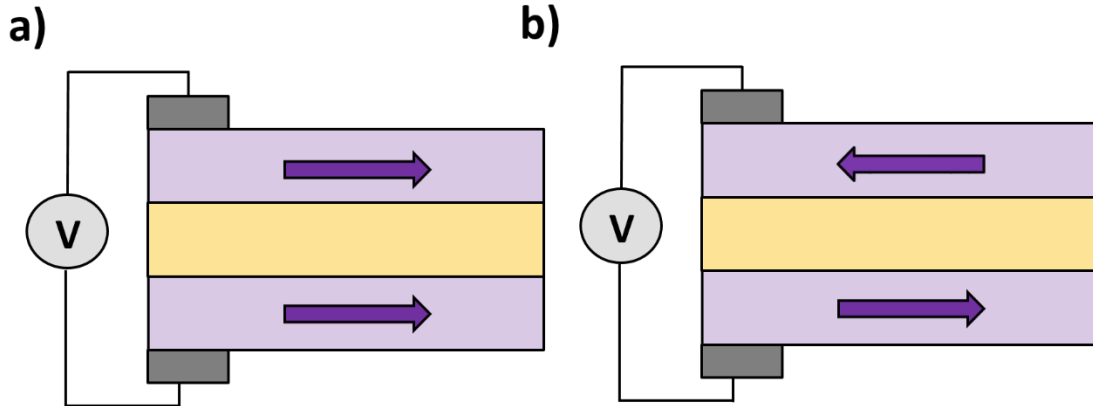


Figure 1.6: (a) When the magnetization of two layers are oriented in the same direction, current flows through the system more easily—the structure has a low resistance. (b) When the magnetizations of the layers are anti-parallel there is more spin scattering resulting in a higher resistance.

1.4.3 Bit Patterned Media

In general there are two ways to address the super-paramagnetic limit. From equation 1.1 we see that in order to maintain the industry stability criteria we can either increase K or V . While at first glance it would seem that increasing V would be counterproductive to increasing areal densities this is not entirely true. Replacing granular media with bit patterned media increases the volume term responsible for the superparamagnetic effect while decreasing the size of a bit. (Fig. 1.7) This is the case because in patterned media the KV energy is a function of the isolated nanomagnet rather than an individual grain as in the case of granular media. [17] While the patterned nanomagnet is bigger than a grain, it is smaller than the bit area which is

made up of many grains. Another advantage of patterned media is that transition noise which occurs due the imperfect boundary between bits in granular media is eliminated. The major issues facing bit patterned media are systemic. The HDD industry relies on the technological infrastructure already in place. Fabrication of patterned bits at competitive dimensions would require a change in the industrial fabrication process. [12] Additionally, addressing each bit for the read and write process would require vast improvements to the synchronization between the read and write heads and the location of the bits. Currently, in granular media the bit positions are determined by the location of the write head. [17]

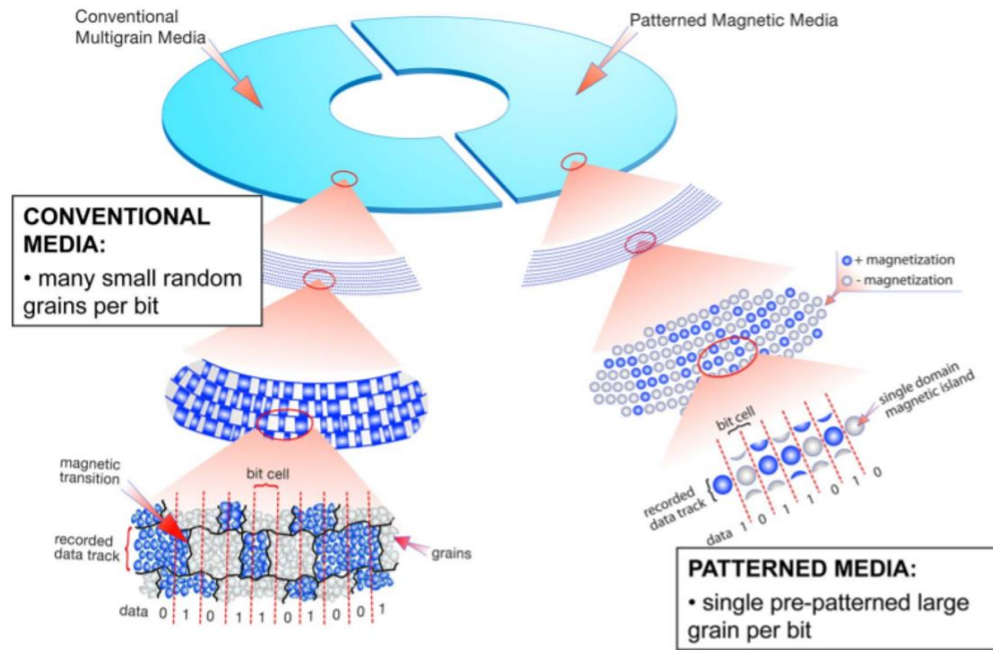


Figure 1.7: Schematic showing the difference between conventional granular media and patterned magnetic media. Taken from [12].

1.4.4 Heat Assisted Magnetic Recording

Increasing K is another way of addressing the superparamagnetic limit. A higher K material is more stable and therefore less likely to be affected by thermal fluctuations. However, it also requires a larger magnetic field to switch the magnetization direction. This is limited by the capabilities of the write head. A new technology which addresses this problem is known as heat assisted magnetic recording (HAMR). (Fig. 1.8) In this device a laser is incorporated into the write head. The laser locally heats up the magnetic material which lowers the material's coercivity enabling it to be switched by the magnetic field from the write head. When the material cools, the coercivity returns to normal and the bit remains in its switched state. This allows higher K materials to be used so that grains can be shrunk down. This technology was launched in 2019 by Seagate with an areal density of 2 TB/in². However, areal densities of 10 TB/in² have been theoretically proposed. [18]

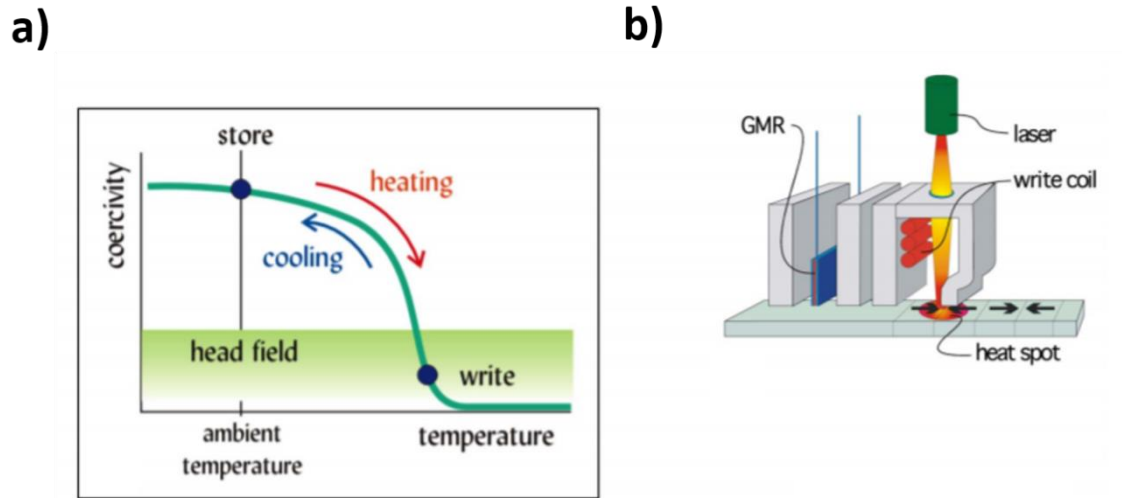


Figure 1.8: (a) Example of the write process in HAMR. Initially the bit is stored in a state which is too hard to switch (high coercivity). Application of a laser heats the magnetic material resulting in a decrease of the coercivity so that the bit can be affected by the magnetic field from the write coil. As the magnetic material cools it assumes its original stable state. (b) Schematic of HAMR write head. Taken from [12].

1.4.5 All-Optical Switching

In addition to improvements of the recording media and read head, novel effects for writing the bits are being explored. One of the most exciting recent discoveries concerning ultrafast manipulation of magnetism was all-optical switching (AOS). [19] Using circularly polarized femtosecond laser pulses, the orientation of the magnetization could be switched deterministically. (Fig. 1.9) The switching occurs in

the absence of an external field and depends on the helicity of the light. The most likely mechanism causing the switching has been thought to result from the optomagnetic field induced by the circular polarization of the light and is known as the inverse Faraday effect. Initially demonstrated in ferrimagnetic films with circularly polarized light, AOS has also been demonstrated in thin ferromagnetic films. [20] Additionally, switching has been demonstrated using linearly polarized pulses in ferrimagnetic structures. [21] In these systems the heat from the laser pulse causes the different sub-lattices to demagnetize at different rates. The interaction between the different sublattices' demagnetization dynamics causes the system to switch orientation. [22] The full microscopic description of AOS that accounts for the interaction of optomagnetic effects, heating effects, and scattering of the different sub-systems is STILL being debated. [23]

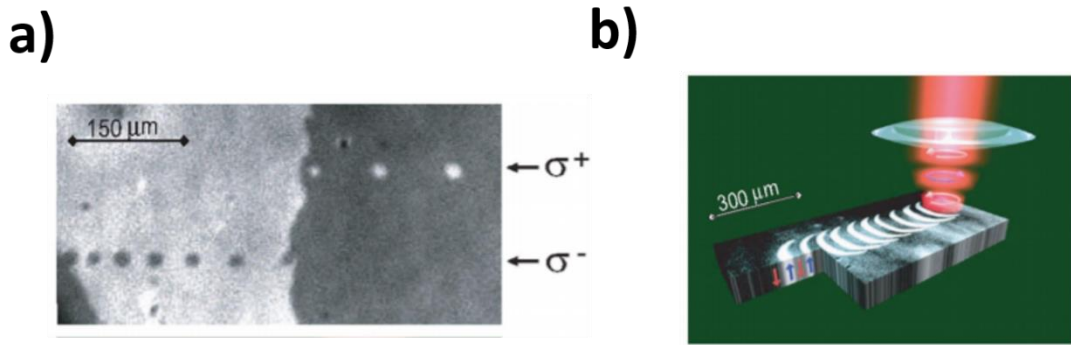


Figure 1.9: (a) Experimental demonstration of all-optical switching (AOS) on a GdFeCo thin film. The different contrasts of the film are obtained using a Kerr

microscope and represent the magnetization orientation. Right handed circularly polarized light (σ^+) only affects the magnetization oriented in one direction while left handed circularly polarized light (σ^-) affects the magnetization oriented in the other direction. **(b)** Schematic showing how AOS could be used to write bits. Taken from [19].

1.4.6 Fundamental Questions and Other Technological Applications

Part of the reason AOS is still not understood is that the timescales which govern the electronic interactions are only recently becoming experimentally accessible. The advent of femtosecond laser systems have provided a means of probing these interactions at relevant time scales. The phonon system typically has dynamics around ~ 1 ps, the spin system ~ 100 fs and electron system ~ 10 fs. [24] Understanding and manipulating interactions at these timescales could have implications for future magnetic technologies operating at THz frequencies. (Fig. 1.10 a) A burgeoning field is that of spintronics (magnonics) which uses the spin of the electron or spinwaves (magnons) to improve data storage, information processing and communication technology. [25] Spintronics may supplement or even replace certain areas of electronics which use the charge as the information processing unit. (Fig. 1.10 b) Using magnons instead of charge to process information has certain benefits such as non-dissipative heating (transport of magnons does not cause heating of the device). Additionally, as device dimensions shrink and the wavelength of the spin wave decreases, the exchange interaction becomes dominant. The wave velocity of these

exchange magnons increases with increasing wave vector which has potential in nanoscale signal transmission devices. [25] Additionally, computing speeds could increase due to the quadratic scaling of the exchange magnon frequency. [26] Achieving these technologies will require solutions to problems that are deeply fundamental in nature.

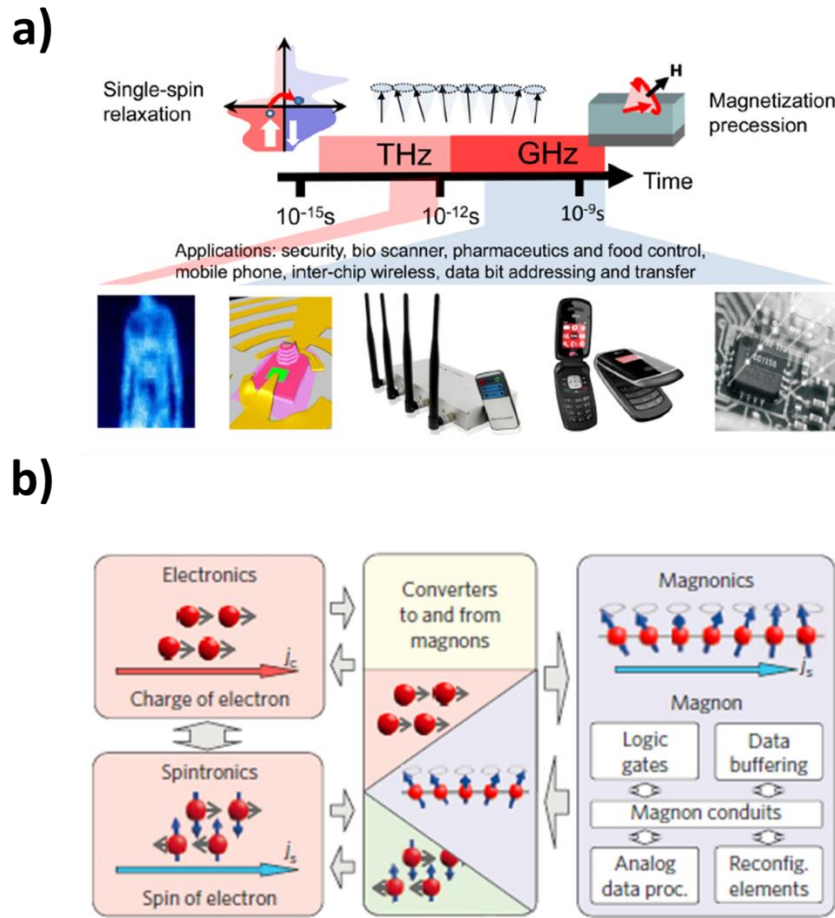


Figure 1.10: (a) Illustration of the timescales of magnetic processes and some potential technologies which could be impacted. Taken from [24]. (b) Magnons have

many data processing applications. In some instances magnonics may replace electronics. However, realistically they will be implemented into existing technologies which will require mechanisms for converting between spin and charge. Taken from [26].

1.5 Contemporary Information Technology

We are currently in the throes of an information revolution, where individuals, businesses and governments alike store every possible bit of data obtainable. The demands of processing this data faster as well as addressing the massive amount of energy required to store it is going to be a major technological challenge in the ensuing decades. Trends in big data, e-commerce and a shift towards internet based media are contributing to the ever growing energy consumption of data centers. Currently data centers use roughly 200 terawatt-hours each year. This accounts for 1% of global electricity use. This could rise to 8% of global demand by 2030. [27] Additionally, the information and communication technology (ICT) industry accounts for 2% of global carbon emissions. ICT consists of not just data centers which comprise 0.3% of emissions, but also personal electronic devices, and the network infrastructure supporting them. This percentage will only increase with the rise of artificial intelligence and the internet of things in which the number of internet connected devices is expected to double by 2020. [28] Therefore, in order to meet the

future electricity demands facing the ICT sector improvements in energy efficiency is extremely important.

1.6 Metamaterials

As we are faced with new technological challenges sometimes it is necessary to create a material with novel characteristics. These engineered materials are known as metamaterials and are created by periodically modifying various parameters to affect the wavelength of the system of interest (e.g. electromagnetic, magnetic or elastic). For example, the index of refraction can be altered to produce novel electromagnetic effects. [29] In this thesis, we will see how the periodic arrangement of nanomagnetic elements as well as the geometry of an individual element can give rise to novel elastic and magnetic effects which are connected via the magnetoelastic effect.

1.7 Problem Statement and Chapters

Being a dominant means of storing information, faster and more energy efficient means of manipulating the spins in magnetic materials is important. As discussed, femtosecond laser pulses provide a means of manipulating and probing the spin dynamics at unprecedentedly fast time scales. Additionally, the elastic (phononic) degree of freedom is an alternative means of manipulating the spins which may aid in improving the efficiency of future devices. At the very least, a complete understanding of the various mechanisms concerning the manipulation of the spin system is necessary from a fundamental point of view. In this thesis, we use ultrafast optical spectroscopic techniques to characterize and manipulate magnetic materials as

well as exploring the coupling of elastic and magnetic degrees of freedom in technologically relevant nanomagnetic arrays and individual isolated nanomagnets.

In Chapter 2 we discuss the quantum mechanical origins of magnetism. Starting from a single electron and ending with multi-electron atoms in a crystalline environment we cover the underlying forces which are responsible for the effects discussed in later chapters. A complete understanding of magnetism is only possible if the quantum mechanics of atoms and crystals is understood.

In Chapter 3 we continue the theoretical exploration of magnetism into the macroscopic limit. When a sufficient number of atoms are present, the quantum physics converges to classical physics and continuum mechanics can be used to model the magnetization dynamics. In this realm, understanding the magnetic system is accomplished by breaking the system down into different phenomenological energy terms. While the quantum physics discussed in Chapter 2 is essential for understanding the origin of these energies, the dynamics in this thesis are mathematically described in this macroscopic realm.

In Chapter 4 we cover the theory behind the Time-Resolved Magneto-Optic Kerr Effect which is the experimental technique used to measure the dynamics in this thesis. We also discuss the experimental setup and some intuitive concepts necessary to correctly implement the experiment and analyze the experimental data.

In Chapter 5 we demonstrate how the experimental techniques of chapter 4 can be applied to characterize magnetic materials. We measure intrinsic magnetic parameters

of individual magnetic thin films as well as measuring the interlayer exchange coupling in magnetic multilayer structures.

In Chapter 6 we introduce a novel all-optical technique for manipulating the spin resonances in multilayer magnetic structures. We show that by appropriately tuning the timing between two femtosecond laser pulses we are able to selectively quench or enhance a specific spin wave mode within the multilayer structure.

In Chapter 7 we discuss the magnetic damping parameter in more detail, covering intrinsic and extrinsic contributions. We also introduce the concept of magneto-elastic coupling and how it affects the dynamics in arrays of nanomagnetic elements. We discuss how magneto-elastic effects can be mitigated by controlling the geometry of the array as well as how they can be used to measure the damping the arrays. These array structures are metamaterials due to the ability to control their properties through altering their geometry.

In Chapter 8 we discuss the magneto-elastic dynamics in an individual nanomagnet which is also dependent on the structure's geometry. In the individual nanomagnet we are able to spectroscopically resolve the strong coupling between magnetic and elastic modes. We show how we can control the extent of the coupling by using an external magnetic field. Finally, we provide a 2-dimensional mathematical description of the phenomenon.

In Chapter 9 we summarize the results of the thesis.

CHAPTER 2: MICROSCOPIC MAGNETISM

“One can still say that quantum mechanics is the key to understanding magnetism. When one enters the first room with this key there are unexpected rooms beyond, but it is always the master key that unlocks each door.”

-John H. Van Vleck

2.1 Single electron

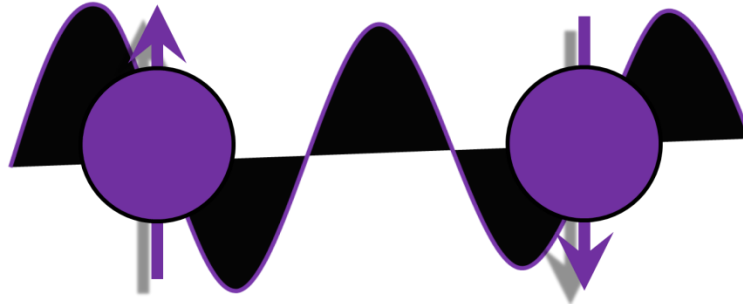


Figure 2.1: The electron is a wavelike particle with an intrinsic property known as spin. The name spin comes from the similarity to angular momentum. However, the exact nature of what causes spin is debated.

What is the electron spin? Does it come from the little ball of mass spinning faster than the speed of light? Does it stem from the circular flow of energy due to the electron's wave field? [30] Is it just the basic fundamental quanta of angular momentum? Can the internal structure of the electron explain it? The origin of the spin angular momentum has been the source of much debate. What is sure, is that it exists. For an electron, the spin can take on two quantized values along a given axis [31]

$$\mathbf{S}_z |\pm\rangle = \pm \frac{\hbar}{2} |\pm\rangle \quad (2.1)$$

Where \mathbf{S}_z is the spin angular momentum operator projected along the z axis, $|\pm\rangle$ are the eigenkets of \mathbf{S}_z , $\pm \frac{\hbar}{2}$ are the eigenvalues, and \hbar is the reduced Planck constant. The two spin states are degenerate in the absence of any external perturbations. If an external field is applied along the positive z-direction then the degeneracy of the two states is lifted so that $|+\rangle$ is the lower energy state.

Additionally, if the electron is prepared in a particular spin state ($|+\rangle$ or $|-\rangle$), the spin component measured along a different axis is given by [31]

$$|S_u; \pm\rangle = \frac{a}{\sqrt{2}} |+\rangle \pm \frac{b}{\sqrt{2}} |-\rangle \quad (2.2)$$

Where $|S_u; \pm\rangle$ are the eigenkets of the observable \mathbf{S}_u along the new axis. \mathbf{S}_u also has eigenvalues $\pm \frac{\hbar}{2}$. If $u = x$ then $a = b = 1$. If $u = y$ then $a = 1$ and $b = i$. The total angular momentum operator can also be defined as

$$\mathbf{S} \cdot \mathbf{S} = S^2 = S_x^2 + S_y^2 + S_z^2 = \frac{3}{4} \hbar^2 \quad (2.3)$$

Figure 2.2 shows the relationship between the total angular momentum and the quantized values along the z-axis.

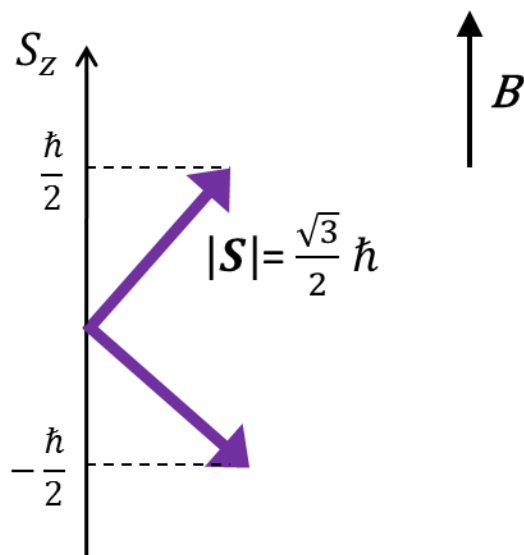


Figure 2.2: Relationship between the total spin angular momentum and the projections onto the z-axis.

2.2 Electron and Nucleus

2.2.1 Angular Momentum and Magnetic Moments

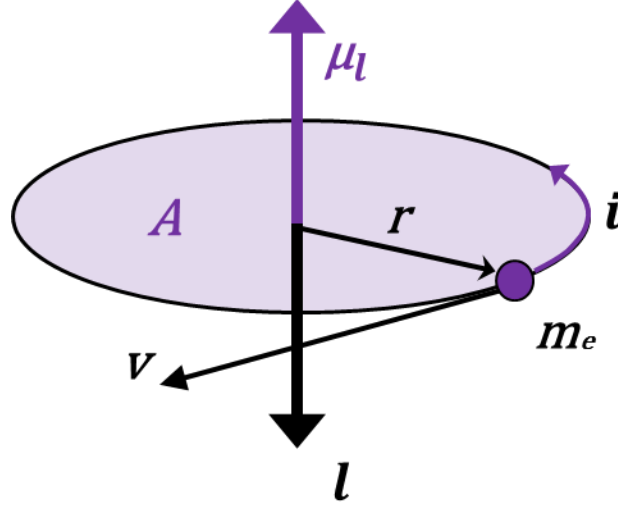


Figure 2.3: Vector diagram showing the relationship between the angular momentum, l , of the electron, which arises due to the circulating electron mass, m_e , and the magnetic dipole, μ_l resulting from the circulating current, i .

In the presence of a nucleus the electron's circular motion around the nucleus results in another form of angular momentum called *orbital* angular momentum. [32] The classical equation for angular momentum is

$$\mathbf{l} = m_e(\mathbf{r} \times \mathbf{v}) \quad (2.4)$$

Where m_e is the mass of the electron, \mathbf{r} is the distance from the nucleus and \mathbf{v} is the electron's velocity. Because the electron has an intrinsic charge, e , associated with it,

this circular motion corresponds to a current loop which leads to a *magnetic moment*.

The classical relation is $\mu = iA$, with $i = \frac{ev}{2\pi r}$ and A is the area of the circular loop.

(Fig. 2.3) Putting these together results in the following equation for the orbital magnetic dipole moment

$$\boldsymbol{\mu}_l = \frac{e}{2m_e} \mathbf{l} \quad (2.5)$$

Since e is negative the magnetic moment is antiparallel to the angular momentum.

The importance of this relation cannot be understated as it serves to highlight the intimate relation between the magnetic moment and angular momentum. It is often expressed as

$$\boldsymbol{\mu}_l = -g_l \frac{\mu_B}{\hbar} \mathbf{l} \quad (2.6)$$

Where $\mu_B = \frac{e\hbar}{2m_e}$ is the Bohr magneton, the fundamental unit for the magnetic moment. Comparing with equation (2.5) we can see that μ_B is the magnetic dipole moment of an electron with $|\mathbf{l}| = \hbar$. g_l is the *orbital* g-factor which is a dimensionless scaling term that depends on the particle or system it represents. Additionally, we can assign a *spin* magnetic moment to the electron due to the intrinsic *spin* angular momentum discussed previously

$$\boldsymbol{\mu}_s = -g_s \frac{\mu_B}{\hbar} \mathbf{s} \quad (2.7)$$

Where $g_s = -2.0023$ is the g-factor for the *spin* of the electron. From this we see that the projection of $\boldsymbol{\mu}_s$ onto an axis of quantization is approximately equal to μ_B .

2.2.2 Hydrogen-Like Atoms and Atomic Orbitals

A single electron orbiting a nucleus is the Hydrogen atom. The time-independent Hamiltonian of the Hydrogen atom is given by a kinetic energy term due to the motion of the electron and a potential energy term due to the binding Coulomb potential of the nucleus. It is given by

$$\mathcal{H} = \frac{p^2}{2m_e} - \frac{Ze^2}{r} \quad (2.8)$$

where p is the momentum of the electron and Z is the nuclear charge ($Z=1$ for the Hydrogen atom and can take other values for Hydrogen-like atoms). Equation (2.8) is a quantum well in a spherically symmetric potential and leads to the following eigenvalue equation known as the *Schrödinger equation*

$$\mathcal{H}\phi_{nlm} = E_{nlm}\phi_{nlm} \quad (2.9)$$

Where E_{nlm} is the energy eigenvalue and ϕ_{nlm} are the eigenfunctions (wavefunctions) for the electron. Since the potential is spherical the eigenfunctions are expressed in spherical coordinates

$$\phi_{nlm} = R_{nl}(r)Y_l^m(\theta, \varphi) \quad (2.10)$$

where $R_{nl}(r)$ is the radial component which depends on the distance of the electron from the nucleus, r , and $Y_l^m(\theta, \varphi)$ are spherical harmonics, which describe the polar (θ) and azimuthal (φ) distribution of the wavefunctions. Their expressions are in every quantum mechanics textbook [31,33] and will not be repeated here.

These wavefunctions serve as a basis for determining the configuration of more complex atoms. As we add more electrons, they occupy successive eigenfunctions given by equation (2.10). The wavefunctions (and thus a particular electron within an atom) can be identified by the quantum numbers n , l and m . Finding the lowest energy state of an atom consists in identifying which atomic orbital wavefunctions are occupied with electrons and which are not. This is accomplished by identifying the lowest energy orbital wavefunctions in a particular atomic environment. Additionally, this ground state can be a superposition of multiple wavefunctions. In the spherically symmetric potential of a Hydrogen-like atom with a single nucleus, the energies of the eigenfunctions do not depend on θ or φ and we are left with the eigenvalue equation

$$\mathcal{H}R_{nl}(r) = E_n R_{nl}(r) \quad (2.11)$$

Where E_n are the energy eigenvalues given by [31]

$$E_n = -\frac{Z^2 e^2}{2n^2 a_0} = -\frac{Z e^2}{2r_n} \quad (2.12)$$

where $a_0 = \frac{\hbar^2}{me^2}$ is the *Bohr radius* and $r_n = \frac{n^2 a_0}{Z}$. The energies depend on the principal quantum number n , which designates the electron shell. For each successive n the electron is located farther from the nucleus and another node is introduced in the radial function. For the n -th level there are n^2 degenerate states, which can be further branded by the quantum numbers l and m_l . The angular quantum number l designates the subshell or orbital of the electron with the requirement that $l < n$. The values of

$l=0,1,2,3,\dots$ correspond to letters s,p,d,f which were chosen based off the first letter of the spectral properties of alkali metals (sharp, principal, diffuse and fundamental). Within each subshell (characterized by l) there is a subset of $2l + 1$ different spatial configurations of the orbitals. These are further identified by the magnetic quantum numbers m_l . This number corresponds to the projection of the orbital momentum onto an arbitrarily chosen axis and can take values $\{l, l - 1, \dots, -l\}$. In the spherically symmetric potential of the Hydrogen-like atom the orbitals in the electron shell are degenerate. The degeneracy within a subshell can be broken by application of an external magnetic field (*Zeeman Effect*)—hence the name *magnetic* quantum number.

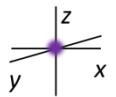
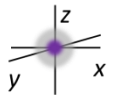
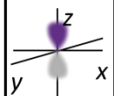
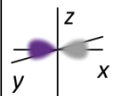
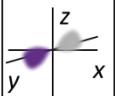
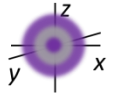
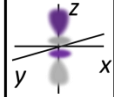
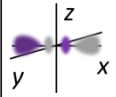
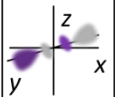
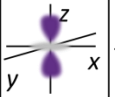
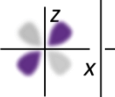
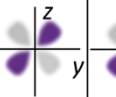
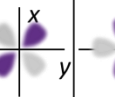

	<i>s</i>	<i>p</i>			<i>d</i>				
<i>l</i>	0	1			2				
<i>m_l</i>	0	0	± 1		0	± 1		± 2	
	$ 0\rangle$	$ z\rangle$	$ x\rangle$	$ y\rangle$	$ z^2\rangle$	$ xz\rangle$	$ yz\rangle$	$ xy\rangle$	$ x^2 - y^2\rangle$
n=1									
n=2									
n=3									

Figure 2.4: Atomic orbitals. Each row of orbitals is a successive electron shell characterized by quantum number n . The columns separate the different electron orbitals or subshells (s,p and d) which are specified by their orbital quantum number l . The different spatial configurations of the subshells are further specified by their

magnetic quantum number m_l . The spatial designation of each orbital is shown below its magnetic quantum number.

The two most widely studied and technologically relevant groups of magnetic materials are the iron group magnetic materials characterized by elements with unfilled $3d$ shells and the rare earth elements characterized by elements with an unfilled $4f$ shell. Because both of these shells have many orbital states for the electrons to occupy, elements with unfilled shells can have a large net magnetic moment even at room temperature. [34]

2.3 Multi-Electron Atoms

2.3.1 Hartree-Fock Approximation and Slater Determinant

As we add more electrons to the atom, they begin to interact and another term enters into the Hamiltonian. In the absence of spin orbit interaction or a magnetic field, the Hamiltonian is given by

$$\mathcal{H} = \sum_{i=1}^Z \frac{p_i^2}{2m} - \sum_{i=1}^Z \frac{Ze^2}{r_i} + \sum_{i<j}^Z \frac{e^2}{|r_i - r_j|} \quad (2.13)$$

Where similar to above, the first term represents the kinetic energy, summed over all of the electrons. The second term is the sum of all the potentials due to the nuclear-electron interactions and the third term is the Coulomb repulsion due to the presence of the other electrons.

In order to describe the configuration of an atom using this Hamiltonian a global eigenfunction which depends on the coordinates of *all* the electrons must be chosen. Since electrons are *fermions*, no two electrons can occupy the same state simultaneously. This is known as the *Pauli exclusion principle* and requires that the global wave function be anti-symmetric* upon interchanging the coordinates of two electrons (spin or position) and is zero if they occupy the same state.[35] J.C. Slater in 1929 came up with a global wavefunction known as the Slater determinant which satisfies the antisymmetry criteria

$$\psi = \frac{1}{\sqrt{N!}} \begin{vmatrix} \phi_1(r_1) & \phi_2(r_1) & \cdots & \phi_N(r_1) \\ \phi_1(r_2) & \phi_2(r_2) & \cdots & \phi_N(r_2) \\ \vdots & \vdots & \ddots & \vdots \\ \phi_1(r_N) & \phi_2(r_N) & \cdots & \phi_N(r_N) \end{vmatrix} \quad (2.14)$$

Where $\phi_i(\mathbf{r}_j)$ refers to electron i located at position j . We still use single electron orbitals to describe the state of the multi-electron atoms. Self-consistently solving

* To see why this is the case, assume two particles, each in a different state $\phi_1(r_1)$ and $\phi_2(r_2)$. If the particles are indistinguishable, then the global state ψ of the two-particle system is either $\phi_1(r_1)\phi_2(r_2)$ or $\phi_2(r_1)\phi_1(r_2)$. Before measurement, we say that the particles exist in a superposition of both states. Therefore, $\psi = \phi_1(r_1)\phi_2(r_2) \pm \phi_2(r_1)\phi_1(r_2)$, where the plus sign indicates the symmetric state and the minus sign the anti-symmetric state. If the particles are in the same state, then the anti-symmetric state is $\psi = \phi_1(r_1)\phi_1(r_2) - \phi_1(r_1)\phi_1(r_2) = 0$. This cannot be the case because then the wavefunction vanishes. Therefore, making the global wave function antisymmetric ensures that the particles do not occupy the same state simultaneously. [35]

equation (2.13) with the Slater determinant wavefunction is known as the *Hartree-Fock Approximation*. It captures some of the basic physics but unsurprisingly fails to explain all atomic phenomena. However, the true behavior of the atoms can be explained by introducing perturbations to this approximation, thus making it relevant from a conceptual perspective. [36]

As we add electrons to the atom, we are interested in the overall ground state atomic configuration—which orbitals get occupied first. Due to the Pauli exclusion principle an electron can only occupy one quantum state at a given time. However, the spin of the electron provides another degree of freedom. *Kramers degeneracy theorem* tells us that in the case of a spin $\frac{1}{2}$ particle, every state is double degenerate. [36] This means two electrons can occupy the same orbital as long as they have opposite spin. We now need another quantum number that we can use to identify a particular electron, the spin quantum number m_s ($1/2, -1/2$). Additionally, within a given subshell there are now $2(2l + 1)$ possible quantum states for the electron to occupy, where the 2 comes from the two spin states.

2.3.2 LS-Coupling

The angular momentum of all the electrons in a particular atomic configuration can be summed to get the total orbital angular momentum $\mathbf{L} = \sum_i \mathbf{L}_i$ and total spin angular momentum $\mathbf{S} = \sum_i \mathbf{s}_i$. If a specific shell is completely filled with electrons, \mathbf{L} and \mathbf{S} are zero and the atom has no net magnetic moment. If this is not the case, then the m

electrons in the unfilled shell will have $N = \binom{2(2l+1)}{m}$ possible ways to be distributed among the $2(2l+1)$ orbital states. [36] The N sets of configurational states each have an L and S associated with them. The sum of total orbital L and spin S angular momentum results in a Total angular momentum $\mathbf{J} = \mathbf{L} + \mathbf{S}$, and the sets of configurations which have the same J are called *multiplets*. Without other perturbations to the system (such as spin-orbit coupling) these multiplets are *degenerate*.

If spin orbit coupling is introduced to the system then the multiplet energy levels no longer all have the same energy. There are two methods of coupling the spin and orbital components which depend on the relative strength of the spin-orbit interaction. The first method couples the total orbital and spin moments of the atomic configuration ($\mathbf{J} = \mathbf{L} + \mathbf{S}$) and is known as *Russel-Saunders Coupling*. It is valid for the lighter elements when the coulombic interaction between the electrons (last term in Eq. 2.13) is greater than the individual electron's spin-orbit interaction. In this case the multiplets' energies are split by introducing spin-orbit coupling as a perturbation. With heavier elements spin-orbit or jj coupling is stronger than the coulombic repulsion from the other electrons. In this case the coulombic interaction acts as the perturbation. (Fig. 2.5)

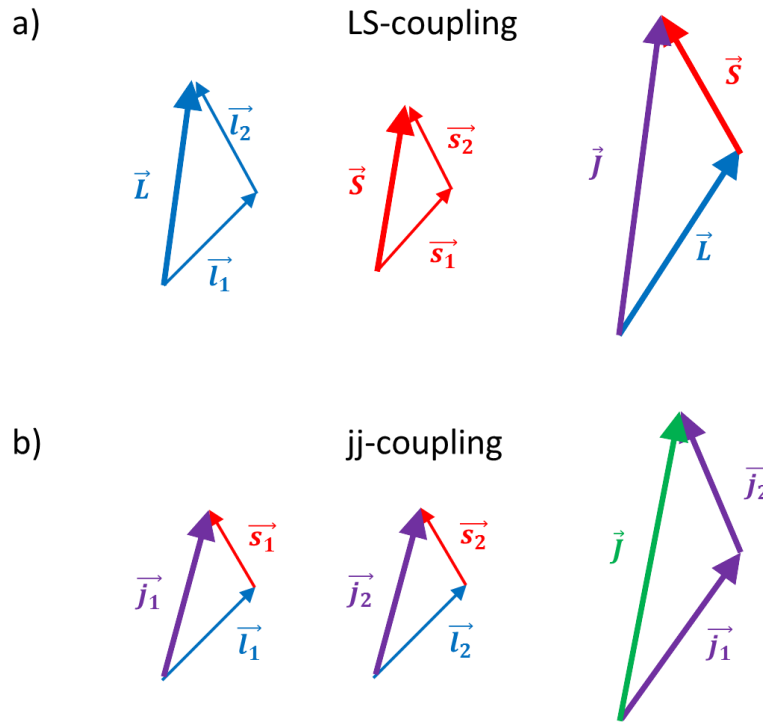


Figure 2.5: Vector diagram demonstrating the difference between LS-coupling and jj-coupling. **(a)** When electron-electron coulombic interaction is larger than the spin orbit interaction ($V_{ee} > V_{so}$) the sum of the electrons' orbital moments is coupled to the sum of their spins. **(b)** If $V_{ee} < V_{so}$ then the individual electron's orbital moment is coupled to its spin moment and then the total J is found by summing up the individual j 's from the different electrons.

2.3.3 Spin-Orbit Coupling

Spin-orbit coupling is a relativistic interaction between the electron and the nucleus. In the frame of the electron it is the nucleus that is rotating around the electron, not

the other way around. Therefore the electron feels a magnetic field from the nucleus.
[36]

$$H_N = Ze \frac{\mathbf{r} \times \mathbf{v}}{r^3} = \frac{Ze\hbar}{m} \frac{1}{r^3} \mathbf{l} \quad (2.15)$$

Where c is the speed of light. The energy of the electron's spin magnetic moment in this field is [36]

$$V_{SO} = \frac{Ze\hbar}{m} g\mu_B \frac{1}{r^3} \mathbf{s} \cdot \mathbf{l} \quad (2.16)$$

The coordinate frame of the electron is not constant. The electron is being accelerated by the interaction with the nucleus. Considering this problem relativistically the electron frame rotates opposite to the rest (Nucleus) frame at half the Larmor frequency. Therefore a factor of two is added. This is called the *Thomas Correction*. [36]

This is only considering the potential from the nucleus $\frac{Ze}{r^3}$ and not the potential from the other electrons. We can absorb the other electrons' Coulomb potential into the potential from the nucleus and replace Z with Z_{eff} . Averaging over all the electrons the energy is given by

$$V_{SO} = \lambda(\mathbf{L} \cdot \mathbf{S}) \quad (2.17)$$

Where $\lambda = \frac{gZ_{eff}\mu_B^2}{2S} \langle \frac{1}{r^3} \rangle$.

As mentioned earlier, in the realm where Russel-Saunders coupling is valid, the energy levels of the LS-multiplet are split due to a perturbation from V_{SO} . The eigenvalues from the spin-orbit interaction are given by

$$\lambda(\mathbf{L} \cdot \mathbf{S}) = \frac{1}{2} \lambda[(L + S)^2 - L^2 - S^2] = \frac{1}{2} \lambda[J(J + 1) - L(L + 1) - S(S + 1)] \quad (2.18)$$

Where J can have values $J = L + S, L + S - 1, \dots, |L - S|$. Without spin-orbit coupling the multiplet states can be classified by $|L, S, m_l, m_s\rangle$. These configurations with a given value of L and S all have the same energy. Diagonalizing the Hamiltonian in the presence of spin-orbit coupling causes the state space to change resulting in the new basis states

$$|L, S, J, m_J\rangle = \sum_i c_i |L, S, m_l, m_s\rangle \quad (2.19)$$

Where c_i are the *Clebsh-Gordon coefficients*. The new atomic configurational states are now described by J and m_J and are superpositions of the states described by m_l and m_s . [31]

2.3.4 Hund's Rules

As electrons are added to an unfilled shell, Hund's rules can be used to predict the ground state. These rules are empirical, meaning they have been rationalized after experimental evidence. However, hindsight has explained them as arising from the Coulomb repulsion of charges as well as the antisymmetric nature of the global wavefunction. The rules hold well for the $4f$ atoms which are close to the nucleus and less exposed to the surrounding crystalline environment. They are not as successful in

explaining the $3d$ atoms where the effects of crystal field and quenching of the orbital angular momentum must be considered. If the first rule does not successfully isolate the ground state, move on to the second rule, if the second rule still leaves some degeneracy move on to the third.

1) The multiplet with the maximum multiplicity lies in the lowest energy level.

Since the multiplicity is proportional to $(2S + 1)$, the ground state is the multiplet that maximizes the value of S . The wavefunction can be decomposed into a spin and spatial part $\psi_{tot} = \phi_{space}\chi_{spin}$. If the spins are aligned in the same direction (maximizing S) then χ_{spin} is symmetric. This means that ϕ_{space} must be antisymmetric. The opposite is true if the spins are anti-parallel to one another (minimizing S). Since the probability of an antisymmetric spatial wavefunction $|\phi_{space}|^2 = 0$ at the origin, there is less of an overall probability of the electrons occupying the same space at the same time which is preferable since it lowers the Coulomb potential. Therefore, the lower energy state is the one where the spins are in the same direction, which maximizes S which maximizes the multiplicity. [37]

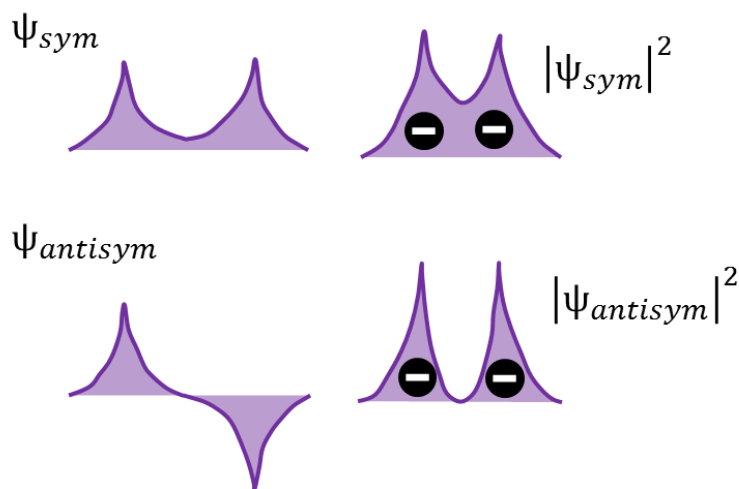


Figure 2.6: Diagram showing symmetric and anti-symmetric wavefunctions and their probability amplitudes. The anti-symmetric wavefunction has a probability of zero at the origin which makes it a lower energy state from a coulombic potential point of view. Taken from [37].

2) **Within a given multiplet the term with the largest value of L has the lowest energy.** The reason for this stems from the orbit-orbit interaction and a tendency to minimize the Coulomb energy. Since electrons in orbits with the same sign of angular momentum travel the same direction around the nucleus, they will pass one another less frequently. Thus they will in general be farther away from each other—lowering the Coulomb energy. [37]

3) If the outermost subshell of the atom is less than half filled ($m < 2l + 1$), then the lowest energy state is the one with the lowest value of J . If the outermost subshell is more than half filled ($m > 2l + 1$) then the opposite is true—the lowest energy state

is the one with the highest value of J . This is a consequence of spin-orbit coupling. [39]

2.4 Multiple Atoms

2.4.1 Crystal Field

As we add atoms together to form a crystal, the atom's surrounding environment changes. The neighboring atoms within the crystal add potentials to the Hamiltonian. One way to imagine how this would affect the environment is to imagine the neighboring atoms as being represented by point charges. [36]

$$V_{cryst} = \sum_i \frac{e_i}{|\mathbf{r} - \mathbf{R}_i|} \quad (2.20)$$

Where \mathbf{R}_i is the position of the neighboring ion and e_i is its charge. This added term to the Hamiltonian in equation (2.13) lifts the degeneracy of the $(2l + 1)$ orbitals within a subshell. However, the energy of the orbitals depends entirely on the position of the ions and therefore on the symmetry of the crystal. Transforming equation (2.20) into spherical coordinates and expanding in spherical harmonics gives the following series [38]

$$V_{cryst} = \sum_{k=0}^{\infty} \sum_{m=-k}^k r^k q_{km} C_m^{(k)}(\theta, \varphi) \quad (2.21)$$

Where

$$q_{km} = \left(\frac{4\pi}{2k+1} \right)^{1/2} \frac{Ze^2}{a^{k+1}} \sum_{i=1}^{N_s} Y_{km}^*(\theta_i, \varphi_i) \quad (2.22)$$

And

$$C_m^{(k)}(\theta, \varphi) = \left(\frac{4\pi}{2k+1}\right)^{1/2} Y_{km}(\theta, \varphi) \quad (2.23)$$

N_s is the number of surrounding point charges, a is the radial position of the point charges, r the radial position of the electron and $Y_{km}(\theta, \varphi)$ are spherical harmonics. Although this expression looks daunting, the main point is that the exact representation of the expanded terms changes depending on the symmetry of the crystal (location of point charges). Additionally, since the wavefunctions are also comprised of spherical harmonics, each term in the expansion is responsible for the perturbation of a different orbital.[†] [39]

[†] An interesting side note is the application of group theory to the splitting of the orbitals. Assume all the orbitals in a particular subshell form a space. Applying transformations dictated by the symmetry of a particular crystalline environment allows certain orbitals to transform into others. The sets of orbitals that transform into themselves form a subspace and have the same energy. [39]

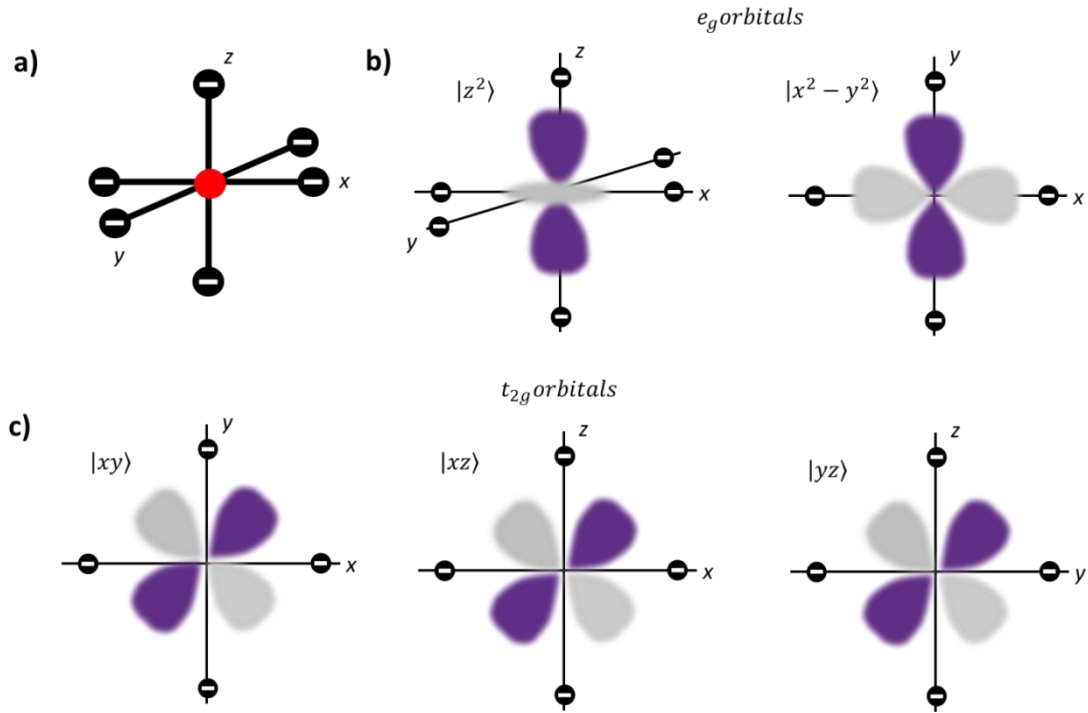


Figure 2.7: (a) Position of atom (red dot) in cubic crystalline environment surrounded by negative point charges. (b) The d -orbitals that point in the direction of the point charges have a higher energy and form e_g doublet group. (c) The orbitals that do not point directly at the negative point charges form the t_{2g} triplet group and have a lower energy. Taken from [40].

The different energies of the orbitals relates back to the Coulomb repulsion. As an example, for a free ion the d -orbitals all have the same energy in free space. But in a cubic crystalline environment $|xy\rangle$, $|xz\rangle$ and $|yz\rangle$ (t_{2g} orbitals) have lower energy than $|z^2\rangle$ and $|x^2 - y^2\rangle$ (e_g orbitals). (Fig. 2.7) This is because the t_{2g} orbitals do not

point in the direction of the neighboring ions whereas the e_g orbitals do which costs coulombic energy. [40]

2.4.2 Quenching of Orbital Angular Momentum

Depending on the strength of the Crystal field compared to the spin orbit interaction, the crystal field can *quench* the orbital momentum of the electrons. If the ground state configuration is degenerate the state can be composed into a superposition of wavefunctions with the same m_l . As an example we consider the $|xy\rangle$ and $|x^2 - y^2\rangle$ wave functions which are characterized by $m_l = \pm 2$. These are real wavefunctions with the only difference arising in their azimuthal dependence. The superposition of these two real wavefunctions is also a solution to the Schrödinger equation. The linear combination is a complex wavefunction represented as [40]

$$|\pm 2\rangle = |x^2 - y^2\rangle \pm |xy\rangle = R_{nl}(r)T_l^m(\theta)e^{\pm i2\varphi} \quad (2.24)$$

Where $R_{nl}(r)$ is the radial function defined earlier and $T_l^m(\theta)$ is a function which only depends on the polar angle.

The expectation value for orbital momentum of the wavefunction is

$$\langle \pm 2 | L_z | \pm 2 \rangle = \pm 2\hbar \quad (2.25)$$

Where $L_z = -i\hbar \frac{\partial}{\partial \varphi}$. The probability distribution of this wavefunction is shown in figure 2.8a. However, if the crystal field is strong enough it can split this degenerate ground state so that the new ground state is non-degenerate. Assuming the cubic

crystal field discussed earlier this would make the $|xy\rangle$ state the new ground state.

This state is a real eigenfunction and since L_z is imaginary the expectation value is

$$\langle xy|L_z|xy\rangle = 0 \quad (2.26)$$

Hence the term *quenching* of the orbital momentum. The electric field from the crystalline environment locks in the orbital moment so the wavefunction is more of a standing wave ($\cos \varphi$) rather than a travelling wave ($e^{im\varphi}$). [40] Quenching the orbital momentum costs energy through the spin-orbit interaction, so depending on the relative strengths of the crystal field and the spin-orbit interaction intermediate cases can arise as well.

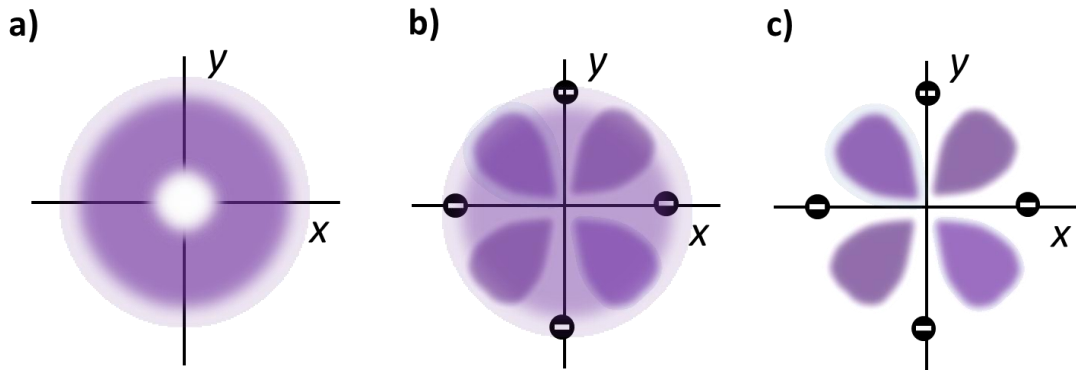


Figure 2.8: Probability amplitude of wavefunctions demonstrating (a) No quenching of the orbital moment. The wavefunction is complex, made up of a superposition of wavefunctions with the same m_l . (b) Partial quenching of the orbital momentum. In this case the spin-orbit interaction still has some effect so as to mix the two real wavefunctions with the same m_l . (c) Total quenching of the orbital momentum. The

effect from the crystal field causes $|xy\rangle$ to be the ground state. This is a real eigenfunction and therefore has zero expectation value for L_z . Taken from [40].

Quenching of the orbital moment is dominant in the iron-series elements since the $3d$ electrons which are responsible for the magnetism are more exposed to the electric field from the surrounding crystalline environment. Quenching is not present in the rare-earth elements, where the magnetism arises from the $4f$ electrons which are located closer to the nucleus and are shielded from the surrounding crystalline electric field by $5d$, $5s$ and $6s$ electrons.

2.4.3 Hubbard Model

One consequence of this change is that the outer electrons' wavefunctions start to overlap with neighboring atoms. The electrons are then allowed to move around to nearest neighbor atoms. Their probability of “hopping” to neighboring atoms is given by a hopping integral, t_{ij} . However, each hop comes at a cost of Coulomb energy if the electrons occupy the same orbital (obviously with different spin). [41] This is the Hubbard model for electrons in solids named after John Hubbard. It was originally intended to explain the itinerant nature of electrons in $3d$ metals. The Hamiltonian of this system is given by

$$\mathcal{H}_{Hubb} = \sum_{i,j,\sigma} t_{ij} a_{i,\sigma}^\dagger a_{j,\sigma} + U \sum_i n_{i,\uparrow} n_{i,\downarrow} \quad (2.27)$$

Where $a_{i,\sigma}^+$ creates, $a_{i,\sigma}$ annihilates and $n_{i,\sigma} = a_{i,\sigma}^+ a_{i,\sigma}$ is the number of electrons with spin σ at lattice point i . The first term is the kinetic energy term and arises from the overlap of the wave functions

$$t_{ij} = \int d^3r \phi_i^*(\mathbf{r}) V_{cryst} \phi_j(\mathbf{r}) \quad (2.28)$$

Where V_{cryst} is the crystal potential (Eq. 2.21).[36] The second term is the potential energy that arises from electrons that occupy the same site.

$$U = \int d^3r_1 d^3r_2 |\phi_j(\mathbf{r}_1)|^2 \frac{e^2}{|\mathbf{r}_{12}|} |\phi_j(\mathbf{r}_2)|^2 \quad (2.29)$$

If t_{ij} is large compared to U , then electrons are free to move about the crystal. This is the case for the $4s$ electrons in the transition metal ferromagnets. The $3d$ electrons are somewhere in between. Because they are closer to the nucleus they are less screened than the $4s$ electrons and feel the draw of the nuclear potential more. Although they are able to move about the crystal the Coulomb interaction correlates them with one another through the exchange interaction. Finally if U is much greater than t_{ij} the electrons behave more like the isolated atom. This is the case in the rare-earth $4f$ electrons which are localized close to the nucleus. This model has been used to explain *Mott transitions* when the values of U and t_{ij} are varied to change the state from an insulator to a metal. [41]

2.4.4 Exchange Interaction

If the neighboring atoms are also magnetic in their isolated state and are close together in a crystalline environment the *inter*-atomic exchange tends to align all the electrons' spins. Assuming two hydrogen like atoms, the Hamiltonian of the *electrons* is given by

$$\mathcal{H} = \sum_{i=1}^N \frac{p_i^2}{2m} - \sum_{A=1}^2 \sum_{i=1}^N \frac{Z_A e^2}{r_{A,i}} + \sum_{i < j}^N \frac{e^2}{|\mathbf{r}_i - \mathbf{r}_j|} \quad (2.30)$$

Notice the similarity to equation (2.13) except that instead of adding up the electrons on a particular atomic site, are adding up the electrons on the outer orbitals of each atom. We assume that the filled lower energy orbitals are all tightly bound to the nucleus and so do not feel the influence of the electrons on neighboring atoms as much as the outer electrons do. Considering two electrons, since their total wavefunction must be anti-symmetric and $\psi_{tot} = \phi_{space}\chi_{spin}$ then we have the following possibilities

$$\psi_S = \phi_{sym}\chi_{anti} \quad (2.31)$$

$$\psi_T = \phi_{anti}\chi_{sym} \quad (2.32)$$

$$\phi_{sym} = \frac{1}{\sqrt{2}} [\phi_1(\mathbf{r}_1)\phi_2(\mathbf{r}_2) + \phi_2(\mathbf{r}_1)\phi_1(\mathbf{r}_2)] \quad (2.33)$$

$$\phi_{anti} = \frac{1}{\sqrt{2}} [\phi_1(\mathbf{r}_1)\phi_2(\mathbf{r}_2) - \phi_2(\mathbf{r}_1)\phi_1(\mathbf{r}_2)] \quad (2.34)$$

$$\phi_1(\mathbf{r}_1)\chi_{sym} = \begin{cases} \chi_{\uparrow}(\mathbf{r}_1)\chi_{\uparrow}(\mathbf{r}_2) \\ \frac{1}{\sqrt{2}}[\chi_{\uparrow}(\mathbf{r}_1)\chi_{\downarrow}(\mathbf{r}_2) - \chi_{\downarrow}(\mathbf{r}_1)\chi_{\uparrow}(\mathbf{r}_2)] \\ \chi_{\downarrow}(\mathbf{r}_1)\chi_{\downarrow}(\mathbf{r}_2) \end{cases} \quad (2.35)$$

$$\chi_{anti} = \frac{1}{\sqrt{2}}[\chi_{\uparrow}(\mathbf{r}_1)\chi_{\downarrow}(\mathbf{r}_2) - \chi_{\downarrow}(\mathbf{r}_1)\chi_{\uparrow}(\mathbf{r}_2)] \quad (2.36)$$

Where $\phi_i(\mathbf{r}_j)$ refers to electron i located at position j . $\chi_{\sigma}(\mathbf{r}_j)$ refers to the electron at position j with spin $\sigma \in \{\uparrow, \downarrow\}$. Simply considering the last term in the Hamiltonian (Eq. 2.30), which is the Coulombic interaction (\mathcal{H}_{Coul}) between the electrons, we can express the expectation value as [42]

$$E = \langle \psi | \mathcal{H}_{Coul} | \psi \rangle = K_{12} \pm J_{12} \quad (2.37)$$

Where $+$ corresponds to ψ_S and $-$ to ψ_T and

$$K_{12} = \int |\phi_i(\mathbf{r}_1)|^2 \frac{e^2}{|\mathbf{r}_i - \mathbf{r}_j|} |\phi_j(\mathbf{r}_2)|^2 d^3r_1 d^3r_2 \quad (2.38)$$

$$J_{12} = \int \phi_i^*(\mathbf{r}_1) \phi_j^*(\mathbf{r}_2) \frac{e^2}{|\mathbf{r}_i - \mathbf{r}_j|} \phi_i(\mathbf{r}_2) \phi_j(\mathbf{r}_1) d^3r_1 d^3r_2 \quad (2.39)$$

The expectation value becomes a function of the spatial wavefunctions due to the orthogonality of the spin eigenfunctions. The first term (Eq. 2.38) is the Coulombic interaction between electrons on neighboring sites. It is the same as the energy given in the Hubbard Model. The second term (Eq. 2.39) is a coulombic interaction that arises due to the quantum nature of fermions. It stems from the anti-symmetric nature of the wavefunctions which are represented as Slater Determinants in order to account for the Pauli exclusion principle.

2.4.5 Heisenberg Approximation

Although it is the spatial overlap of the orbitals that dictate the value of J_{12} , it is convenient to relate this interaction to the spin system since the orbital state directly corresponds to the state of the spin system (Eqs. 2.31-2.36). The total spin of the two electron system is given by $\mathbf{S} = \mathbf{s}_1 + \mathbf{s}_2$ so that the operator $\mathbf{S}^2 = \mathbf{s}_1^2 + \mathbf{s}_2^2 + 2\mathbf{s}_1 \cdot \mathbf{s}_2$. This shows that the eigenvalues of the total spin system depend on the mutual orientation of \mathbf{s}_1 and \mathbf{s}_2 . [40] Using the operator $-\frac{1}{2} - 2\mathbf{s}_1 \cdot \mathbf{s}_2$ we can rewrite the energy (Eq. 2.37) as [42]

$$E = K - \frac{1}{2}J_{12} - 2J_{12}\mathbf{s}_1 \cdot \mathbf{s}_2 \quad (2.40)$$

Rather than expressing the different energy eigenvalues as arising due to the symmetric or asymmetric *spatial* wave functions, they are expressed as the mutual orientation of the spins. The spin dependent part of this energy is referred to as the *Heisenberg Exchange Hamiltonian*

$$\mathcal{H}_{ex} = -2J_{12}\mathbf{s}_1 \cdot \mathbf{s}_2 \quad (2.41)$$

Referring back to equation (2.30) where each atom has more than one spin the last term due to the coulombic interaction takes the form

$$\mathcal{H}_{ex} = -2 \sum_{i < j}^N J_{ij} \mathbf{s}_i \cdot \mathbf{s}_j = -2J\mathbf{S}_1 \cdot \mathbf{S}_2 \quad (2.42)$$

Where $\mathbf{S}_1 = \sum_i \mathbf{s}_i$ and $\mathbf{S}_2 = \sum_j \mathbf{s}_j$ and the exchange interaction was assumed to be isotropic and the same between all the electrons on the neighboring atoms. If $J > 0$

then the lowest energy arises from parallel spins and the material is said to be ferromagnetic. On the other hand, if $J < 0$, then the lowest energy state is when the spins are anti-parallel and the material is said to be anti-ferromagnetic. [42]

This model works well for explaining the magnetism of insulating magnetic atoms, but not as well at explaining the ferromagnetism that arises in materials such as *Fe*, *Ni*, and *Co* where the electrons are itinerant (allowed to move around the crystal). [42] However, it is an important phenomenological result and plays an important role in macroscopic magnetization theory discussed in the next chapter.

CHAPTER 3: MACROSCOPIC MAGNETISM (MICROMAGNETICS)

“Electric and magnetic forces. May they live forever, and never be forgot, if only to remind us that the science of electromagnetics, in spite of the abstract nature of its theory, involving quantities whose nature is entirely unknown at the present, is really and truly founded on the observations of real Newtonian forces, electric and magnetic respectively”

-Oliver Heaviside

3.1 Magnetization Vector

When the material under consideration is much larger than the atomic distances between atoms, the quantum mechanical effects discussed earlier manifest themselves in classical analogues and the behavior of the system can be modelled using continuum mechanics. This realm of magnetism is known as Micromagnetics. The magnetization of the material is represented by the macroscopic magnetization vector which is a sum of all of the dipoles per unit volume [43]

$$\mathbf{M}(T) = \frac{\sum \mu}{V} \quad (3.1)$$

\mathbf{M} is not a constant of temperature, T . Thermal contributions excite the spins, which cause them to lose coherence with one another. At a critical temperature known as the

Curie Temperature (T_c) the spins lose total coherence and $\mathbf{M}(T_c) = 0$. (Fig. 3.1) Furthermore, the Magnetization vector is a continuous function of the position, \mathbf{r} , throughout the material

$$\mathbf{M}(\mathbf{r}) = M_S \mathbf{m}(\mathbf{r}) \quad (3.2)$$

Where M_S is the saturation magnetization, and $\mathbf{m} \cdot \mathbf{m} = 1$. Since we are now in a realm consisting of many atoms whose energies depend on temperature, thermodynamics and statistical physics become useful in describing the macroscopic magnetic states.

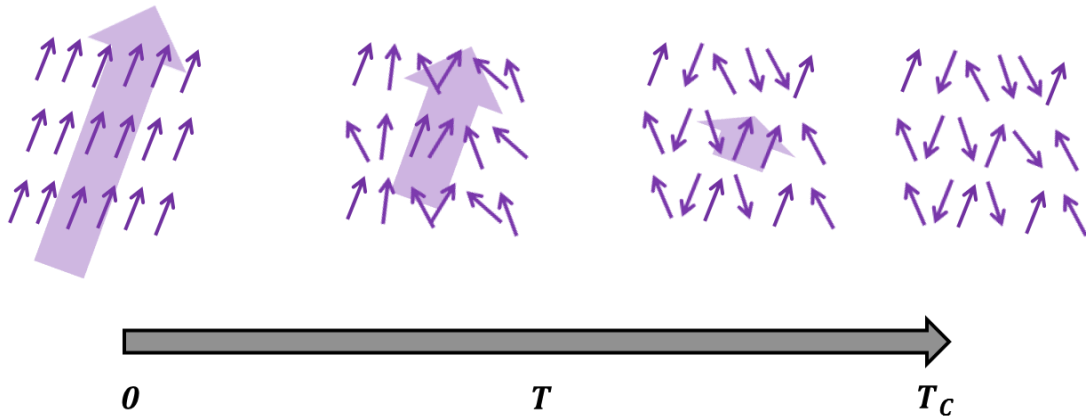


Figure 3.1: At lower temperatures all of the dipoles are aligned due to the exchange interaction and the magnetization vector which is the net dipole moment per unit volume is large. As the temperature increases, thermal energy excites the spins so that they are no longer perfectly aligned with one another. This causes the magnitude of the magnetization vector to decrease. The temperature at which the net magnetic moment is zero is known as the Curie Temperature.

3.2 Free Energy

An extremely useful thermodynamic potential for understanding the properties of a magnetic material is the magnetic free energy

$$F(T, \mathbf{M}, \epsilon) = U - TS \quad (3.3)$$

Where U is the internal energy of the magnetic system, T is the temperature, S is the entropy, \mathbf{M} is the magnetization vector which has a directional dependence and ϵ is the strain.[44]. The internal energy U is fixed and intrinsic to the particular magnetic system while TS is the extra energy due to the temperature and entropy. $F(T, \mathbf{M}, \epsilon)$ is therefore a measure of the amount of work obtainable from the magnetic system. The directional dependence of \mathbf{M} arises from various energy terms such as exchange energy, anisotropy energy (magneto-crystalline and shape), magnetostatic energy and magnetostriction, which all compete to preferentially align the magnetization vector in particular directions. A more experimentally useful thermodynamic potential is the *Gibbs free energy* [45]

$$G(T, \mathbf{B}, \epsilon) = F - \mathbf{B}\mathbf{M} \quad (3.4)$$

Where \mathbf{B} is the magnetic flux. \mathbf{B} can be altered experimentally by application of an applied field, \mathbf{H}_a . In equilibrium at constant temperature, $\left(\frac{\partial F}{\partial \mathbf{M}}\right)_T = 0$ which gives the following relation

$$\left(\frac{\partial G}{\partial \mathbf{M}}\right)_T = -\mathbf{B} = -\mu_0 \mathbf{H}_{eff} \quad (3.5)$$

Where \mathbf{H}_{eff} is the effective field within the magnetic material. As we will see in this section, the resonance of the magnetic system depends on the effective field (and therefore on the Gibbs free energy). Therefore, by changing the applied field \mathbf{H}_a we can change the Gibbs free energy, which changes the resonance characteristics of the system, which we can probe experimentally. This allows us to learn about inherent characteristics of the magnetic material. But first, we must discuss the various contributions to the free energy.

3.2.1 Zeeman Energy

The first energy term is due to the presence of an externally applied magnetic field and is known as the *Zeeman energy*. [43] It is given by

$$E_Z = - \int \mathbf{M} \cdot \mathbf{H}_a dV \quad (3.6)$$

The energy minimum is the direction in which the magnetization is aligned parallel to the magnetic field.

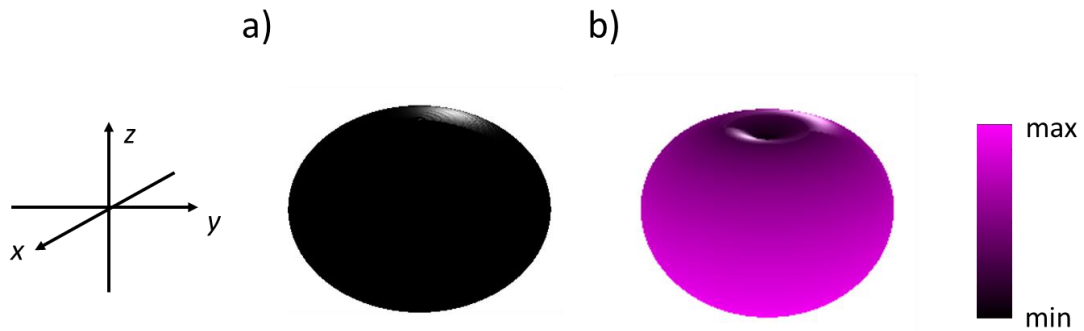


Figure 3.2: Free energy landscape (a) only considering the exchange energy causes all the spins to be aligned but with no preferential direction. All directions are

energetically equivalent. **(b)** Applying an external field along the z -direction will deform the free energy surface creating an energy minimum. The direction of the magnetization vector is normal to the surface at the minimum (along the z -direction).

3.2.2 Exchange Energy

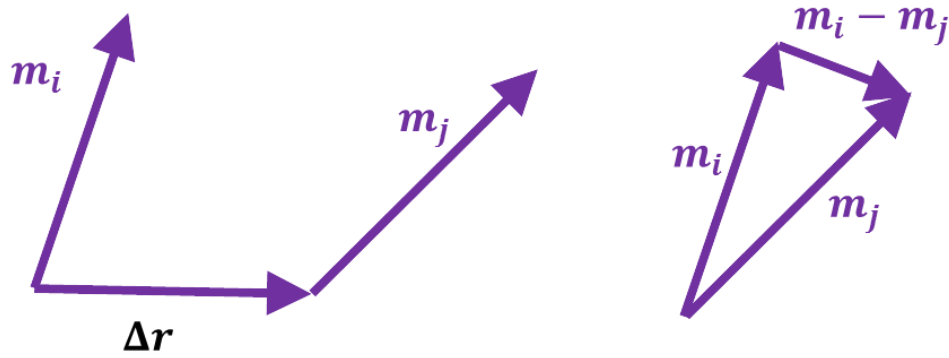


Figure 3.3: Magnetization vectors for different spins, m_i and m_j separated by a distance Δr .

The exchange energy arises from the *Heisenberg exchange Hamiltonian*. Considering the exchange between two spins [46]

$$E_{ex} = -2J_{ij}\mathbf{S}_i \cdot \mathbf{S}_j = -2JS^2\cos\phi_{ij} \quad (3.7)$$

Where ϕ_{ij} is the angle between neighboring spins. Since the exchange energy is extremely strong at short distances we can assume that there is negligible difference

in the orientation of neighboring spins so that $\phi_{ij} \approx |\mathbf{m}_i - \mathbf{m}_j|$ (Fig. 3.3). The exchange energy then becomes

$$E_{ex} = -2JS^2 \left[1 - \frac{1}{2} (\mathbf{m}_i - \mathbf{m}_j)^2 \right] \quad (3.8)$$

Because $\mathbf{m}(\mathbf{r})$ is a continuous function of position, eq. (3.8) can be re-written as

$$E_{ex} = -2JS^2 \left[1 - \frac{1}{2} (\mathbf{m}(\mathbf{r}) - \mathbf{m}(\mathbf{r} + \Delta\mathbf{r}))^2 \right] \quad (3.9)$$

Where $\Delta\mathbf{r}$ is the distance between two magnetic moments. Taylor expanding $\mathbf{m}(\mathbf{r} + \Delta\mathbf{r})$ in $\Delta\mathbf{r}$ gives

$$E_{ex} = JS^2 (\Delta\mathbf{r} \cdot \nabla \mathbf{m})^2 \quad (3.10)$$

Where the constant term has been dropped since we can always redefine the zero point of energy and so it doesn't affect any energy minimization procedures. In order to obtain the total energy of the system we sum up the contribution over the nearest neighbors, $\Delta\mathbf{r}$, then integrate over the entire material

$$E_{ex} = JS^2 \int \sum_i (\Delta\mathbf{r}_i \cdot \nabla \mathbf{m})^2 dV \quad (3.11)$$

Because the summation depends on the position of the nearest neighbors, the exact representation of the exchange energy depends on the crystalline symmetry of the material. As an example, for a simple cubic lattice the summation is over the six nearest neighbors $\Delta\mathbf{r}_i = a(\pm 1, \pm 1, \pm 1)$, where a is the lattice spacing. Since one volume element is one unit cell of the lattice (a^3 for the cubic lattice), the Exchange energy becomes

$$E_{ex} = A \int (\nabla \mathbf{m})^2 dV \quad (3.12)$$

Where A is the exchange constant or stiffness constant and depends on the symmetry of the crystal. Various expressions of A for different crystal lattices are shown in figure 3.4. It should be emphasized that this expression is valid only if the angle between neighboring spins is very small, so that changes in the direction of \mathbf{m} occur over long distances. Therefore, the model is not valid at higher temperatures when thermal fluctuations are of comparable magnitude between the neighboring exchange energy. [46] Additionally this energy only depends on the mutual orientation of the spins. There is no reference to an outside coordinate system, so if this were the only energy term the spins would all be aligned, but could point in any direction. (Fig. 3.3)

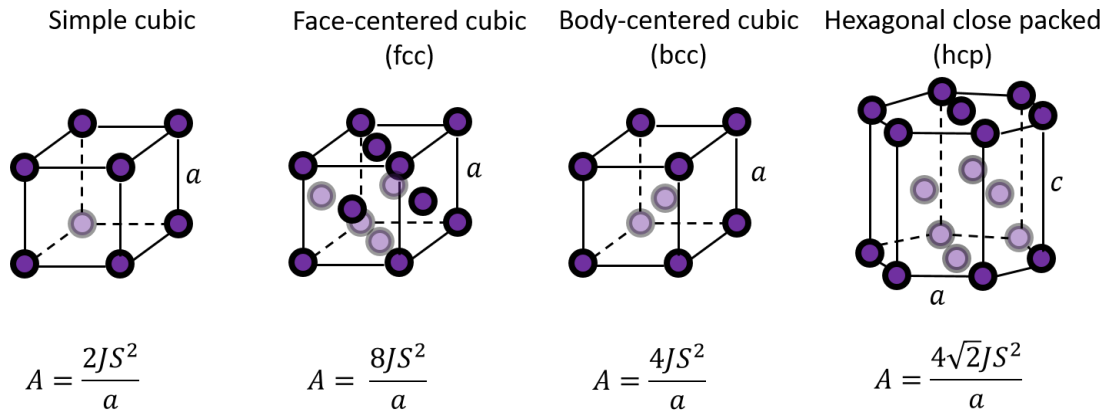


Figure 3.4: Exchange constant terms for different crystallographic structures.

3.2.3 Bilinear Exchange Energy

In addition to the *intralayer* exchange energy mentioned earlier, there also exists an *interlayer* exchange energy due to the presence of another magnetic material in close proximity. [47,48] This is known as the *bilinear exchange coupling*. Instead of measuring the energy as a gradient due to slight variations of the spins over (comparatively) long distances, we treat the two magnetic materials as macrospins. The bilinear exchange coupling energy between the two magnetization vectors is

$$E_{BL} = -J_1 \frac{\mathbf{M}_1 \cdot \mathbf{M}_2}{M_{S1} M_{S2}} \quad (3.13)$$

Where J_1 is the temperature dependent exchange coupling between the two layers. Similar to the intralayer exchange term, a positive value tends to align the spins in the same direction and a negative value aligns the spins in opposite directions. Typically, J_1 decreases with increasing spacer thickness, and for certain spacers J_1 has been shown to be an oscillatory function of the distance between the layers, switching between ferromagnetic and anti-ferromagnetic coupling with decreasing magnitude. [49]

3.2.4 Demagnetization Field and Shape Anisotropy Energy

In addition to the quantum mechanical exchange interaction orienting the spins, the classical dipole-dipole interaction between magnetic moments on different atomic sites, μ_i plays a role.

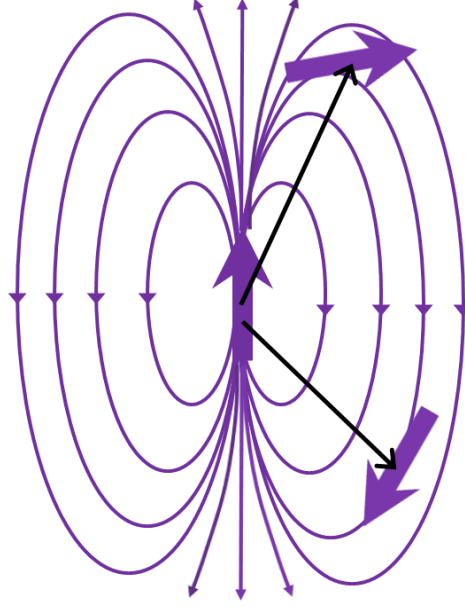


Figure 3.5: Field generated by a magnetic dipole which tends to align neighboring dipoles along the field lines. The field strength depends inversely on the distance, but it also depends on the mutual orientation between the dipoles which can cause alignment in different directions.

Taking into account the interaction between all the dipoles gives [46]

$$\mathbf{E}_M = -\frac{1}{2}\sum_i \boldsymbol{\mu}_i \cdot \mathbf{h}_i \quad (3.14)$$

Where the $\frac{1}{2}$ adjusts for counting the interactions between the same dipoles twice. The field \mathbf{h}_i at point i is given by the contribution from all the other dipoles. (Fig. 3.5)

$$\mathbf{h}_i = \sum_j -\frac{\boldsymbol{\mu}_j}{|\mathbf{r}_{ij}|^3} + \frac{3(\mathbf{r}_{ij} \cdot \boldsymbol{\mu}_j)\mathbf{r}_{ij}}{|\mathbf{r}_{ij}|^5} \quad (3.15)$$

To find the equilibrium configuration of the magnetic body using equations (3.14) and (3.15) would require a summation over the entire magnetic material and would be quite cumbersome. Therefore, it is useful to decompose the magnetic body into two regions. (Fig. 3.6)

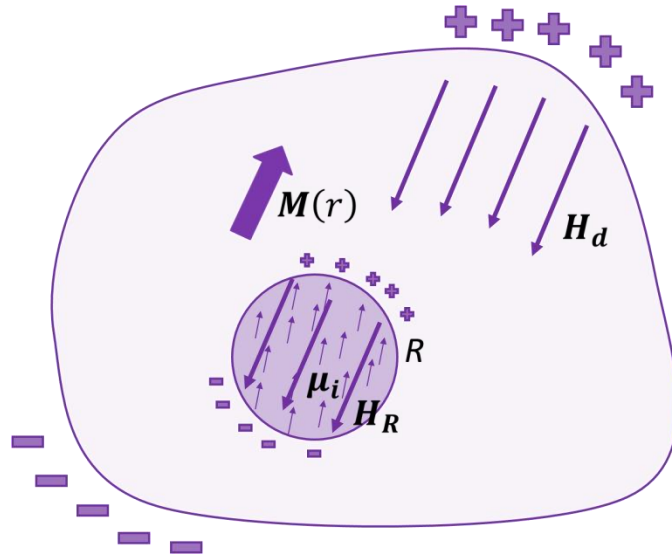


Figure 3.6: Diagram showing the different regions used to derive the demagnetization energy. The total dipole field H_{dip} is obtained by subtracting from the internal demagnetization field H_d the field H_R which is the field within a sphere of radius R and then adding the individual dipole interactions within the sphere, $h_{i,r < R}$. The summation within the sphere depends on the relative positions of the dipoles and can be absorbed into the magnetocrystalline anisotropy. Furthermore, if the magnetization is homogeneous within the sphere, then H_R can be attributed solely to the surface charge which is given by the equation for the volume of a sphere. This

term is constant and can be neglected. \mathbf{H}_d can also be decomposed into surface and volume terms, and if the magnetization is homogeneous within the magnetic body then \mathbf{H}_d arises solely due to the surface contribution, which leads to the concept of shape anisotropy. Taken from [46].

The first region is a sphere surrounding lattice point i with a radius R , and the other region the rest of the magnetic body. [44] Within the sphere, the field at point i can be obtained by summing up the contributions from all of the dipoles within the sphere (eqns. (3.14) and (3.15)). This contribution to the energy is more sensitive to the distribution of the dipoles in direct proximity of point i . If R is sufficiently large compared with the atomic distance between atoms, then the field at point i due to the distribution of dipoles outside of R can be approximated as arising from the continuous magnetization vector $\mathbf{M}(r)$ which can further be decomposed into a surface and a volume contribution as shown in the following. [46]

Assuming the absence of any currents or displacement currents Maxwell's equations are given by

$$\nabla \cdot \mathbf{B} = 0 \quad (3.16)$$

$$\nabla \times \mathbf{H} = 0 \quad (3.17)$$

Where \mathbf{B} is the *magnetic induction* and \mathbf{H} is the *magnetic field*. \mathbf{B} is related to \mathbf{H} and \mathbf{M} by

$$\mathbf{B} = (\mathbf{H} + 4\pi\mathbf{M}) \quad (3.18)$$

Introducing a scalar potential ϕ , the magnetic field can be rewritten as

$$\mathbf{H} = -\nabla\phi \quad (3.19)$$

Equation (3.16) and (3.18) then give

$$\nabla^2\phi = 4\pi\nabla \cdot \mathbf{M} \quad (3.20)$$

Which is only valid inside the magnetic body, since $\mathbf{M} = 0$ outside. Due to the mathematical similarity with electrostatics and electric charge, it is helpful to introduce the concept of a *volume magnetic charge density* which is given by

$$\rho = -4\pi\nabla \cdot \mathbf{M} \quad (3.21)$$

So that we are left with *Poisson's equation*

$$\nabla^2\phi = -\rho \quad (3.22)$$

It should be re-emphasized that this similarity is purely a mathematical convenience that doesn't necessarily reflect a similarity in the intrinsic mechanisms causing the charge effects. Namely, the electric charge is a point charge whereas the magnetic charge arises from a dipole. However, the mathematical similarity allows the partial differential equation (Eq. 3.22) to be solved in the same manner as the electrostatic problem of a point charge. By introducing the function [50]

$$G(\mathbf{r}, \mathbf{r}') = \frac{1}{4\pi|\mathbf{r}-\mathbf{r}'|} \quad (3.23)$$

known as *Green's function* which is meant to represent a unit point charge and integrating over all space we get the following solution for the potential

$$\phi = \int d^3 r' \mathbf{G}(\mathbf{r}, \mathbf{r}') \cdot \boldsymbol{\rho}(\mathbf{r}') = - \int d^3 r' \frac{\nabla \cdot \mathbf{M}(\mathbf{r}')}{|\mathbf{r} - \mathbf{r}'|} \quad (3.24)$$

However, the discontinuity of $\mathbf{M}(\mathbf{r}')$ on the boundary of the magnetic material must be taken into consideration. Applying *Gauss's theorem* to the surface of the body gives the surface contribution to the potential. The potential can then be decomposed into volume and surface parts so that

$$\phi = - \int d^3 r' \frac{\nabla \cdot \mathbf{M}(\mathbf{r}')}{|\mathbf{r} - \mathbf{r}'|} + \int dS \frac{\hat{\mathbf{n}} \cdot \mathbf{M}(\mathbf{r}')}{|\mathbf{r} - \mathbf{r}'|} \quad (3.25)$$

Where $\hat{\mathbf{n}}$ is the normal vector to the surface. Continuing with the electrostatics analogy leads to the concept of an effective *surface magnetic charge* given by

$$\sigma = \hat{\mathbf{n}} \cdot \mathbf{M}(\mathbf{r}') \quad (3.26)$$

The field is then given by

$$\mathbf{H}_d = \int d^3 r' \frac{\nabla \cdot \mathbf{M}(\mathbf{r}')(\mathbf{r} - \mathbf{r}')}{|\mathbf{r} - \mathbf{r}'|^3} - \int dS \frac{\hat{\mathbf{n}} \cdot \mathbf{M}(\mathbf{r}')(\mathbf{r} - \mathbf{r}')}{|\mathbf{r} - \mathbf{r}'|^3} \quad (3.27)$$

This internal field is known as the *demagnetizing field* since it tends to oppose the direction of an externally applied field. (Fig. 3.6)

Returning to the magnetic body decomposed into two regions, we can calculate the field a dipole within the sphere feels by taking the internal demagnetization field (\mathbf{H}_d), and subtracting from it the field within the volume of the sphere (\mathbf{H}_R), then adding the field due to the dipoles in the sphere ($\mathbf{h}_{i,r < R}$)

$$\mathbf{H}_{dip} = \mathbf{H}_d - \mathbf{H}_R + \mathbf{h}_{i,r < R} \quad (3.28)$$

Substituting this field into equation (3.14) and integrating over the magnetic body gives the energy

$$E_M = -\frac{1}{2} \int \mathbf{M} \cdot \mathbf{H}_{dip} dV \quad (3.29)$$

If we assume that the magnetization is homogeneously magnetized ($\nabla \cdot \mathbf{M}(\mathbf{r}') = 0$) then the volume contribution disappears for both \mathbf{H}_d and \mathbf{H}_R . Equation (3.29) can then be re-written

$$E_M = -\frac{1}{2} \int \mathbf{M} \cdot \left(\mathbf{H}_d + \frac{4\pi}{3} \mathbf{M} + \mathbf{h}_{i,r < R} \right) dV \quad (3.30)$$

Where $\frac{4\pi}{3} \mathbf{M}$ is the surface contribution from the sphere. Since this term is a constant, it doesn't affect any energy minimization procedure and can be removed. The last term will depend on the symmetry of the crystal just like the *magnetocrystalline* energy and so can be absorbed into that term. Furthermore, its strength is negligible in most cases. [44] Therefore, we are left with

$$E_M = -\frac{1}{2} \int \mathbf{M} \cdot \mathbf{H}_d dV \quad (3.31)$$

Where in the case of a homogeneously magnetized body, \mathbf{H}_d is only a function of the surface charge and therefore determined by the shape of the magnetized body. \mathbf{H}_d can be represented as a tensor N which depends on the shape of the object so that [46]

$$E_M = -\frac{1}{2} \int \mathbf{M} \cdot N \cdot \mathbf{M} dV \quad (3.32)$$

The internal demagnetization field orients the magnetization along certain directions dictated by the shape of the magnetic body. This effect is known as *shape anisotropy*

3.2.5 Magnetocrystalline Anisotropy Energy

Due to the effects from the crystal field discussed in the previous chapter, certain orbitals have lower energy than others. This leads to a preferential direction for the spins due to spin-orbit coupling, which from a macroscopic point of view translates into a preferential direction for the magnetization vector along certain crystallographic directions. This macroscopic energy preference is known as *magnetocrystalline anisotropy*.

If we assume no applied field and no strain to the magnetic system, the free energy becomes a function of only the temperature and the direction of the magnetization $F(T, \mathbf{\Omega}_M)$. [44] In spherical coordinates $\mathbf{\Omega}_M = (\sin \theta \cos \phi, \sin \theta \sin \phi, \cos \theta)$ where θ and ϕ are the polar and azimuthal directions defined relative to the crystal axis. This free energy can be expanded in a series and the Temperature dependence can be absorbed into the coefficients to obtain

$$F(T, \mathbf{\Omega}_M) = K_0(T) + K_1(T)f_1(\theta, \phi) + K_2(T)f_2(\theta, \phi) + \dots \quad (3.33)$$

Where $K_i(T)$ are the anisotropy constants and the functions f_i combine terms of the same order. Due to time inversion symmetry which states that the Hamiltonian must be unchanged with respect to time, $F(\mathbf{\Omega}_M) = F(-\mathbf{\Omega}_M)$ —the opposite orientation must be a local minimum as well. This allows us to cancel odd power terms in the series. [44] The functions $f_i(\theta, \phi)$ depend on the symmetry of the crystal which should come as no surprise since the microscopic mechanism of the magnetocrystalline anisotropy is the crystal field. The difference between the two lies

in the representation. Whereas the crystal field potential was represented as a series expansion of atomic orbitals, the magnetocrystalline anisotropy energy is represented phenomenologically by expanding trigonometric functions along crystallographic directions.

The simplest case is known as *uniaxial anisotropy* and is exhibited in hcp crystal structures. The energy is given by [51]

$$E_{MC} = K_0(T) + K_1(T) \sin^2 \theta_c + K_2(T) \sin^4 \theta_c \quad (3.34)$$

With θ_c defined relative to the c -axis. In this case magnetization is stable along the c -axis if $K_1(T) > 0$ and along the a -axis if $K_1(T) < 0$. (Fig. 3.7) For hcp Co, $K_1(T) = 7.66 \times 10^6 \text{ erg} \cdot \text{cm}^{-3}$.

For a cubic crystal structure the energy is given by [51]

$$E_{MC} = K_0(T) + K_1(T)(\alpha_1^2 \alpha_2^2 + \alpha_2^2 \alpha_3^2 + \alpha_3^2 \alpha_1^2) + K_2(T) \alpha_1^2 \alpha_2^2 \alpha_3^2 + \dots \quad (3.35)$$

Where $\alpha_i = \cos(\theta_i)$ and $i \in \{a, b, c\}$ are the crystallographic axes. (Fig. 3.7) For bulk bcc Fe the easy axis is along the $[100]$ direction and $K_1(T) = 5.48 \times 10^5 \text{ erg} \cdot \text{cm}^{-3}$. For fcc Ni the easy axis is along the $[111]$ direction and $K_1(T) = -12.63 \times 10^5 \text{ erg} \cdot \text{cm}^{-3}$. [44]

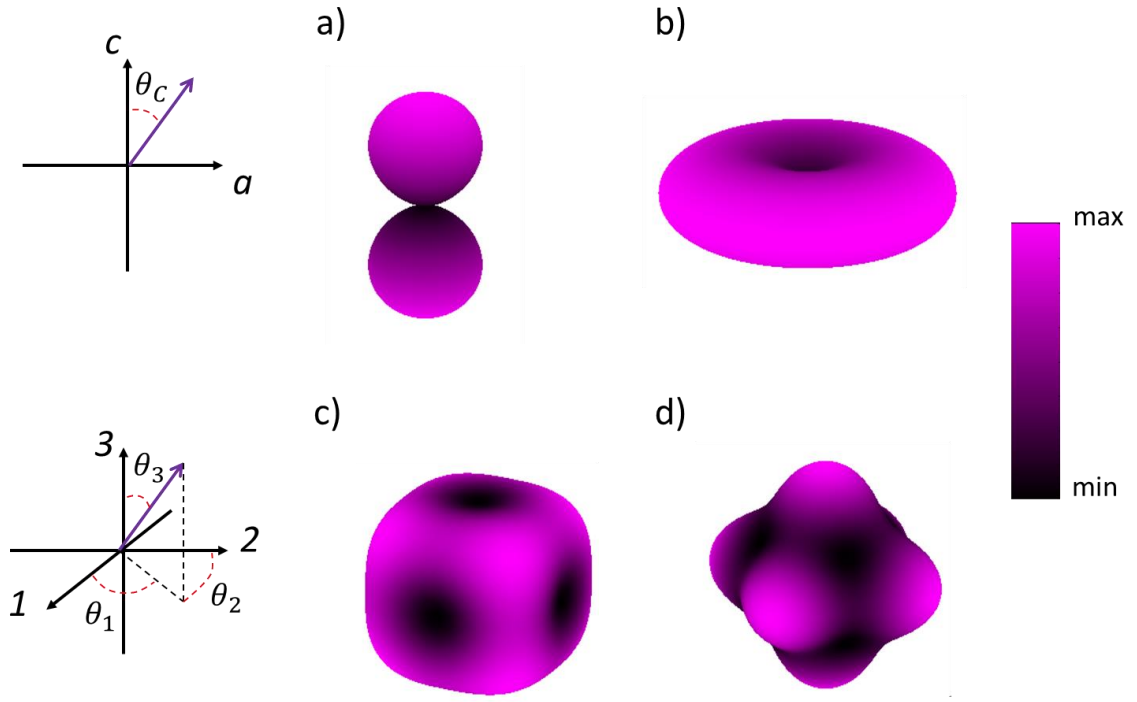


Figure 3.7: Coordinate systems and free energy landscapes for **(a)** uniaxial anisotropy given by equation (3.34) with $K_0 = 0$ and $K_1 < 0$. **(b)** $K_0 = 0$ and $K_1 > 0$ (similar to hcp Co) **(c)** Magnetocrystalline anisotropy energy landscape for cubic crystal with $K_0 = 1$ and $K_1 = 1$ (similar to bcc Fe) **(d)** $K_0 = 1$ and $K_1 = -1$ (similar to fcc Ni).

3.2.6 Magnetostriction

The magnetocrystalline anisotropy discussed in the previous section assumed that there is no strain in the system ($\varepsilon = 0$) which implied that the positions of the anions were fixed. The energy minimum was the direction that minimized the coulombic repulsion between the orbitals and the anions. If we apply a magnetic field, the spins

(which are coupled to the orbitals) want to point along the direction of the field. If the field is not oriented along an *easy direction* (direction of minimum anisotropy energy) but rather a *hard direction* (direction of maximum anisotropy energy) then the spins cannot fully align with the magnetic field due to the repulsion of the orbitals from the neighboring anions. However, if we allow the anions to move from their equilibrium position by introducing strain into the system, then the coulombic repulsion may be minimized at the cost of some of strain energy. This effect results in an elongation of the magnetized sample and is known as *magnetostriction*. It was first recognized in 1842 by James Prescott Joule. [52]

This occurs in magnetic materials without the presence of external fields as well, since there are internal fields such as the demagnetization field. If the magnetic body is not homogeneously magnetized, it can break up into domains where the magnetization points in different directions. The demagnetizing fields and thus the strain will then vary throughout the magnetic body especially at the edges of the domains.

Energy consideration of magnetostriction requires three energy terms which all depend on the symmetry of the crystal: the magnetocrystalline energy, the elastic energy and the magnetoelastic energy. For the case of a crystal with cubic symmetry the elastic energy is given by [52]

$$E_L = \frac{1}{2}c_{11}(\varepsilon_{11}^2 + \varepsilon_{22}^2 + \varepsilon_{33}^2) + c_{12}(\varepsilon_{11}\varepsilon_{22} + \varepsilon_{22}\varepsilon_{33} + \varepsilon_{33}\varepsilon_{11}) + 2c_{44}(\varepsilon_{12}^2 + \varepsilon_{13}^2 + \varepsilon_{23}^2) \quad (3.36)$$

Where $\epsilon_{ij} = \left(\frac{\partial u_i}{\partial x_j} + \frac{\partial u_j}{\partial x_i} \right) / 2$ is the strain along various crystallographic directions, \mathbf{u}_i is the displacement vector and $i, j = \{1, 2, 3\}$ are the crystallographic directions.

The magnetocrystalline energy discussed in the previous section depends on the location of the neighboring atomic sites. However, these positions are displaced due to the presence of strain in the system. This dependence of the magnetocrystalline anisotropy on the strain energy is called the magneto-elastic energy and can be obtained by expanding the magnetocrystalline anisotropy as a Taylor series with respect to the strain [53]

$$E_{MC} = E_{MC}^0 + \sum_{i,j} \left(\frac{\partial E_{MC}}{\partial \epsilon_{ij}} \right)_0 \epsilon_{ij} \quad (3.37)$$

Where E_{MC}^0 is the undistorted magnetocrystalline anisotropy. Considering only the lowest order term gives

$$\frac{\partial E_{MC}}{\partial \epsilon_{ii}} = B_1 \alpha_i^2 \quad (3.38)$$

$$\frac{\partial E_{MC}}{\partial \epsilon_{ij}} = B_2 \alpha_i \alpha_j \quad (3.39)$$

Where B_1 and B_2 are called the magneto-elastic coupling constants and α_i are directional cosines with respect to a crystallographic axis. These terms represent the rate of change of the anisotropy with respect to strain along particular directions. [52]

The lowest order contribution to the magneto elastic energy is

$$E_{ME} = B_1 (\alpha_1^2 \epsilon_{11} + \alpha_2^2 \epsilon_{22} + \alpha_3^2 \epsilon_{33}) + 2B_2 (\alpha_1 \alpha_2 \epsilon_{12} + \alpha_2 \alpha_3 \epsilon_{23} + \alpha_3 \alpha_1 \epsilon_{31}) \quad (3.40)$$

The total energy of the system given by

$$E = E_{MC} = E_{ME} + E_L \quad (3.41)$$

In order to find the equilibrium configuration the energy is minimized with respect to the strain

$$\frac{\partial E}{\partial \varepsilon_{ij}} = 0 \quad (3.42)$$

This results in six equations which can be solved to find the change in length of the magnetized body. The usual form is given by for a demagnetized sample and is [51,54]

$$\frac{\delta l}{l} = \frac{3}{2} \lambda_{100} \left(\alpha_1^2 \beta_1^2 + \alpha_2^2 \beta_2^2 + \alpha_3^2 \beta_3^2 - \frac{1}{3} \right) + 3 \lambda_{111} (\alpha_1 \alpha_2 \beta_1 \beta_2 + \alpha_2 \alpha_3 \beta_2 \beta_3 + \alpha_3 \alpha_1 \beta_3 \beta_1) \quad (3.43)$$

Where α_i are directional cosines for the magnetization and β_i are directional cosines for the direction of δl . [53] λ_{100} and λ_{111} are the magnetostriction constants and correspond to the maximum strain when a magnetic crystal is fully magnetized along the [100] and [111] crystallographic directions respectively. They are related to the magneto-elastic and the strain tensor components by [52]

$$\lambda_{100} = -\frac{2}{3} \frac{B_1}{c_{11} - c_{12}} \quad (3.44)$$

$$\lambda_{111} = -\frac{B_2}{3c_{44}} \quad (3.45)$$

In the case of a polycrystalline sample, the magnetostriction is averaged out over the crystallographic directions within each grain and becomes isotropic. In this case the magnetostriction constant takes a single value given by [52]

$$\lambda_S = \frac{2}{5} \lambda_{100} + \frac{3}{5} \lambda_{111} \quad (3.46)$$

The inverse effect is also possible whereby an induced strain in the system can affect the magnetization and is known as *inverse magnetostriction*. In chapter 7 we will look at how dynamic strain waves drive the magnetization via inverse magnetostriction. In chapter 8 we will look at the case when both magnetistraction and inverse magnetostriction processes are coupled—the precessing magnetization induces a dynamic strain which in turn modifies the magnetization and vice versa.

3.3 Dynamics

From a technological perspective, understanding the dynamic motion of the spins is extremely important. For example, writing speeds in hard disk drives are determined by how fast the spins reorient themselves with an applied field. Improving writing speeds thus relies on understanding the properties governing the spins' collective motion. [55] Additionally, from a fundamental point of view, the collective motion can provide insight into the microscopic interactions between the atoms.

The quantum mechanical motion of the spins in the presence of a magnetic field is given by [43]

$$i\hbar \frac{d}{dt} \langle \mathbf{S} \rangle(t) = \langle [\mathbf{S}, \mathcal{H}(t)] \rangle \quad (3.47)$$

Where $\langle \mathbf{S} \rangle(t)$ is the mean value of the spin operator, and $\mathcal{H}(t)$ is the Hamiltonian associated with the spins' interaction with the magnetic field and is given by

$$\mathcal{H}(t) = -\frac{g\mu_B}{\hbar} \mathbf{S} \cdot \mathbf{B}(t) \quad (3.48)$$

Plugging in equation (3.48) into equation (3.47) and applying the commutation relations $[S_i, S_j] = i\hbar\epsilon_{ijk}S_k$ where $i, j, k \in \{x, y, z\}$ and ϵ_{ijk} is the Levi-Civita symbol gives the following

$$\frac{d}{dt}\langle \mathbf{S} \rangle(t) = \frac{g\mu_B}{\hbar}(\langle \mathbf{S} \rangle \times \mathbf{B}(t)) \quad (3.49)$$

From Chapter 2 we recall that $\boldsymbol{\mu}_S = -g_S \frac{\mu_B}{\hbar} \mathbf{S} = -\gamma \mathbf{S}$ where $\gamma = g_S \frac{\mu_B}{\hbar}$ is known as the gyromagnetic ratio. Equation (3.49) can now be rewritten as

$$\frac{d}{dt}\boldsymbol{\mu}_S = -\gamma(\boldsymbol{\mu}_S \times \mathbf{B}(t)) \quad (3.50)$$

Summing up the collective motion of all of the dipoles in a unit volume allows us to replace $\boldsymbol{\mu}_S$ with the magnetization vector (Eq. 3.1). Additionally, we can replace the magnetic induction with the magnetic field giving [43]

$$\frac{d}{dt}\mathbf{M}(t) = -\gamma_0(\mathbf{M} \times \mathbf{H}(t)) \quad (3.51)$$

Where $\gamma_0 = \mu_0\gamma$. This equation is known as the *Landau-Lifshitz Equation* and represents the motion of the magnetization vector around the effective field. (Fig. 3.8) The frequency of precession depends on the strength of both M_S and \mathbf{H} . However, in this form the magnetization will precess around the magnetic field forever. Damping of the system can be introduced into the equation phenomenologically by replacing \mathbf{H} with

$$\mathbf{H}_{eff,\alpha} = \mathbf{H} - \alpha \frac{1}{\gamma M_S} \frac{d\mathbf{M}}{dt} \quad (3.52)$$

Where α is a phenomenological parameter known as the *Gilbert damping parameter* that describes the damping of the magnetization vector towards the equilibrium

direction along the effective field. (Fig. 3.8) Plugging equation (3.52) into equation (3.513.) gives

$$\frac{d}{dt}\mathbf{M}(t) = -\gamma_0(\mathbf{M} \times \mathbf{H}(t)) + \frac{\alpha}{M_S} \left(\mathbf{M} \times \frac{d\mathbf{M}}{dt} \right) \quad (3.53)$$

This equation is known as the *Landau-Lifshitz-Gilbert Equation* (LLG) and is the core of micromagnetics. (Fig. 3.8) All magnetic processes in the micromagnetic regime are modelled according to this equation or with equations that have slight modifications to it.

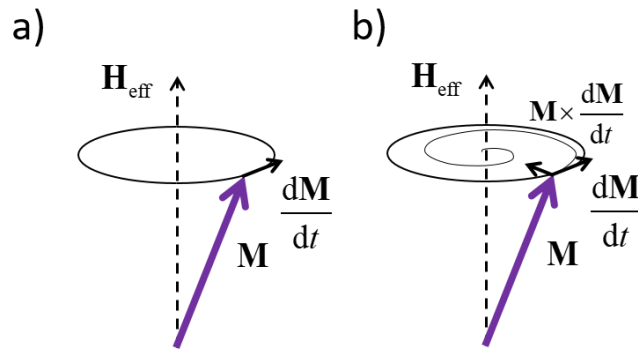


Figure 3.8: (a) Landau-Lifshitz (LL) equation dictates the magnetization vector's rotation around the effective field, H_{eff} . (b) The Landau-Lifshitz-Gilbert (LLG) equation models the precession of the magnetization while including a phenomenological damping term, α in the direction $\mathbf{M} \times \frac{d\mathbf{M}}{dt}$.

3.4 Free Energy Resonance

We are now in a position to revisit the Free energy and see how it relates to the precessional motion of the magnetization. One common method of deriving the resonance condition is known as the Smit and Beljers method [56] and uses spherical coordinates. However, here we will introduce a method which relies on Cartesian coordinates.

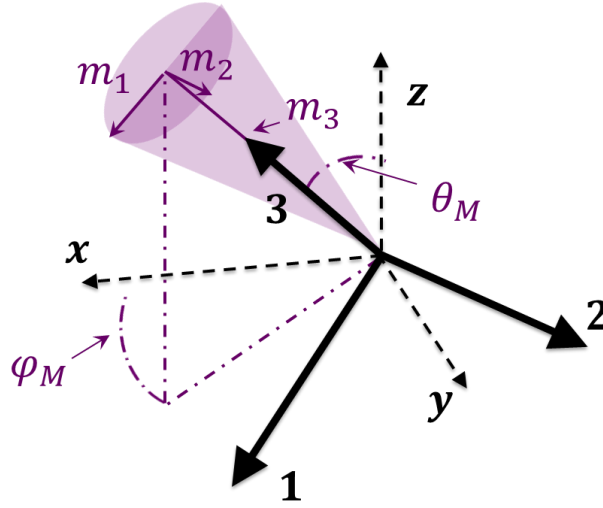


Figure 3.9: The Magnetization precession can be mapped to the $\{1, 2, 3\}$ coordinate system defined by the direction of the magnetization vector and the plane of the cone due to the precession of \mathbf{M} . \mathbf{m}_3 is along the direction of \mathbf{M} at equilibrium (3), \mathbf{m}_2 is parallel to the xy plane (2) and \mathbf{m}_1 is orthogonal to \mathbf{m}_2 and \mathbf{m}_3 (1) .

The expressions for the free energy discussed so far utilize coordinate systems that are defined relative to either the crystallographic axes or some sort of lab frame of reference determined by the geometry of the sample. We were able to construct free energy landscapes based on these coordinate systems which had energetically favorable directions for the magnetization vector. In order to see how the free energy landscape affects the resonance frequency of the magnetic system it is convenient to transform to a coordinate system given by the variables $\{\mathbf{1}, \mathbf{2}, \mathbf{3}\}^\ddagger$ where $\mathbf{3}$ points along the equilibrium magnetization direction, $\mathbf{2}$ is in the film plane and $\mathbf{1}$ is orthogonal to $\mathbf{2}$ and $\mathbf{3}$. Since we assume small variations in the $\mathbf{1}$ and $\mathbf{2}$ directions and no change in M_s the $\{\mathbf{1}, \mathbf{2}, \mathbf{3}\}$ coordinate system allows us to represent the precession as two systems of equations instead of three. The change in coordinate systems is shown in figure 3.9 and the transformation is given by

$$\begin{pmatrix} x \\ y \\ z \end{pmatrix} = \begin{pmatrix} \cos \theta_M \cos \varphi_M & -\sin \varphi_M & \sin \theta_M \cos \varphi_M \\ \cos \theta_M \sin \varphi_M & \cos \varphi_M & \sin \theta_M \sin \varphi_M \\ -\sin \theta_M & 0 & \cos \theta_M \end{pmatrix} \begin{pmatrix} \mathbf{1} \\ \mathbf{2} \\ \mathbf{3} \end{pmatrix} \quad (3.54)$$

The tendency for the magnetization to orient along certain energetically preferable directions can be thought of as arising due to an effective field with contributions

[‡] Although the same numbers are used, it is important to emphasize that this is a different coordinate system than the (1,2,3) coordinate system defined earlier along the crystallographic directions. The crystallographic coordinate system should be reconciled with the lab frame for the discussion in this section.

from each of the energy terms. From equation (3.5) the effective field can be derived from the Gibbs free energy in the $\{\mathbf{1}, \mathbf{2}, \mathbf{3}\}$ coordinate system by

$$\nabla_m G = \left(\frac{\partial G_1}{\partial m_1} \mathbf{1} + \frac{\partial G_2}{\partial m_2} \mathbf{2} + \frac{\partial G_3}{\partial m_3} \mathbf{3} \right) = -\mu_0 \mathbf{H}_{eff} \quad (3.55)$$

Where $\nabla_m = \frac{\partial}{\partial m_1} \mathbf{1} + \frac{\partial}{\partial m_2} \mathbf{2} + \frac{\partial}{\partial m_3} \mathbf{3}$. Taylor expanding the $\mathbf{1}$ and $\mathbf{2}$ components along the 2-dimensional surface given by the base of the cone of precession gives

$$\frac{\partial G_1}{\partial m_1} = \frac{\partial}{\partial m_1} \left(\frac{\partial G_1}{\partial m_1} \right) \mathbf{m}_1 + \frac{\partial}{\partial m_2} \left(\frac{\partial G_1}{\partial m_1} \right) \mathbf{m}_2 \quad (3.56)$$

$$\frac{\partial G_2}{\partial m_2} = \frac{\partial}{\partial m_1} \left(\frac{\partial G_2}{\partial m_2} \right) \mathbf{m}_1 + \frac{\partial}{\partial m_2} \left(\frac{\partial G_2}{\partial m_2} \right) \mathbf{m}_2 \quad (3.57)$$

Which allows us to write the effective field as

$$\mu_0 \mathbf{H}_{eff} = - \begin{pmatrix} G_{11}m_1 + G_{12}m_2 \\ G_{12}m_1 + G_{22}m_2 \\ G_3 \end{pmatrix} \quad (3.58)$$

Where $G_{ij} = \frac{\partial}{\partial m_i \partial m_j} G \big|_{\mathbf{m}=\mathbf{m}_0}$ with \mathbf{m}_0 being the equilibrium position. Since we are only interested in the resonance frequency we can neglect the damping and use the Landau-Lifshitz equation (Eq. 3.51). Replacing \mathbf{H} with \mathbf{H}_{eff} and using $\mathbf{M}_j(t) = \mathbf{M}_{0j} e^{-i\omega t}$ we obtain after some algebra the following system of equations

$$\begin{pmatrix} G_{12} - \frac{i\omega_M}{\gamma} & G_{22} - G_3 \\ G_{11} - G_3 & G_{12} + \frac{i\omega_M}{\gamma} \end{pmatrix} \begin{pmatrix} m_1 \\ m_2 \end{pmatrix} = \begin{pmatrix} 0 \\ 0 \end{pmatrix} \quad (3.59)$$

Since a system of equations has a solution other than the trivial solution if and only if the determinant is zero, we set the determinant of the coefficient matrix equal to zero which yields

$$\frac{\omega^2}{\gamma^2} = (G_{22} - G_3)(G_{11} - G_3) - G_{12}^2 \quad (3.60)$$

The frequency ω is therefore a function of the partial derivatives of the Free energy.

This is a rather general result, but is important for learning about the intrinsic properties of the magnetic system as we will see in later chapters.

CHAPTER 4: EXPERIMENTAL SETUP AND THEORY

“I happen to have discovered a direct relation between magnetism and light, also electricity and light, and the field it opens is so large and I think rich.”

-Michael Faraday

4.1 Introduction

Femtosecond pump-probe spectroscopy is an extremely powerful experimental method which allows for the time-domain study of ultrafast dynamical processes in a variety of systems. [57,58,59] Pump-probe experiments are used to study carrier lifetimes in semiconductor materials and nanostructures, [60] vibrational modes of molecules, [61] and to image tissue. [62,63] In the field of magnetism, the development of femtosecond pulsed laser systems not only provided a novel excitation mechanism of the magnetic order but also enabled the observation of the dynamics on femtosecond timescales. Pump-probe experiments on magnetic materials seek to expose fundamental phenomena related to the scattering and energy channels between electron, spin and lattice systems [64,65,66] and provide a means for observation of the dynamical motion of the spins.

4.2 Stroboscopic Measurements

The experiments in this thesis were conducted using the Time Resolved Magneto-Optic Kerr Effect (TR-MOKE) which is an all optical method where the magnetic system is both excited and probed using ultrashort laser pulses. Furthermore, it is a stroboscopic technique, which means that the full time evolution of the system is comprised of a series of snapshots taken at various stages. (Fig. 4.1) Some advantages to TR-MOKE are that the magnetic resonances can be measured at a continuous set of field strengths and angles simply by changing the position of permanent magnets and no consideration has to be given to the relative geometry between static and driving fields as in microwave experiments. Additionally, there are no extra fabrication steps to prepare the sample for measurement (e.g. deposition of co-planar waveguides). TR-MOKE also possesses a high spatial resolution that is limited only by the diffraction limit of the focusing optic. [67] The time resolution, which is limited by the pulse duration, is typically in the sub-picosecond range, which allows for the observation of the spin dynamics into the THz regime. [67]

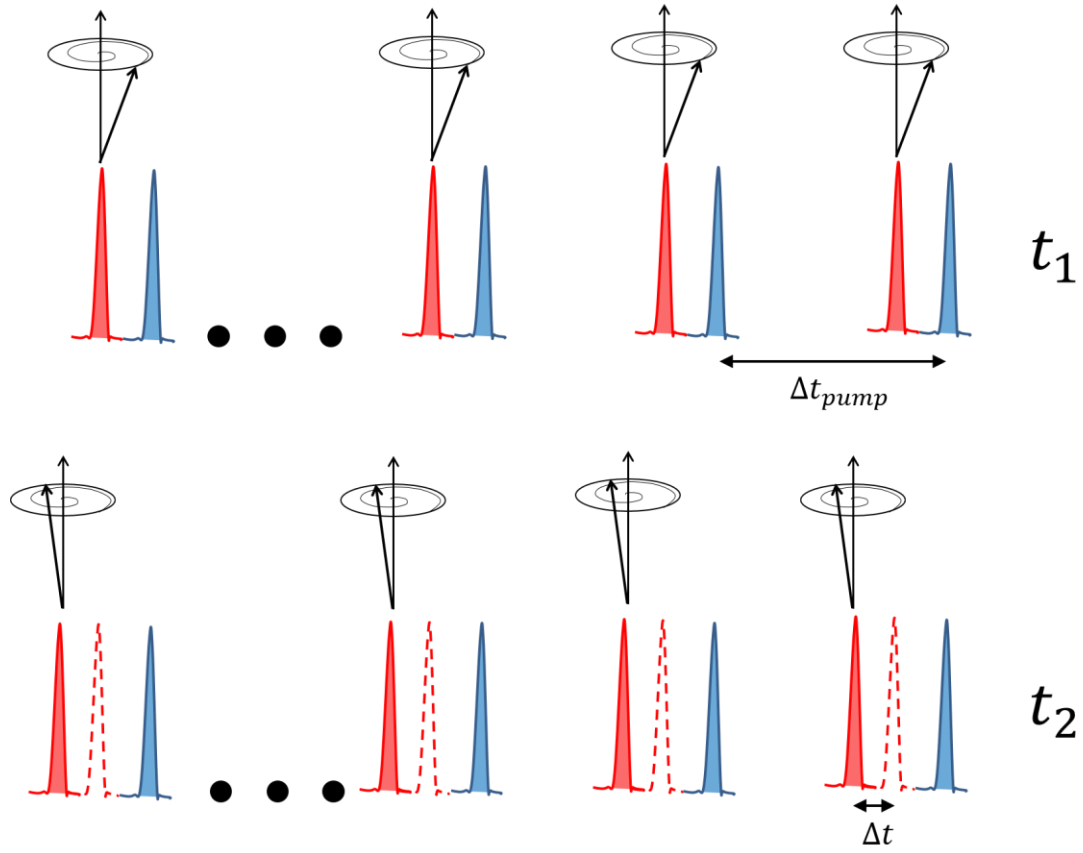


Figure 4.1: Illustration of the concept behind the stroboscopic pump-probe method.

The pump ($\lambda_{pump} = 400$ nm) pulses are separated by Δt_{pump} which for a repetition rate of 76MHz is 13ns. By the time each new pump pulse arrives, the system has fully relaxed back to equilibrium. At time t_1 each probe ($\lambda_{probe} = 400$ nm) pulse (which has the same repetition rate as the pump pulses) is separated from a corresponding pump pulse. Since the magnetization follows the same dynamical path upon excitation, the probe pulse for a given pump-probe separation reads the same magnetic state. The data for each time step is an average of the signal from all the probe pulses. In order to read a later state of the magnetic evolution and acquire the

next data point (t_2), the path length of the probe pulse is increased which results in the probe pulse being delayed by Δt .

A 400nm pump pulse excites the magnetic system which causes the spins to precess at a characteristic frequency determined by the various energy terms discussed in chapter 3. The characteristic frequencies of ferromagnetic materials are typically in the GHz range corresponding to picosecond oscillation periods. The timing between sequential pump pulses is such that the system has completely damped back to its equilibrium position by the time the next pump pulse arrives. An 800nm probe pulse arrives after the pump pulse and reads the state of the system. The pump and probe pulses are different wavelengths so that they can be separated using an optical filter. Because the magnetization follows the same trajectory on its journey from excitation to equilibrium, if the probe pulse arrives at the same time after the pump it will be probing the same state of the spin system. The state of the magnetic system for a given time after excitation can be extracted from the signals of multiple probe pulses averaged out using a lock-in detector. The next snapshot in time can be obtained by elongating the optical path length of the probe pulse which causes it to arrive at a later time. This process continues until the system has damped to equilibrium resulting in a series of snapshots which show the time evolution of the magnetic system. This process is represented in figure 4.1 for two time snapshots.

4.3 The Pump Excitation

The excitation of magnetic materials with ultrashort electromagnetic pulses is a rich topic of fundamental research. Laser pulses on the femtosecond timescale place the system into a highly non-equilibrium state which offers the possibility to explore the intimate relationship between electron, phonon and spin subsystems. In 1996 Beaupaire et al. demonstrated the ultrafast demagnetization of a nickel film following the excitation of a femtosecond laser pulse. [68] This was a startling result since the observed time for demagnetization required a transfer of angular momentum on a timescale that challenged existing theories concerning energy transfer between different subsystems. Additionally, the experiment opened up the idea for manipulation of the magnetization state using light rather than conventional excitation techniques such as an applied magnetic field. The manipulation of the magnetization using light can be broken down into three types of effects that are attributed to different interactions between the electromagnetic wave and the material—thermal effects, nonthermal effects and optomagnetic effects. [69] Materials with different electronic structures such as metals, semiconductors and dielectrics provide different means for uncovering the physics governing the interplay between electromagnetic energy and the interactions between subsystems. So far, the intrinsic material response to an ultrashort light pulse in the first picosecond after excitation is poorly understood.

4.3.1 Three Temperature Model

Although the atomistic mechanisms governing the interactions between the subsystems is elusive, a phenomenological description describing their energy transfer rates does exist. This model consists of three coupled differential rate equations modeling the temperature evolution of the subsystems. [69,70]

$$C_e \frac{\partial T_e}{\partial t} = \nabla \cdot (\kappa \nabla T_e) - G_{el}(T_e - T_l) - G_{es}(T_e - T_s) + S(t) \quad (4.1)$$

$$C_s \frac{\partial T_s}{\partial t} = -G_{es}(T_s - T_e) - G_{sl}(T_s - T_l) \quad (4.2)$$

$$C_l \frac{\partial T_l}{\partial t} = -G_{el}(T_l - T_e) - G_{sl}(T_l - T_s) \quad (4.3)$$

κ is the thermal conductivity, $S(t)$ is the heat generated from the laser pulse, G_{ij} is the coupling between the i and j systems, T_i is the temperature and C_i the heat capacity of system i . The subscripts e , l and s stand for electron, lattice and spin systems. This model can be further simplified into a two-temperature model between the electron and lattice (phonon) systems. [71,72]

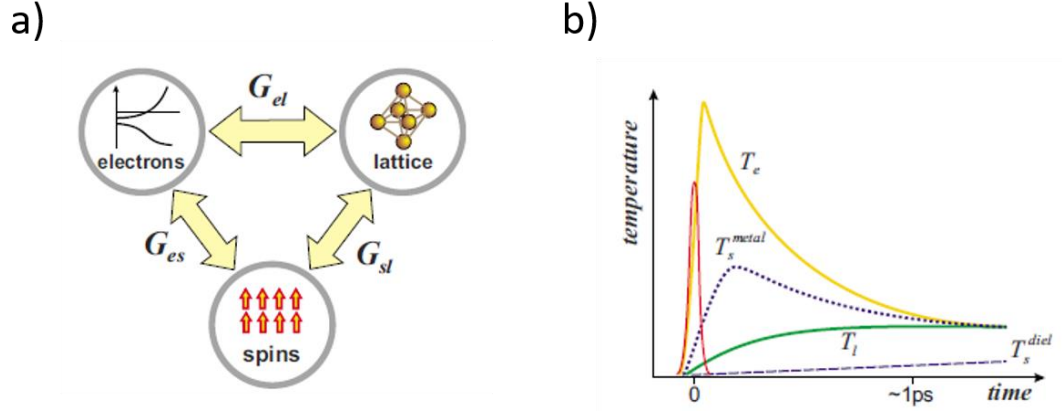


Figure 4.2: (a) Schematic showing the interaction between the electron, lattice and spin subsystems and (b) an example of the time evolution of the different subsystems governed by the rate equations (4.1) – (4.3). The red line corresponds to the excitation laser pulse. The subscripts e , l , and s correspond to the electron, lattice and spin systems, respectively. The evolution of the spin system is shown for a metal (blue dotted line) and a dielectric (blue dashed line). Taken from [69].

Due to the high optical frequencies of the femtosecond laser pulse, the electron system is the only system able to immediately respond. Additionally, the smaller heat capacity of the electron system means it can reach an extremely high temperature. Following excitation, the electron system equilibrates with the lattice system due to electron-phonon coupling, which gradually heats up the lattice system (generating phonons) while cooling off the electron system. The coupling with the spin system offers channels for the angular momentum transfer from the electron system into the

other subsystems. [69] Within the first few picoseconds all three systems approach equilibrium.

4.3.2 Thermal Anisotropy Pulse

As interesting and mysterious as the first picosecond is, the dynamics studied in this thesis took place on longer timescales ($\sim 1-2\text{ns}$) where the systems were all in equilibrium. The excitation of the magnetic system by the pump pulse is the tool to initiate magnetic dynamics rather than the direct object of study. Its effect on the magnetization vector can be understood as arising due to thermal effects.

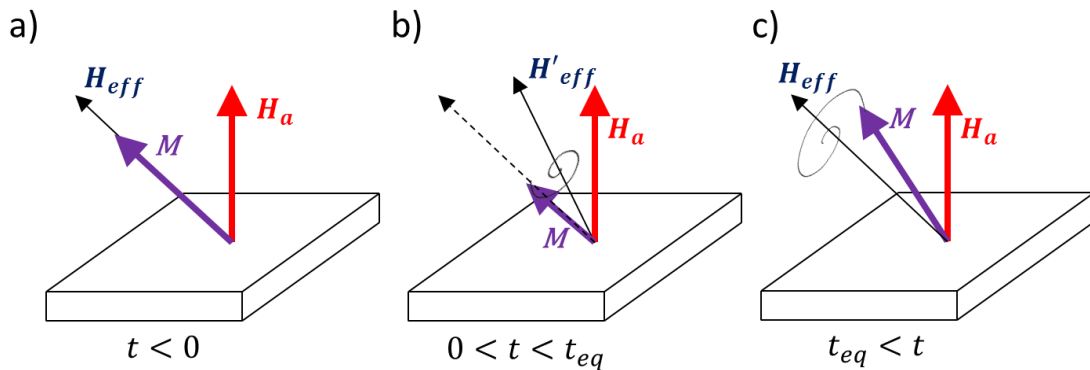


Figure 4.3: Schematic demonstrating how the influence of a thermal pulse acts as an excitation mechanism for the precession of the magnetization. (a) Initially the magnetization (M) is at rest, oriented along the equilibrium direction of the effective field (solid black arrow, H_{eff}). (b) Upon irradiation from an ultrashort laser pulse

($t = 0$), the elevated temperature causes the value of M_S to decrease. This changes the direction of the effective field and causes the magnetization to precess around the new effective field direction, \mathbf{H}'_{eff} . (c) After a short time ($t = t_{eq}$) the system has cooled and the magnetization has regained the original value of M_S . However it is no longer aligned along the initial effective field direction, \mathbf{H}_{eff} . Therefore, it again begins to precess around the new (original) equilibrium direction.

In order to initiate the magnetization dynamics, an external magnetic field is applied in a direction with some component along a hard anisotropy axis. The direction of the magnetization is oriented along the direction of the effective field which is a combination of the internal energy terms and the applied field as discussed in chapter 3. For example, in the case of a thin film the demagnetization energy attempts to align the magnetization in-plane and is proportional to the magnitude of M_S . If an external field is applied with a component out of plane, the external field will partially counteract the demagnetization field resulting in the magnetization vector oriented somewhat out of plane. When the system is irradiated by the pump pulse the electron system is excited, which changes the magnitude of the magnetization vector since $\mathbf{M}(T_{e,2}) < \mathbf{M}(T_{e,1})$ when $T_{e,2} > T_{e,1}$. Because the demagnetization field (and magnetocrystalline anisotropy) is proportional to the value of the magnetization vector, the excitation changes the direction of the effective field. If this happens on a timescale faster than the precessional period of motion, then the magnetization cannot

follow this change and \mathbf{M} begins to precess around the new effective field. [73] After the temperature has returned to equilibrium (restoring the original value of the magnetization vector and thus the original value of the anisotropy terms) \mathbf{M} once again finds itself displaced and begins to precess around the original equilibrium direction. [74] The excitation by the pump pulse thus acts as an effective anisotropy pulse knocking the magnetization vector out of equilibrium. This process is demonstrated in figure 4.3. The precessional motion that occurs after the subsystems have equilibrated in temperature and the magnetization vector has returned to its original magnitude is the motion which is probed in the experiments in this thesis.

4.4 The Probe Detection

Having explained the manner in which the magnetization is excited by the pump pulse we turn to the probe pulse. Understanding the interaction of the probe pulse with a magnetic material is more nuanced for the purposes of this thesis and the remainder of this chapter will be devoted to elucidating this interaction.

4.4.1 Gyrotropic Media

The electronic response to a propagating light wave in a medium is given by

$$\mathbf{D} = \epsilon_0 \epsilon_r \mathbf{E} \quad (4.4)$$

Where \mathbf{D} is the electric displacement, \mathbf{E} the electric field ϵ_0 is the permittivity of free space and ϵ_r is the relative permittivity. [75] In gyrotropic (optically active) media the corresponding equation is given by

$$\mathbf{D} = \varepsilon \mathbf{E} + i\varepsilon_0 \mathbf{G} \times \mathbf{E} \quad (4.5)$$

Where $\varepsilon = \varepsilon_0 \varepsilon_r$ is the absolute permittivity and \mathbf{G} is the gyration vector. It is instructive to understand the mechanisms responsible for an electronic response given by equation (4.5). Gyrotropic responses to electromagnetic waves can occur in materials with helical structures. The motion of the electrons in a helical structure acts like a solenoid of current which generates a time varying \mathbf{B} -field (Fig. 4.4). [76]

$$-\frac{\partial B}{\partial t} = \nabla \times \mathbf{E} \quad (4.6)$$

All of the little solenoids in the material further modify the polarization state of the electrons. Assuming a monochromatic plane wave of the form $\mathbf{E} = E_0 e^{i(\mathbf{k} \cdot \mathbf{r} - \omega t)}$ the change in the polarization is given by

$$\Delta \mathbf{P} = \left(-\frac{\partial B}{\partial t} \right) = \nabla \times \mathbf{E} = i\xi \mathbf{k} \times \mathbf{E} \quad (4.7)$$

Where ξ is a scalar that changes sign depending on the helicity of the intrinsic structure (right vs. left). This change in polarization contributes to the electric displacement vector so that the medium behaves gyrotropically [75]

$$\mathbf{D} = \varepsilon \mathbf{E} + \Delta \mathbf{P} = \varepsilon \mathbf{E} + i\xi \mathbf{k} \times \mathbf{E} \quad (4.8)$$

In this case $\mathbf{G} = \frac{\xi \mathbf{k}}{\varepsilon_0}$.

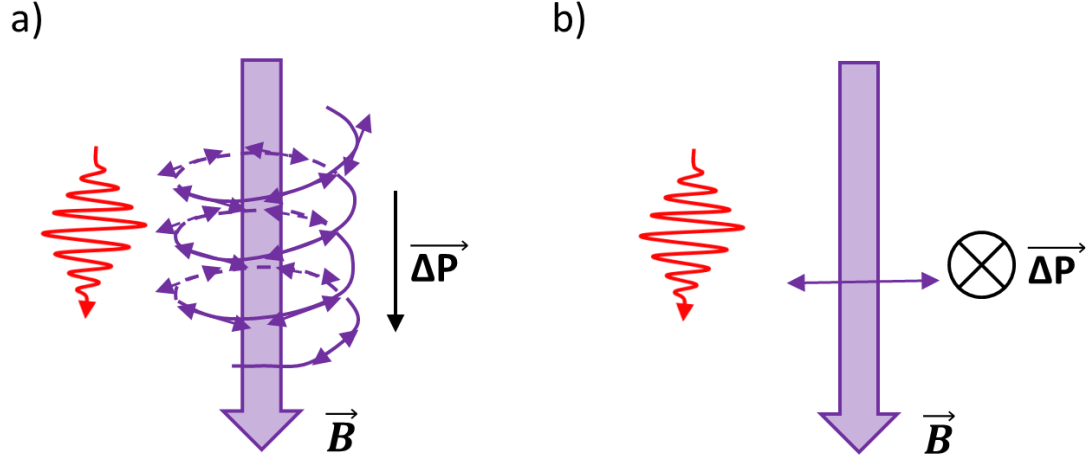


Figure 4.4: (a) Electrons oscillate around their equilibrium positions as they interact with an electromagnetic field. Due to their orientation in a helical structure their motion will cause a time varying B -field along the direction of electromagnetic wave propagation. This induces an extra polarization of the electrons in the medium. (b) For the case of a plasma in an external B -field, the motion of the electrons due to the electromagnetic wave causes an additional Lorentz force on the electrons. This induces an extra polarization of the electrons.

Another example is the electronic response of a plasma in the presence of a magnetic field. [76] The instantaneous velocity \mathbf{v} due to the displacement of the electrons from the propagating electric field can be obtained by considering the force acting on the electrons by the Electric field

$$m \frac{dv}{dt} = eE \quad (4.9)$$

Again assuming a monochromatic plane wave for the electric field and solving for \mathbf{v} we get

$$\mathbf{v} = \frac{-ime}{\omega} \mathbf{E} \quad (4.10)$$

If a magnetic field is applied to a material the electrons will feel the Lorentz force

$$\mathbf{F} = e\mathbf{v} \times \mathbf{B} \quad (4.11)$$

This force will cause an additional displacement of the electrons which results in a contribution to the polarization

$$\Delta \mathbf{P} = -e\mathbf{F} = -e \left(\frac{-ime}{\omega} \mathbf{E} \right) \times \mathbf{B} \quad (4.12)$$

This contribution gets added to the electric displacement

$$\mathbf{D} = \varepsilon \mathbf{E} + \Delta \mathbf{P} = \varepsilon \mathbf{E} + i\gamma \mathbf{B} \times \mathbf{E} \quad (4.13)$$

Where in this case $\mathbf{G} = \frac{\gamma \mathbf{B}}{\varepsilon_0}$ and γ is the magnetogyration coefficient. [76]

These two examples serve to show how the interaction of an electric field and matter in different environments can lead to additional polarization effects which influence the electronic response of the medium. The first example is a case of spatial dispersion due to the helical organization of the structure and is related to \mathbf{k} , and the second case is an example of temporal dispersion due to the presence of the magnetic field and is related to ω . [76]

Ferromagnetic materials have gyrotropic responses without the influence of an external field. The effect in ferromagnetic materials is considerably stronger as well. Using the model of a plasma in the presence of a uniform field the effective field necessary to explain the observed effects in ferromagnetic bodies is on the order of $10^6 - 10^7$ Oe. This is the same order of magnitude as the Weiss field which was intended to explain the origin of ferromagnetism. [77] Although, we know that the mechanism responsible for the alignment of the spins in ferromagnetic materials is due to the exchange interaction, the order of magnitude correspondence is a clue that the mechanism causing the gyrotropy in ferromagnets is related to the alignment of the spins in the same direction. It was shown that ferromagnetic gyrotropy arises from the electromagnetic field interaction with the atomic orbitals which has a net direction of the angular momentum due to the exchange interaction. Due to the spin-orbit interaction this corresponds to a dependence on the spin direction. [78] Regardless of the intrinsic mechanisms involved optically active media are characterized by an electric displacement vector in the form of equation (4.5) which causes ϵ to become a tensor with off diagonal terms.

4.4.2 Normal Modes

Now that we have a classical sense of what causes materials to be optically active we can go into more detail concerning the effect the off-diagonal dielectric tensor elements have on electromagnetic waves. The simplest case to analyze is when \mathbf{G} is in the z -direction and the electromagnetic wave also propagates along z so that the

only oscillations occur in the x - y plane. [79] If the material is isotropic then the electric permittivity tensor becomes

$$\boldsymbol{\varepsilon} = \begin{pmatrix} \varepsilon_{xx} & \varepsilon_{xy} & 0 \\ -\varepsilon_{xy} & \varepsilon_{xx} & 0 \\ 0 & 0 & \varepsilon_{zz} \end{pmatrix} \quad (4.14)$$

Where all of the components can be complex, and the microscopic mechanisms concerning ε_{xy} depend on the gyrotropic media under consideration.

The Maxwell equations concerning the propogating electromagnetic wave are given by

$$\nabla \times \mathbf{E} = -\mu_0 \frac{\partial \mathbf{H}}{\partial t} \quad (4.15)$$

$$\nabla \times \mathbf{H} = \varepsilon_0 \boldsymbol{\varepsilon} \cdot \frac{\partial \mathbf{E}}{\partial t} \quad (4.16)$$

Again we consider a plane wave. The \mathbf{E} and \mathbf{H} componenets are given by

$$\mathbf{E} = E_0 e^{i(\mathbf{k} \cdot \mathbf{r} - \omega t)} \quad (4.17)$$

$$\mathbf{H} = H_0 e^{i(\mathbf{k} \cdot \mathbf{r} - \omega t)} \quad (4.18)$$

So that equations (4.15) and (4.16) become

$$\mathbf{k} \times \mathbf{E} = \omega \mu_0 \mathbf{H} \quad (4.19)$$

$$\mathbf{k} \times \mathbf{H} = -\omega \varepsilon_0 \boldsymbol{\varepsilon} \cdot \mathbf{E} \quad (4.20)$$

Plugging (19) into (16) and noting that $\mathbf{k} \times (\mathbf{k} \times \mathbf{E}) = \mathbf{k}(\mathbf{k} \cdot \mathbf{E}) - k^2 \mathbf{E}$ we get

$$\mathbf{k}(\mathbf{k} \cdot \mathbf{E}) - k^2 \mathbf{E} + \omega^2 \mu_0 \varepsilon_0 \boldsymbol{\varepsilon} \cdot \mathbf{E} = 0 \quad (4.21)$$

We set $k_0^2 = \omega^2 \mu_0 \varepsilon_0$, $\mathbf{N} = \mathbf{k}/k_0$ and keep in mind the electric field oscillations are perpendicular to the propagation direction ($\mathbf{k} \cdot \mathbf{E} = 0$). [79] Finally, since there is no electric field component along the z -direction (along propagation) we can reduce the matrix to a two-dimensional eigenvalue equation

$$\begin{pmatrix} \varepsilon_{xx} & \varepsilon_{xy} \\ -\varepsilon_{xy} & \varepsilon_{xx} \end{pmatrix} \cdot \mathbf{E} = N^2 \mathbf{E} \quad (4.22)$$

Solving the characteristic equation gives the following eigenvalues

$$N_{\pm}^2 = \varepsilon_{xx} \pm i\varepsilon_{xy} \quad (4.23)$$

With eigenvectors $\frac{1}{\sqrt{2}} \begin{pmatrix} 1 \\ i \end{pmatrix}$ and $\frac{1}{\sqrt{2}} \begin{pmatrix} 1 \\ -i \end{pmatrix}$, which means that $E_x = \pm iE_y$. These eigenvectors correspond to right (RHC) and left (LHC) handed circularly polarized light and form an orthonormal basis in gyrotropic media. The eigenvalues are the refractive indices of the two modes. The normal modes are

$$\mathbf{D}_{\pm} = N_{\pm}^2 \begin{pmatrix} 1 \\ \pm i \end{pmatrix} E_0 e^{-i\omega t} \quad (4.24)$$

The physical interpretation is that light propagating in gyrotropic materials is decomposed into components of the normal modes—right and left handed circularly polarized light. The respective amplitude of these two modes dictates the amount of ellipticity. The phase difference between the modes determines the angle of the major axis of the ellipse (angle of polarization). (Fig. 4.5)

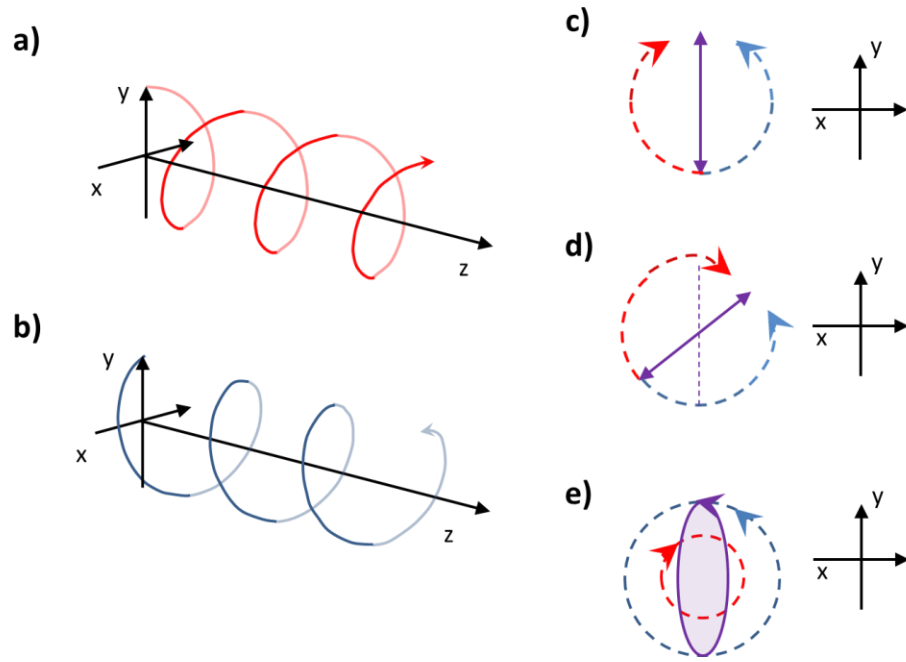


Figure 4.5: The normal modes in gyrotropic media are (a) Left (LHC) and (b) right handed circular polarization (RHC). (c) When RHC and LHC have the same amplitude and phase their sum results in linear polarization along the y-direction. (d) If there is a phase offset between the RHC and LHC modes then the resultant linear polarization is rotated. (e) If the amplitudes of the RHC and LHC modes are different then the summed wave is elliptically polarized.

4.4.3 Faraday Effect

From equation (4.24) it is clear that the two normal modes experience different indices of refraction within gyrotropic media. The implications are twofold and arise

due to the real and imaginary parts of the indices of refraction. First, as the modes propagate through gyrotropic media they travel at different speeds $v_{\pm} = c/Re\{N_{\pm}\}$ ($N = \varepsilon^{1/2}$). Second, they are attenuated at different rates $\alpha_{\pm} = -\omega \cdot Im\{N_{\pm}\}/c$. Therefore, as light travels through a gyrotropic medium for a distance l , it will experience a phase difference between the two circular polarization components due to their different velocities. This will result in a rotation of the polarization angle given by [79]

$$\theta_F = \frac{\omega l}{2c} Re(N_+ - N_-) \quad (4.25)$$

Also, they will attenuate at different rates. This changes the relative amplitudes of the normal modes which affects the ellipticity of the light

$$\eta_F = -\frac{\omega l}{2c} Im(N_+ - N_-) \quad (4.26)$$

The different absorption coefficient for RHC and LHC light is the basis for magnetic circular dichroism experimental techniques. We can decompose the refractive indices of the RHC and LHC light into their corresponding real and imaginary parts $N_{\pm} = n_{\pm} + ik_{\pm}$. Subtracting the two eigenvalues given by equation (4.23), and keeping in mind that the dielectric tensor components can be complex so that $\varepsilon_{xy} = \varepsilon'_{xy} + i\varepsilon''_{xy}$. Then setting $n = \frac{n_+ + n_-}{2}$, $k = \frac{k_+ + k_-}{2}$, $\Delta n = Re(N_+ - N_-) = n_+ - n_-$ and $\Delta k = Im(N_+ - N_-) = k_+ - k_-$ gives [79]

$$\varepsilon'_{xy} = n\Delta k + k\Delta n \quad (4.27)$$

$$\varepsilon''_{xy} = k\Delta k - k\Delta n \quad (4.28)$$

Which allows us to express the rotation angle and the ellipticity as [79]

$$\theta_F = \frac{\omega l}{2c} \frac{k\varepsilon'_{xy} - n\varepsilon''_{xy}}{n^2 + k^2} \quad (4.29)$$

$$\eta_F = -\frac{\omega l}{2c} \frac{n\varepsilon'_{xy} + k\varepsilon''_{xy}}{n^2 + k^2} \quad (4.30)$$

Therefore, the rotation and the ellipticity are related to the off-diagonal ε_{xy} dielectric tensor components.

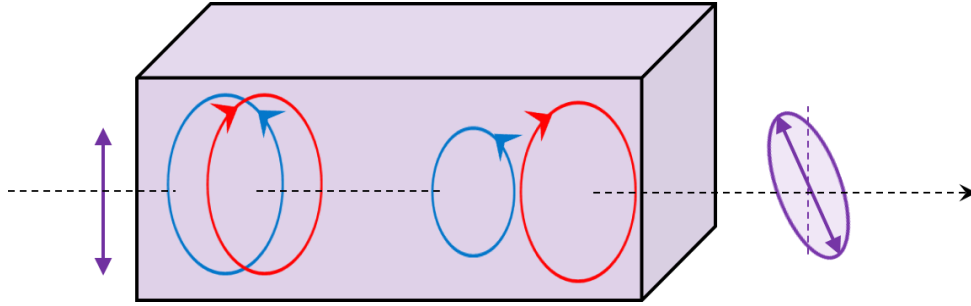


Figure 4.6: When linearly polarized light enters an optically active medium, it splits into two circularly polarized modes. Because the medium has different refractive indices, the two modes propagate at different speeds and a phase difference is introduced between the modes as it propagates through the medium. This leads to a rotation of the polarization. Additionally, the two modes have different attenuation coefficients so that the relative amplitudes are different after propagating through the

medium. This introduces ellipticity to the light. The light that emerges is thus elliptically polarized with the major axis of the ellipse rotated.

4.4.4 Magneto-Optic Kerr Effect

The different indices of refraction for the RHC and LHC modes also cause reflected light to experience a rotation and change in ellipticity as well. So far we have been discussing the effect the off diagonal components of the dielectric tensor have on light in rather specific configurations. In the general case of light reflecting off a ferromagnetic sample the dielectric tensor becomes

$$\varepsilon = \varepsilon_{xx} \begin{pmatrix} 1 & -iQm_z & iQm_y \\ iQm_z & 1 & -iQm_x \\ -iQm_y & iQm_x & 1 \end{pmatrix} \quad (4.31)$$

Where $Q = i \frac{\varepsilon_{xy}}{\varepsilon_{xx}}$ and m_x , m_y and m_z are directional cosines of the magnetization vector \mathbf{M} . [80,81] By solving Maxwell's equations subject to the following boundary conditions (no surface charges)

$$\mathbf{n} \cdot (\mathbf{D}_2 - \mathbf{D}_1) = 0 \quad (4.32)$$

$$\mathbf{n} \times (\mathbf{E}_2 - \mathbf{E}_1) = 0 \quad (4.33)$$

$$\mathbf{n} \cdot (\mathbf{B}_2 - \mathbf{B}_1) = 0 \quad (4.34)$$

$$\mathbf{n} \times (\mathbf{H}_2 - \mathbf{H}_1) = 0 \quad (4.35)$$

we obtain a relation between the s and p components of the incident and reflected light which is given by

$$\begin{pmatrix} \mathbf{E}_s^{(r)} \\ \mathbf{E}_p^{(r)} \end{pmatrix} = \begin{pmatrix} r_{ss} & r_{sp} \\ r_{ps} & r_{pp} \end{pmatrix} \begin{pmatrix} \mathbf{E}_s^{(i)} \\ \mathbf{E}_p^{(i)} \end{pmatrix} \quad (4.36)$$

Where [80]

$$r_{pp} = \frac{n_2 \cos(\theta_1) - n_1 \cos(\theta_2)}{n_2 \cos(\theta_1) + n_1 \cos(\theta_2)} - \frac{i2n_1 n_2 \cos(\theta_1) \sin(\theta_2) Q m_x}{n_2 \cos(\theta_1) + n_1 \cos(\theta_2)} \quad (4.37)$$

$$r_{sp} = \frac{in_1 n_2 \cos(\theta_1) (m_y \sin(\theta_2) + m_z \cos(\theta_2)) Q}{(n_2 \cos(\theta_1) + n_1 \cos(\theta_2))(n_1 \cos(\theta_1) + n_2 \cos(\theta_2)) \cos(\theta_2)} \quad (4.38)$$

$$r_{ss} = \frac{n_1 \cos(\theta_1) - n_2 \cos(\theta_2)}{n_1 \cos(\theta_1) + n_2 \cos(\theta_2)} \quad (4.39)$$

$$r_{ps} = -\frac{in_1 n_2 \cos(\theta_1) (m_y \sin(\theta_2) - m_z \cos(\theta_2)) Q}{(n_2 \cos(\theta_1) + n_1 \cos(\theta_2))(n_1 \cos(\theta_1) + n_2 \cos(\theta_2)) \cos(\theta_2)} \quad (4.40)$$

θ_i is the angle with respect to the surface normal vector in medium i ., Analyzing these reflection coefficients reveals the manner in which the reflected light is altered. The effect on the light arises from the angle of incidence (θ_1) and the directional

components of the magnetization. The Kerr rotation θ_K and ellipticity η_K for s and p polarized light can be given by the reflection coefficients [80]

$$\theta_K^{(s)} + i\eta_K^{(s)} = \frac{r_{ps}}{r_{ss}} \quad (4.41)$$

$$\theta_K^{(p)} + i\eta_K^{(p)} = \frac{r_{sp}}{r_{pp}} \quad (4.42)$$

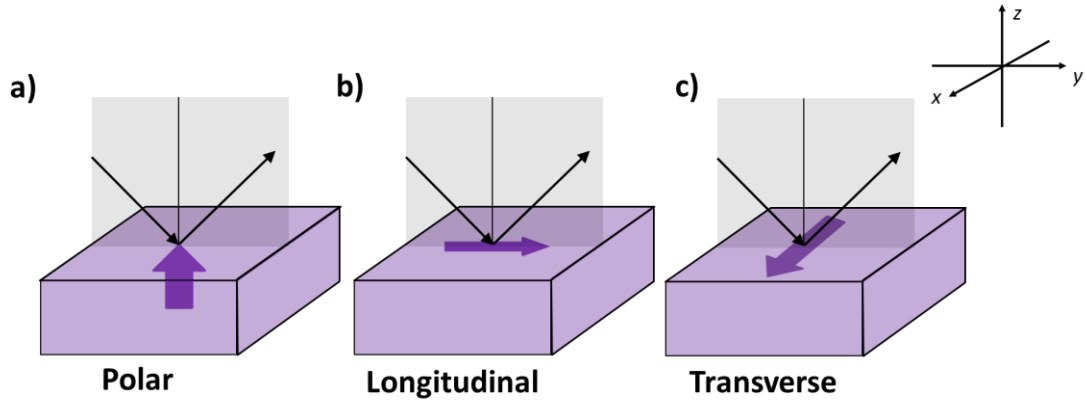


Figure 4.7: Schematic showing the different Kerr effect layouts. **(a)** In the Polar configuration the the z -component, m_z , of the magnetization is responsible for affecting the light. The incident light can come at an angle or normal to the sample surface. **(b)** The longitudinal configuration is sensitive to the in-plane component of the magnetization that is parallel to the plane of incidence, m_y . The incident light must come at an angle in order to be affected, therefore it is necessary to be careful to separate any possible polar effects. **(c)** In the Transverse configuration the magnetization that is perpendicular to the plane of incidence is responsible for

affecting the light. Unlike the previous two configurations which affect the angle and ellipticity of the light, this configuration only affects the reflectivity.

The effects can be decomposed into three configurations. (Fig. 4.7)

- 1) Polar configuration – The polar configuration is sensitive to the z -component of the magnetization and has the effect of mixing the s and p components of the incident beam via r_{sp} and r_{ps} . This results in a rotation of the polarization axis and introduction of ellipticity upon reflection from the sample. Tracing back to the dielectric tensor this effect is the result of the ϵ_{xy} and ϵ_{yx} components. There are two manners in which this effect can be taken advantage of. First, if the sample is magnetized only along the z -direction then m_z will be the only term entering into the reflection coefficients. Any effect on the polarization of the light at any angle of incidence can be attributed to the m_z component. Second, if the sample is magnetized in some arbitrary direction so that m_x , m_y and m_z components are present, then incident light which is normal to the sample surface will only be sensitive to the m_z component.
- 2) Longitudinal configuration – The Longitudinal configuration is sensitive to the magnetization component that lies within the plane of incidence, m_y . m_y also leads to a mixing of the s and p components of the incident beam via r_{sp} and r_{ps} which results in a rotation of the polarization and introduction of

ellipticity. This effect comes from the ϵ_{xz} and ϵ_{zx} components of the dielectric tensor. If the sample is magnetized entirely along the y -direction then any effect on the polarization will be due to m_y . However, the incident light must come at an angle due to the $\sin(\theta_2)$ dependence. If the sample is magnetized in an arbitrary direction then the change in polarization will be due to m_y and m_z components.

- 3) Transverse Configuration – The transverse configuration is sensitive to the magnetization component that is orthogonal to the plane of incidence, m_x . This effect comes from the ϵ_{yz} and ϵ_{zy} components of the dielectric tensor. r_{pp} is the only reflection coefficient with an m_x dependence. In this case the amplitude of the incident p -polarized light is affected with the maximum effect occurring at an angle of incidence of 45 degrees.

4.5 Detection

So far we have seen how light is affected by interacting with magnetic materials. Therefore, if we know the state of the light before the interaction with the magnetic material and we analyze the light after it has been altered we can make inferences concerning the magnetic system. Detecting the change in the light upon reflection can be accomplished utilizing a few different measurement schemes. [73]

4.5.1 Crossed Polarizer

In the crossed polarizer configuration two linear polarizers are used in order to analyze the probe signal. (Fig. 4.8) The first polarizer sets the initial state of the

incoming light by polarizing the light along a certain direction and is known as the polarizer. The second polarizer is responsible for separating out the effect the magnetic material has on the polarization and is known as the analyzer. In order to calculate how light is affected as it interacts with various optical components and materials we use the methods of *Jones matrices*, which breaks down each interaction the light has into matrices which describe the effect on the polarization of light.

Assuming the electric field is polarized (if it is unpolarized the method of Mueller Matrices must be used [82]), it can be decomposed into s and p components so that

$$\mathbf{E} = \begin{pmatrix} E_s \\ E_p \end{pmatrix} \quad (4.43)$$

The matrix for a linear polarizer is given by

$$L(\alpha) = \begin{pmatrix} \sin^2 \alpha & \sin \alpha \cos \alpha \\ \sin \alpha \cos \alpha & \cos^2 \alpha \end{pmatrix} \quad (4.44)$$

Where α is the angle measured from the plane of incidence. In the crossed polarizer configuration light first interacts with the polarizer oriented at an angle α_p , then is reflected off the magnetic material and finally passes through the analyzer oriented at an angle α_A . (Fig. 4.8) The mathematical description relating the final electric field, \mathbf{E}_f to the initial electric field, \mathbf{E}_i in matrix form is given by

$$\mathbf{E}_f = L(\alpha_A) \cdot R \cdot L(\alpha_p) \cdot \mathbf{E}_i \quad (4.45)$$

Where R is the 2×2 reflection matrix (Eq. 4.36).

If $\alpha_p = 90^\circ$ so that the light is completely s -polarized as it irradiates the sample, and making the further assumption that $\alpha_A \ll 1$, so that the polarizer and analyzer are essentially “crossed” leads to [73]

$$\mathbf{E}_f = \begin{pmatrix} \alpha_A^2 r_{ss} + r_{ps} \alpha_A \\ \alpha_A r_{ss} + r_{ps} \end{pmatrix} \mathbf{E}_i \quad (4.46)$$

The detectors are sensitive to the intensity, $I = \mathbf{E}_f \mathbf{E}_f^*$. Keeping terms only up to 2nd order we get

$$I = R(\alpha_A^2 + 2\alpha_A \theta_K + \theta_K^2 + \eta_K^2) \quad (4.47)$$

Where the θ_K and η_K are given by equation (4.41) with the superscript dropped. In order to see how this signal is modified by the action of the pump pulse we take the partial derivatives and keep terms that are linear with respect to θ_K . This gives the dynamic change in the intensity. [73]

$$\Delta I(t) = \alpha_A^2 \Delta R(t) + 2R_0 \alpha_A \Delta \theta_K(t) \quad (4.48)$$

From this we can see that the change in the intensity of the light is proportional to the change in the Kerr rotation, $\Delta \theta_K(t)$ and has a background scaling factor due to the nonmagnetic contributions of $\alpha_A^2 \Delta R(t)$. These two effects cannot be separated in this configuration.

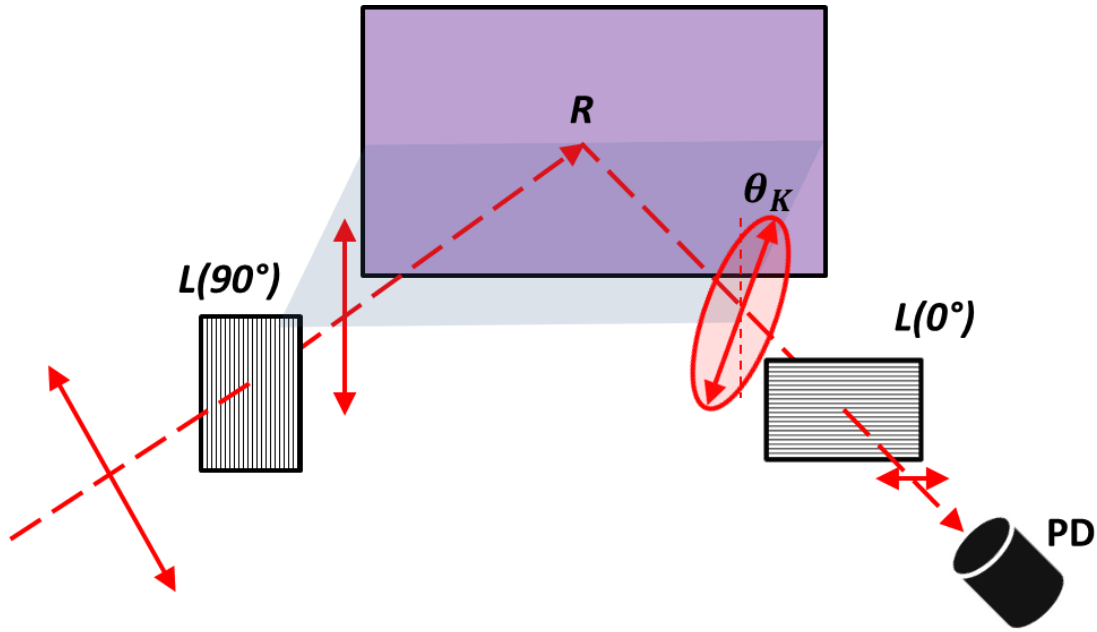


Figure 4.8: Schematic of the crossed polarizer configuration discussed in text. Light is sent through a polarizer (L) oriented at 90° with respect to the plane of incidence so that the light is s -polarized. After light is reflected off the sample (R) the polarization is rotated (θ_K) and it becomes slightly elliptic due to the Kerr effect. The light then passes through another polarizer (L) oriented at 0° with respect to the plane of incidence. The light that passes through the second polarizer is proportional to the Kerr rotation due to the reflection. The intensity is detected by a photodiode (PD).

4.5.2 Balanced Photodiodes

In a balanced photodetector configuration the light that is reflected off of the magnetic sample is passed through a polarizing beam splitter (PBS) which splits the light into two components orthogonal to one another. (Fig. 4.9) The magnitude of the

two components depends on the relative orientation of the polarized light with the plane of incidence of the PBS. For simplicity we assume that the plane of incidence of the PBS is the same as the plane of incidence given by the reflection off the magnetic sample. In the Jones formulism, the orthogonal components of the light are represented as two equations [73]

$$\mathbf{E}_{f,1} = L(\alpha_{PBS}) \cdot R \cdot L(\alpha_P) \cdot \mathbf{E}_i \quad (4.49)$$

$$\mathbf{E}_{f,2} = L(\alpha_{PBS} - 90) \cdot R \cdot L(\alpha_P) \cdot \mathbf{E}_i \quad (4.50)$$

Where as in the crossed polarizer case $\alpha_P = 90^\circ$. Taking the difference in the intensity of the two beams gives

$$I = I_1 - I_2 = R[(\sin^4 \alpha_{PBS} - \cos^4 \alpha_{PBS})(\theta_K^2 + \eta_K^2 - 1) + 4\theta_K \sin \alpha_{PBS} \cos \alpha_{PBS}] \quad (4.51)$$

Where $I_i = \mathbf{E}_{f,i} \mathbf{E}_{f,i}^*$. If $\alpha_{PBS} = 45^\circ$, then the beam will be split into two equal parts so that the signal from the two photodetectors is “balanced”. Taking the partial derivatives of equation (4.51) gives the dynamic signal which is given by [73]

$$\Delta I(t) = 2\theta_0 \Delta R(t) + 2R_0 \Delta \theta_K(t) \quad (4.52)$$

Since $\Delta R(t)/R_0 \ll \Delta \theta_K(t)/\theta_0$ the dynamic response becomes

$$\Delta I_\Delta(t) = 2R_0 \Delta \theta_K(t) \quad (4.52)$$

Where the Δ subscript indicates that the dynamic signal is due to the difference in the intensity of the two signals. This is an improvement over the crossed polarizer configuration because the magnetic and non-magnetic contributions to the signal have been separated. [73]

Additionally, if we take the sum of the intensities

$$I = I_1 + I_2 = R + \theta_K^2 + \eta_K^2 \quad (4.53)$$

Since $R \gg \theta_K$ the dynamic response becomes

$$\Delta I_\Sigma(t) = \Delta R(t) \quad (4.54)$$

Where the Σ subscript indicates that the dynamic signal is due to the sum of the intensity of the signals. Using the balanced photodetector configuration we are able to detect the magnetic and non-magnetic contributions to the signal at the same time by splitting the reflected light into equal components and taking the difference and the sum of the intensities. For the previous two examples, it is not critical that the initial polarization be s polarized. That was only used as a means to simplify the mathematics. However, it is always a good idea to consider the polarization state of the probe pulse since it does affect the reflection coefficients in certain configurations.

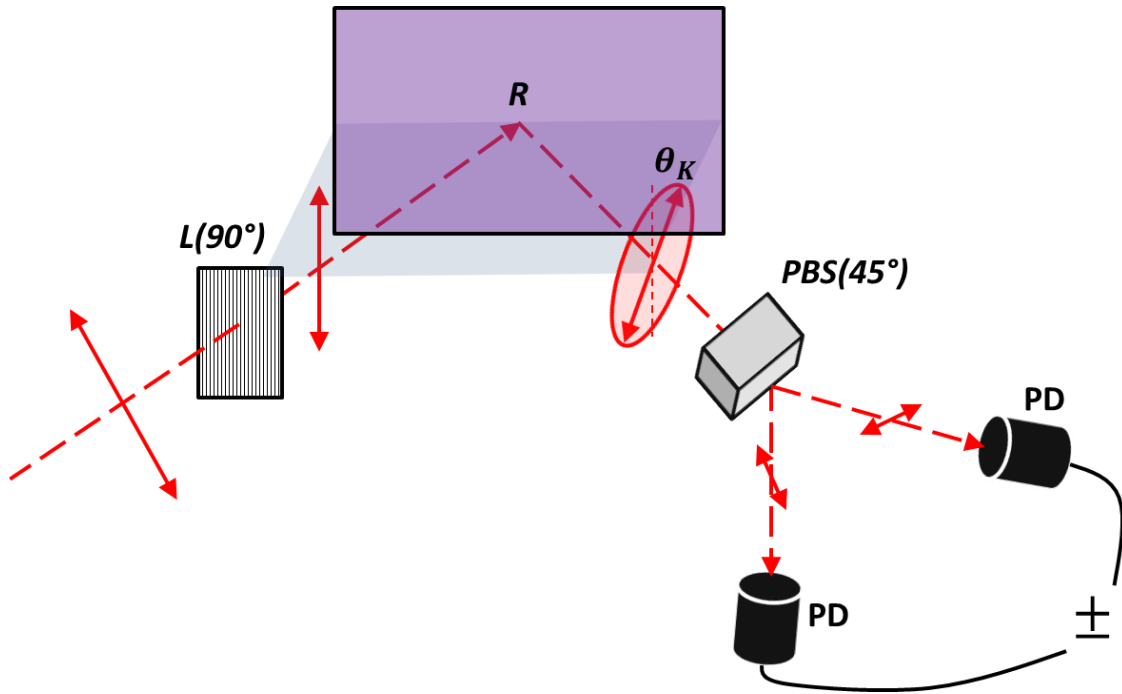


Figure 4.9: Schematic of the balanced polarizer configuration discussed in text. Light is sent through a polarizer (L) oriented at 90° with respect to the plane of incidence so that the light is s -polarized. After light is reflected off the sample (R) the Kerr effect causes the polarization to be rotated (θ_K) and become slightly elliptic. The light then passes through a polarizing beam splitter (PBS) oriented at 45° with respect to the plane of incidence. This splits the light into two even components so that the difference signal is “balanced”. Dynamic changes in the difference (-) of the signal from the two photodiodes (PD) give information on the magnetic system and changes in the sum (+) of the signal from the photodiodes give information on the non-magnetic system.

4.6 TR-MOKE Experiment

The experiments in this thesis were conducted using the balanced photo detector configuration. The reason is because for magneto-phononic structures the non-magnetic and magnetic information complement one another. The 165-fs probe (800nm) and pump (400nm) pulses were focused onto the sample using various microscope objectives. A microscope (Witec alpha300) was used to position the objective and the sample with submicron resolution. An external magnetic field was applied using a pair of Nd permanent magnets and the orientation and magnitude of the field was characterized using a gauss meter. At each applied field the time-dependent signal from the magnetic and non-magnetic channels were background corrected and converted into the frequency domain using a Fast Fourier Transform (FFT).

4.6.1 Beam Paths

Figure 4.10 shows a schematic of the experimental setup. The light exiting the fs Laser cavity is split by a beam splitter (BS1). Part of the split light is sent through a second harmonic generator (SHG) where the frequency is doubled to produce the pump pulse at a wavelength of 400nm. The pump pulse is then sent through a mechanical chopper wheel (MCW) which serves as a reference to the lock-in amplifiers. The other component of light serves as the probe pulse and has a much lower power than the pump pulse so that it has a negligible effect on the magnetic system. After the beam splitter the probe pulse goes through a delay stage which is

used to adjust the arrival time Δt of the probe pulse. Then the probe pulse is polarized ($L(\alpha_p)$). The orientation of the polarizer is adjusted to balance the difference signal. Next the probe passes through a beam splitter (BS2) which is used to recombine the reflected light. Next, the two beams are recombined using a dichroic filter (DF). The two beams are then sent through another beam splitter which is positioned so as to be able to image the beams and the sample surface using a camera (CCD). Both beams are then focused onto the sample using the Witec Microscope (WM). The reflected beams are sent back along their incoming paths. The dichroic filter should reflect most of the pump pulse out of the reflected path. When the probe reaches BS2 it is diverted from the path and sent through a color filter so as to get rid of any possible residual 400nm pump energy. The 800nm beam is then split by a polarizing beam splitter (PBS) and focused onto a pair of photo-diode detectors (BPD) which had been balanced as discussed previously. The detectors are connected to a circuit which outputs the difference (Δ) and sum (Σ) signals to two lock-in amplifiers which are then read by a LabView program on a computer.

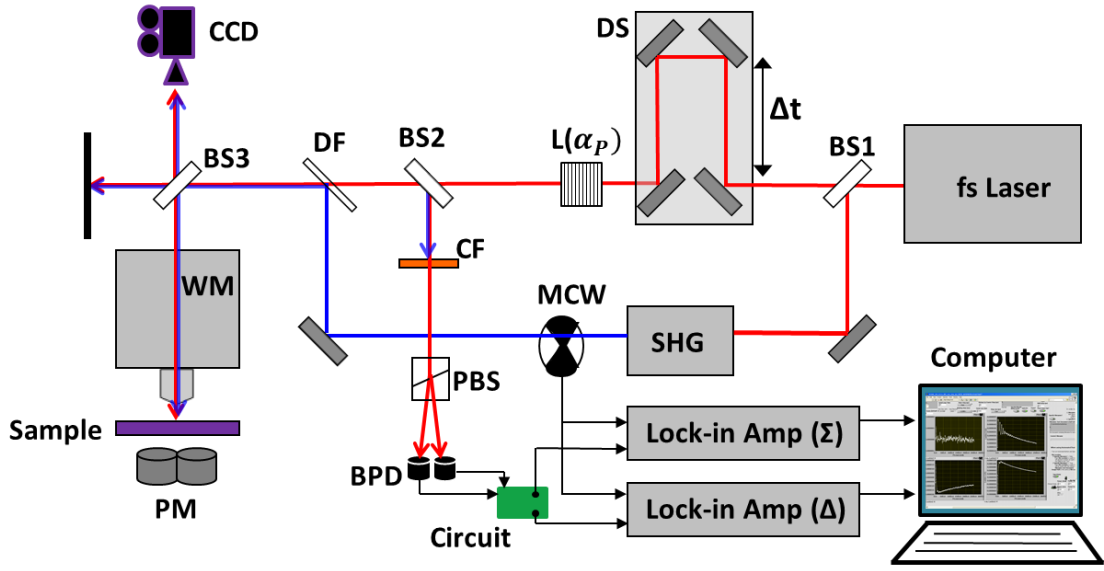


Figure 4.10: Schematic illustration of the experimental setup described in the text. Beam Splitter (BS); Delay Stage (DS); Linear Polarizer ($L(\alpha_p)$); Dichroic Filter (DF); Charge Coupled Device camera (CCD); Witec Microscope (WM); Permanent Magnets (PM); Second Harmonic Generator (SHG); Mechanical Chopper Wheel (MCW); Color Filter (CF); Polarizing Beam Splitter (PBS); Balanced Photodiodes (BPD)

4.6.2 Excitation Geometry Considerations

In the configuration shown in figure 4.10, the probe beam is sensitive to the z -component of the magnetization. Therefore, the relative geometry of the applied field and the anisotropy directions of the sample are important for excitation and detection. For example, assuming for simplicity the sample is a polycrystalline thin film, so that the demagnetization field is the dominant anisotropy term and acts to orient the

magnetization vector in the film plane. If the effective field points normal to the sample surface (this can be accomplished by applying a significantly strong external field in the direction normal to the plane) then the magnetization precession will only be in the xy plane. (Fig. 4.11a) Despite the fact that the magnetization is rotating, the precession will have no z -component and therefore will not be detectable in the polar Kerr configuration. Additionally, if the effective field is within the film plane which is an easy direction for the magnetization vector, then the pump heat pulse will not act as an anisotropy pulse and no precession will be initiated. (Fig. 4.11b) Alternatively, if the magnetization vector is canted at an angle then the magnetization can be perturbed and the precession will have a component along the z -direction so that it can be detected in the polar Kerr configuration.

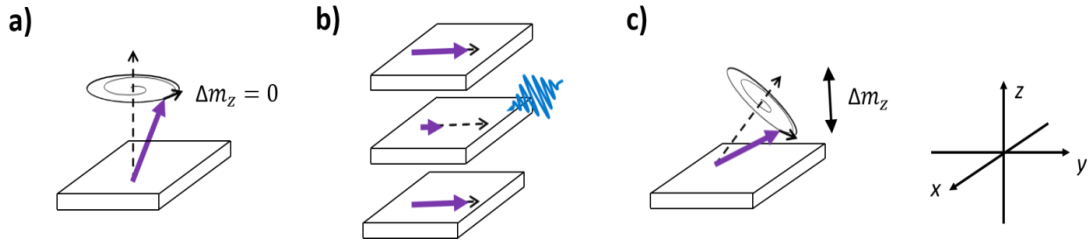


Figure 4.11: Precessional and excitation characteristics for a thin film with an in-plane easy axis. **(a)** If the magnetization is oriented normal to the surface by application of a strong external magnetic field, then the precession will be in the xy plane and will contribute no z -component. Therefore, there will be no detected signal in a polar Kerr configuration. **(b)** If the magnetization is oriented along the easy axis,

then the pump pulse will heat up the magnetization which will cause the magnitude of the magnetization vector to decrease. However, there will be no subsequent precession because the effective field direction will not change. (c) If the magnetization is canted with respect to the easy axis, then the pump pulse will perturb the system so that the magnetization precesses and there will also be a component of the precession along the z -direction so that it will be detectable in the polar Kerr configuration.

Considerations such as these must be tailored to the particular sample under study and to the Kerr configuration of the experiment. For example, if the frequency characteristics are needed for the out of plane magnetization configuration then the longitudinal or transverse Kerr effects could be used. In fact, it is possible to utilize multiple Kerr configurations simultaneously [83,84] to construct a profile of the magnetization trajectory in multiple dimensions.

4.6.3 Time Domain Analysis

For the experimental configuration discussed above, the TR-MOKE signal is due to a single component of the magnetization (m_z) and can be modelled as [85]

$$\theta_K = a + be^{-(t/t_0)} + A \sin(\omega t + \varphi)e^{-(t/\tau)} \quad (4.55)$$

Where a is a background signal, the second expression is a decaying signal which is due to the transient heating of the electron system by the heat pulse and the final term

is due solely to the precessional dynamics of the magnetization vector as given by the LLG equation. By subtracting out the exponential background we are left with a pure decaying sinusoid

$$\theta_K = A \sin(\omega t + \varphi) e^{-(t/\tau)} \quad (4.56)$$

Where ω is the resonance frequency discussed in chapter 3 and

$$\tau = \frac{1}{\omega \alpha} \quad (4.57)$$

Where α is the Gilbert damping parameter. This term will be discussed in more depth in Chapter 7. Figure 4.12 shows an example of the process of converting the raw signal into the pure oscillation dynamics modelled in the LLG equation.

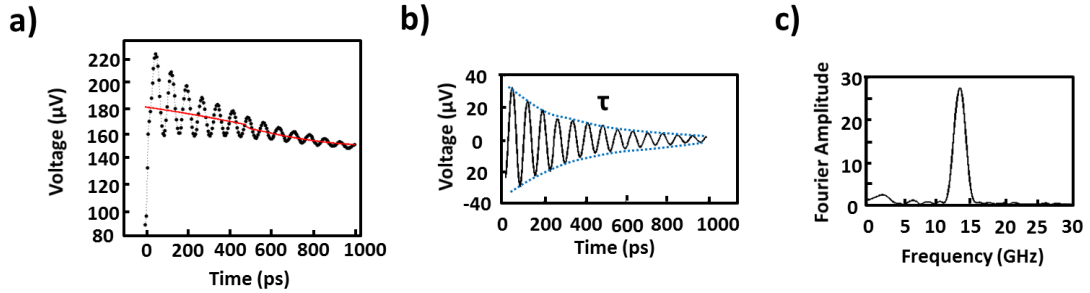


Figure 4.12: (a) Raw TR-MOKE signal from a thin Ni film with $H_a = 5kOe$ and $\theta_H = 30^\circ$. At $t = 0$ the pump pulse excites the system. This causes the sample to heat up and demagnetize which is represented as a rapid change in the signal. On a slower time scale the magnetization precesses around the effective field. There is still

some residual heat in the system which is represented as a slowly decaying backdrop to the oscillation. (red line) **(b)** By subtracting the slowly decaying backdrop from the raw signal the pure dynamical motion given by the LLG equation is left. **(c)** Using an Fast Fourier Transform (FFT) algorithm we can transform the time signal into the frequency domain.

4.6.4 Discrete Fourier Transform Linewidth

An important question is whether we can extract the damping of the system based on the linewidth of the discrete Fourier transform spectra (DFT is calculated using FFT algorithm). Since the TR-MOKE signal is of finite duration (limited either by the length of the scan, or when the signal drops below the noise level), this is equivalent to a decaying sinusoid multiplied by a rectangular windowing function in the time domain. In the frequency domain, this corresponds to a Lorentzian convolved with a Sinc function, which leads to broadening of the DFT linewidth. [86]

This effect is demonstrated on a clean Ni film resonance in figure 4.13 below. The decaying oscillation of a Ni film ($H = 6$ kOe) is fit to equation 4.56 which gives a relaxation time $\tau = 300$ ps. (Fig. 4.13a) Equation 4.56 Fourier transformed is a Lorentzian centered at $f = \omega/2\pi$. Since the relaxation time dictates the width of the Lorentzian, the full width at half maximum of the Lorentzian should be $FWHM = 1/\pi\tau = 1.06$ GHz. However, fitting the experimental DFT spectra to a Lorentzian gives a much larger value of $FWHM = 2.8 \pm 0.14$ GHz. (Fig. 4.13b)

In order to mimic the effect of the finite time window, we take a Lorentzian with a $FWHM = 1.06$ GHz corresponding to the intrinsic loss of the oscillation and then convolve the Lorentzian with a Sinc function corresponding to a rectangular window of 1000 ps in the time domain (length of the scan). Fitting the convolved signal gives $FWHM = 2.89$ GHz which matches the FWHM given by the DFT from the data within error and supports the fact that the finite length of the data is causing a spread in the spectra. (Fig. 4.13c)

Although we apply a Hamming window to the time signal in order to decrease the effects of the broadening by reducing the effect of the side lobes of the Sinc function, the DFT linewidth is still broadened (1.6x larger than the intrinsic value). (Fig. 4.13d)

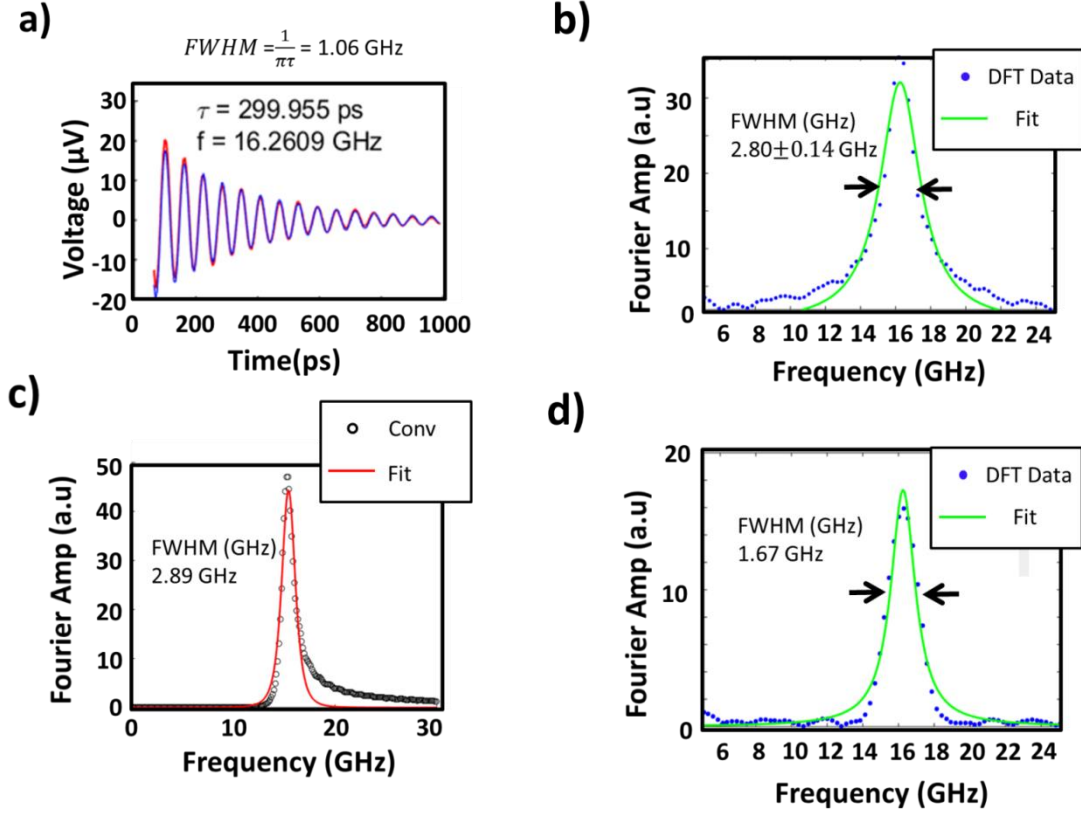


Figure 4.13: (a) The decaying oscillation of a Ni film ($H=6 \text{ kOe}$) (b) Fitting the DFT spectra from (a) to a Lorentzian gives $FWHM = 2.8 \pm 0.14 \text{ GHz}$. (c) Demonstration of the effect of the broadening due to the finite scan length. The Conv data points are obtained by convolving a Lorentzian associated with the intrinsic loss with a Sinc function associated with the finite time duration. Fitting the convolved signal gives $FWHM = 2.89 \text{ GHz}$. (d) DFT spectra and fit to a Lorentzian after using a Hamming window to the data in (a), showing a smaller but non-negligible broadening.

CHAPTER 5: ALL-OPTICAL MEASUREMENT OF INTERLAYER EXCHANGE COUPLING IN Fe/Pt/FePt THIN FILMS

“Simple it may be, but not ineffectual; rude, but not crude.”

- John Kerr

5.1 Introduction

In this chapter we will apply a few of the concepts introduced in chapters 3 and 4 to the characterization and manipulation of Fe/Pt(x)/FePt multilayer films (Fig. 5.1). The results have been published in ref [87]. The experimental procedure for extracting magnetic parameters will be demonstrated for the measurement of the interlayer exchange coupling in the Fe/Pt(x)/FePt multilayers. However, this general procedure can be applied to measure other magnetic parameters as well.

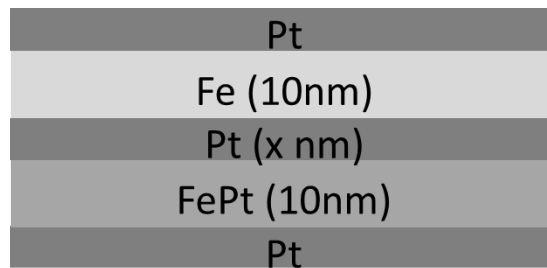


Figure 5.1: Schematic of the multilayer structure studied in this chapter.

5.2 Film Properties

The films were deposited by DC magnetron sputtering from Fe and Pt targets at an argon pressure of 3.5 μ bar, while the substrates were at room temperature. Co-deposition was applied to create the Fe₅₂Pt₄₈ alloy. The substrates are thermally oxidized, (100)-cut, p-doped silicon wafers with an oxide thickness of 100 nm. These films are polycrystalline with the chemically disordered A1 phase of FePt. The A1 phase is an fcc crystal structure with a random distribution of the Fe and Pt atoms. [88] The L10 phase is another formation of FePt that is extensively studied due to its extremely high magnetocrystalline anisotropy. It is characterized by the successive layering of Fe and Pt atoms in the fcc crystalline structure. [89] (Fig. 5.2)

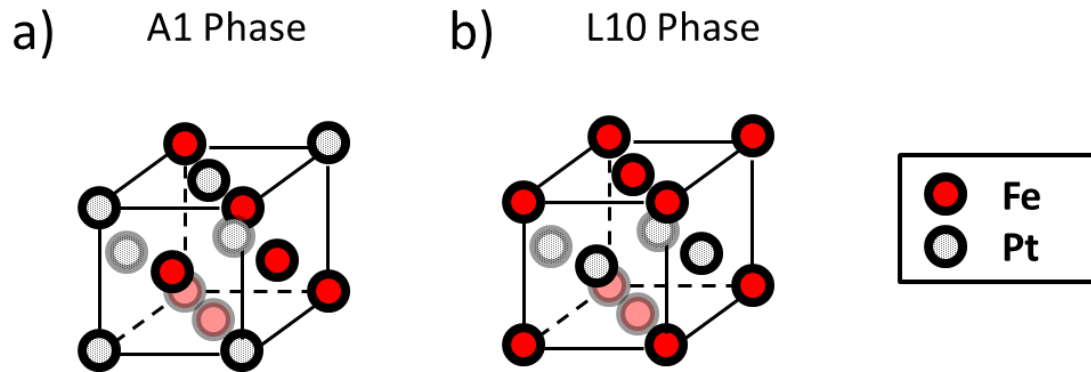


Figure 5.2: (a) The Fe and Pt atoms are randomly distributed in the A1 phase. (b) The L10 phase is characterized by a very high magnetocrystalline anisotropy. The Fe and Pt atoms occupy successive planes in the crystal.

5.3 Acoustic and Optic Modes

Magnetic multilayers are critical in magnetic storage technology. The giant magnetoresistance (GMR) effect, where the resistance of a magnetic multilayer depends on the relative orientations of the layers, has transformed the industry [90]. GMR is used in devices such as sensors, read heads and MRAM. [91] Additionally, multilayers in the form of exchange-coupled composite and exchange spring composite media have improved ultrahigh-density magnetic recording media by enabling the scaling down of magnetic grain size while also overcoming the superparamagnetic limit.[92] Critical to the design of these devices is knowledge of the interlayer exchange coupling constant J_1 . As the coupling of the layers (J_1) increases, the dynamics of the film sample changes, giving rise to coupled modes which exist in both layers, an in-phase acoustic mode and an out of phase optic mode with frequencies and intensities that depend on the strength of J_1 . (Fig. 5.3)

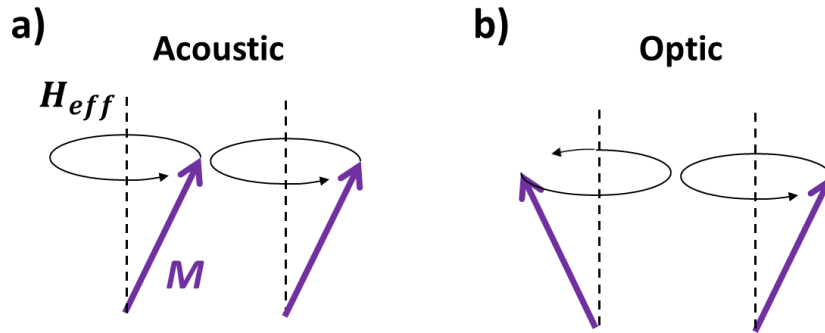


Figure 5.3: The exchange coupled modes consist of (a) an Acoustic Mode in which the two coupled magnetization vectors oscillate in-phase with one another, and (b) an

Optic mode in which the magnetization vectors oscillate out-of-phase with one another. The sign of J_1 dictates which mode has the lower energy.

The sign of J_1 determines whether the coupling is parallel (ferromagnetic) or anti-parallel (anti-ferromagnetic). Additionally, it dictates the relative energies of the modes. For $J_1 > 0$ (ferromagnetic) the lower energy state is the one which aligns the spins parallel to one another. In the acoustic mode all the spins precess in phase and are not canted with respect to each other—satisfying the energy minimum criteria. For the Optic mode, the spins precess out of phase and are therefore slightly canted relative to one another. This canting causes the optic mode to have a higher energy, which corresponds to a higher resonance frequency than the acoustic mode. [93] Applying the opposite argument for when $J_1 < 0$ (anti-ferromagnetic) explains why the optic mode has a lower energy (lower frequency) than the acoustic mode. In field swept Ferromagnetic Resonance (FMR, constant frequency), ferromagnetic coupling can be inferred from a spectrum where the optic mode resonance is at a lower field than the acoustic mode. In a TR-MOKE experiment the field is fixed and so a higher frequency optic mode is indicative of ferromagnetic coupling.

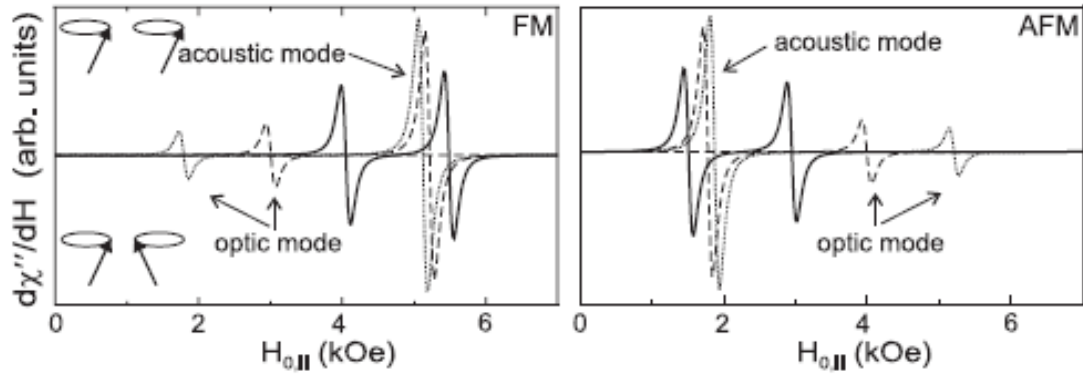


Figure 5.4: FMR spectra demonstrating the resonance fields of Ferromagnetic and Anti-ferromagnetically coupled films. The solid line is the uncoupled case. The dashed and the dotted lines are the coupled cases, with the dotted line corresponding to a coupling twice that of the dashed line. Care should be taken when comparing results from TR-MOKE and FMR experiments. In FMR with a fixed frequency, the external field is varied through resonance so that the position of the higher energy mode occurs at a lower applied field. In TR-MOKE the field is held fixed and the frequencies measured simultaneously so that the higher energy mode has a higher frequency at that applied field. Taken from [93].

5.4 Single Film Resonance –Kittel Formula

In order to measure the exchange coupling in the multilayers we must first study the properties of the individual layers. For a single film, the Gibbs Free energy is given by

$$G = -\mu_0 \mathbf{H} \cdot \mathbf{m} + B_d m_z^2 \quad (5.1)$$

Where m_z is the z -component of the magnetization and $B_d = 2\pi M_S$ is the demagnetization energy of a thin film. In the $\{\mathbf{1}, \mathbf{2}, \mathbf{3}\}$ coordinate system introduced in chapter 3, this becomes

$$G = -\mu_0(H_1 m_1 + H_2 m_2 + H_3 m_3) + B_d(-\sin \theta_M m_1 + \cos \theta_M m_3)^2 \quad (5.2)$$

Where θ_M is the angle of the magnetization with respect to the z -axis. Referring back to equation (3.60) we get the following for the partial derivatives of the free energy

$$G_{11} = \frac{\partial^2 G}{\partial m_1^2} = 2B_d(\sin^2 \theta_M) = 4\pi M_S(\sin^2 \theta_M) \quad (5.3)$$

$$G_{21} = G_{12} = \frac{\partial}{\partial m_1} \frac{\partial G}{\partial m_2} = \frac{\partial}{\partial m_1} \mu_0(H_2) = 0 \quad (5.4)$$

$$G_{22} = \frac{\partial}{\partial m_2} \frac{\partial G}{\partial m_2} = \frac{\partial}{\partial m_2} \mu_0(H_2) = 0 \quad (5.5)$$

$$G_3 = -\mu_0 H_3 + 4\pi M_S \cos^2 \theta_M \quad (5.6)$$

So that the equation for the resonance frequency (Eq. 3.60) becomes

$$\frac{\omega^2}{\gamma^2} = \sqrt{(\mu_0 H_3 - 4\pi M_S \cos^2 \theta_M)(\mu_0 H_3 - 4\pi M_S \cos 2\theta_M)} \quad (5.7)$$

Where $H_3 = H_a \cos(\theta_M - \theta_H)$ and θ_H is the angle of the applied field with respect to the z -axis. This is the well known *Kittel Formula* for a thin magnetic film. [94] The term $4\pi M_S$ comes from the demagnetization energy and has units Oe . It is responsible for aligning the magnetization in the plane. There are cases where the magnetocrystalline anisotropy may prefer to orient the magnetization out of the plane

while the demagnetization field may try and align it in the plane. When there are competing anisotropies they may be combined into one effective term, M_{eff} whose sign elucidates the overall tendency of the anisotropies. $M_{eff} > 0$ indicates a stable direction for the magnetization oriented normal to the film plane and $M_{eff} < 0$ orienting the magnetization in the film plane. The samples studied here are polycrystalline, so that the only contribution to M_{eff} is from the demagnetization field and we can write $M_{eff} = -4\pi M_S$. Equation (5.7) then becomes

$$\omega^2 = \gamma \sqrt{(\mu_0 H_3 + M_{eff} \cos^2 \theta_M)(\mu_0 H_3 + M_{eff} \cos 2\theta_M)} \quad (5.8)$$

In order to find θ_M equation (5.2) can be minimized with respect to θ_M

$$\begin{aligned} \frac{\partial G}{\partial \theta_M} &= \frac{\partial}{\partial \theta_M} (-\mu_0 H_a M_S \cos(\theta_M - \theta_H) + 2\pi M_S \cos^2 \theta_M) = 0 \\ \Rightarrow H M_S \sin(\theta_M - \theta_H) + 2\pi M_S \sin(2\theta_M) &= 0 \end{aligned} \quad (5.9)$$

Which can be solved self-consistently with equation (5.8) in order to calculate the resonance frequency, ω .

5.4.1 Single Film TR-MOKE Measurements

Using the TR-MOKE setup discussed in chapter 4 we measured the frequencies of the magnetic systems at various applied fields and angles. Then the magnetic parameters γ and M_{eff} were numerically fit to the precession frequencies at all applied field strengths and angles simultaneously by self-consistently solving for the equilibrium

magnetization positions, θ_M (Eq. 5.9) and the single film Kittel formula. (Eq. 5.8) [94]

H_a and θ_H were known from the experimental geometry and so were held fixed. Fitting three sets of angles as opposed to one or two lowered the sum of squared error by roughly 20% for the Fe fits and 40% for the FePt fits. Additionally, multiple angles ensures that the sign of M_{eff} is accurate, since fitting only one angle can have degenerate solutions for in-plane and out-of-plane anisotropies.

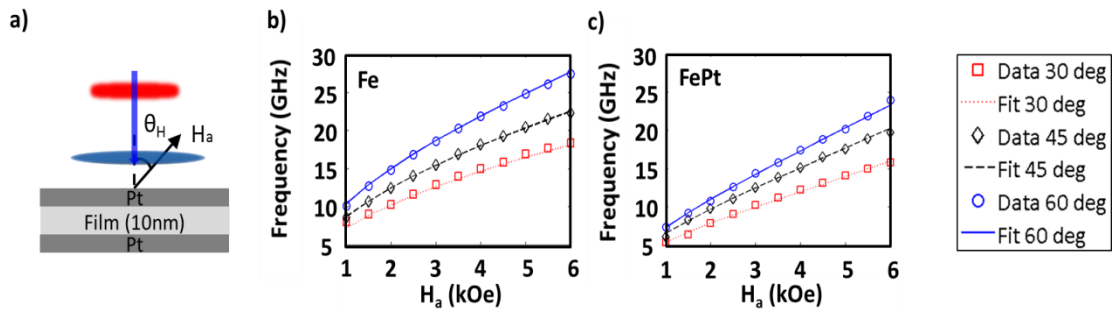


Figure 5.5: **a)** Experimental geometry for single film measurements (Fe or FePt) **b)** Fits of equation (5.8) (lines) to experimental data (symbols) at three angles over a range of applied fields for **(b)** single Fe film and **(c)** single FePt film. Taken from [87].

Fitted values for Fe were $\gamma = 1.89e7 \text{ rad Oe}^{-1} \text{ s}^{-1}$ and $M_{eff} = -19.07 \text{ kOe}$. The FePt values were $\gamma = 1.91e7 \text{ rad Oe}^{-1} \text{ s}^{-1}$ and $M_{eff} = -7.95 \text{ kOe}$. The absence

of any in-plane anisotropy was verified by taking resonance measurements at multiple in-plane angles and observing no changes in the frequencies. Therefore, the demagnetization field is the only anisotropy term and, $M_S = 1526 \text{ emu cm}^{-3}$ for Fe and $M_S = 633 \text{ emu cm}^{-3}$ for FePt. The fits to the single film data are shown in figure 5.5 and show excellent agreement with the data. The single film γ and M_S values were then used as constants in the fitting algorithm of the Fe/Pt(x nm)/FePt film samples.

5.5 Multilayer Film Resonance

When two ferromagnetic films are separated by a non-magnetic spacer, the interlayer exchange couples the two films so that the total free energy of the multilayer system is a combination of the individual energies of the multilayer films in addition to a term which exchange couples the layers. [95] It is given by:

$$G = \sum_{i=1}^2 -d_i \mathbf{H} \cdot \mathbf{m}_i + d_i B_{d,i} m_{z,i}^2 - J_1 \mathbf{m}_1 \cdot \mathbf{m}_2 \quad (5.10)$$

Where d_i is the thickness of film i , $M_{eff,i} = -4\pi M_{S,i}$, \mathbf{m}_i is the normalized magnetization vector of film i and \mathbf{H} is the applied field vector. The first term is the Zeeman energy, the second the demagnetization energy and the last the exchange energy due to the coupling between the films.

Following the procedure outlined in chapter 3 for solving the Landau-Lifshitz (LL) equation of motion for the time dependent components of the magnetization, leads to the following characteristic equation:

$$-\frac{\omega^4}{\gamma_1\gamma_2} + a\omega^2 + b = 0 \quad (5.11)$$

with

$$a = -\frac{H_1^{(2)}H_3^{(2)}}{\gamma_1^2} - \frac{H_4^{(1)}H_2^{(2)}}{\gamma_1\gamma_2} + \frac{H_1^{(1)}H_3^{(1)}}{\gamma_2^2} - \frac{H_2^{(1)}H_4^{(2)}}{\gamma_1\gamma_2} \quad (5.12)$$

$$b = H_1^{(1)}H_1^{(2)}H_3^{(2)}H_3^{(1)} - H_1^{(1)}H_4^{(1)}H_1^{(2)}H_4^{(2)} - H_2^{(1)}H_3^{(1)}H_2^{(2)}H_3^{(2)} + H_2^{(1)}H_4^{(1)}H_2^{(2)}H_4^{(2)} \quad (5.13)$$

Where γ_i is the gyromagnetic ratio of film i , and the $H_j^{(i)}$ values are given by:

$$H_1^{(i)} = -M_{eff,i} \cos(2\theta_{M,i}) - \frac{J_1}{M_{S,i}d_i} \cos(\theta_{M,i} - \theta_{M,j}) - H \cos(\theta_{M,i} - \theta_H) \quad (5.14)$$

$$H_2^{(i)} = \frac{J_1}{M_{S,i}d_i} \cos(\theta_{M,i} - \theta_{M,j}) \quad (5.15)$$

$$H_3^{(i)} = M_{eff,i} \cos^2(\theta_{M,i}) - \frac{J_1}{M_{S,i}d_i} \cos(\theta_{M,i} - \theta_{M,j}) - H \cos(\theta_{M,i} - \theta_H) \quad (5.16)$$

$$H_4^{(i)} = \frac{J_1}{M_{S,i}d_i} \quad (5.17)$$

Where $\theta_{i,j}$ is the angle of the magnetization of film i,j , and θ_H is the angle of the applied field, both with respect to the surface normal. The real and positive solutions of eqn. (5.11) are the acoustic (in-phase) and optic modes (out-of-phase).[93,96]

5.5.1 Multilayer TR-MOKE Measurements

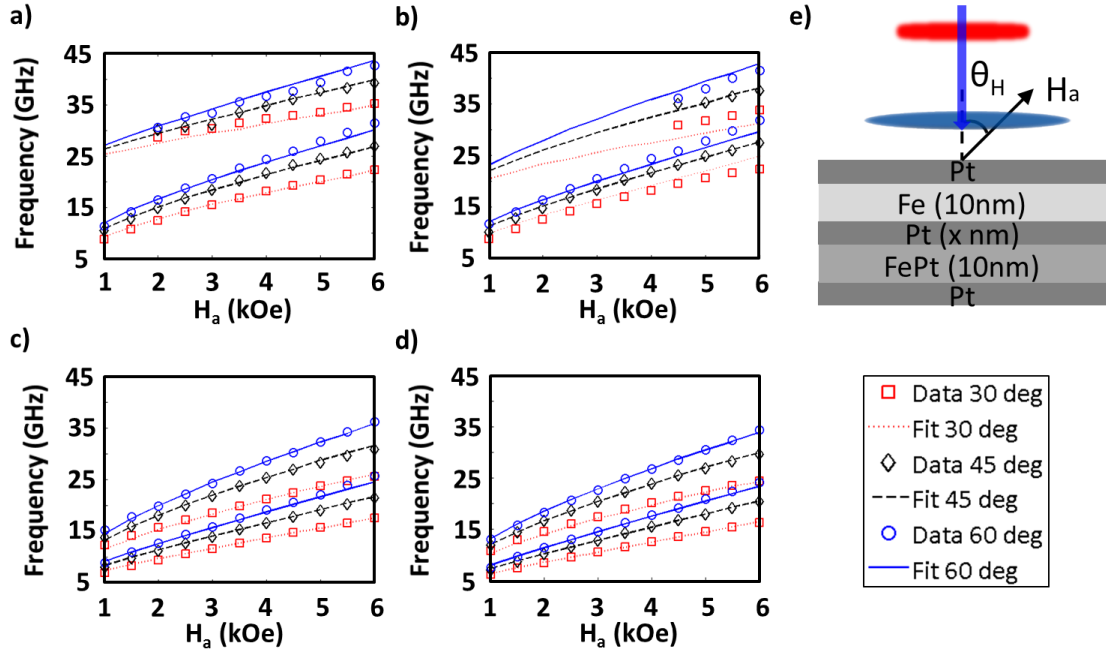


Figure 5.6: Fits of equation (5.11) (lines) to experimental data (symbols) at three angles over a range of applied fields for (a) Fe / Pt(x = 0 nm) / FePt (b) Fe / Pt (x = 0.5 nm) / FePt (c) Fe / Pt (x = 1.0 nm) / FePt and (d) Fe / Pt (x = 1.5 nm) / FePt (e) Experimental geometry of multilayer measurements. Taken from [87].

TR-MOKE scans at multiple applied fields and angles were performed on the multilayers as well. This yielded two frequencies for each scan (acoustic and optic). These frequencies were then fit by self-consistently solving for both magnetization orientations and using equations (5.11 – 5.17) to fit the frequencies, with J_1 and

$M_{eff,i}$ as fitting parameters. The fits of the Fe / Pt (x nm) / FePt films are displayed in figure 5.6.

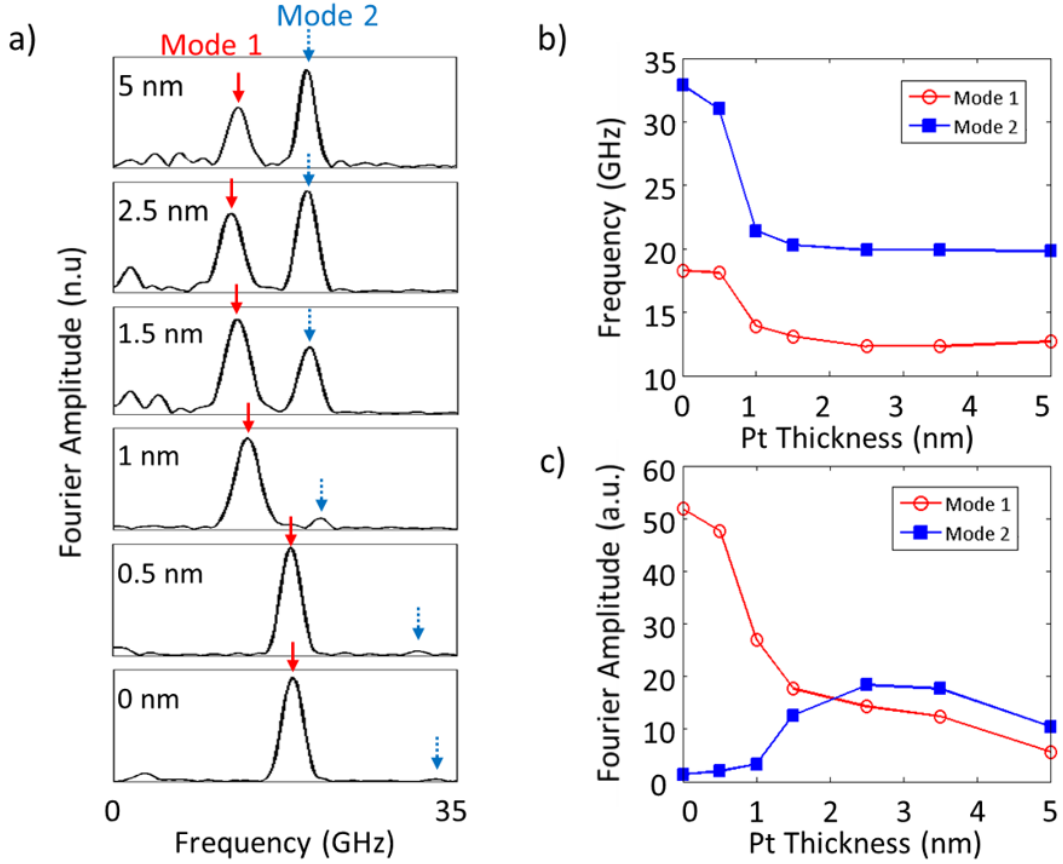


Figure 5.7: (a) Fourier transforms of TR-MOKE time traces for the trilayers with different Pt spacer layer thickness at $\theta_H = 30^\circ$ and $H_a = 4$ kOe. The solid red arrow is a guide to mode 1 and the dashed blue arrow a guide to mode 2. (b) Mode frequencies vs. Pt thickness for $H_a = 4$ kOe. (c) Fourier amplitudes of the modes at different Pt thickness. Taken from [87].

Figure 5.7a) shows the TR-MOKE Fourier spectra of the multilayer films taken at $\theta_H = 30^\circ$ at $H_a = 4 \text{ kOe}$ for the different Pt spacer thicknesses. There is an obvious qualitative difference between the spectra. For $x > 1.5 \text{ nm}$, there are two clearly resolvable modes which maintain their positions and relative amplitudes. In this regime ($x > 1.5 \text{ nm}$) these modes are attributed to the Kittel modes of the individual layers—indicating that the two films are decoupled. When $x \leq 1.5 \text{ nm}$, the dynamics begin to change. The system enters the exchange coupled regime and the two layers begin to be coupled through the bilinear exchange constant J_1 . [97] In the exchange coupled regime, the in-phase acoustic mode (mode 1) and the out-of-phase optic mode (mode 2) exist throughout the whole structure. As the Pt thickness decreases further, the acoustic mode frequency approaches an asymptotic limit and the optic mode frequency continues to increase (figure 5.7a) and 5.7b)). $x = 1.5 \text{ nm}$ can be identified as the threshold between the two regimes due to the change in the relative amplitudes of the two modes (figure 5.7c). As the coupling increases (Pt thickness decreases) energy from the optic mode is funneled into the acoustic mode.[93] This is visualized in figure 5.7c) which shows the Fourier amplitudes of the two modes as a function of Pt thickness. In the exchange coupled regime ($x \leq 1.5 \text{ nm}$), the low intensity optic mode exists at a higher frequency indicating ferromagnetic coupling ($J_1 > 0$) at all Pt thicknesses measured.

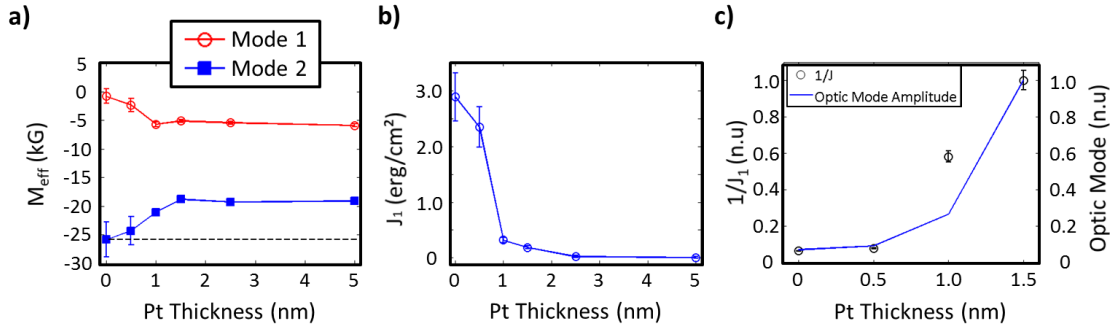


Figure 5.8: (a) Effective magnetization of the two layers. The dotted line is the strongly coupled M_{eff}^* where the two films can be treated as having a single effective magnetization. (b) Extracted interlayer exchange constant vs. Pt thickness. (c) Optic mode amplitude and $1/J_1$ normalized to Pt = 1.5 nm values vs. Pt thickness. Taken from [87].

Using the methodology described previously, J_1 and $M_{eff,i}$ were fit for all the film samples. Figure 5.8 shows the evolution of these parameters as a function of Pt thickness. For $x \geq 1.5$ nm the effective magnetizations of the two layers are the same as the single film values. At the threshold of exchange coupling ($x = 1.5$ nm) the effective magnetizations begin to evolve. As the layers are brought closer together $M_{eff,1}$ (FePt single film) approaches zero and $M_{eff,2}$ (Fe single film) approaches the strongly coupled M_{eff}^* (dashed line). At this point most of the dynamics arise within the in-phase acoustic mode and the system is better represented as a single film with a modified effective magnetization and gyromagnetic ratio given by:

$$M_{eff}^* = \frac{d_1 M_1 M_{eff,1} + d_2 M_2 M_{eff,2}}{d_1 M_1 + d_2 M_2} \quad (5.18)$$

$$\gamma^* = \frac{d_1 M_1 + d_2 M_2}{d_1 M_1 / \gamma_1 + d_2 M_2 / \gamma_2} \quad (5.19)$$

Figure 5.8b) is the extracted bilinear exchange constant (J_1) at the different Pt thicknesses. Once again, effects from the ferromagnetic coupling start emerging at $x = 1.5$ nm. Between $x = 1$ nm and $x = 0.5$ nm there is a drastic increase in the magnitude of J_1 . When the system is fully coupled ($x = 0$ nm) the exchange constant reaches a maximum of 2.89 erg/cm^2 . The thickness at which the coupling begins as well as the J_1 values derived are consistent with those measured in similar systems.[97,97] The positive values of J_1 at all Pt thicknesses indicate no antiferromagnetic coupling which can be attributed to the electronic structure of Pt. [98] A confirmation of the exchange coupling can be seen in the intensity of the optic mode which follows a dependence given by

$$I_{OP} \propto \frac{|M_{eff,1} - M_{eff,2}|}{J_1} \quad (5.20)$$

The optic mode intensity decreases as the coupling strength (J_1) increases and is zero with identical films. [93,99] This is shown in figure 5.8c) by normalizing both the optic mode's Fourier amplitude and $1/J_1$ value to the $x = 1.5$ nm values where the coupling begins. Additionally, consideration must be given to the temperature increase of the material due to the absorption of the laser pulse. Using a two-temperature model the estimated temperature increase in the samples measured in this

study is around 20 K.[100] The effect that this increase has on J_1 is less than the error associated with the fits and can therefore be neglected.[101,102]

5.6 OOMMF Simulations

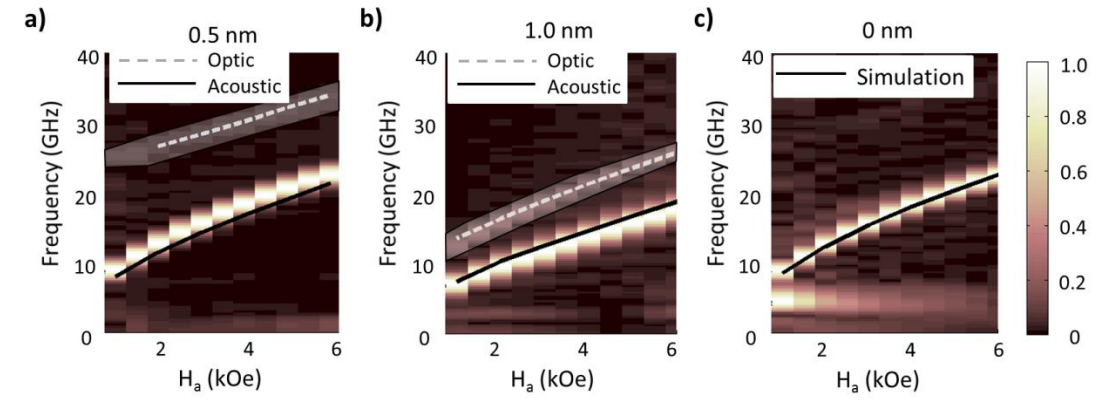


Figure 5.9: Simulation (lines) on top of experimental Fourier maps normalized at each H_a . The small Fourier amplitude of the optic mode is difficult to see in the Fourier map so it has been highlighted in the (a) Fe / Pt(0.5 nm) / FePt film and the (b) Fe / Pt(1.0 nm) / FePt film. (c) The experimental Fourier map of the strongly coupled Fe/FePt film with simulation (line) using the modified magnetic parameters M_{eff}^* and γ^* . Taken from [87].

In order to further confirm the extracted parameters, micromagnetic simulations were performed using the OOMMF (Object Oriented MicroMagnetic Framework) software package. Figure 5.9 shows the micromagnetic simulations for three of the exchange coupled samples. The colormaps show the experimental data from the TR-MOKE scans normalized at each magnetic field value. The solid black and dotted gray lines

are the simulated acoustic and optic frequencies respectively. A $20 \times 20 \text{ nm}^2$ lateral area is simulated with film thicknesses of 10nm for each layer. Periodic boundary conditions are applied along the x and y edges so as to mimic an infinite thin film. Cell sizes of 2.5 nm are used in the x , y and z directions. The input parameters for the Pt = 0.5 nm and 1 nm trilayers (Fig. 5.9a and 5.9b) were the single film M_s and γ values and J_1 from the fits of the trilayers' mode spectra. The simulations display excellent agreement with the optic mode, validating the J_1 parameter that was extracted. The positions of the simulated acoustic modes are slightly off with an average discrepancy of less than 1 GHz. The duration of the TR-MOKE time scans are 1ns which corresponds to a frequency resolution of 1 GHz. Therefore, the simulations are within acceptable experimental error. However, this discrepancy can be explained by the modified anisotropy of the coupled layers which is not taken into account in the simulations. Figure 5.9c) shows a simulation of the strongly coupled layer stack with no spacer (Pt = 0 nm). In this case, a single, homogeneous film was simulated using the modified M_{eff}^* and γ^* (Eqns. 5.18 and 5.19). The simulation and the experimental results match extremely well, corroborating the conclusion that the two films are strongly coupled with a modified gyromagnetic ratio and effective magnetization. This represents further validation of the effective magnetization trends that were seen in the exchange coupled fits of figure 5.8.

5.7 Conclusion

In this chapter we applied the concepts introduced in the previous chapters in order to measure the dynamics of Fe/Pt(x)/FePt multilayers. The ferromagnetic exchange coupling varied as a function of x. By fitting the precession frequencies at multiple magnetic field strengths and angles, the accuracy of the fitting algorithm was improved. As the Pt thickness was decreased below 1.5 nm, the effective magnetizations of the multilayer system changed. $M_{eff,1}$ approached zero and $M_{eff,2}$ approached that of a strongly coupled system, which is phenomenologically described as being a single film with a modified effective magnetization and gyromagnetic ratio. Additionally, the bilinear exchange constant was found to reach a maximum value of 2.89 erg/cm². These findings were backed through micromagnetic calculations.

CHAPTER 6: MULTI-PULSE METHOD FOR SELECTIVE CONTROL OF MAGNETIZATION PRECESSIONS IN MAGNETIC MULTILAYERS

“There is no perfectly shaped part of the motorcycle and never will be, but when you come as close as these instruments take you, remarkable things happen, and you go flying across the countryside under a power that would be called magic if it were not so completely rational in every way.”

-Robert M. Pirsig (Zen and the Art of Motorcycle Maintenance)

6.1 Introduction

In this chapter, we demonstrate a new method to manipulate the magnetic multilayer structures which were characterized in the previous chapter. By introducing another pump pulse so we have a double-pump configuration, and by tuning the delay between the two pump pulses we can selectively suppress a given spin wave within a multimodal magnetic structure while maintaining the precession of the other. This effect has been demonstrated using acoustic pulses, [103] and in garnets, [104] but we show that the same control can be initiated by pure optical excitation in a structure consisting of technologically relevant metallic magnetic materials. The desire for techniques which can manipulate the magnetization without an external magnetic

field is motivated by the data storage and communication industries.[105] Some advantages of all-optical control are that it is extremely fast, and non-destructive to the magnetic material. From a materials science perspective, magnetic multilayers have been extensively studied to explore fundamental questions on topics such as interfacial magnetism [106] and spin transport phenomena.[107,108] Tailoring magnetic multilayers gives rise to novel physical characteristics which have been exploited for technological benefits, [109,110,111] With all of this in mind, direct access to a specific layer in a multilayer structure by optical means is highly desirable.

6.2 Double-Pump Configuration

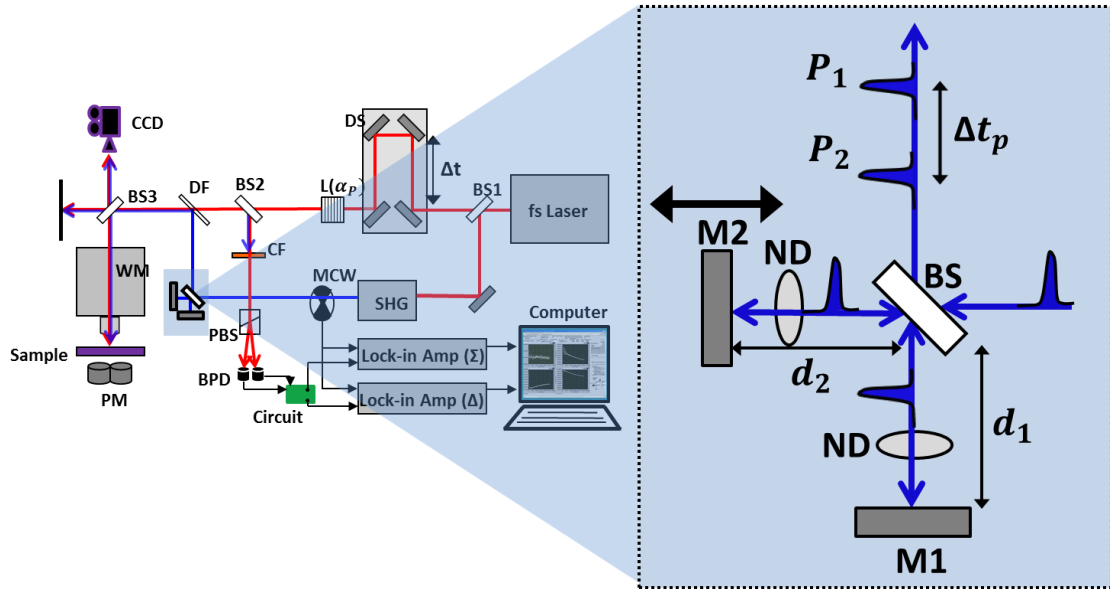


Figure 6.1: Schematic of the double pump experimental setup discussed in the text.

Beam Splitter (BS); Neutral Density Filter (ND); Mirror 1 (M1); Mirror 2 (M2);

Distance between BS and M1 (d_1); Distance between BS and M2 (d_2); Pump 1 power (P_1); Pump 2 power (P_2); Time delay between pump pulses (Δt_p).

For the double-pump approach, a beam splitter (BS) is introduced into the blue pump path which splits the 400nm pump pulse into two paths. (Fig. 6.1) The two paths have neutral density filters (ND) so as to independently control the power of the two pump pulses (P1 and P2). After being reflected off mirrors (M1 and M2) their paths are recombined at the beam splitter. The position of M1 is held fixed so d_1 does not change. M2 is placed on a micrometer to change d_2 which controls the separation in time of the two pulses, Δt_p . The separation of the two pulses $\Delta t_p = c/2\Delta d$ where $\Delta d = d_2 - d_1$ and the 2 comes from the fact that the light will have to travel distance $2d_i$ before being recombined at the beamsplitter. Δt_p is therefore adjusted by changing d_2 .

Various magnetic materials were used in order to demonstrate the breadth of this technique. A 30nm thick Ni film was prepared by electron beam deposition at room temperature on a Si(100) substrate. Additionally, a 10nm Fe film and a multilayer structure of Fe (10nm) / Pt (5nm) / FePt (10nm) were deposited by DC magnetron sputtering from Fe and Pt targets using an argon pressure of 3.5 μ bar while the substrates were at room temperature. Co-deposition was applied to create the chemically disordered A1 FePt alloy. The substrates are thermally oxidized, (100)-

cut, p-doped silicon wafers with an oxide thickness of 100nm. All magnetic thin layers exhibit an easy axis magnetization in the film plane.

6.3 Demonstration on Single Layer

We first demonstrate the technique on a 30nm thick Ni film. The dynamic control of the magnetization vector can be understood by looking down the cone of precession and visualizing the rotation of the magnetization as a phasor given by $M(t) = e^{i\theta}$ where $\theta = \omega t$ and $\omega = 2\pi f$ (Fig. 6.2a). At $t = 0$ the pump pulse hits the sample and acts as an effective anisotropy pulse which perturbs the magnetic system, knocking the magnetization vector out of equilibrium. [112,113] The displacement of the magnetization vector is proportional to the fluence of the laser pulse, and in the phasor diagram corresponds to $M(0) = 1$. When $t > 0$, the magnetization evolves as a damped oscillation at a frequency given by the Kittel formula. [114] The damping of the precession is a function of various material and structural properties and is an important parameter in the characterization of magnetic materials. [115,116] While the magnetization is precessing, its location can be mapped to the unit circle by translating by θ (Fig. 6.2a). Our core idea is that by tuning the timing of the arrival of the second pump pulse after the first pulse, the magnetization can be either quenched or enhanced. The position of M for these situations is given by

$$e^{i\theta} = \begin{cases} -1, & \theta = (2m - 1)\pi, \\ 1, & \theta = 2m\pi, \end{cases} \begin{matrix} \text{quenched} \\ \text{enhanced} \end{matrix} \quad m \in \mathbb{N} \quad (6.1)$$

Each successive value of m corresponds to a different time $t^{(m)}$ which is visualized by looking at the real part of $M(t)$ (Fig. 6.2b). The magnetization precession of the Ni film initiated by a single pump pulse is shown in figure 6.2(c) which shows a damped sinusoid and a single peak in Fourier space corresponding to the Kittel mode. Figure 6.2(d) shows the effect of quenching on the precession and figure 6.2(e) shows the effect of enhancement.

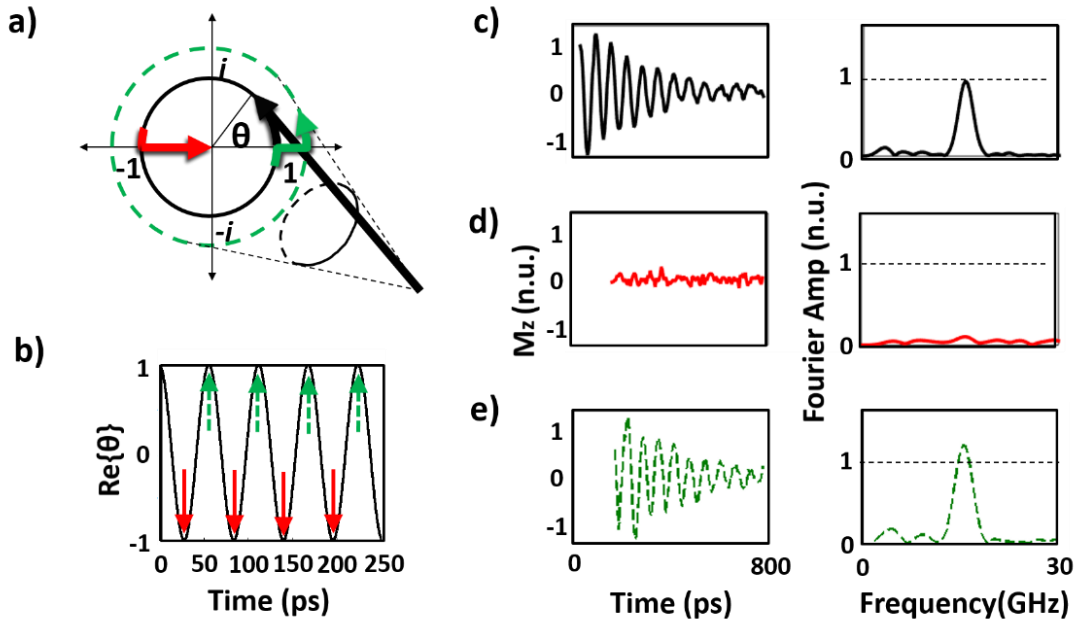


Figure 6.2: (a) Representation of the magnetization vector as a phasor in the complex plane. The black arrow is the precession of the magnetization due to the initial pulse. If the second pulse is timed such that the position of the magnetization vector is $e^{i\theta} = -1$ or π out of phase with respect to $t = 0$, the precession can be quenched (solid red). If the second pulse arrives when the magnetization vector is $e^{i\theta} = 1$ or back in phase with respect to the 1st pulse, the precession can be enhanced (dotted

green). **(b)** The real part of the phasor can be used to visualize the time dependence of the control. Each arrow indicates a different time $t^{(m)}$ discretized by successive values of m . **(c)** TR-MOKE time and frequency domain signals of the dynamics from a single pulse on a Ni thin film (30nm). **(d)** By tuning the arrival time of the 2nd pulse, the magnetic precession can be quenched or **(e)** enhanced. Taken From [117].

Due to the damping, quenching of the magnetization requires an appropriate balance of the power ratio between the two pump pulses. In figure 6.3(a), time traces of the magnetization dynamics and illustrations of the corresponding phasor diagrams in a 10nm Fe film show the effect of different power ratios (P_2/P_1). For larger ratios, the magnetization precession is not suppressed—it is knocked past equilibrium and precesses in a smaller cone. Only at the correct ratio is the precession quenched. If the ratio were decreased further, M would not be knocked far enough towards the equilibrium position and would continue to precess around a smaller cone. The level of suppression of the precession for the different pump ratios is displayed clearly in the Fast Fourier Transform (FFT) of the signals, which shows a range of control, from partial suppression to full quenching (Fig. 6.3b). With each successive m , the power ratio required for quenching will change since at each $t^{(m)}$ the magnetization has damped out closer to equilibrium (Fig. 6.3c). Since the pulse energy is proportional to the displacement of M , for larger m , smaller pulse energies are necessary to bring M back to equilibrium—lowering the power ratio.

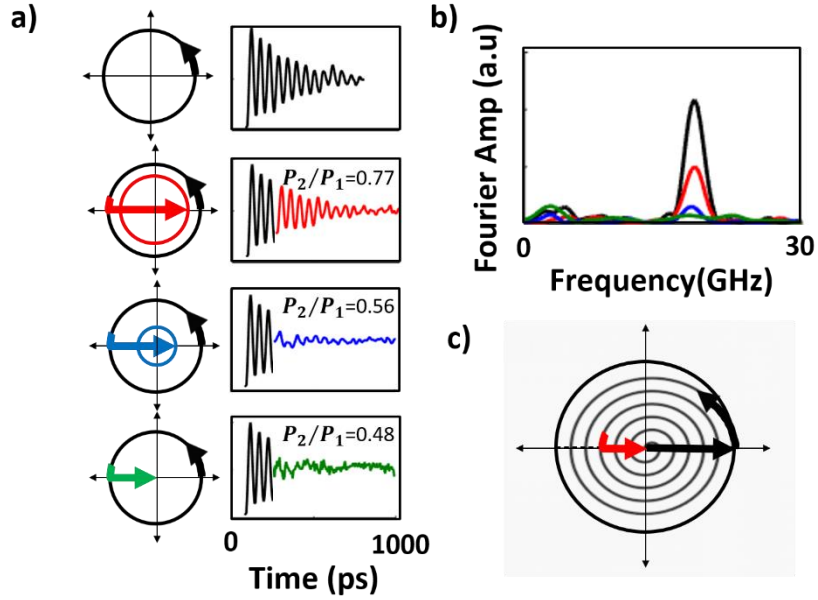


Figure 6.3: (a) Phasor and time domain signals of a 10nm Fe film for different pump power ratios (P_2/P_1). (b) Fast Fourier Transform (FFT) of the time domain signals corresponding to the different ratios. (c) The reason the ratio is less than unity is that as the magnetization precesses it spirals closer and closer to the equilibrium position in the center of the circle. The quenching is shown for the case where $m = 3$. Taken From [117].

6.4 Demonstration on Multilayer Structure

The same line of reasoning can be extended to selectively control the magnetization dynamics in a system consisting of multiple resonances such as a magnetic multilayer structure. Technologically relevant spintronic devices such as magnetic random access memory (MRAM) have multiple layers consisting of different materials. [118]

The new double-pump technique opens an opportunity to excite and analyze them individually. As a demonstration of this control, we use two resonances and assume we would like to observe a single resonance in the structure. This means we will quench one resonance while maintaining the precession of the other. Figure 6.4(a) shows a schematic of the multilayer magnetic films used in this demonstration. The structure of Fe (10nm) / Pt (5nm) / FePt (10nm) displays two distinct frequencies due to the different saturation magnetizations, M_s , of the Fe and the FePt layers. The 5nm of Pt ensures that the exchange coupling between the two layers is suppressed.[119] There are now two parameters to consider, θ_1 and θ_2 .

At an external field of 6kOe applied at 30° with respect to the surface normal the frequencies of the two magnetic layers are $f_1 = 16$ GHz (FePt) and $f_2 = 25$ GHz (Fe), where the subscript denotes the layer index. If we are trying to suppress the FePt resonance (R1) which precesses with an angular frequency ω_1 , then the second pulse must arrive at times $t_1^{(m)} = \frac{(2m-1)\pi}{\omega_1}$. If we chose the correct power ratio, then for any time $t_1^{(m)}$, R1 will be quenched. However, we also need to consider the effect of the second pulse on the Fe resonance (R2). Its magnetization vector's map onto the unit circle will be given by the discrete locations $\theta_2^{(m)} = \omega_2 t_1^{(m)}$. In figure 6.4(b) the location of the magnetization vector of R2 in the unit circle at times $t_1^{(m)}$ is shown for $m = 1 - 16$. A safe way to assume that R2 is maintained is to require that $\text{Re}\{e^{i\theta_2^{(m)}}\} > 0$. This ensures the magnetization is mapped onto the right half of the unit circle. The m values that satisfy this criterion are shown in the shaded portion of

figure 6.4(b). The first m that satisfies this criterion is $m = 2$. Depending on the damping and how close R2 is to the +1 position on the unit circle, R2 may even be enhanced. The real component of the phasors for the two frequencies is shown in figure 6.4(c) with the solid red arrow indicating the time $t_1^{(2)} = 83ps$ corresponding to $m = 2$ (the second time the R1 vector is at a quenching location). In figure 6.4(d) the frequency spectrum for a single pulse is shown. There are two clear modes corresponding to the two resonances of the FePt (R1) and the Fe (R2) systems.

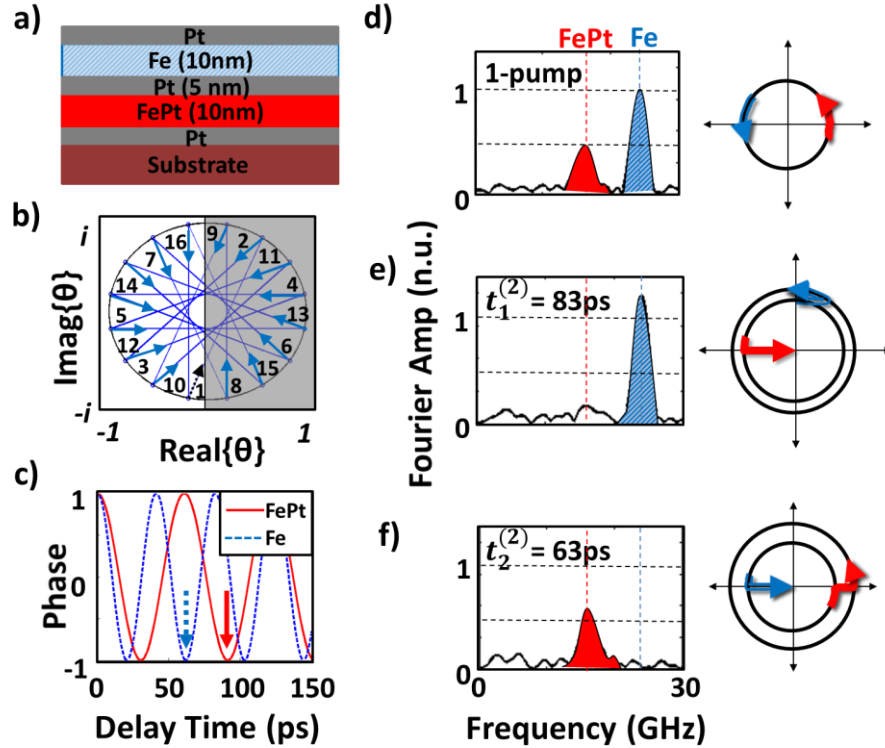


Figure 6.4: (a) Schematic of the magnetic multilayer structure. (b) Attempting to quench the FePt resonance (R1) gives discrete values of the location of the Fe resonance (R2) in time $t_1^{(m)}$ which can be mapped onto the complex plane. The

arrows show a symmetric path of the position of R2 for successive m traced out in the complex plane starting with the black dashed arrow at $m = 1$. **(c)** Real component of the phasors for the Fe(10nm) / Pt(5nm) / FePt(10nm) multilayer. **(d)** Fourier transform and phasor diagram of the stack subjected to only one pulse displaying two resonances corresponding to the different magnetic layers. **(e)** Fourier transform and phasor diagram demonstrating the quenching of the FePt layer and **(f)** the Fe layer. Taken From [117].

Figure 6.4(e) shows the case discussed above where the second pulse arrives at $t_1^{(2)} = 83ps$, quenching the FePt resonance. The frequency spectrum clearly indicates that only the Fe system is precessing whereas the FePt resonance has been completely turned off. The same procedure can be applied to shut off the Fe resonance while maintaining the FePt system. In this case, $t_2^{(2)} = 63ps$ which is shown by the dotted blue arrow in figure 6.4(c). The frequency spectrum where Fe has been quenched is shown in figure 6.4(f). This procedure allows for the selective excitation of particular magnetic systems in a complex magnetic structure. This same reasoning can be applied to control N oscillations precessing at different frequencies. If we are trying to quench frequency i , we require $t_i^{(m)} = \frac{(2m-1)\pi}{\omega_i}$, and then find the value of m for which $Re\{e^{i\theta_j^{(m)}}\} > 0$ for all $i \neq j$ where $\theta_j^{(m)} = \frac{f_j}{f_i}(2m-1)\pi$ to sustain all the other precessions.

6.5 Representation in the Complex Plane

For the remaining discussion we will assume a system consisting of two frequencies and that we are quenching layer 1, while maintaining the resonance of layer 2. The projections of R2 onto the unit circle when R1 is at a quenching location depend on the ratio of frequencies f_2/f_1 , since $\theta_2^{(m)} = \frac{f_2}{f_1}(2m - 1)\pi$. The path traced out in the complex plane determines the variability of control of the magnetic systems. Two extreme examples are if f_2/f_1 is an odd integer, then R1 will not be able to be quenched without also quenching R2. Alternatively, if f_2/f_1 is an even integer, then for each time $t_1^{(m)}$, R1 will be quenched and R2 enhanced. Increased control of the systems is possible with more elaborate paths in the complex plane and analyzing the symmetries can be useful for optimizing the control of the two oscillations.

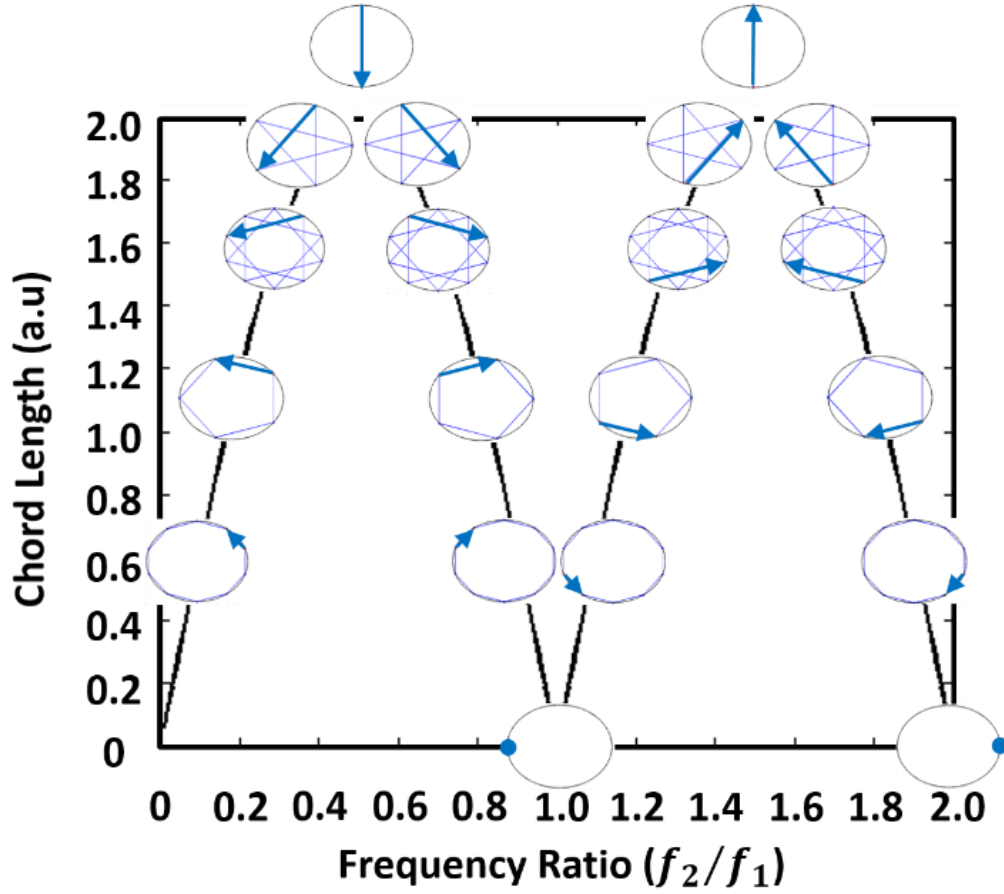


Figure 6.5: Chord length in the complex plane as a function of the frequency ratio of two resonances. Assuming R1 is being quenched ($\theta_1 = (2m - 1)\pi$), the insets show the location and direction of R2 for increasing m at ratio intervals of 0.1. For $f_2/f_1 = 1$ both resonances will be quenched for all m and when $f_2/f_1 = 2$, R2 will always be enhanced. More complex symmetries are possible depending on the ratio, but this example shows how the chord length and the path symmetry depend on the ratio and how by tuning the frequency ratio different locations of R2 can be obtained for different values of m . Taken From [117].

The chord length of the path traced out in the complex plane by the unquenched resonance (R2) at successive $t_1^{(m)}$ is given by $l = \sqrt{\sin^2\left(\pi \frac{f_2}{f_1}\right)}$, and serves as a convenient metric for determining the location of the R2 magnetization vector. Aside from the length, the path direction and symmetry are also determined by f_2/f_1 . Figure 6.5 shows the chord length as a function of the ratio of the frequencies. The insets in the graph show the paths for different frequency ratios at intervals of 0.1. The arrows indicate the starting point ($m = 1$) and direction of the R2 path. If materials with different frequency vs. applied field relations are used, different ratios could be accessible simply by tuning the external field. This would allow the position R2 to be tuned utilizing an external magnetic field and would allow for a more complex control of the magnetization dynamics of the system. Depending on the ratio, larger or smaller values of m may be necessary to obtain the desired position of R2. Therefore, the damping must be taken into consideration. For a given frequency ratio, the desired position of R2 may not be accessible if R1 has already damped out to equilibrium.

6.6 Spin Pumping and Damping

When a spin polarized current is injected into a ferromagnetic material a torque is applied to the magnetization via the spin current. This is known as spin-transfer-torque (STT) and is a widely studied effect with extensive technological implications. [120] However, the opposite effect also occurs—a precessing magnetization emits a spin polarized current. Because the angular momentum is carried away by the spin

currents, this effect can have drastic consequences for the damping of the magnetic system. [121] Therefore, the ability to suppress a given spin wave resonance in multilayer structures opens up the opportunity to investigate any influence that a precessing magnetization in one layer may have on the damping in the adjacent layer in a novel manner.

In order to understand the spin pumping effect in a bit more detail, we will at first focus on a single layer surrounded by a non-magnetic material. The magnitude of the change in the damping of the magnetic system depends on the thickness of the magnetic material. In *3d* ferromagnetic materials the spin-coherence length is smaller than a nanometer.[122] Therefore, the spin current is reabsorbed in the magnetic material and there is no loss of angular momentum. However, at the interface of the magnetic material with a non-magnetic material the spin current can propagate into the adjacent material causing an increase in the damping of the magnetic system.

Additionally, the effect on the damping depends on the spin relaxation properties of the adjacent material. If the spin relaxation time is short, spin states are consistently available and the adjacent material acts as a spin sink. This leads to an increase in the damping of the magnetic material. Conversely, if the adjacent non-magnetic material has a long spin relaxation time, new spin states are not available for occupancy so the spin current cannot propagate into the adjacent material and less angular momentum is lost from the magnetic material. The spin-pumping induced increase in damping is given by the difference between the measured damping, α , and the intrinsic damping,

α_0 . The dependence of the spin-pumping induced damping ($\alpha - \alpha_0$) on the thickness of the magnetic material for various non-magnetic adjacent materials is shown in figure 6.6.

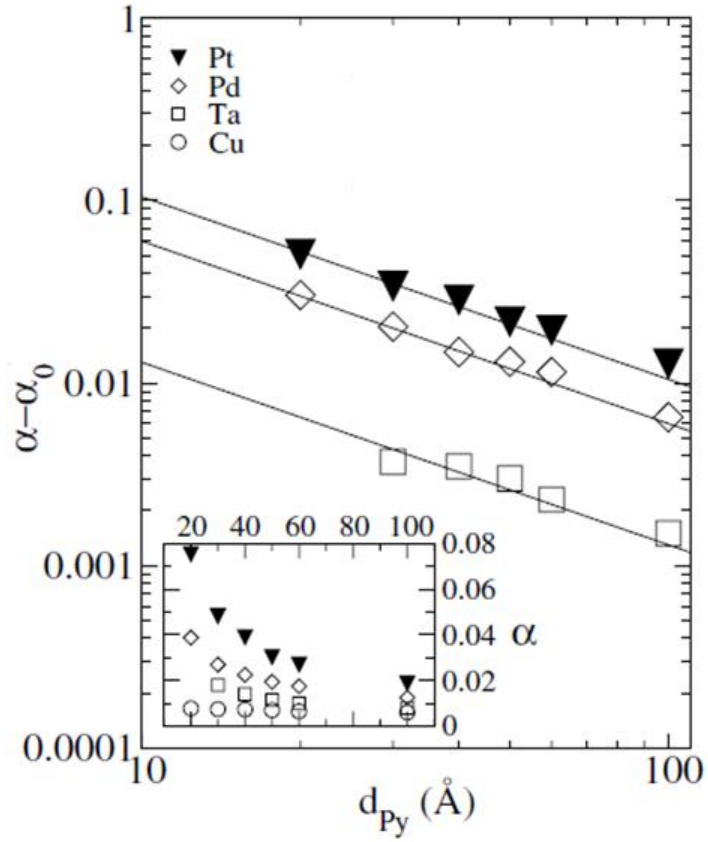


Figure 6.6: Spin pumping induced damping ($\alpha - \alpha_0$) for Py films of varying thicknesses for different adjacent non-magnetic materials. The additional damping due to spin pumping depends on the thickness of the Py layer as well as on the adjacent material. Pt and Pd have short spin relaxation times and act as strong spin

sinks causing a larger effect on the damping than Ta. Cu has a long spin relaxation time and has virtually no effect on the damping. Taken from [121].

In a multilayer magnetic structure, if the spacer between the magnetic layers has a long spin relaxation time then spins can propagate through the spacer layer and both magnetization precessions are able to pump spin currents back and forth. Therefore, the angular momentum lost from one layer due to pumping out spin current is balanced by the spin current coming in from the other magnetic layer (assuming similar magnetic materials). If one of the layers is shut off, then that layer would act as a spin sink, absorbing the spin current from the adjacent layer. This would cause the damping of the precessing layer to increase. This has been demonstrated experimentally using FMR [122,123]

Utilizing the technique discussed in this chapter opens up the possibility for observation of the enhanced damping due to spin pumping using TR-MOKE. Some benefits to this over FMR would be that measurements of both layers precessing vs. only one layer precessing could be obtained for a wide variety of magnetization configurations.

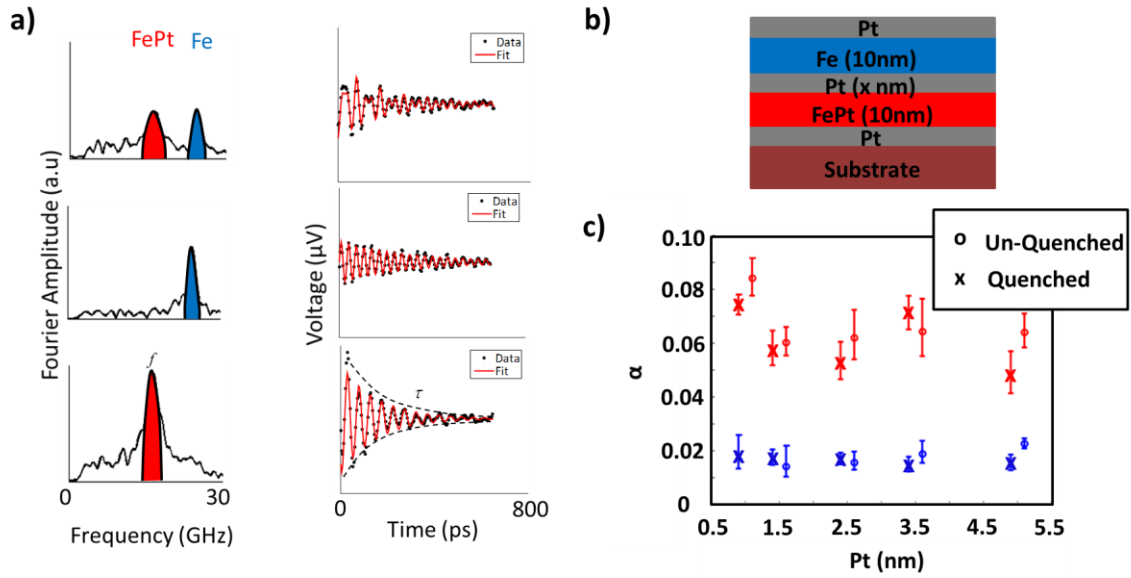


Figure 6.7: (a) Fourier spectra and the corresponding time traces with the fits for the unquenched case where both layers are precessing and for the quenched case where only one layer is left precessing. (b) colorcoded schematic of the multilayer structure to serve as a reference to the (c) damping analysis of the quenched and unquenched resonances. Quenched refers to the case where the other layer has been shut off. For example, red quenched means that the Fe layer has been shut off so only FePt layer is precessing.

With all of this in mind, we analyzed the damping parameters of the different layers in the Fe / Pt(xnm) / FePt structures while both layers were oscillating and while only one was active (Fig. 6.7). [124] Somewhat surprisingly, we observed no dependence on the damping of a layer on the oscillation of the other. This could be due to a few reasons. First, it is unclear how the spin pumping/absorption effect occurs with

different magnetic materials. Second, the layers were relatively thick (10nm). Lastly, the Pt layer which separates the magnetic materials acts as a strong spin scatterer so that minimal spin current could penetrate to the adjacent layers for larger Pt thicknesses. [125] For thinner Pt spacers the exchange interaction becomes relevant which adds an additional complication to the analysis.

In order to mitigate these issues, we designed an Fe (2nm) / Cu (5nm) / Fe (10nm) multilayer. As can be seen in figure 6.6 Cu has little effect on the damping of a ferromagnetic layer. This is because Cu has a long spin relaxation time. Therefore, the spins should be able to traverse the length of the Cu layer into the other ferromagnetic layer without scattering. Any change to the damping of one ferromagnetic layer would therefore be attributed to spins being pumped from the other ferromagnetic layer. The different thicknesses of the ferromagnetic materials were used so that the different layers have different frequencies due to different demagnetization fields. If both layers are precessing at the same time then the spin currents through the Cu should balance one another and the damping should remain low. However, if the 10nm Fe layer is shut off then it should act as a spin sink, absorbing all the spin current from the 2nm Fe layer causing the damping of the 2nm Fe layer to increase. We would expect to see less of an effect on the 10nm Fe layer due to shutting off the 2nm Fe layer since the effect is less strong for thicker samples. The results can be seen in figure 6.8 and once again show no dependence of the precession of one layer on the damping of the other. One explanation for this could be due to the fact that at each applied field the different layers have different energies

for the spin states due to the different demagnetization fields. Therefore, there are no spin states available in one layer for the spins emerging from the other. In order to utilize the two-pump technique two different frequencies are required. Perhaps this complication can be mitigated through clever design of magnetic structures or methods of excitation.

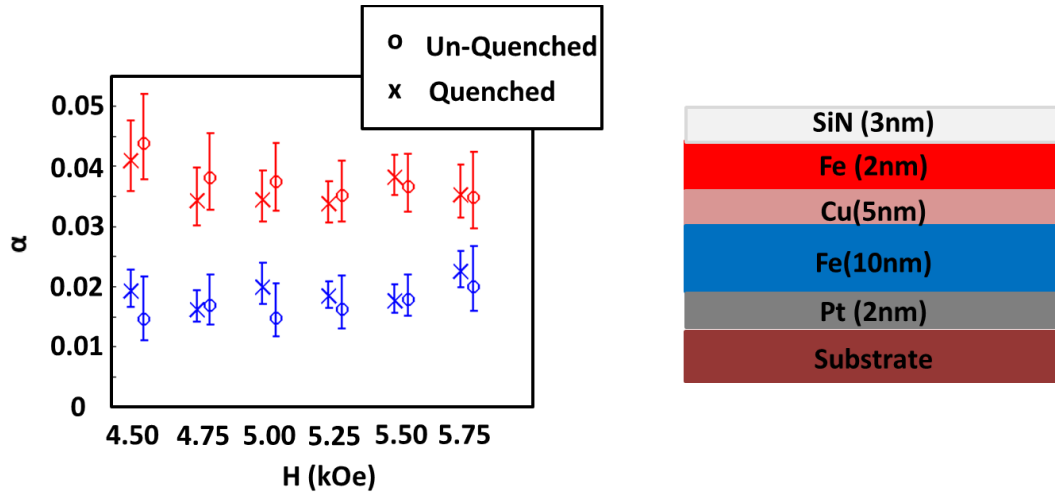


Figure 6.8: Quenched and Unquenched damping for the Fe(2nm) / Cu (5nm) / Fe (10nm) multilayer. Quenched refers to the case where the other layer has been shut off. For example, red quenched means that the 10nm Fe layer has been shut off so only 2nm Fe is precessing.

6.7 Conclusion

We have introduced a new ultrafast pump-probe technique for selectively manipulating the magnetization dynamics of metallic multimodal magnetic structures. This is accomplished by purely optical means. The manipulation of the magnetic oscillations is demonstrated experimentally on a magnetic multilayer system with two resonances. By tailoring the delay of the two pump pulses, the resonance of an individual system was quenched while maintaining the resonance of the other system. A convenient representation for the manipulation of the systems was discussed in the context of mapping out the magnetization vector's position in the complex plane. Additionally, the technique was utilized in order to measure the precession dependent damping in various multilayer structures.

CHAPTER 7: MAGNETO-ELASTIC DYNAMICS DUE TO SURFACE ACOUSTIC WAVES IN NANOMAGNETIC ARRAYS

“He connected the mechanism for the clock to a mechanical ballerina ,and the toy danced uninterruptedly to the rhythm of her own music for three days. That discovery excited him so much more than any of his other hair-brained undertakings”
— Gabriel García Márquez (*One Hundred Years of Solitude*)

7.1 Introduction

Manipulating the spins in magnetic materials has been the focus of intense research with the end goal being increasing the performance of computing. These spintronic devices utilize the spin degrees of freedom and depend critically on various material properties. One parameter, the Gilbert damping constant α , has received bounteous attention in the field. Knowledge of this parameter is critical for the development of many spintronic devices, including spin transfer torque magnetic random access memories (STT-MRAMs) and heat-assisted magnetic recording (HAMR). In these devices, α determines critical device operation characteristics such as the threshold switching current density [126], switching time [127], and transition jitters [128] and can be determined using different experimental techniques [129,130].

Time-resolved magneto-optical Kerr effect (TR-MOKE) analysis is one of them that is well suited to investigating nanomagnets due to its high spatial resolution and sensitivity [131,132]. This technique is based on using the decay time and frequency to calculate the damping of optically excited small angle magnetization precessions [130]. At low fields, this effective damping contains both intrinsic and extrinsic mechanisms and converges to the intrinsic Gilbert damping at high fields [130,133]. Separation of extrinsic effects from the intrinsic magnetic relaxation is essential in order to make a valuable assessment of the Gilbert damping parameter. In this chapter, we will discuss sources of relaxation in TR-MOKE measurements. Additionally, we will discuss complications that arise when using TR-MOKE to study relaxation dynamics in nanomagnetic arrays—the pump pulse initiates both magnetic dynamics as well as generating surface acoustic waves (SAWs) which couple to one another via the magneto-elastic interaction. Furthermore, this chapter will serve as an introduction to experimental measurements on magneto-elastic dynamics in nanomagnetic arrays. We will see that the geometry of the array is a critical parameter controlling the elastic as well as the magnetic dynamics. Lastly, we will show how these magneto-elastic effects can be lessened as well as utilized in order to extract a meaningful determination of the Gilbert damping parameter. Because the system dynamics can be engineered to produce novel properties through altering the geometry, this system falls under a class of materials known as metamaterials.

7.2 Intrinsic vs. Extrinsic Damping

The damping in magnetic systems is one of the most experimentally and theoretically studied aspect of magnetic dynamics. The relaxation of the magnetic system is a collective many body process which makes separating all the different relaxation mechanisms extremely difficult. [134] Before continuing, a distinction must be made between what differentiates intrinsic and extrinsic mechanisms. In a nutshell, intrinsic mechanisms are those which are inherent to the magnetic system, where the relaxation is a direct effect of the “intrinsic” timescales relating interactions between spin, electric and phononic degrees of freedom and is rooted in the spin orbit coupling. [135] Extrinsic mechanisms are caused by magnetic disorder or non-local dissipation process and are typically the result of modifications to the magnetic structure’s environment or of inhomogeneities throughout the sample. In order to gain an understanding of intrinsic and extrinsic mechanisms we will review some examples which contribute to relaxation in magnetic systems.

7.2.1 Elliot-Yafet (Spin-Flip) Scattering

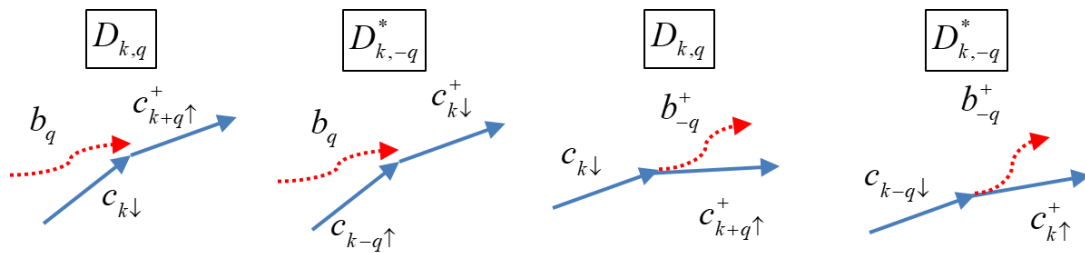


Figure 7.1: Schematic of different scattering processes between electrons (blue solid arrows) and phonons (red dotted arrows).

The relaxation mechanism in Elliot-Yafet scattering arises due to the interaction between a phonon and an electron. (Fig. 7.1) Because of the spin orbit interaction the spin states of an electron wavefunction are mixed [136]

$$\varphi_{k,\uparrow} = [a_k(r)|\uparrow\rangle + b_k(r)|\downarrow\rangle]e^{ik\cdot r} \quad (7.1)$$

Where k is the wave-vector and a_k and b_k are the probabilities of spin up and spin down states respectively. We assume that $a_k > b_k$ so that the majority of spins are in the spin up state. The Hamiltonian describing the spin-flip interaction is [137]

$$\mathcal{H}_{sf} = \sum_{k,q} D_{k,q} c_{k+q,\uparrow}^+ c_{k,\downarrow} b_q + D_{k,-q}^* c_{k,\downarrow}^+ c_{k-q,\uparrow} b_q + D_{k,q} c_{k+q,\uparrow}^+ c_{k,\downarrow} b_{-q}^+ + D_{k,-q}^* c_{k,\downarrow}^+ c_{k-q,\uparrow} b_{-q}^+ \quad (7.2)$$

Where q is the wave vector of the phonon, the electron and phonon creation and annihilation operators are $c_{k,\sigma}^+$, $c_{k,\sigma}$ and b_q^+ , b_q with $\sigma \in \{\uparrow, \downarrow\}$. We are interested in the matrix element which mixes spins of different orientations. This will occur with a transfer of angular momentum and can be given by

$$\langle \varphi_{k+q,\downarrow} | \mathcal{H}_{sf} | \varphi_{k,\uparrow} \rangle \quad (7.3)$$

Where the key terms of interest are those which mix spin up or down states and are represented by $W_{\uparrow,\downarrow} = \langle \uparrow | \mathcal{H}_{sf} | \downarrow \rangle$ and $W_{\downarrow,\uparrow} = \langle \downarrow | \mathcal{H}_{sf} | \uparrow \rangle$. The total magnetic moment is proportional to the population difference of the spins $\Delta N = N_{\uparrow} - N_{\downarrow}$. Furthermore, the change in the population difference is given by [136]

$$\frac{d\Delta N}{dt} = 2(W_{\uparrow,\downarrow} - W_{\downarrow,\uparrow}) \quad (7.4)$$

Where the 2 comes from the fact that a spin-flip changes the population difference by 2. [136] If N_0 is the equilibrium population difference then the relaxation time τ can be given by [138]

$$\frac{d\Delta N}{dt} = -\frac{\Delta N - N_0}{\tau} \quad (7.5)$$

This expression describes the rate of change of the population difference of the spin-up and spin-down electrons and since the population difference is proportional to the magnetic moment, the relaxation time describes the damping of the magnetic moment. In a nutshell the spin-flip scattering occurs because due to the spin orbit interaction the orthogonal spin states are mixed for an electron. Even though the probability of being in one state is overwhelming there does exist a non-zero probability of being in the other state. Through scattering with a phonon the state of the electron is able to change to a state with the opposite spin with the angular momentum associated with this change being transferred to the phonon. Eventually the magnetic system will relax to equilibrium. This relaxation process is an intrinsic mechanism. Other sources of intrinsic damping are the breathing fermi surface [139,140] and the s-d orbital interaction [141].

7.2.2 Extrinsic Mechanisms

Extrinsic damping mechanisms cause the experimentally observed damping to be larger than the intrinsic value. [142] Experimental conditions make it impossible to

measure a single lattice cell or an individual atom. Therefore, the signal that is acquired comes from the dynamics of many regions within a relatively large area. These different regions may have slightly different properties due to imperfections in fabrication which can affect the local anisotropy field. In the case of nanomagnet arrays, slightly different shapes will cause slightly different demagnetization fields. Additionally, spins located at a surface or at an interface experience different conditions than spins located in the bulk of the magnet. Due to these different anisotropy fields the precession frequencies will be slightly different for each local region. The signal is a summation of all of the different regions, and so the spread in frequencies will lead to a dynamic dephasing of the TR-MOKE signal which will cause the signal to damp out quicker than that associated with the intrinsic relaxation of the material. (Fig. 7.2) [143]

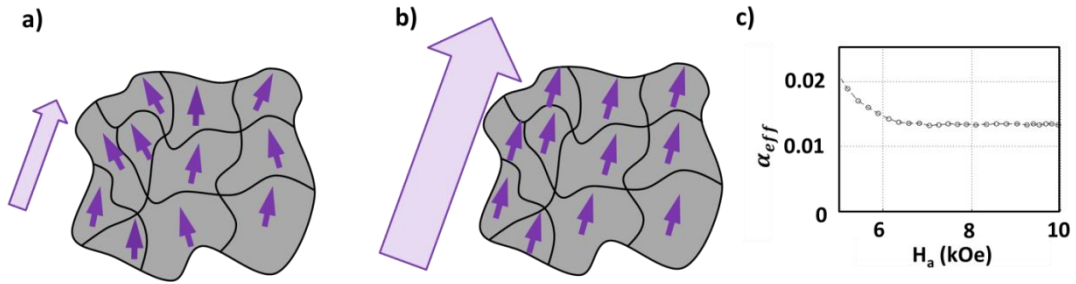


Figure 7.2: (a) In the presence of a weak magnetic field the distribution of local anisotropy fields causes slightly different effective fields in each region (visualized by different directions of the magnetization vectors within different regions). This causes the different regions to precess at different frequencies which causes the

damping to appear to be larger. **(b)** When the applied field is sufficiently strong, the local variation of the anisotropy field is negligible (arrows all same direction) and all the regions precess at the same frequency. **(c)** This effect can be seen in the α_{eff} vs. H_a graph. At low fields the damping is higher until it approaches a saturation point at high fields which is approximately the intrinsic Gilbert damping.

The measured damping including extrinsic contributions is called the effective damping, α_{eff} . It is convenient to work in the frequency domain in order to mathematically express these relationships. The damping of a system is related to the linewidth in the frequency domain. The effective damping is thus given by the effective linewidth which has contributions from intrinsic $\Delta\omega_{int}$ and extrinsic $\Delta\omega_{IH}$ (also known as inhomogeneous) effects. The effective linewidth is given by

$$\Delta\omega_{eff} = \Delta\omega_{int} + \Delta\omega_{IH} \quad (7.6)$$

Where $\Delta\omega_{int} = 2/\tau$ and τ is the intrinsic relaxation of the system. [144,145] The inhomogeneous broadening is given by $\Delta\omega_{IH} = |\partial\omega/\partial M_{eff}|\Delta M_{eff}$ where M_{eff} is the effective anisotropy field defined in Chapter 5. For the case where the magnetization is applied in the film plane an analytic solution can be found for the effective linewidth. In this case $\omega = \gamma H_a$ and when $H_a > M_{eff}$, $\Delta\omega_{eff}$ is given by

$$\Delta\omega_{eff} = \alpha\gamma(2H_a - M_{eff}) + \frac{\gamma H_a}{2\sqrt{H_a^2 - H_a M_{eff}}} \Delta M_{eff} \quad (7.7)$$

If $H_a \gg M_{eff}$ and $\Delta M_{eff} \ll 1$ then $\Delta\omega_{eff} = \Delta\omega_{int} = 2\alpha\gamma H_a$ so that

$$\alpha = \frac{1}{\tau\omega} \quad (7.8)$$

Therefore, the intrinsic damping is typically found by applying a sufficiently high magnetic field so that the inhomogeneous contributions are negligible to the signal.

7.2.3 Pump Probe Alignment

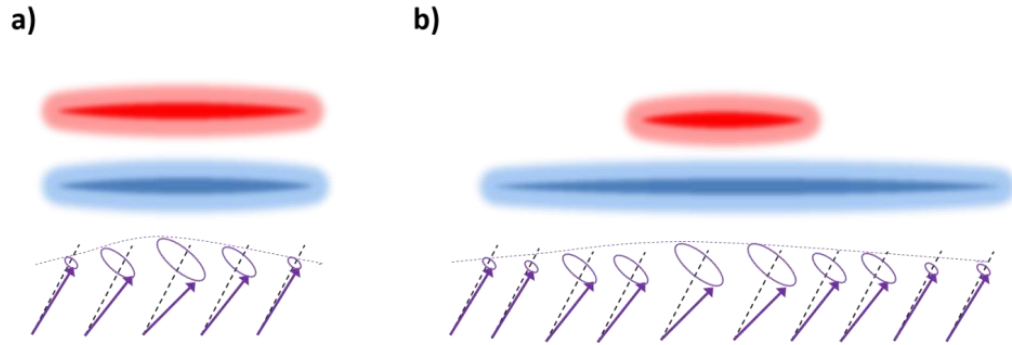


Figure 7.3: (a) Schematic of inhomogeneous excitation due to similarity in the sizes of the pump (blue) and probe (red) pulses. The different amplitudes of the excited region cause a spin wave with non zero k to form and cause an increase in the damping of the system. (b) When the pump is large, the effects of disorder are reduced and with a smaller probe pulse, the area that is being probed is more homogeneous.

An example which serves to show how increased damping can occur due to experimental conditions arises if there is imperfect overlap between the pump and

probe beams, or if the size of the pump beam is too small. Since the effective anisotropy pulse is proportional to the fluence of the laser pulse, the excitation by the pump pulse is spatially inhomogeneous. (Fig. 7.3a) The spins are therefore not perfectly collinear and so the exchange and demagnetization energy cause an additional torque to the mean magnetization vector contributing to an enhanced damping. [135] This is known as disorder broadening and arises due to the formation of spin waves with non-zero values of k — this enhanced damping is proportional to the spatial gradient of \mathbf{M} ($\mathbf{M} \times d\nabla^2 \mathbf{M}/dt$). [146]. This example shows why the pump pulse should be as large as possible—the closer the excited spins are to a $k=0$ spin wave, the less of an effect due to the disorder of the spins. Additionally, if the probe is smaller than the pump, the signal will be from a more homogeneously excited area. (Fig. 7.3b)

7.3 Damping in Nanomagnet Arrays Using TR-MOKE

Understanding nanomagnet dynamics in densely packed arrays is important due to their potential applications in next generation spintronic devices. While the intrinsic magnetic response of a nanomagnet is most naturally studied using a single element [147], measurements on arrays are valuable as they may be the only way to generate large enough magneto-optical signals to observe the dynamics of a given system and because they provide a complementary set of information that helps identify extrinsic effects due to inter-element variations and interactions. However, a side effect of pumped pulse excitation in regularly patterned arrays is the simultaneous generation

of surface acoustic waves (SAWs) due to the thermal expansion of the elements upon irradiation with the pump pulse.

7.3.1 Magnetoelastic Coupling in Arrays

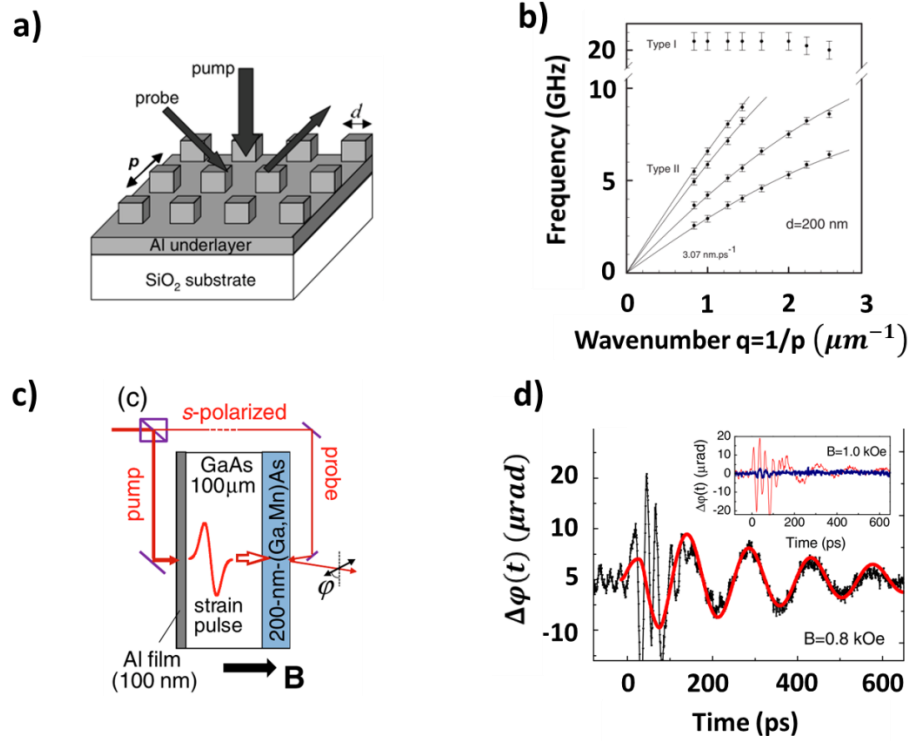


Figure 7.4: (a) Non-magnetic Al periodic nanostructures of size d with pitch, p . Taken from [150]. (b) After irradiation of a femtosecond pump pulse the elastic dynamics of a structure with $d = 200 \text{ nm}$ displays a $1/p$ dependence on the array pitch (Type II modes). The Type I modes are independent of the pitch and are due to the vibration of the elements themselves (depend on d). Taken from [150]. (c) A strain pulse is launched in the Al film which travels through the GaAs Substrate to the (Ga,Mn)As magnetic film where the dynamics are detected by the probe pulse. Taken

from [148]. **(d)** The strain pulse initiates magnetic dynamics due to the magneto-elastic interaction in the magnetic film. A combination of these two effects occur in nanomagnetic arrays. Taken from [148].

The heating from the pump pulse has two important effects on the array. Firstly, the anisotropy is rapidly modified causing the magnetization to precess around the effective field [149]. Secondly, the heating causes a ubiquitous thermal expansion of all the elements. This thermal expansion launches elastic waves in the substrate. Each element thus acts as a node for launching elastic oscillations into the substrate. The periodic arrangement of the elements cause the elastic waves to interfere constructively to create surface acoustic waves (SAWs). These SAWs exist at specific frequencies determined by the array geometry and the substrate material [150] and have been extensively investigated recently due to the emerging field of phononic bandgap materials. In these systems, the phononic band structure is a function of material properties as well as the position and size of elements in arrays which create stopbands in the spin-wave spectrum [151,152,153]. Time-resolved studies on periodic arrays of Al nanoelements revealed that the SAW frequencies depend inversely on the array pitch. (Fig. 7.4) For small mass loading, the eigen-frequencies of the SAWs can be approximated as [150]

$$f_{ij} = \frac{v\sqrt{i^2+j^2}}{p} \quad (7.9)$$

where v is the velocity of the SAW in the substrate, p is the pitch of the array, and (i, j) the indices of the SAW mode k-vector.

The SAWs travel through the substrate according to the elastic wave equation

$$\rho \frac{\partial^2 u_i}{\partial t^2} = \sum_{j=1}^3 \frac{\partial \sigma_{ij}}{\partial x_j} \quad (7.10)$$

where $i, j = 1, 2, 3$ denote the Cartesian coordinates, ρ is the density, u_i is the displacement. σ_{ij} is the Cauchy stress tensor [154] given by

$$\sigma_{ik} = \frac{1}{2} C_{ijkl} \frac{\partial}{\partial \varepsilon_{ik}} \varepsilon_{ij} \varepsilon_{kl} \quad (7.11)$$

Where C_{ijkl} are the components of the stiffness tensor, $\varepsilon_{ij} = \left(\frac{\partial u_i}{\partial x_j} + \frac{\partial u_j}{\partial x_i} \right) / 2$ are the strain components and u_i are the mechanical displacements.

The elements are on top of the substrate and therefore the SAWs dynamically modify the elastic strain in the elements, $\varepsilon_{ij}(\vec{r}, t)$, which magneto-elastically drives the magnetic system. (Fig. 7.4) This interaction manifests itself as an additional energy term in the free energy of the nanomagnetic element

$$\begin{aligned} E_{ME} = & B_1 (\varepsilon_{xx}(r, t) m_x^2 + \varepsilon_{yy}(r, t) m_y^2 + \varepsilon_{zz}(r, t) m_z^2) \\ & + 2B_2 (m_x m_y \varepsilon_{xy}(r, t) + m_x m_z \varepsilon_{xz}(r, t) + m_y m_z \varepsilon_{yz}(r, t)) \end{aligned} \quad (7.12)$$

where B_1, B_2 are the magneto elastic constants defined in chapter 3.2.6. This is the energy term describing magnetostriction, however the strain components ε_{ij} now have a position and time dependence since they are caused by propagating SAWs.

This additional energy term dynamically modifies the frequency and lifetime of the magnetic oscillations. It causes an extrinsic contribution to the magnetic relaxation.

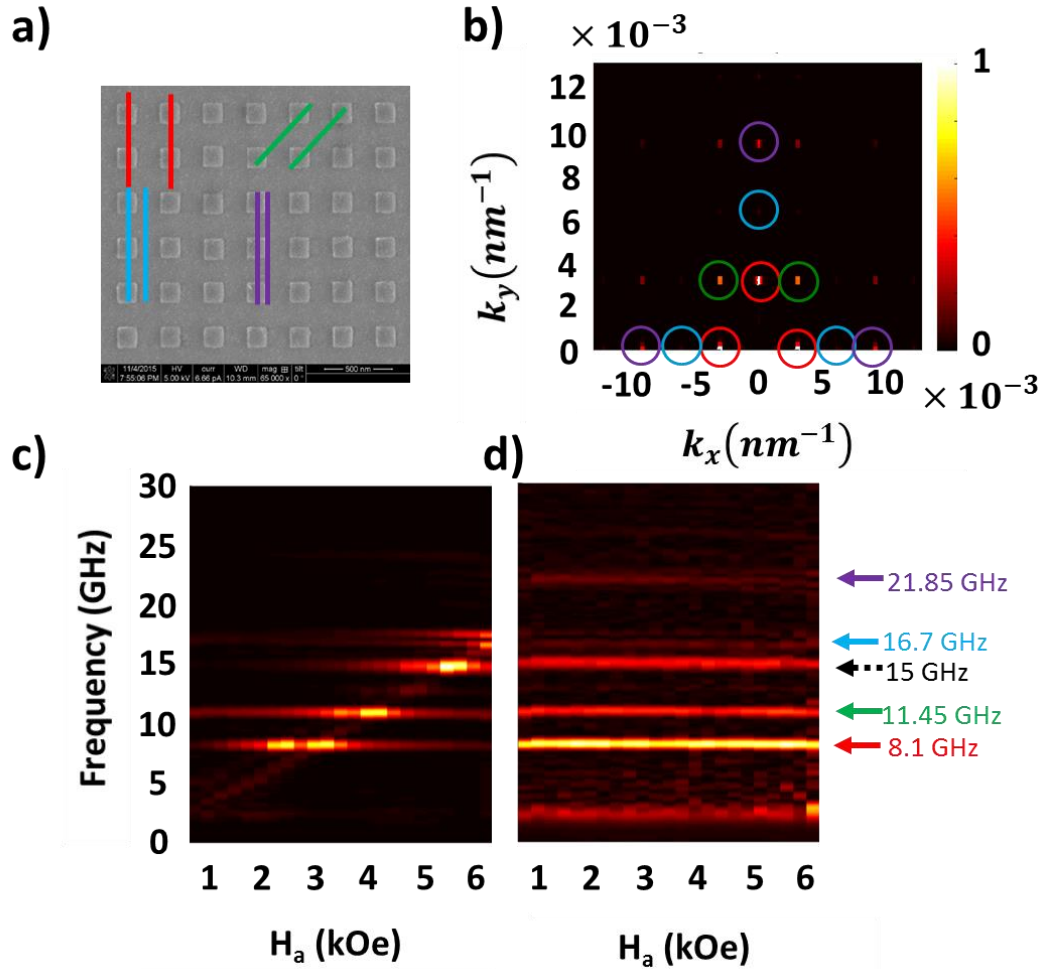


Figure 7.5: (a) SEM image of a periodic Ni array of 156 nm wide squares with a pitch of 330nm. The colors indicate the wavelength and direction of the different SAW modes. (b) 2D Spatial Fourier transform of the periodic array from (a). The geometric arrangement of the elements cause discrete points in the spatial Fourier transform which correspond to the different SAWs. (c) Magnetic and (d) non-

magnetic (elastic) H_a vs. Frequency dynamics. The non-magnetic spectra shows field independent frequencies corresponding to the SAWs. In the magnetic spectra (c) there is a magnetic mode that changes with H_a . However, as it passes through the SAW frequencies it is pinned and enhanced.

Due to the magneto-elastic coupling (Eq. 7.12), the optically generated SAWs can drive the magnetization dynamics in nanostructured arrays. This causes the spin precession resonances to be pinned at the SAW frequencies over an extended applied field range around the point where the magnetic and SAW resonances are degenerate. (Fig. 7.5) We will discuss how this opens up the possibility for utilizing SAWs as an extra degree of freedom for investigating nanomagnet arrays in section 7.3.4 However, for traditional TR-MOKE measurements the SAW induced magnetization dynamics complicate the extraction of the intrinsic magnetic response.

7.3.2 Effect of Array Geometry on SAW Influence

The effects of the SAWs on the magnetization dynamics can be mitigated by altering the array geometry from a periodic to a randomized pattern so as to restore the intrinsic magnetic response. Figure 7.6 (a) shows SEM images of the two samples investigated, exhibiting a periodic (top) and an aperiodic randomized (bottom) pattern, respectively. They were fabricated using electron beam lithography on a (100) Si substrate capped by a 110 nm thick hafnium oxide antireflection coating as reported [155]. They are both comprised of 30nm thick 156nm wide polycrystalline

Ni squares. In the periodic array the elements have a pitch of 330nm corresponding to a fill factor of 0.22. This same fill factor is used in the randomized pattern so that the only difference between the two is the arrangement of the Ni squares. The elements have an easy axis in the sample plane with an $M_{eff} = 1807$ Oe.

In order to understand the influence of the nanomagnet array geometry on the generation of SAWs, it is instructive to analyze the array geometry in Fourier space. Figure 7.6 (b) shows the two-dimensional spatial Fourier transforms of the two samples under investigation. In the periodic array, the regular arrangement of elements in particular directions manifests itself as discrete points in Fourier space. The spacing of these points is a function of the array pitch. Each point corresponds to a different SAW eigenmode launched in that direction. The observed frequencies (Fig. 7.7) agree well with equation (7.9) using $v = 2673$ m/s - predominantly determined by the elastic properties of the antireflection coating layer, where the majority of the elastic energy is confined [154]. In figure 7.6 (c), the average spatial Fourier amplitude vs. k-vectors of constant magnitude i.e. $k_r = \sqrt{k_x^2 + k_y^2}$ is plotted.

This is instructive since the (1,0) and (0,1) SAW modes are propagating in orthogonal directions, yet have the same magnitude in k-space for this square array, and therefore the same frequencies. This means they are both responsible for modifying the magnetization precession at that frequency. The same is true with higher order SAWs as well.

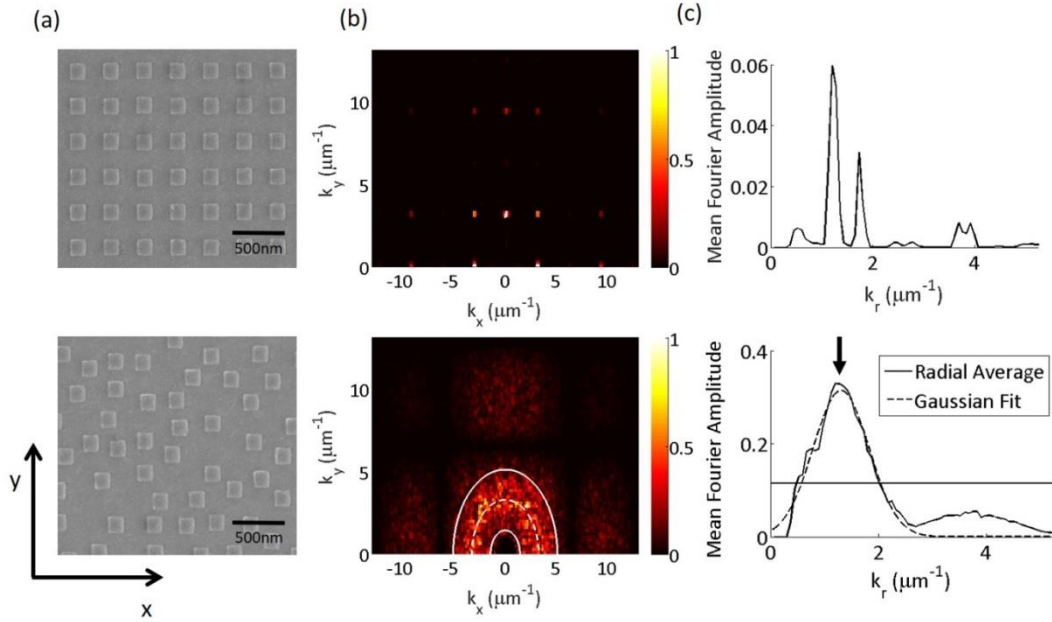


Figure 7.6: (a) SEM images of the periodic array (top) and the random aperiodic pattern (bottom). (b) 2D Spatial Fourier Transforms of the patterns. The dashed line in the Random 2D Fourier Transform corresponds to the k -vector with the largest average Fourier amplitude, and the solid lines to the limits of SAW influence as defined in the text. (c) Average radial Fourier amplitude as a function of k -vector magnitude (k_r). The periodic array displays discrete k -vectors while the randomized pattern has a continuous spread in k -vectors. The dashed line is a Gaussian fit to this distribution and the solid line the e^{-1} cutoff. The arrow is the maximum average radial Fourier amplitude. Taken from [156].

In contrast, the randomized pattern exhibits a smeared isotropic ring in k-space. The spread of the ring corresponds to a distribution of distances of neighboring elements, and the radial symmetry emphasizes that this distribution exists in all directions. The average spatial Fourier amplitude for k-vectors of different magnitude is more continuous in nature as seen in figure 7.6 (c), indicating a spread in the radial periodicity. By fitting a Gaussian distribution to this average we can estimate e^{-1} limits of the spread in radial pitches to be 196nm – 694nm, where $p = 1/k$. This distribution of pitches causes a spread in the launched SAWs. Assuming the same speed of sound in the substrate as in the periodic array (~2700m/s), SAWs may exist across a broad band of frequencies between 3.8-13.8 GHz. These limits are displayed in figure 7.6 (b) and 1(c) as solid lines. The k-vector with the maximum radial averaged Fourier amplitude corresponds to a pitch of 305nm and is displayed as a dashed line in Fig. 1(b). The SAW that corresponds to this pitch has a frequency of 8.8 GHz. From this analysis, it can be expected that the SAW influence on the magnetization dynamics is substantially reduced, while not being completely eliminated.

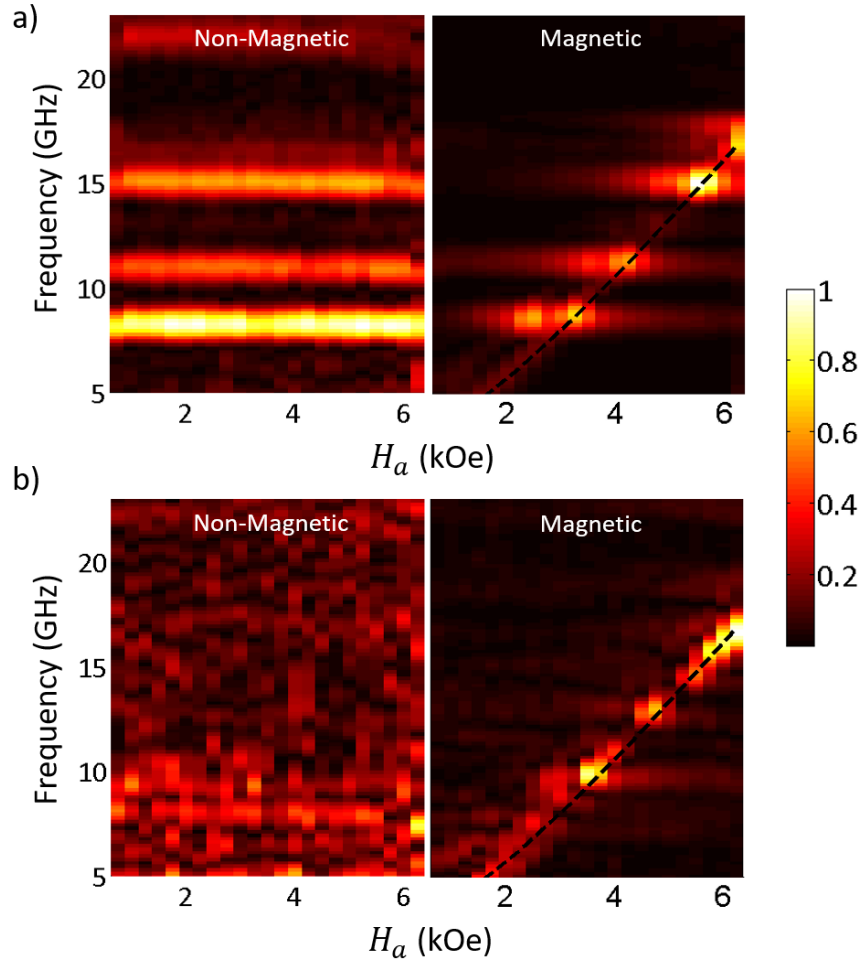


Figure 7.7: (a) Measured TR-MOKE Fourier spectra of the periodic array. The non-magnetic channel displays well-defined field-independent SAW resonances. The magnetic response is pinned at these SAW frequencies. Dotted black line is the simulated Kittel mode. (b) In the randomized array, the non-magnetic channel shows a drastically reduced signal from the SAWs, indicating that their dominant influence has been suppressed. In the magnetic channel the intrinsic Kittel mode has been restored. There is still slight driving of the magnetization from SAWs at 9.6 GHz and 12.7 GHz. Dotted black line is the simulated Kittel mode. Taken from [156].

Figure 7.7 shows the magnetic and non-magnetic response of the two samples represented as TR-MOKE Fourier spectra maps at each external applied field value, calculated from the background-corrected time traces of the magneto-optic signal [154]. The signals were normalized to the intensity of the highest Fourier peak in each figure. The following results are all independent of laser spot location. In the periodic array, the non-magnetic channel displays a field-independent response with constant frequencies. These frequencies correspond to the discrete SAW eigenmodes given by equation (7.9). The resonance near 15 GHz corresponds to the surface skimming longitudinal wave which has an in-plane displacement and higher phase velocity than the SAW Rayleigh waves [154,157].

The magnetic channel shows a much more complex response. Two field-dependent center and edge Kittel modes are present at low applied fields, but as the H-field is increased, the intrinsic modes and the SAW frequencies approach degeneracy. As this occurs, the mechanical oscillations of the SAWs magneto-elastically couple to the magnetization. This drives the magnetic precession and pins it at a fixed frequency across a large field range. The TR-MOKE Fourier amplitude reaches a maximum at degeneracy. The coupling of the elastic and magnetic degrees of freedom occur at all SAW eigenmodes in the array and makes observation of the intrinsic Kittel modes nearly impossible, especially at high fields—above 4kOe. Furthermore, it is impossible to initiate magnetic precession without SAWs by reducing the laser fluence. As the pump fluence is lowered SAWs continue to be excited even after the Kittel mode signal disappears.

Figure 7.7 (b) shows the same plots for the aperiodic random pattern. In the non-magnetic channel, the field-independent SAW resonances are no longer present. A comparison of the TR-MOKE frequency spectra of the non-magnetic plots obtained from the two samples demonstrates how effective altering the pattern geometry is on the suppression of the SAWs. A similar effect was recently observed in CoFeB films that were vertically stacked in a periodic and aperiodic fashion [158]. In the aperiodic pattern's magnetic channel the intrinsic Kittel modes have been restored. The dotted black line is the simulated Kittel Mode for these elements and shows that the intrinsic magnetic response can be measured all-optically by altering the array geometry. A slight enhancement of the TR-MOKE Fourier Amplitude through weaker residual radial SAWs is observed. This is a result of the fact that the spatial frequency content of the randomized array is not perfectly flat due to constraints from element size and fill factor as discussed above. The strongest residual pinning occurs at 9.6 GHz, close to the predicted value of 8.8 GHz. A second, weaker pinning site at 12.7 GHz also falls within the e^{-1} range specified previously. This deviation in the maximum pinning frequency can be explained by a slightly different SAW propagation speed in this array. Another source of this discrepancy could arise from a larger periodicity in a specific direction that is averaged out in the radial average. Apart from these slight enhancements, the SAW influence on the magnetization dynamics has been removed. We further corroborate this conclusion by directly comparing the Fourier spectra at selected fields as shown in Fig. 3. At low fields the Kittel Mode in the Periodic array is still visible. However, at high fields we see that the spectrum in the periodic array

is dominated by the SAW modes at the frequencies extracted from the non-magnetic channel (dashed lines) which do not shift with applied field. In contrast, the spectrum for the randomized array show a single dominant peak at the frequency of the Kittel mode which does show the expected field dependence. The absolute value of the Fourier amplitude at the Kittel resonance (red arrows) is $\sim 2\times$ larger in the randomized array at 4.5kOe, clearly showing that the intrinsic magnetic response has been restored. We note that the Kittel mode amplitudes cannot be directly compared at 6kOe because the SAW dominates the response at that field.

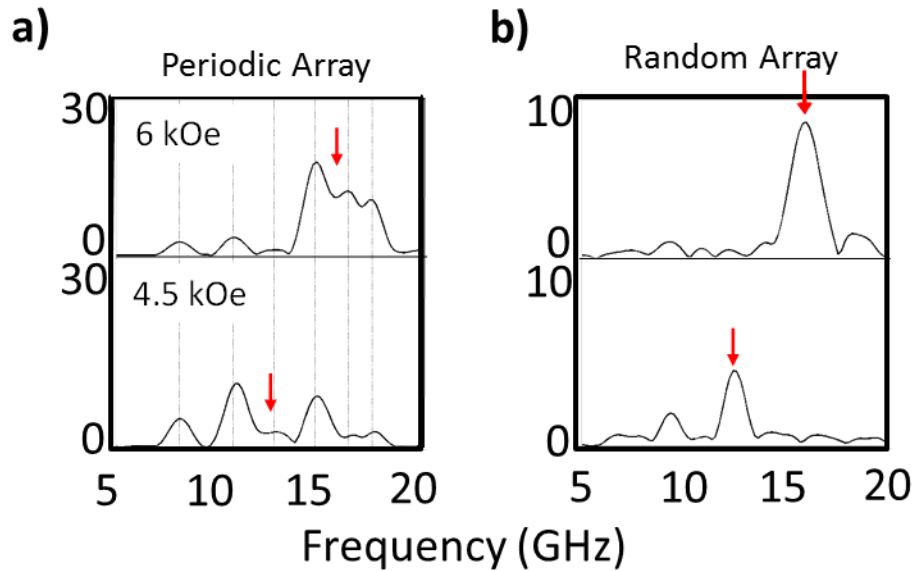


Figure 7.8: Side-by-side comparison of absolute Fourier spectra at different applied fields for (a) periodic and (b) randomized array. The periodic spectra are dominated by field-independent modes at the SAW frequencies (dashed lines), while the randomized array shows a dominant, strongly field-dependent peak at the Kittel

resonance (red arrows). At 4.5 kOe, the absolute Fourier amplitude of the restored Kittel mode is $\sim 2\times$ larger than the amplitude at that frequency in the periodic array. Taken from [156].

7.3.3 Effect of Array Geometry on Damping

The question arises whether this degree of randomization is sufficient to enable a meaningful analysis of the magnetic properties of the sample. In order to answer this question, we analyzed the effective damping, an important parameter in the characterization of magnetic materials. The effective damping, α_{eff} , was extracted from the TR-MOKE time traces by fitting exponentially decaying sinusoidal oscillations to all the resonances visible in the Fourier spectrum using

$$M(t) = \sum_i^n M_0 e^{-t/\tau_i} \sin(\omega_i t + \varphi_i) \quad (7.13)$$

where ω_i is the Kittel frequency and τ_i is the decay time of oscillation i , which are related to the effective damping through $\tau_i = 1/\omega_i \alpha_{\text{eff},i}$. At each field at which the Kittel mode was resolvable $\alpha_{\text{eff},i}$ corresponding to the Kittel mode was extracted. This was not always possible in the periodic array because the precession was pinned at the SAW frequencies, often times with multiple pinning frequencies occurring at the same field. In these cases, the dominant resonance, defined as the frequency with the largest TR-MOKE Fourier Amplitude in the vicinity of the Kittel mode, was analyzed. Fig. 4 shows the effective damping at each field value in the periodic and random arrays along with the 95% confidence intervals of the fit. In an unpatterned

film, as the applied field is increased, the effective damping gradually decreases, approaching the intrinsic Gilbert damping at high fields [159,160] (red dashed line). However, the effective damping in the periodic array follows this trend only at low fields at which the Kittel mode could still be observed. Once pinning to SAWs occurs, the sample displays a much lower apparent damping than the film damping because the SAWs driving the magnetization precession are less damped. There are a few intermediate points where the Kittel mode could be resolved. However, the SAW frequencies dominate the signal which leads to very large uncertainty in the Kittel mode fit. Therefore, the intrinsic damping cannot be reliably extracted from the periodic array.

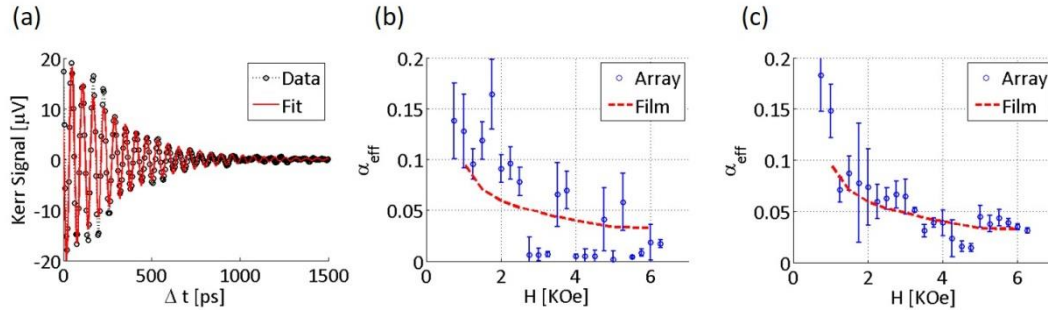


Figure 7.9: (a) Example of random array TR-MOKE time trace ($H = 6$ kOe) and fit to Eqn. (2) ($R^2=0.88$); (b) Effective damping of the Kittel mode or dominant mode in the periodic array along with 95% confidence intervals of the fit. (c) The effective damping in the random pattern shows a restoration of the intrinsic relaxation with high confidence especially at higher fields. In the intermediate region there is still some driving due to weaker radial SAWs. Taken from [156].

In the random pattern, on the other hand, the intrinsic response has been restored, and the extracted effective damping matches that of the unpatterned film over the entire field range (Fig. 7c). In particular, α_{eff} approaches the same value as the film at high fields (~ 0.035) [154,158] with high confidence. This indicates that the damping is the same in both the film and the nanoelements, suggesting that the fabrication process of the nanomagnets does not have an effect on the intrinsic damping in these Ni squares. We note that α_{eff} is slightly lower than the film values at various intermediate points due to the residual effects from SAWs in the frequency range ~ 4 -14 GHz as discussed above. Additionally, the high-field damping value is slightly higher than intrinsic values reported on Ni. This can be attributed to other extrinsic damping effects such as variations in the local anisotropy field and two-magnon scattering [161].

7.2.4 Measurement of Damping using SAW Pinning Width

As mentioned earlier the effect of the SAWs on the magnetization dynamics offers a new degree of freedom for manipulating the spins in nanopatterned devices. In ref [162], arrays of different materials with different damping coefficients and magneto-elastic coefficients were compared in order to determine the influence on the pinning width. It was shown that the width of the pinning region depends on the effective damping coefficient α_{eff} . This enables us to extract the field-dependent effective damping α_{eff} directly from the pinning linewidth, and even recover the intrinsic

Gilbert damping at large applied fields. Therefore, the magneto-elastic coupling to SAWs is not detrimental, but rather provides an alternative path towards damping analysis in patterned arrays for a wide range of damping values.

In order to understand this pinning effect, we must understand how the elastic deformations alter the magnetic free energy. In the static regime, without an external perturbation, the magnetic free energy density G^0 of an isotropic thin film, is given by [163]

$$G^0 = -\mathbf{H}_a \cdot \mathbf{m} + M_{eff} m_z^2 + const \quad (7.14)$$

where $\mathbf{m} = \mathbf{M}/M_S$, \mathbf{H}_a is the externally applied magnetic field and $M_{eff} = 4\pi M_S$ is the effective field given by the shape anisotropy. In equilibrium, the magnetization is oriented along a minimum of G^0 .

In addition to the magnetostatic energy there is a magnetoelastic energy term E_{ME} (Eq. 7.12) that depends on the time-varying elastic deformations caused by the SAWs. [164] It will be repeated here for convenience

$$E_{ME} = B_1(\varepsilon_{xx}(r, t)m_x^2 + \varepsilon_{yy}(r, t)m_y^2 + \varepsilon_{zz}(r, t)m_z^2) + 2B_2(m_x m_y \varepsilon_{xy}(r, t) + m_x m_z \varepsilon_{xz}(r, t) + m_y m_z \varepsilon_{yz}(r, t))$$

The LLG equation describes the motion for the magnetization subjected to an effective field \mathbf{H}_{eff} [163]

$$\partial_t \mathbf{m} = \gamma \mathbf{m} \times \mathbf{H}_{eff} + \alpha_{eff} \mathbf{m} \times \partial_t \mathbf{m} \quad (7.15)$$

where γ is the gyromagnetic ratio and α_{eff} is the phenomenological damping parameter. The effective field, $\mathbf{H}_{eff} = -\nabla_m G^{tot}$, can be derived from the total free energy which is comprised of a static component arising from the applied and internal anisotropy fields (Eq. 7.14) and of a dynamic component due to the magnetoelastic coupling to the SAWs (Eq. 7.12) [163].

$$\mathbf{H}_{eff} = -\nabla_m G^{tot} = -\nabla_m (G^0 + E_{ME}) = \mathbf{H}_{eff}^0 + \mathbf{h}_{ME}(t) \quad (7.16)$$

As the SAW propagates it dynamically modifies the free-energy of the magnetic system which acts as a driving-term $\mathbf{h}_{ME}(t)$, in the total effective field \mathbf{H}_{eff} . As the intrinsic magnetic mode approaches resonance with $\mathbf{h}_{ME}(t)$, the magnetization precesses.

In order to analyze the pinning width of this cross-over resonance, we make two important assumptions. Firstly, we assume that there is negligible back-action from the magnetization dynamics onto the SAWs [154,164]. This is an important assumption which we will not make in chapter 8. Secondly, due to the much larger decay time of the SAWs in comparison to the intrinsic magnetization dynamics, we can assume a pseudo-steady magnetoelastic driving field $\mathbf{h}_{ME}(t)$, to model the magnetic system's response. We assume the effective magnetic field and the magnetization to be sums of static and dynamic components $\mathbf{H}_{eff} = \mathbf{H}_{eff}^0 + \mathbf{h}_{ME}(t)$, and $\mathbf{m} = \mathbf{m}^0 + \mathbf{m}(t)$ where the oscillatory part of both $\mathbf{h}_{ME}(t)$, and $\mathbf{m}(t)$ is given by $e^{i\omega t}$. Redefining the z-axis along the equilibrium magnetization direction, \mathbf{m}^0 , and assuming a small angle precession allows us to linearize the LLG equation (7.15) as

shown in chapter 3.4. This results in two coupled equations relating the transverse components of the magnetization to the components of the driving field $\mathbf{m}(t) = \chi \mathbf{h}_{ME}(t)$, where $\chi = \chi' + i\chi''$ is the complex susceptibility tensor and the imaginary part is a Lorentzian. If we assume a constant driving frequency $\omega = 2\pi f_{SAW}$, then the field-dependent linewidth of this Lorentzian is given by $\Delta H_P = 4\pi\alpha_{eff}f_{SAW}/\gamma$. The derivation is adapted from [165] and further details can be found there. Thus, instead of the SAW pinning being detrimental to damping analysis, it allows us to extract α_{eff} from the measured ΔH_P as

$$\alpha_{eff} = \frac{\gamma\Delta H_P}{4\pi f_{SAW}} \quad (7.17)$$

Details of the procedure for extracting the pinning width can be found in [162,166].

Here we present the pinning at several well defined SAW frequencies for both nickel and cobalt. (Fig. 7.10) This allows us to extract field-dependent effective damping values at multiple crossover points to investigate the extrinsic damping mechanisms. These Fourier Maps are derived from time sections of $t = 1500\text{--}2500$ ps where the precession was exclusively driven by the SAWs. In Ni (Fig. 7.10a), both center and edge modes are visible in the magnetic response, crossing f_{SAW} at different fields. The Co array response (Fig. 7.10b) exhibits similar behavior with multiple SAW crossings through one dominant Kittel mode. The lower signal from the Co array could explain the absence of two modes in the data, and the smaller pitch in the Co array means there are more higher order SAWs in the frequency range of interest which sustains the Kittel mode at more resonances than in the Ni array. Both Fourier

maps were analyzed as described above using one or two Lorentzian peaks of equal width and a single effective damping value for each SAW crossing. Figures 7.10c and 7.10d show that the model fits all resonances well and allows for extraction of a field-dependent effective damping for both arrays. Fig. 7.10e displays the extracted α_{eff} behavior and a comparison to the high-field damping measured in unpatterned films (0.033 for nickel and 0.02 for cobalt) using TR-MOKE. The effective damping values contain contributions from both the intrinsic damping and extrinsic mechanisms as discussed in section 7.2. The values of α_{eff} display the typical decrease with applied field. α_{eff} approaches the film damping in the high field limit for the nickel array. The high field value of the pinning width for Ni was $\Delta H_p = 293$ Oe and for Co was $\Delta H_p = 462$ Oe.

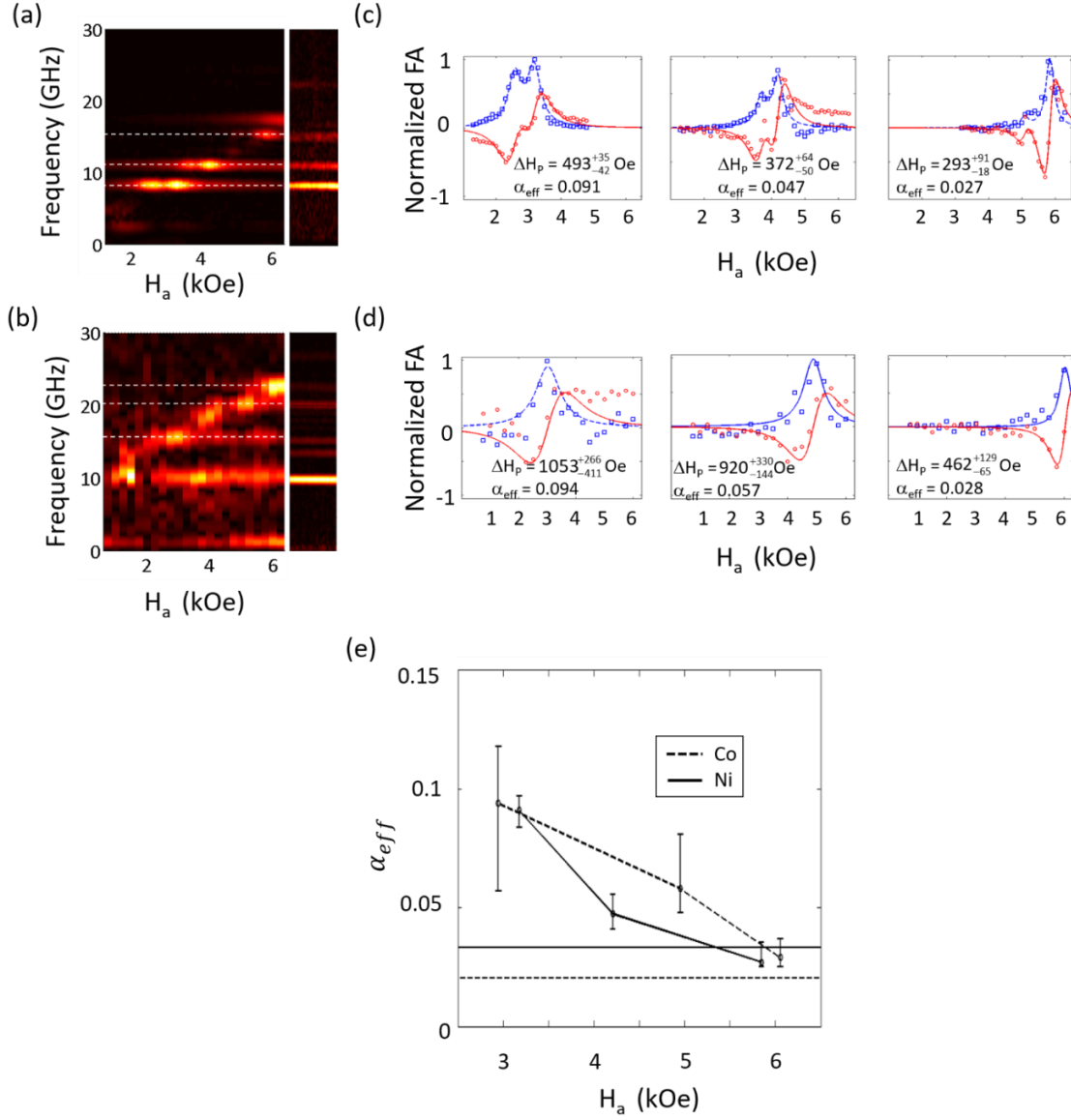


Figure 7.10: Magnetic channel Fourier amplitude spectra measured on the (a) Ni and (b) Co arrays with comparison to non-magnetic reflectivity channel. Time sections of $t = 1500\text{--}2500$ ps were analyzed. The dashed white lines indicate the SAW frequencies analyzed. (c-d) Normalized complex Fourier amplitude of the magnetic signal traced at f_{SAW} , after phase adjustment and scaling with the nonmagnetic signal.

The circles and squares represent the real and imaginary parts, respectively. The solid and the dashed lines are the fits with the Lorentzian shape. The obtained pinning width ΔH_p , pinning width error and Gilbert damping parameter estimated with Eq. (6) are also displayed. (e) α_{eff} displays effects due to inhomogeneous broadening and approaches the value of a film measured at 6 kOe (straight lines).

While these high-field limits correspond to the intrinsic Gilbert damping for nickel, the value for cobalt is still higher than the expected $\alpha=0.005$ [167]. This is due to the imperfect elimination of inhomogeneous broadening for both the film and the array due to limitations in the maximum applied field available in our experimental setup (~ 6.3 kOe) [168].

7.4 Conclusion

In conclusion, we have covered various aspects of magneto-elastic dynamics in densely packed arrays. The dynamics in these metamaterials are determined by the geometric arrangement of the elements. By exploring this geometric dependence, we demonstrated a method for drastically reducing the influence of SAWs on the magnetization dynamics by randomizing the array geometry. The constructive mechanical interaction between individual elements can be reduced which leads to a near-complete elimination of the magneto-elastic interactions within the elements. This allows for the determination of intrinsic material parameters such as the Kittel

mode and the effective damping in densely packed arrays using conventional TR-MOKE techniques.

Additionally, we showed that the SAW pinning could be used as a means to extract the effective damping from a nanomagnet array all-optically. The effective damping shows the well-known decrease with applied field and approaches the intrinsic Gilbert damping in the high-field limit indicating the common causes of extrinsic damping contributions at low applied fields. In the next chapter we will look at the magneto-elastic coupling dynamics in a single isolated nanomagnet.

CHAPTER 8: STRONGLY COUPLED MAGNON-PHONON DYNAMICS IN A SINGLE NANOMAGNET

“All my life through, the new sights of Nature made me rejoice like a child.”

- Marie Curie

8.1 Introduction

Magnonics is an extremely active research area which exploits the wave nature of magnons, the quanta of spin waves, in order to advance data storage, communication and information processing technology. However, a current drawback in the excitation, manipulation and detection of magnons exists due to relatively low conversion efficiencies. [169] Coupling to the phononic system is a less explored avenue for the manipulation of magnons and has been shown to be a promising means of lowering the switching energy of nanoelements.[170,171] With this in mind, a more thorough understanding of the coupling between the spin and phonon systems in nanostructures is necessary.

Because of this, the magnon-phonon interaction has recently been the focus of increased research, specifically as it is applied to surface acoustic wave ferromagnetic resonance (SAW-FMR). [172,173,174,175] In chapter 7 we saw how optically excited SAWs affect the magnetization dynamics of patterned nanomagnet arrays,

[12] and how the SAW frequencies in arrays arise from the geometric arrangement of the elements.[176] In these systems, the SAW energy is located in the substrate layer below the nano-elements and the dynamics are akin to a driven oscillation—the effect of the magnetization precession on the elastic vibrations is neglected. [177]

In this chapter, we report on the first direct observation of coupled magnon-phonon dynamics *within* a single thin nickel nanomagnet. Because the structure is isolated there are no SAWs, but there do exist intrinsic vibrations of the element itself. These depend on the geometry (size and shape) and material properties of the structure, rather than the geometric arrangement of the elements and material properties of the substrate as in the case of the nanomagnetic arrays discussed in chapter 7. Additionally, the effect of the magnetization precession on the elastic (phononic) vibrations can no longer be ignored and the system is modelled as a pair of coupled oscillators which are characterized by hybridization (mode splitting) of the modes when their energies are degenerate. Using an external magnetic field in the appropriate geometries, the magnonic mode is tuned through the phononic resonances and the hybridization characteristic of coupled systems is observed. [178,179] The vibrational dynamics of the structure are in the GHz frequency range (5 GHz – 25 GHz) as are the intrinsic magnetic resonances of the magnet. Access to this higher frequency range has been a limiting factor in resolving the mode splitting in previous experiments using interdigital transducers. [180] Furthermore, we demonstrate tuning of the magnon-phonon interaction into the strong coupling regime via the orientation of the applied magnetic field. This is a novel method of observing the coupling

between magnon and phonon systems and is the first time the magnon-phonon hybridization has been observed in a system of this kind.

8.2 Coupled Resonances and Avoided Crossings

If we include the back-action of the magnetic precession on the elastic vibrations then the system becomes a pair of coupled oscillators. A hallmark of coupled oscillators is the splitting of the normal modes when the energies of the systems are degenerate. This is a well-studied effect in physics and goes by many names—hybridization of the modes, avoided crossing, level repulsion, mode splitting. To see how the avoided crossing depends on the coupling parameter assume we consider two states with energies E_1 and E_2 . The Hamiltonian of the system is [181]

$$\mathcal{H} = \begin{pmatrix} E_1 & 0 \\ 0 & E_2 \end{pmatrix} \quad (8.1)$$

The eigenvectors are $\begin{pmatrix} 1 \\ 0 \end{pmatrix}$ and $\begin{pmatrix} 0 \\ 1 \end{pmatrix}$ with eigenvalues E_1 and E_2 . If we introduce coupling between the two states, W , the Hamiltonian becomes

$$\mathcal{H} = \begin{pmatrix} E_1 & W \\ W & E_2 \end{pmatrix} \quad (8.2)$$

Diagonalizing this matrix gives new eigenvectors, $\begin{pmatrix} 1 \\ 1 \end{pmatrix}$ and $\begin{pmatrix} 1 \\ -1 \end{pmatrix}$ and new eigenvalues given by

$$E_{\pm} = \frac{(E_1 + E_2) \pm \sqrt{(E_1 - E_2)^2 + 4W^2}}{2} \quad (8.3)$$

When the two systems are degenerate, and coupled ($E_1 = E_2$, and $W > 0$) the energies of the normal modes are separated by $2W$. There are many examples of coupled systems which display this type of behavior. For example, the field of cavity quantum electrodynamics is focused on understanding and harnessing coupled interactions between light and elementary excitations—light coupled to electrons (exciton-polaritons), [182] light coupled to phonons (phonon-polariton) [183], light coupled to magnons (magnon-polariton) [184]. Additionally, the field of optomechanics explores light coupled to mesoscopic mechanical vibrations. [185] Despite the upsurge in research on SAW-FMR, observation and quantification of the hybridized magnon-phonon modes remains a challenging task. [186] So far, dynamics of the hybridized modes have not been resolved spectroscopically in relevant structures. [180]

8.3 Analytical Derivation

The theoretical groundwork for the magneto-elastic coupling was laid down in one dimension in ref [180]. They calculate how elastic waves with various strain components couple to the magnetization and how the coupling is influenced by the relative angles between the k -vector of the elastic waves and the magnetization vector. By generating SAWs using interdigital transducers (appropriately modeled in one dimension), they detect the attenuation of the SAWs after travelling under a Ni film. Depending on the magnetization direction of the Ni (controlled with an external field), the SAWs experience different levels of attenuation. The experimental results match the calculations excellently. Additionally, they derive an equation for the

hybridization of the elastic and magnetic modes based off the elastic wave equation. However, they do not see the hybridization of the magnetic and phononic modes experimentally. Because we have a two dimensional vibrating structure, we extend the analysis of ref [180] to two dimensions. Additionally, whereas the results of ref [180] were based off measurements of the elastic system, the results in this chapter are based off measurements on the magnetic system and so the derivation of the coupled dynamics is derived for the magnetic system. First, the equations describing the individual phonon and magnon dynamics are introduced. Then the coupling term which is responsible for the hybridized dynamics is considered. The basis for the derivation as well as the symbolic representation has been adopted from ref. [180]

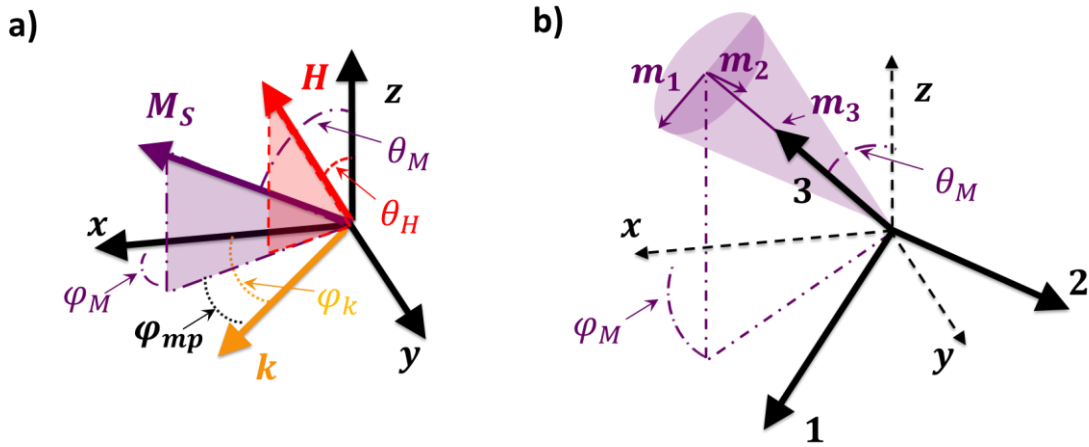


Figure 8.1: (a) In the $\{x, y, z\}$ coordinate system, the x and y directions are defined by the edges of the nanomagnet and the z -direction is the surface normal. The external field H is applied at $\theta_H = 60^\circ$ with respect to the surface normal. This cants the

magnetization vector \mathbf{M}_s out of the plane to an angle θ_M with respect to the surface normal and to an in-plane angle, φ_M from the x-axis. The phononic modes \mathbf{k} are characterized by their mode indices and their in-plane angle, φ_k . φ_{mp} is the in-plane angle between \mathbf{M}_s and \mathbf{k} . **(b)** The magnetization precession can be mapped to the $\{1,2,3\}$ coordinate system defined by the direction of the magnetization vector and the plane of the cone due to the precession of \mathbf{M}_s . \mathbf{m}_3 is along the direction of \mathbf{M}_s at equilibrium, \mathbf{m}_2 lies in the film plane and \mathbf{m}_1 is orthogonal to \mathbf{m}_2 and \mathbf{m}_3 .

8.2.1 2D Elastic Dynamics

The elastic energy density is given by:

$$W = \frac{1}{2} C_{ijkl} \varepsilon_{ij} \varepsilon_{kl} \quad (8.4)$$

Where $i, j = \{x, y, z\}$, C_{ijkl} are the components of the stiffness tensor, $\varepsilon_{ij} = \left(\frac{\partial u_i}{\partial x_j} + \frac{\partial u_j}{\partial x_i} \right) / 2$ are the strain components and u_i is the displacement vector. In order to quantify the phononic eigenmodes the elastic wave equation is solved

$$\rho \frac{\partial^2}{\partial t^2} u_i = \sum_{j=1}^3 \frac{\partial \sigma_{ji}}{\partial x_j} \quad (8.5)$$

Where

$$\sigma_{ik} = \frac{\partial W}{\partial \varepsilon_{ik}} \quad (8.6)$$

is the Cauchy stress tensor and ρ is the density of the material. Due to the small z dimension of the element we can consider the nanomagnet to be two-dimensional in the x and y directions (Fig. 8.1). [187]

We assume a solution of the form $u_{x,y} = u_{x,y}^0 e^{i(k \cdot r - \omega t)}$ where $k^2 = \sqrt{k_x^2 + k_y^2}$, $k_{x,y} = \frac{n_{x,y}\pi}{l_{x,y}}$ and $l_{x,y}$ is the dimension of the nanoelement along the x or y direction. [188] Furthermore, since each phononic mode is degenerate for every value of k_x and k_y we set $k_{x,y} = \frac{k}{\sqrt{2}}$ which ensures $k^2 = k_x^2 + k_y^2$. The in-plane angle of k is $\varphi_k = \tan^{-1}(n_y/n_x)$. Because the system is elastically isotropic, the expansion of the element due to a heat pulse from the laser is the same in the x and y directions such that $u_x^0 = u_y^0$. The system of equations can be solved by setting the determinant equal to zero. This yields the eigenfrequencies for the phononic system given by

$$\omega_{ph}^2 = \frac{(2\lambda + 3\mu)k^2}{2\rho} \quad (8.7)$$

Where the Lamé parameters μ and λ are given by $C_{xxxx} = 2\mu + \lambda$, $C_{xxyy} = \lambda$ and $C_{xyxy} = \mu$. The Lamé parameters can be related to the Young's Modulus, E and the Poisson ratio, ν through $\lambda = E\nu/(1 + \nu)(1 - 2\nu)$ and $\mu = E/(2(1 + \nu))$. [189] Assuming the density of Ni, $\rho = 8900 \text{ kg/m}^3$ and $\nu = 0.31$, [190] the experimentally measured phononic mode frequencies (Fig. 8.2a) were fit to equation (8.7) (Fig. 8.2b) yielding a value for the Young's Modulus of $209_{-29}^{+31} \text{ GPa}$ which matches well with literature values. [190]

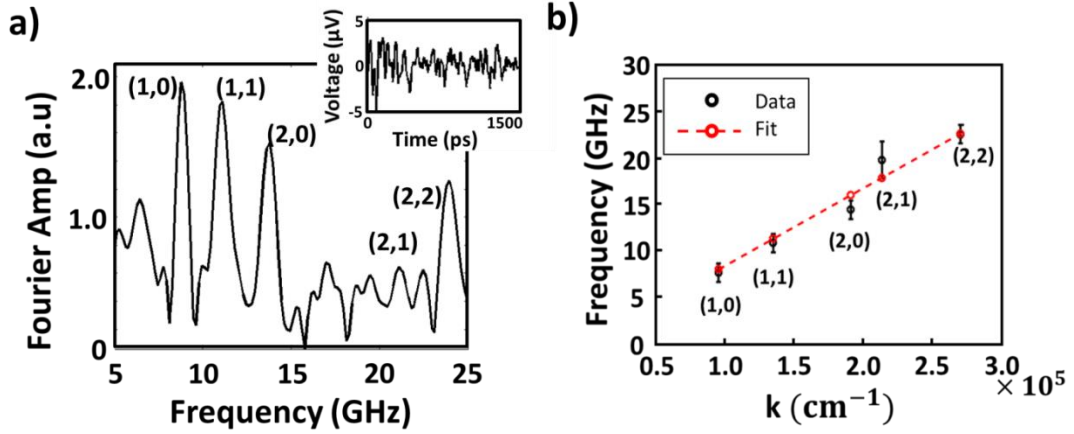


Figure 8.2: (a) DFT spectra from TR-MOKE measurement at 3.6 kOe of the non-magnetic signal. The time trace is shown in the inset. These frequencies do not change with applied field. Although the (2,1) mode is hard to see in this scan due to its much smaller amplitude compared to the other modes, its presence is verified by observing the full colormap of the magnetic signal. (b) Fit of the phononic modes to equation (8.7).

8.2.2 Magnetic Dynamics

The magnetic dynamics in the absence of damping are given by the well known Landau-Lifshitz (LL) equation

$$\frac{\partial \mathbf{m}}{\partial t} = -\gamma \mathbf{m} \times \mathbf{H}_{eff} \quad (8.8)$$

Where γ is the gyromagnetic ratio, $\mathbf{m} = \frac{\mathbf{M}}{M_S}$, M_S is the saturation magnetization and \mathbf{H}_{eff} is the effective field. We neglect the magnetic permeability, μ_0 since $\mu_0 = 1$ in the cgs system. As is customary, a new Cartesian frame of reference is introduced where the 3-axis is along direction of the magnetization vector, the 2-axis is in the film plane, and the 1- axis is orthogonal to the 1 and 2 directions. (Fig 8.1b) The transformation is given by

$$\begin{pmatrix} m_x \\ m_y \\ m_z \end{pmatrix} = \begin{pmatrix} \cos \theta_M \cos \varphi_M & -\sin \varphi_M & \sin \theta_M \cos \varphi_M \\ \cos \theta_M \sin \varphi_M & \cos \varphi_M & \sin \theta_M \sin \varphi_M \\ -\sin \theta_M & 0 & \cos \theta_M \end{pmatrix} \begin{pmatrix} m_1 \\ m_2 \\ m_3 \end{pmatrix} \quad (8.9)$$

The effective field is given by

$$\mathbf{H}_{eff} = -\nabla_m G \quad (8.10)$$

Where $\nabla_m = \left(\frac{\partial}{\partial m_1}, \frac{\partial}{\partial m_2}, \frac{\partial}{\partial m_3} \right)$ and G is the free energy of the magnetic system.

Assuming an infinite thin film, the free energy is given by

$$G = -\mathbf{H} \cdot \mathbf{m} + 2\pi M_S m_z^2 \quad (8.11)$$

Where M_S is the saturation magnetization. Assuming the magnetization is pointed along the equilibrium direction and allowing for small deviations in the 1 and 2 directions, we can Taylor expand the partial derivatives keeping only the linear terms.

This gives the following expression for the effective field

$$\mu_0 \mathbf{H}_{eff} = - \begin{pmatrix} G_{11}m_1 + G_{12}m_2 \\ G_{12}m_1 + G_{22}m_2 \\ G_3 \end{pmatrix} \quad (8.12)$$

Where $G_i = \frac{\partial}{\partial m_i} G \big|_{\mathbf{m}=\mathbf{m}_0}$ and $G_{ij} = \frac{\partial}{\partial m_i \partial m_j} G \big|_{\mathbf{m}=\mathbf{m}_0}$. Assuming $m_{1,2} = m_{1,2}^0 e^{i\omega_M t}$ and $m_3 = 1$, the LL equation (Eq. 8.8) is solved which gives the following system of equations

$$\begin{pmatrix} G_{11} - G_3 & \frac{i\omega_M}{\gamma} \\ -\frac{i\omega_M}{\gamma} & -(G_3) \end{pmatrix} \begin{pmatrix} m_1 \\ m_2 \end{pmatrix} = \begin{pmatrix} 0 \\ 0 \end{pmatrix} \quad (8.13)$$

Setting the determinant equal to zero gives the well known Kittel formula

$$\left(\frac{\omega_M}{\gamma}\right)^2 = (H \cos(\theta_M - \theta_H) - 4\pi M_S \cos^2 \theta_M)(H \cos(\theta_M - \theta_H) - 4\pi M_S \cos 2\theta_M) \quad (8.14)$$

Where the angles θ_M and θ_H are the direction of the magnetization and the applied field with respect to the surface normal. (Fig. 8.1) An identical film was grown next to the nanostructure to characterize the magnetic parameters. The fitted frequencies are shown in figure 8.3 and yielded values of $\gamma = 1.98_{-0.01}^{+0.02} \times 10^7$ rad/(Oe.s) and $M_S = 203_{-16}^{+8}$ emu/cm³.

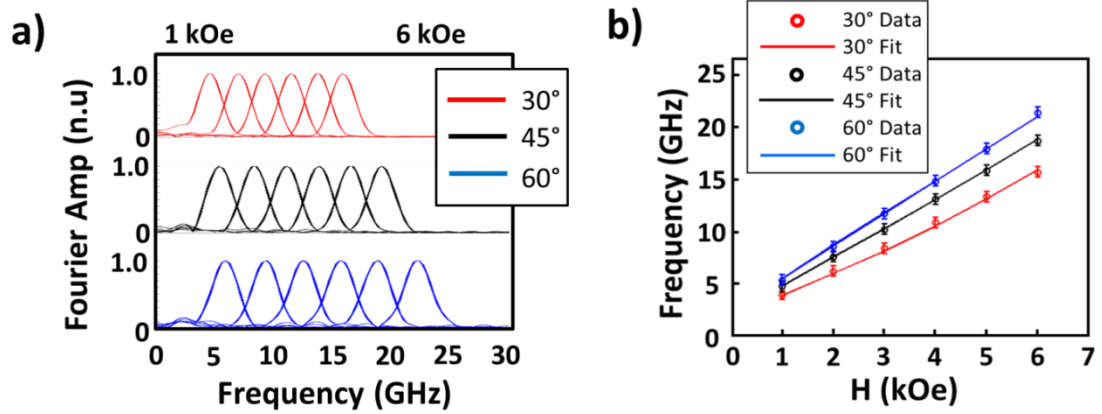


Figure 8.3: (a) DFT spectra of the magnetic channel from TR-MOKE measurements at 1 kOe – 6kOe (left to right) for $\theta_H = 30^\circ$, 45° and 60° (b) Fits of the magnetic resonances to equation (8.14) at $\theta_H = 30^\circ$, 45° and 60° over a range of applied field strengths.

8.2.3 Coupled Dynamics

When magnon-phonon coupling is present, there is an added term to the magnetic free energy as well as the elastic energy density. This term is related to the orientation of the magnetization components with respect to the corresponding dynamic strains. The coupling term is given by

$$G^d = b_1 [\varepsilon_{xx}(x, t)m_x^2 + \varepsilon_{yy}(x, t)m_y^2 + \varepsilon_{zz}(x, t)m_z^2] + 2b_2 [\varepsilon_{xy}(x, t)m_x m_y + \varepsilon_{xz}(x, t)m_x m_z + \varepsilon_{yz}(x, t)m_y m_z] \quad (8.15)$$

The effective field of the magnetic system is now given by $\mathbf{H}_{eff} = -\nabla_m G^{tot}$ where $G^{tot} = G + G^d$. The magnetization components are assumed to follow the spatial profile of the phononic vibrations, so we assume a plane-wave ansatz of the form $m_i = m_i^0 e^{i(\mathbf{k}\cdot\mathbf{r} - \omega t)}$. The system of equations is now

$$\begin{pmatrix} G_{11} - G_3 & \frac{i\omega}{\gamma} \\ -\frac{i\omega}{\gamma} & -(G_3) \end{pmatrix} \begin{pmatrix} m_1 \\ m_2 \end{pmatrix} = \begin{pmatrix} -G_1^d \\ -G_2^d \end{pmatrix} \quad (8.16)$$

Where G_i^d is defined in the same way as G_i . Transforming to the (1,2,3) coordinate system and keeping in mind that the system is two dimensional so that all strain components which have a z-dependence can be neglected gives the following magneto-elastic contribution to the magnetization equations of motion.

$$G_1^d = \left(b_1 w_1 i k_x + \frac{1}{2} b_2 w_2 i k_y \right) u_x + \left(b_1 w_3 i k_y + \frac{1}{2} b_2 w_2 i k_x \right) u_y \quad (8.17)$$

$$G_2^d = \left(-b_1 w_4 i k_x + b_2 w_5 i k_y \right) u_x + \left(b_1 w_4 i k_y + b_2 w_5 i k_x \right) u_y \quad (8.18)$$

$$w_1 = \sin 2\theta_M \cos^2 \varphi_{mp} \quad (8.19)$$

$$w_2 = \sin 2\theta_M \sin 2\varphi_{mp} \quad (8.20)$$

$$w_3 = \sin 2\theta_M \sin^2 \varphi_{mp} \quad (8.21)$$

$$w_4 = \sin \theta_M \sin 2\varphi_{mp} \quad (8.22)$$

$$w_5 = \sin \theta_M \cos 2\varphi_{mp} \quad (8.23)$$

Where φ_{mp} is the in-plane angle between the phononic k-vector and the magnetization vector. In two dimensions the magnetic system is driven by both u_x and u_y displacements. b_1 couples the corresponding magnetization component with normal strains and b_2 with shear strains. Additionally, the coupling depends on the magnitude of the phononic k-vector, k . As can be seen from eq. 8.15 the different strains couple to specific magnetization components. This causes an angular dependence for the coupling which depends on the mutual orientation of \mathbf{M}_s and \mathbf{k} . These dependences are manifested through equations 8.19 - 8.23 which are plotted in figure 8.4. As an example of how to interpret these dependences we consider the first term in equation 8.17. The magnitude of the coupling due to u_x displacements depends on the magneto-elastic coupling term b_1 as well as on the magnitude of the x-component of the phononic k-vector, k_x . Also, there is an angular dependence to the coupling given by w_1 . The angles are defined relative to \mathbf{M}_s and \mathbf{k} . Each term in equations 8.17 and 8.18 has a similar coupling dependence. The different angular dependences are shown in figure 8.4. They all contribute to the total coupling.

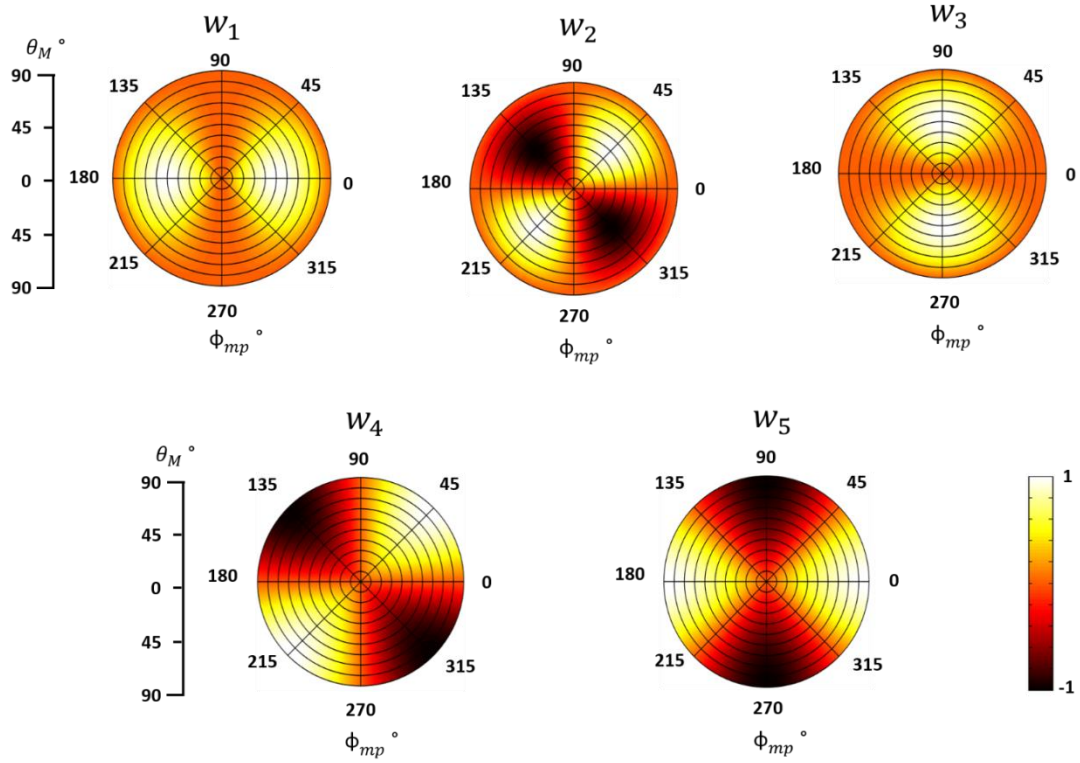


Figure 8.4: Angular dependences of the various trigonometric terms (8.19-8.23) governing the coupling given by equations 8.17 and 8.18.

Additionally, $M_S G^d$ is added to the elastic free energy (Eq. 8.4). This magneto-elastic energy term modifies the stress tensor (Eq. 8.7) due to the precession of the magnetization. Solving equation (8.5) with the modified stress tensor gives elastic equations for the displacement which depend on the magnetization components

$$u_x = \frac{i(2M_S b_1 k_x w_1 + 4M_S b_2 k_y w_2)m_1 - i(2M_S b_1 k_x w_4 - 2M_S b_2 k_y w_5)m_2}{(C_{xxxx}k_x^2 + C_{xxyy}k_x k_y + \frac{C_{xyxy}}{2}(k_y^2 + k_x k_y) - \rho\omega^2)} \quad (8.24)$$

$$u_y = \frac{i(2M_S b_1 k_y w_3 + 4M_S b_2 k_x w_2)m_1 + i(2M_S b_1 k_y w_4 + 2M_S b_2 k_x w_5)m_2}{\left(\frac{C_{xyxy}}{2}(k_x k_y + k_x^2) + C_{yyyy}k_y^2 + C_{xxyy}k_x k_y - \rho\omega^2\right)} \quad (8.25)$$

Plugging equations (8.24) and (8.25) into equations (8.17) and (8.18) and combining like terms in equation (8.16) gives a new system of equations for the precession of the magnetization with only the variables m_1 and m_2 . Solving this system of equations by setting the determinant equal to zero and factoring gives the following

$$(\omega^2 - \omega_{ph}^2)\{(\omega^2 - \omega_M^2)(\omega^2 - \omega_{ph}^2) - \omega_c^4\} = 0 \quad (8.26)$$

Where

$$\omega_c^4 = \frac{\gamma M_S}{\rho}(\omega_1 C_2 + \omega_2 C_1)k^2 \quad (8.27)$$

$$\omega_1 = \gamma(G_{11} - G_3) \quad (8.28)$$

$$\omega_2 = \gamma(-G_3) \quad (8.29)$$

$$C_1 = b_1^2 (\cos^2 \varphi_k w_1^2 + \sin^2 \varphi_k w_3^2) + \frac{3}{4} b_1 b_2 \sin 2\varphi_k w_2 (w_1 + w_3) + \frac{1}{2} b_2^2 w_2^2 \quad (8.30)$$

$$C_2 = b_1^2 w_4^2 + 2b_2^2 w_5^2 \quad (8.31)$$

Equation (8.26) results in three solutions. One is the phononic resonance and the other two are attributed to the hybridized magnon-phonon.

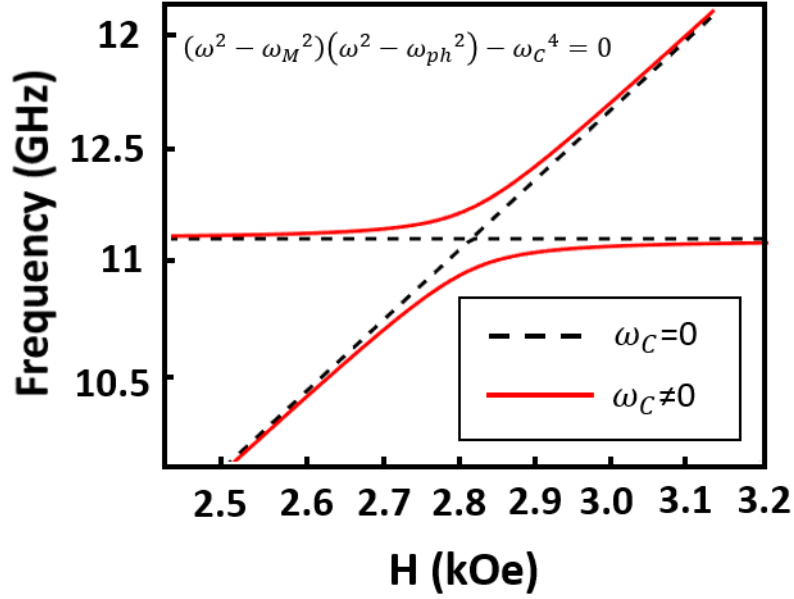


Figure 8.5: Example of solution to the magnon-phonon part of equation (8.26).

When $\omega_C = 0$, the two solutions are attributed to the phononic and magnonic resonances. If $\omega_C \neq 0$, then the two systems are coupled, and close to the region where the magnon and phonon modes are degenerate the modes split and the two solutions have both magnon and phonon character.

8.4 Magnon-Phonon Anti-Crossings

The magnon-phonon dynamics of the nanomagnet were measured using a two-color TR-MOKE setup using a balanced photodiode detection scheme which enables us to measure the magnetic system and the non-magnetic (phononic) system at the same time [191] When the pump pulse hits the nanomagnet, (Fig 8.6a) the energy is absorbed by the electron system which then equilibrates with the phonon systems

within a few picoseconds according to the two-temperature model. [192] This excites the spin and phonon systems concurrently within the nanomagnet (Fig. 8.6b).

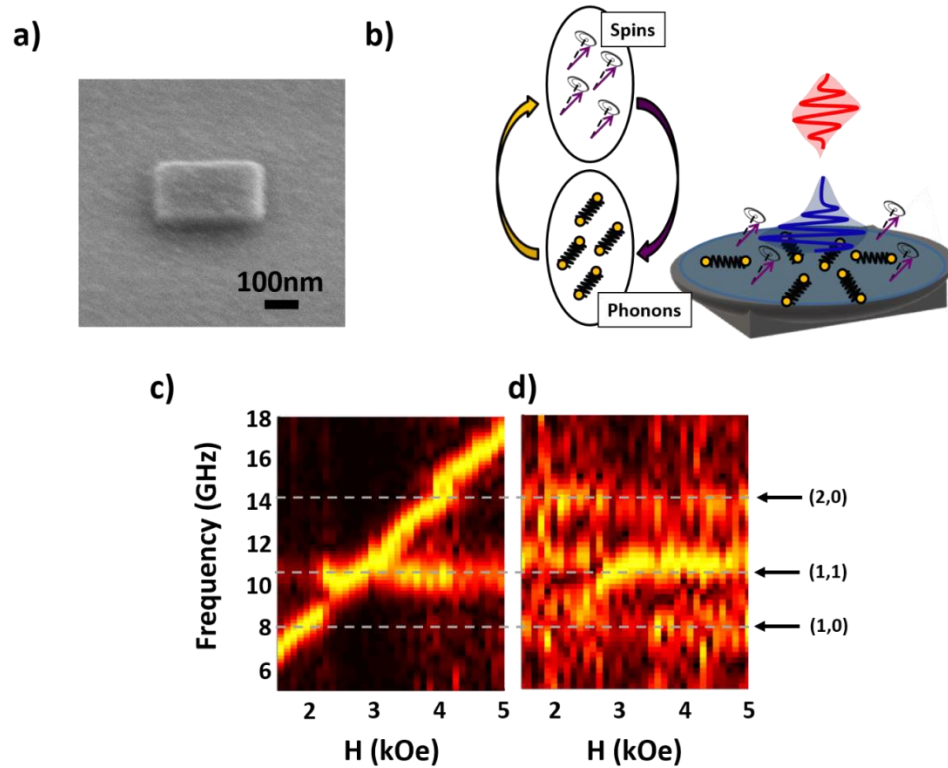


Figure 8.6: (a) Scanning electron microscope image of 330nm x 330nm x 30nm Ni nanomagnet. (b) When the pump pulse (400nm) irradiates the sample, the deposited heat causes the element to thermally expand, which causes the element to vibrate at eigenfrequencies determined by the geometry and material properties. Additionally, the heat perturbs the magnetization causing the spins to precess around the effective field. Due to magnetostriction, the spin and phonon systems are coupled to one another. A probe pulse (800nm) which is delayed in time monitors the dynamics

following excitation. **(c)** Fourier amplitude spectra normalized for each field bin of the magnetic and **(d)** the non-magnetic detection channels. The arrows and dotted lines are indicators of the phononic eigenfrequencies. The positions of these frequencies match in the magnetic and non-magnetic spectra.

In Figure 8.6, colormaps from the magnetic (c) and non-magnetic (d) channels are displayed. Each field represents a different TR-MOKE scan that has been transformed into the frequency domain using an FFT algorithm. The colors represent the frequency components present at that field. In order to see the frequency variation more clearly, the frequency amplitude was normalized for each field bin. The magnetic channel displays a dominant frequency which changes as the external field changes. (Fig. 8.6c) Additionally, there are field independent modes which arise due to the coupling to the phononic system. Confirmation of this is seen in the non-magnetic spectra (Fig. 8.6d), where the frequencies are all H-field independent and match the positions of the magnetic channel's field independent frequencies. These spectra look similar to those observed in patterned arrays. [193] However, in the single isolated nanomagnet the coupling between the two systems is stronger and more direct. It arises within the element itself rather than with surface acoustic waves located in the substrate, leading to qualitatively different behavior around the crossovers between resonances. (Fig. 8.7)

There is a narrow region in the non-magnetic spectrum (Fig. 8.6d) around the (1,1) crossover (~ 3 kOe) that appears to have some field dependence. This could be attributed to a few possibilities. First the (1,1) mode has a larger resonance and lifetime than the (2,0) mode. This causes the signal to be enhanced in the (1,1) crossover and so the magnetic system's influence on the phonon system may be more obvious in the non-magnetic channel due to the higher signals at the (1,1) crossover. Alternatively, there may be some leakage from the magnetic signal into the non-magnetic signal due to the transverse Kerr effect (TKE). As discussed in chapter 4, the TKE is sensitive to the component of the magnetization that is perpendicular to the plane of incidence and affects the reflectivity (non-magnetic) of the probe beam.

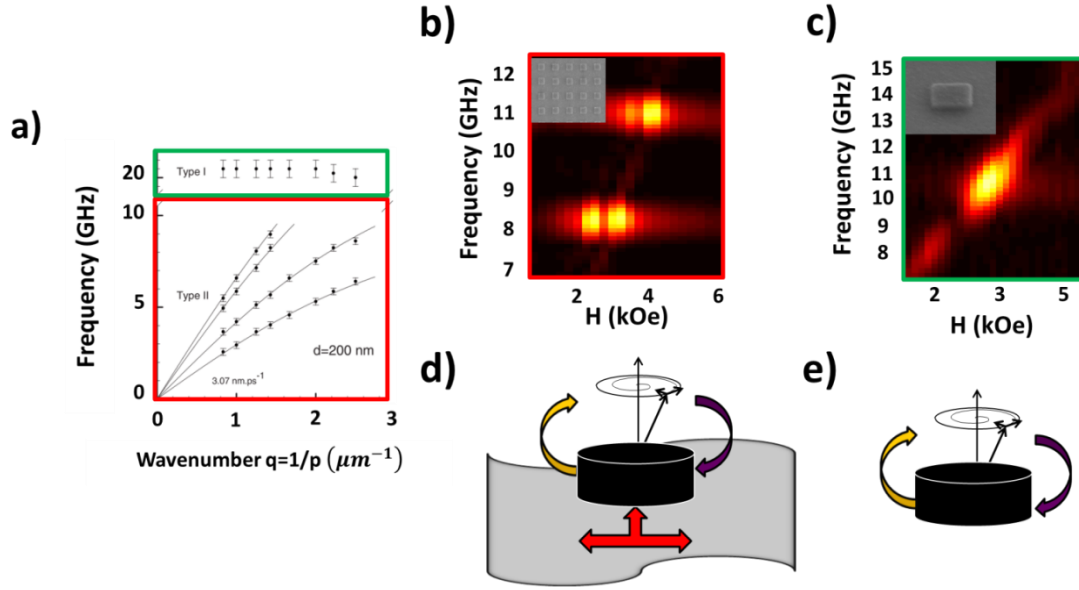


Figure 8.7: (a) Different vibrational modes measured in arrays of 200nm Al nanomagnets. Type II modes (red outline) depend on the pitch of the arrays and Type I are the intrinsic vibrations of the elements themselves and are independent of the pitch. Taken from [194]. (b) The crossings in periodic arrays (SEM in inset) discussed in chapter 7 are due to type II modes (c) whereas the crossings in an isolated nanomagnet (SEM in inset) discussed in this chapter are due to type I modes. (d) The coupling for Type II modes is more akin to a forced oscillation since the elastic energy is dominated by the SAW vibrations (red arrow). (e) With type I modes the coupling is more direct, occurring within the element itself.

Changing the external field modifies the frequency of the magnons so they can be brought into resonance with the various phononic modes. The crossings are

displayed in Figure 8.8a and 8.8b for the (1,1) and (2,0) crossings, respectively. The Fourier spectra exhibit two clear peaks at each field value at and around the crossing field. These two frequencies are attributed to the hybridization of the magnon and phonon eigenstates. In this region, the modes do not have a specific magnon or phonon character but rather exist in both states.

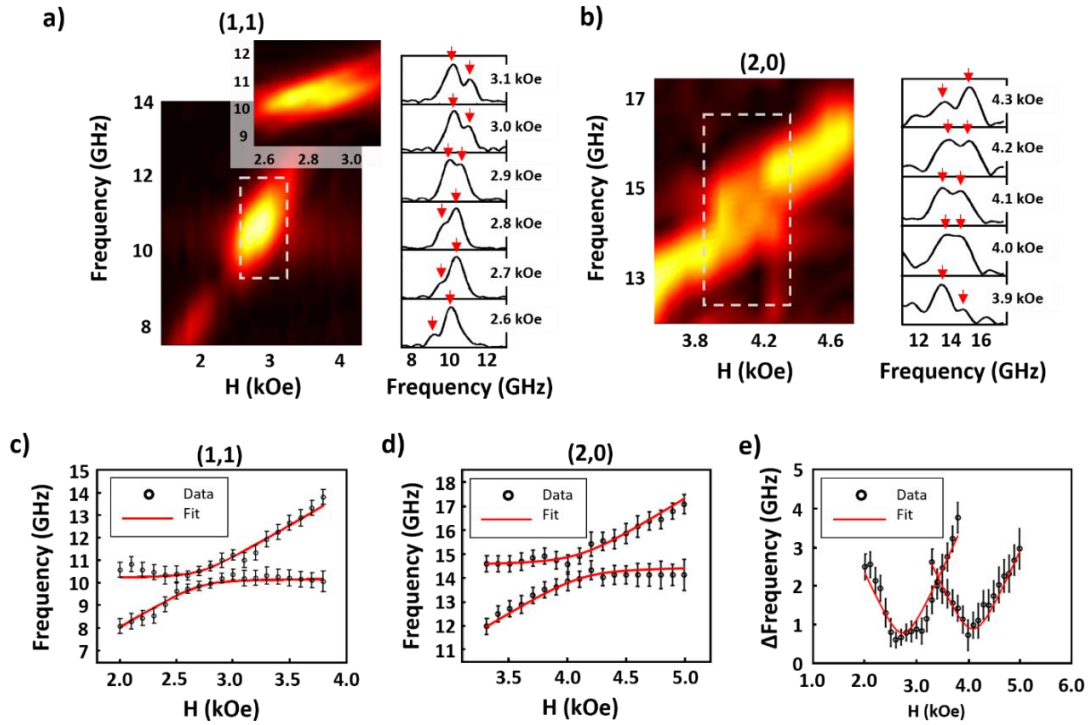


Figure 8.8: Close-ups of the Fourier amplitude spectra exhibiting anti-crossings for the (a) (1,1) and (b) (2,0) modes. The amplitudes are normalized within each figure. Next to each colormap are the Fourier spectra obtained from the TR-MOKE time trace for the range of applied fields selected by the dotted gray box in the colormap.

The two peaks are indicated by the red arrows. The inset in (a) is the boxed region Fourier transformed over a longer time length to display the two modes more clearly. (c) Simultaneous fits of equation (8.26) to the frequencies of the (1,1) and (d) (2,0) modes. The error in the frequencies is the FFT resolution obtained from the time duration of each frequency component in the signal. (e) Mode splitting energy of the (1,1) and (2,0) crossings.

The frequency peaks were selected from the (1,1) and (2,0) modes and fit simultaneously using equation (8.26) which shows an excellent match between data and fits (Fig. 8.8c-d). The parameters γ , M_S and E from the elastic and magnetic fits were used as initial fitting parameters and allowed to vary within their respective errors. Because the nanomagnet is polycrystalline, b_1 and b_2 are equal, and fitting only one coupling parameter, b_1 , was necessary. Additionally, in order to take into consideration the in-plane magnetization distribution within the nanomagnet, as well as the inevitable slight experimental disorientation of the magnetic field, φ_{mp} was also allowed to vary. The fitted value of b_1 was $40 \pm 4 \times 10^4$ Oe. Using $b_1 = -\frac{3\lambda_S c_{44}}{M_S}$, a polycrystalline magnetostriction value of $\lambda_S = -34 \pm 4 \times 10^{-6}$ was obtained [195] which is in agreement with the bulk value [196] of -32×10^{-6} and in reasonable agreement with the value measured in Ni thin films [197]. Figure 8.8e shows the mode splitting corresponding to the coupling strength of the hybridized modes. . We find for the (1,1) mode $\Delta f_{min} = 0.76^{+0.08}_{-0.08}$ GHz and for the (2,0) mode

$\Delta f_{min} = 0.85^{+0.08}_{-0.08}$ GHz. The error is the standard deviation found using a Monte Carlo error propagation scheme by randomly varying the frequencies within the FFT resolution and then fitting them to Equation 8.26. The anticrossing is empirical evidence of the coupling between the magnon and phonon systems and has not been observed in other experiments utilizing acoustic waves as an excitation mechanism.[172,180]

8.4.1 Tuning the Coupling into the Strong Coupling Regime

As evidenced through C_1 and C_2 , the splitting energy depends on the type of strains present (normal, b_1 ; shear, b_2) and is a function of φ_{mp} and θ_M . Additionally, these angular dependences are weighted by the magnetic energy terms ω_1 and ω_2 which depend on M_S and H and limit the range of experimentally accessible angles. As a demonstration of the dependence on the in-plane angle of the magnetization and the phononic k-vector, we focus on the (2,0) mode which is characterized by normal strains ($b_2 = 0$). When both strains are present (depending on the respective amounts), the in-plane dependence disappears due to the orthogonality of the b_1 and b_2 in-plane angular functions.

Taking this into consideration, we calculate the weighted coupling strength, $(\omega_1 C_2 + \omega_2 C_1)$ for our particular experimental configuration and plot it as a function of H and φ_{mp} (Fig. 8.9a). The angle of the magnetization, θ_M , from the surface normal is a function of the applied field configuration. At an applied field angle of $\theta_H = 60^\circ$, figure 8.9b shows the angles of the magnetization θ_M for the range of applied fields

used in the experiment. This H - φ_{mp} dependence is further modified by the geometric and material properties ρ, γ and M_S which dictate the field at which the two resonances cross. In the original configuration (the applied field along the x direction), the (2,0) crossing is shown as a star on the H - φ_{mp} plot (Fig. 8.9a). By rotating the nanomagnet in-plane, we can change φ_{mp} , which changes the coupling strength (moving along the dotted line in figure 8.9a) and is maximum at an angle of 45° . The calculated and experimentally measured minimum frequency splitting vs. φ_{mp} are shown in figure 8.9c. The data match the calculated results quite well. Figure 8.9d shows the configuration and obtained spectra with the magnetization oriented parallel to the (2,0) mode, and figure 8.9e shows the case where the magnetization is oriented 45° to the (2,0) mode. For the 45° spectrum, φ_{mp} was fit to equation (8.26) using the previously obtained material parameters as constants. The value obtained was $\varphi_{mp} = 50^\circ$, a very close match. More importantly, from the spectra in figure 8.9e it is evident that the splitting increases for $\varphi_{mp} = 45^\circ$; the bandgap starts to emerge in the spectrum. The frequency splitting increases to $\Delta f_{min} = 1.41_{-0.16}^{+0.16}$ GHz, a 66% increase from the $\varphi_{mp} = 0^\circ$ case.

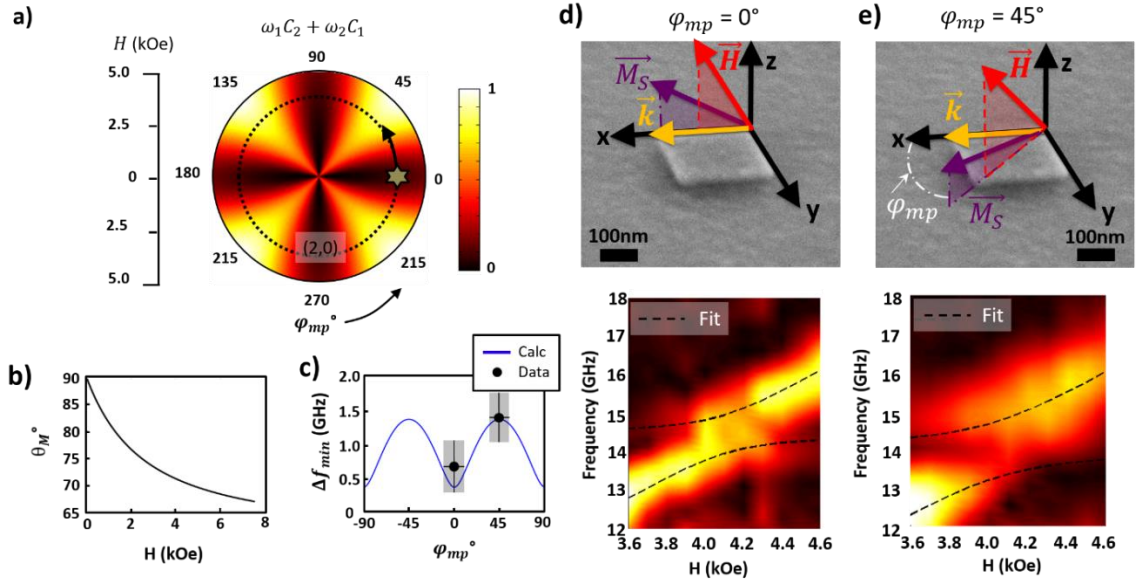


Figure 8.9: (a) Normalized H vs. ϕ_{mp} plot of the weighted angular coupling term ($\omega_1 C_2 + \omega_2 C_1$). (b) Due to the experimental geometry, only certain out of plane angles of the magnetization θ_M were accessible for the range of applied fields employed in the experiment. (c) The calculated frequency splitting as a function of ϕ_{mp} (dotted line in fig 8.9a) as well as the minimum frequency splitting taken from the data. The y-error was calculated from the FFT resolution. For the x-error a resolution of $\pm 10^\circ$ was assumed for the in-plane positioning of the nanomagnet. (d) The experimental configuration and the measured spectra with fits to equation (8.26) when the magnetization is oriented along the edge of the square so that it is parallel with the (2,0) phononic mode and (e) after rotating the nanoelement so that $\phi_{mp} = 45^\circ$. The spectrum shows an increase in the splitting of the two modes and the fit matches the rotation within $\pm 10^\circ$.

8.4.2 Loss Rates and Cooperativity

While the anti-crossing is empirical evidence of the coupling between the two systems, it is necessary to quantify the strength of the coupling. The coupling regime is determined by comparing the rate at which energy is exchanged between the oscillators versus the rate at which the individual oscillators lose energy. Since the linewidth of a Lorentzian is related to the loss rate and the splitting of the modes is proportional to the coupling rate, this comparison is typically done in the frequency domain by comparing the linewidths of the individual resonances to the splitting. Whether the loss rate of the individual systems is equal to the full width at half maximum or the half width at half maximum of the Lorentzian depends on the mathematical model being considered. (Fig. 8.10) In our case the loss rates cannot be taken directly from the linewidth of the FFT spectra since they are artificially broadened due to the finite duration of the signal in the time domain as discussed in chapter 4. [198]

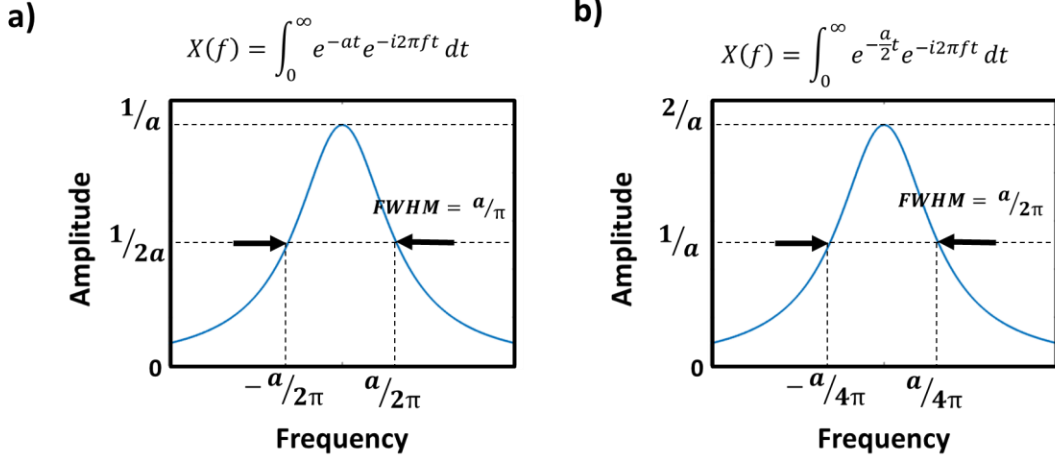


Figure 8.10: A decaying exponential in the time domain has a Fourier transform of a Lorentzian in the frequency domain. Dependences on the amplitude and full width at half max (FWHM) of the Lorentzians depend on the model of the damped exponential used. Note that the Fourier transform starts at zero corresponding to a real signal. (a) The Lorentzian of an exponential given by a loss rate a has the an amplitude $1/a$ and a FWHM given by 2 times the loss rate, $2(a/2\pi)$. (b) The Lorentzian of an exponential given by a loss rate $a/2$ has an amplitude $2/a$ and a FWHM equal to the loss rate, $(a/2\pi)$. Note that the factor of 2π is used in the frequency domain order to give the values in Hz.

In order to determine the coupling regime of the magnon-phonon resonances, we analyze the loss rates of the different systems in the time domain and compare them to the coupling rate. We employ a least squares curve fitting algorithm to the decaying sinusoids in the TR-MOKE signals [199]

$$S(t) = \sum_i^N A_i \cos(\omega_i t + \varphi_i) e^{-\kappa_i t} \quad (8.32)$$

Where S is the signal, A_i is the amplitude, ω_i is the angular frequency, φ_i is the phase, κ_i is the loss rate and N is the number of oscillations present at the applied field. We extract the coupling rate from the splitting of the modes in the frequency domain in units of Hz. Since the loss rate κ_i , has units $\text{rad} \cdot \text{s}^{-1}$ in the frequency domain, in order to compare the loss rates extracted from the time domain fits to the splitting extracted from the frequency domain we divide κ_i by a factor of 2π to obtain a value in Hz. [200]

The field-dependent loss rate for the magnetic signal can be approximated by $\kappa_M = \alpha_e f$, where f is the frequency and α_e is the effective damping. [199] $\alpha_e = 0.038_{-0.03}^{+0.04}$, and was extracted at 4.6 kOe, away from the crossing point, so that the mode is predominantly magnetic in character. This value is consistent with previous measurements we have made on the damping in Ni.[176] The loss rate of the phononic system, κ_P , is extracted from the non-magnetic signal.

The loss rates are $\kappa_M = 0.41_{-0.03}^{+0.05}$ GHz for the magnetic system at the (1,1) crossover (crossing 1) and $\kappa_M = 0.53_{-0.04}^{+0.05}$ GHz for the magnetic system at the (2,0) crossover (crossing 2). $\kappa_P = 0.31_{-0.07}^{+0.12}$ GHz for the (1,1) phononic mode and $\kappa_P = 0.47_{-0.07}^{+0.12}$ GHz for the (2,0) phononic mode. The coupling rate is given by half of the mode splitting, $\Gamma_c = \Delta f_{\min}/2$. This allows us to calculate the cooperativity, a dimensionless parameter that is used in order to determine the strength of the coupling.

$$C = \frac{\Gamma_c^2}{\kappa_M \kappa_P} \quad (8.33)$$

When $C < 0.1$ the system is weakly coupled, when $0.1 < C < 1$ the system is in the intermediate coupling regime, and when $1 < C$ the system is strongly coupled. [201] For crossing 1, $C = 1.14^{+0.48}_{-0.30}$ and for the crossing 2, $C = 0.74^{+0.21}_{-0.14}$. Keeping in mind the error, this places these two crossings in the intermediate coupling regime. [201]

For the (2,0) crossing oriented at 45° (crossing 3), the damping was also measured at 4.6 kOe and is $\alpha_e = 0.047^{+0.03}_{-0.03}$ which corresponds to $\kappa_M = 0.65^{+0.05}_{-0.04}$. At this crossing $\Gamma_c > \kappa_M, \kappa_P$, which translates into a cooperativity of $C = 1.65^{+0.48}_{-0.32}$, placing crossing 3 in the strong coupling regime within error ($C > 1$). The loss rates and Cooperativities are displayed for clarity in Table 1. Therefore, by reorienting the magnetization vector using an externally applied magnetic field, we were able to increase the coupling from the intermediate into the strong coupling regime.

Crossing	Γ_c (GHz)	κ_M (GHz)	κ_P (GHz)	C
1: (1,1)	$0.38^{+0.04}_{-0.04}$	$0.41^{+0.05}_{-0.03}$	$0.31^{+0.12}_{-0.07}$	$1.14^{+0.48}_{-0.30}$
2: (2,0), 0°	$0.43^{+0.04}_{-0.04}$	$0.53^{+0.05}_{-0.04}$	$0.47^{+0.12}_{-0.07}$	$0.74^{+0.21}_{-0.14}$
3: (2,0), 45°	$0.71^{+0.08}_{-0.08}$	$0.65^{+0.05}_{-0.04}$	$0.47^{+0.12}_{-0.07}$	$1.65^{+0.48}_{-0.32}$

Table 8.1: Coupling, Loss rates and cooperativities for the different crossings.

The various coupling regimes can be qualitatively verified by observation of the Fourier spectra at the crossover points. (Fig. 8.11) For crossing 1 and crossing 2 we see the two peaks just starting to become discernable with crossing 1 being slightly more visible. The Fourier spectra of crossing 3 at the crossing point shows two clearly discernable peaks.

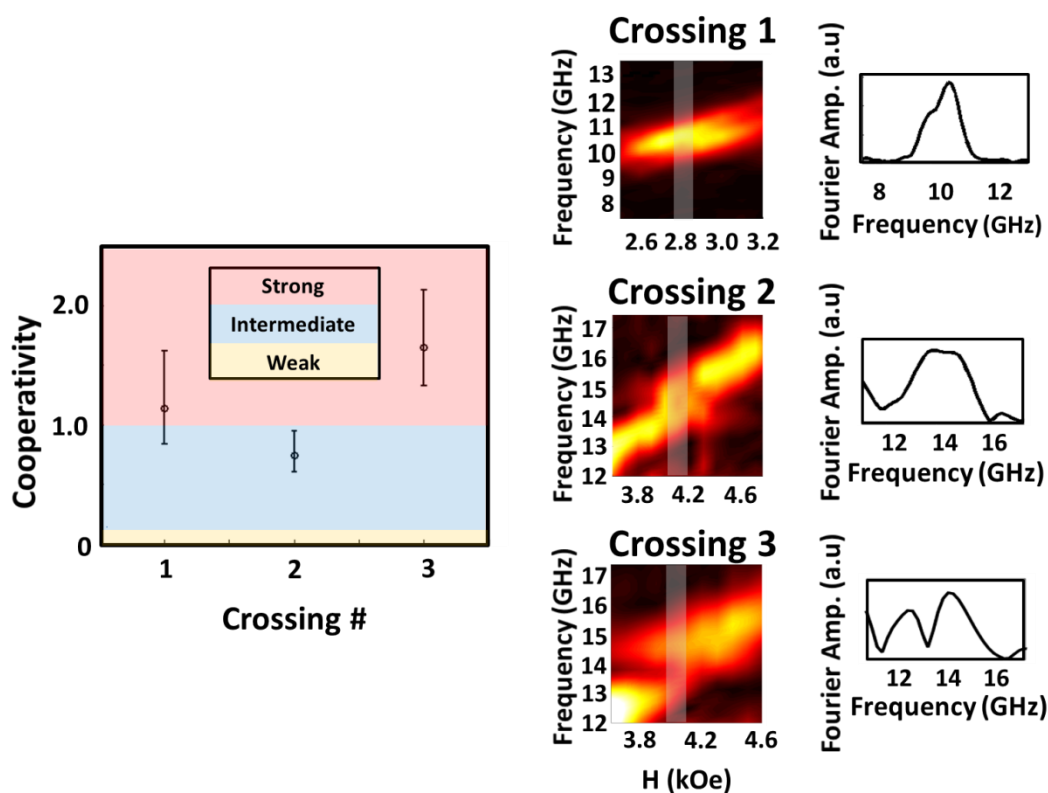


Figure 8.11: Cooperativities of the 3 crossings. The first two are within the intermediate coupling regime while the 3rd is in the strong coupling regime. The DFT spectra at the crossover points are shown next to the colormaps.

As an additional analysis in order to corroborate these results, we present a discussion of the DFT spectra. We use a peakfitting algorithm to fit a sum of two Lorentzians (given by Fig. 8.10a) to the peaks at the crossover points. (Fig. 8.12) We get an upper limit for the loss rate by looking at the larger of the two FWHMs. The loss rate extracted in this manner, κ_{FWHM} , is then given by half of the FWHM. Because the time widow of the scans is 1,500 ps and we use a Hamming window in the time domain in order to mitigate the effect of the sidelobes of the Sinc function (due to finite time window) in the frequency domain, we estimate that the fitted FWHM should be broadened by $\sim 20\%$. Adjusting for this broadening, we get, $\kappa_{FWHM,adj}$. The results are in Table 2. They show very good agreement with the loss rates of the different systems extracted through the time domain analysis above. However, we reiterate that inferences concerning the loss rates based on the DFT linewidths are complicated. As mentioned in chapter 4, the time window of the signal is responsible for increasing the linewidth of the DFT spectra.

Crossing	Γ_c	κ_M	κ_P	κ_{FWHM}	$\kappa_{FWHM,adj}$
1: (1,1)	$0.38^{+0.04}_{-0.04}$	$0.41^{+0.05}_{-0.03}$	$0.31^{+0.12}_{-0.07}$	$0.39^{+0.02}_{-0.02}$	$0.32^{+0.02}_{-0.02}$
2: (2,0), 0°	$0.43^{+0.04}_{-0.04}$	$0.53^{+0.05}_{-0.04}$	$0.47^{+0.12}_{-0.07}$	$0.59^{+0.05}_{-0.05}$	$0.48^{+0.05}_{-0.05}$
3: (2,0), 45°	$0.71^{+0.08}_{-0.08}$	$0.65^{+0.05}_{-0.04}$	$0.47^{+0.12}_{-0.07}$	$0.63^{+0.06}_{-0.06}$	$0.52^{+0.06}_{-0.06}$

Table 8.2: Coupling and loss rates for the different crossings extracted from the time domain fits and from the DFT spectra (all values in GHz).

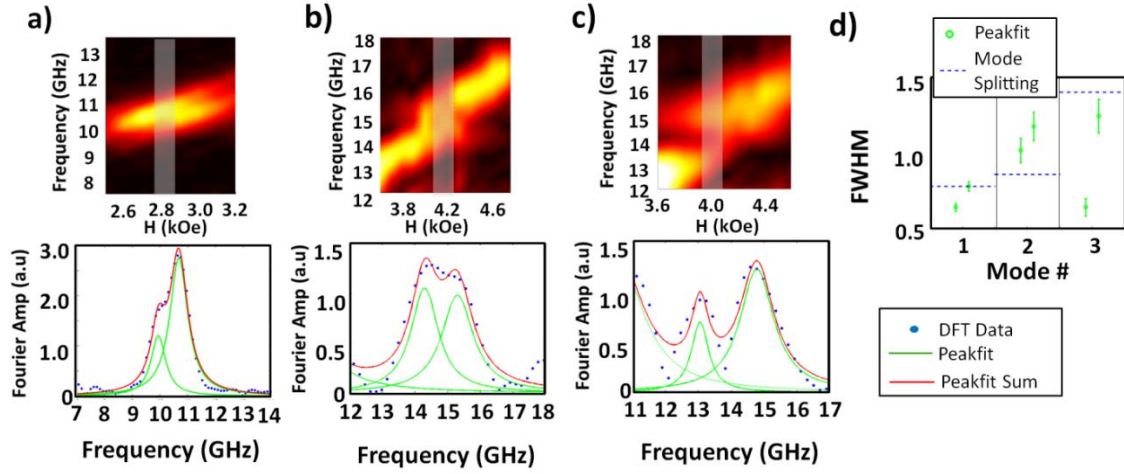


Figure 8.12: Crossover points and peakfit data for (a) the (1,1) crossover, (b) the (2,0) crossover at 0° and (c) the (2,0) crossover at 45° . (d) The FWHM of the peaks and the mode splitting for the different crossings.

8.5 Conclusion

Hybridized magnon-phonon dynamics were measured optically for the first time by tuning the magnonic resonance to that of the intrinsic phononic vibrations of an isolated square nanomagnet. The hybridized modes were clearly resolved in the Fourier transforms of the time-dependent magneto-optic signals at resonance. A two-dimensional equation describing the dynamics was derived which fit the data with high accuracy. Additionally, the coupling was shown to depend on the orientation of the magnetization vector and the phononic vector as predicted by the theory. By tuning the direction of the applied field we were able to enhance the coupling so that the system entered into the strong coupling regime. The ability to uniquely tune the

energy splitting of the hybridized mode using various external degrees of freedom is attractive from the perspective of reconfigurable magnonic devices. [202,203] Additionally, this magnetomechanical system provides a novel means of studying the dynamics of coupled quantum systems which may aid in the development of more efficient transducers between phononic and magnonic systems.

CHAPTER 9: FUTURE OF INFORMATION TECHNOLOGY AND SUMMARY

“Somewhere, something incredible is waiting to be known”

—*Carl Sagan*

The information contained in the thesis is meant to add to the collective effort to advance information technology. This has been an ongoing effort since humans began organizing into groups, with increasing levels of information technology mirroring the increasing complexity of civilizations. Today we are at the forefront of a new revolution. Being an information revolution, the changes to information technology that will occur in the future will most likely be beyond what we are able to imagine. The field of Quantum Information Science seeks to alter the landscape of information technology at a theoretically unprecedented scale. This will require novel storage media, novel algorithms and an entirely new way of conceptualizing the concept of a bit. Classical bits made up of 0's and 1's will be replaced by qubits, superpositions of 0's and 1's which are possible due to the spooky laws of quantum mechanics. This is extremely exciting, however the scientific challenges to achieving this new age of information technology are monumental and the quantum computing of the future may never occur. We are experiencing drastic changes in societies adjusting to a new age of global civilization. The effects from the Industrial revolution are beginning to

be felt which are raising environmental concerns that current technologies are going to be required to address. Therefore, improving existing technologies to respond to these immediate concerns is a necessary prerequisite for a quantum age of computing to occur.

Magnetic materials have been a dominant storage medium for the past 100 years. Additionally, research on magnetic materials has opened up a wealth of fundamental knowledge of condensed matter systems. Femtosecond laser systems have accelerated the understanding of carrier dynamics in these systems as well as providing novel methods of manipulation of the magnetism. The confluence of femtosecond spectroscopy and ultrafast magnetism opens up the opportunity to manipulate magnetic materials at extraordinarily fast timescales. This could allow magnetic materials to be used for a diverse range of technological applications.

In chapters 2-4 we discussed the physics underlying magnetism in condensed matter systems as well the physics concerning the interaction of these systems with ultrashort laser pulses. We then discussed Time-Resolved Magneto-Optical Kerr Effect microscopy (TR-MOKE), in which the magnetization dynamics can be probed at sub-picosecond timescales. TR-MOKE allowed us to characterize critical magnetic parameters. We demonstrated this characterization ability in chapter 5. Additionally, we introduced an all-optical technique to manipulate the magnetism in multilayer magnetic structures. By selectively enhancing or quenching the magnetic dynamics these structures could be characterized in a novel manner.

Another method of manipulating the spins can be achieved utilizing magnetoelastic effects which arise due to spin-orbit coupling. Magnetoelastic effects may be useful in the design of more energy efficient storage devices. Additionally, understanding magnetoelastic effects in technologically relevant devices such as nanomagnetic arrays and single nanomagnetic bits is critical from a device design perspective. In chapter 7 we discussed the coupling of surface acoustic waves (SAW) to the magnetization dynamics in nanomagnetic arrays. TR-MOKE provided a convenient means of studying the magnetoelastic interactions in these systems due to the ability of the pump pulse to initiate dynamics in both the magnetic and elastic systems concurrently. We showed how the magnetoelastic effects in the arrays can be mitigated geometrically, by randomizing the distribution of the elements, and how the magnetoelastic coupling could be used to determine the intrinsic damping of the array.

Chapter 8 took the results of Chapter 7 a step further and focused on the magnetoelastic coupling which occurs in an isolated nanomagnet. In this system, the elastic vibrations do not come from SAWs in the substrate, but from the intrinsic vibrations of the element. The coupling is, therefore, more direct. By focusing on the regions where the elastic and magnetic modes have the same frequency, we were able to spectroscopically resolve the hybridization of the magnon and phonon modes. This was the first time that the anticrossing of the hybridized mode frequencies, a characteristic of the magnon-phonon hybridization, was observed in structures of this type utilizing this technique. Additionally, we derived a 2-dimensional equation

which described the dynamics and enabled us to successfully characterize the magnetoelastic coupling constant. Furthermore, the dependence of the coupling strength on the mutual orientation of the phononic \mathbf{k} -vector and the magnetization vector was demonstrated and matched the results excellently. By tuning the angle between the phononic \mathbf{k} -vector and the magnetization vector we were able to tune the magnon-phonon coupling into the strong coupling regime.

“In the beginner’s mind there are many possibilities, but in the expert’s there are few”

—Shunryu Suzuki

References

- [1] J. Clottes. “Chauvet-Pont d’Arc.” *Encyclopedia Britannica*. Encyclopedia Britannica Inc. Web. Apr. 2019.
- [2] X. Li, G. Harbottle, J. Zhang, and C. Wang, *Antiquity*, **77**, 31-41 (2004).
- [3] S. Odenwalk, “Who was the First Named Human?” (2017). Retrieved Apr. 8, 2019, from https://www.huffpost.com/entry/who-was-the-first-named-h_b_5679829?m=false
- [4] D. Biggs. *Inscriptions from Tell Abū Šalābīkh*. Oriental Institute Publications. University of Chicago Press. ISBN 0-226-62202-9. (1974).
- [5] J. Naveh, “The Origin of the Greek Alphabet.” (Eds.): D. Kerckhove and C. Lumsden. *The Alphabet and the Brain*, 84-91, Springer (1988).
- [6] E. Eisenstein, *The Printing Press as an Agent of Change*, Cambridge University Press, (1980).
- [7] J-I. Nishizawa, *Proceedings of the IEEE*, **96**, 10, (2008).
- [8] J. Delve. *IEEE Annals of the History of Computing*, **29**, 4, 98–102 (2007).
- [9] V. Shilov, S. Silantiev. “Machines à Comparer les Idées’ of Semen Korsakov: First Step Towards AI”. Eds: A. Tatnall, C. Leslie. Springer. IFIP Advances in Information and Communication Technology, AICT-491, 71-86, (2016).
- [10] D. Speliotis, *J. Magn. Magn. Mater*, **193**, 1-3, 29-35, (1999).
- [11] D. Jiles, *Introduction to Magnetism and Magnetic Materials* CRC Press, (2016).
- [12] E.A. Dobisz, Z.Z. Bandic, T.W. Wu, and T. Albrecht, *Proceedings of the IEEE*, **96**, 11, (2008).
- [13] D. Weller, and A. Moser, *IEEE Trans. Magn*, **35**, 6 (1999).
- [14] D.A. Thompson and J. S. Best, “the future of magnetic data storage technology” *IBM J. Res. Develop*, **44**, 3 (2000).

- [15] M. N. Baibich, J. M. Broto, A. Fert, F. Nguyen Van Dau, F. Petroff, P. Etienne, G. Creuzet, A. Friederich, and J. Chazelas, *Phys. Rev. Lett.*, **61**, 2472 (1988).
- [16] J. Heber, *Nat. Phys.*, **4**, S16–S17 (2008).
- [17] C.A. Ross, *Annu. Rev. Mater. Res.*, **31**, 203–35 (2001).
- [18] C. Volger, C. Abert, F. Bruckner, D. Suess, and D. Praetorius, *Appl. Phys. Lett.*, **108**, 102406 (2016).
- [19] C. D. Stanciu, F. Hansteen, A. V. Kimel, A. Kirilyuk, A. Tsukamoto, A. Itoh, and Th. Rasing, *Phys. Rev. Lett.* **99**, 047601 (2007).
- [20] C-H. Lambert, S. Mangin, B. S. D. Ch. S. Varaprasad, Y. K. Takahashi, M. Hehn, M. Cinchetti, G. Malinowski, K. Hono, Y. Fainman, M. Aeschlimann, E. E. Fullerton, *Science*, **345**, 6202 (2014).
- [21] M. L. M. Lalieu, M. J. G. Peeters, S. R. R. Haenen, R. Lavrijsen, and B. Koopman, *Phys. Rev. B*, **96**, 220411(R) (2017).
- [22] R. F. L. Evans, T. A. Ostler, R. W. Chantrell, I. Radu, and T. Rasing, *Appl. Phys. Lett.*, **104**, 082410 (2014).
- [23] A. Kirilyuk, A. V. Kimel, and T. Rasing, *Rep. Prog. Phys.*, **76**, 026501 (2013).
- [24] J. Walowski, and M. Munzenberg, *J. Appl. Phys.*, **120**, 140901 (2016).
- [25] D. Grundler, *Nature Physics Commentary*. **11**, June (2015).
- [26] A.V. Chumak, *et al. Nature Physics*. **11**, 453-461 (2015).
- [27] N. Jones, *Nature*, **561**, 163-166 (2018).
- [28] R. Danilak, “Why energy is a Big and Rapidly Growing Problem for Data Centers” *Forbes Technology Council*. (Dec. 2017).
- [29] R. Grimberg, *Mat. Sci. and Eng, B*. **178**, 19, 1285-1295 (2013).
- [30] H. C. Ohanian, *Am. J. Phys.* **54**, (6), (1986).
- [31] J.J. Sakurai, *Modern Quantum Mechanics*, Addison-Wesley, (1994).

- [32] B. Hillebrands, K. Ounadjela (Eds.): Spin Dynamics in Confined Magnetic Structures I, Topics Appl. Phys. **83**, 1–34 (2002).
- [33] D. C. Mattis, *The Theory of Magnetism Made Simple*, World Scientific (2006).
- [34] D. Gignoux, and M. Schlender, *Magnetism: Fundamentals*, Springer (2005).
- [35] R. Bowley and M Sanchez, *Introductory Statistical Mechanics*, Oxford (1999).
- [36] K. Yosida, *Theory of Magnetism*, Springer (1998).
- [37] R. Nave. Georgia Tech University. (2005). *Hyperphysics tutorial*, Retrieved from <http://hyperphysics.phy-astr.gsu.edu/hbase/Atomic/Hund.html#c2>.
- [38] E. Pavarini, E. Koch, F. Anders, and M. Jarrell *Correlated Electrons: From Models to Materials Modeling and Simulation Vol. 2*, Forschungszentrum Julich (2012).
- [39] N. Majlis, *The Quantum Theory of Magnetism*, World Scientific Publishing Co. (2000).
- [40] R. Skomski, *Simple Models of Magnetism*, Oxford University Press (2008).
- [41] Y. Kakehashi, *Modern Theory of Magnetism in Metals and Alloys*, Springer (2012).
- [42] A. Morrish, *The Physical Principles of Magnetism*, IEEE Press (1980).
- [43] J. Miltat et. al. “An Introduction to Micromagnetics in the Dynamic Regime.” (Eds.): B. Hillebrands, K. Ounadjela. Spin Dynamics in Confined Magnetic Structures I, Topics Appl. Phys. **83**, 1-34. Springer, (2002)
- [44] P. Bruno, *Physical Origins and Theoretical Models of Magnetic Anisotropy* (1993).
- [45] O. Narayan and A.P. Young, *Am. J. Phys.* **73**, 4 (2005)
- [46] A. Aharoni, *Introduction to the Theory of Ferromagnetism*, Oxford University Press (2000).
- [47] J. Lindner and K. Baberschke, *J. Phys.: Condens. Matter* **15**, R193–R232 (2003).

- [48] S.M. Rezend et al. *J. Appl. Phys.*, **84**, 958 (1998).
- [49] J. Lindner, and K. Baberschke. *J. Phys. Condens. Matter.* **15**, R465-R478 (2003).
- [50] G.M. Wysin, *Demagnetization Fields*, Universidade Federal de Santa Catarina (2012). Retrieved from <http://www.phys.ksu.edu/personal/wysin>
- [51] A. Morrish, *The Physical Principles of Magnetism*, IEEE Press (1980).
- [52] E. W. Lee, *Rep. Prog. Phys.* **18**, 184 (1955).
- [53] C. Kittel, *Rev. Mod. Phys.*, **21**, 4 (1949).
- [54] S. Chikazumi, *Physics of Ferromagnetism* (Oxford University Press, Oxford, (1997).
- [55] T. Rasing et. al. “Ultrafast Magnetization and Switching Dynamics.” (Eds.): B. Hillebrands, K. Ounadjela. *Spin Dynamics in Confined Magnetic Structures II*, Topics Appl. Phys. **87**, 213–252. Springer, (2003).
- [56] L. Baselgia, et al., *Phys. Rev. B.*, **38**, 4, (1988).
- [57] M. C. Fischer, J. W. Wilson, F. E. Robles, and W. S. Warren, *Rev. Sci. Instrum.*, **87**, 031101 (2016).
- [58] E. M. Grumstrup, M.M. Gabriel, E. E.M. Cating, E. M. Van Goethem, J. M. Papanikolas, *Chem. Phys.* **458**, 30-40, (2015).
- [59] J. Shah, *Ultrafast Spectroscopy of Semiconductors and Semiconductor Nanostructures*. Springer Verlag (2010).
- [60] G. Hartland, *Chem. Sci.* , **1**, 303–309 (2010).
- [61] Y. Tanimura, and S. Mukamel, *J. Chem. Phys.* **103**, 5 (1995).
- [62] W. Zipfel, R. M. Williams, and W. Webb, *Nat. Biotech.*, **21**, 11, 1369-1377 (2003).
- [63] F. Helmchen, and W. Denk, *Nat. Meth.*, **2**, 12, 932-940 (2005).

- [64] A. Scholl, L. Baumgarten, R. Jacquemin, and W. Eberhardt, *Phys. Rev. Lett.*, **79**, 25 (1997).
- [65] J.-Y. Bigot, M. Vomir, and E. Beaurepaire, *Nat. Phys.*, **5**, 515-520 (2009).
- [66] B. Koopmans, J. J. M. Ruigrok, F. D. Longa, and W. J. M. de Jonge, *Phys. Rev. Lett.*, **95**, 267207 (2005).
- [67] J.M. Freeman and W. Hiebert. “Stroboscopic Microscopy of Magnetic Dynamics.” (Eds.): B. Hillebrands, K. Ounadjela. *Spin Dynamics in Confined Magnetic Structures I*, Topics Appl. Phys. 83, 93-129. Springer, (2002)
- [68] E. Beaurepaire, J.-C. Merle, A. Daunois, and J.-Y. Bigot, *Phys. Rev. Lett.*, **76**, 22 (1996).
- [69] A. Kirilyuk, A.V. Kimel, and Theo Rasing, *Rev. Mod. Phys.*, 82, 3, July–September (2010).
- [70] J. W Kim, K. D. Lee, J.W Jeong, and S.C Shin *Appl. Phys. Lett.* **94**, 192506 (2009).
- [71] T. Q. Qiu and C. L. Tien, *Int. J. Heat Mass Transfer*, **37**, 17. 2789-2797, (1994)
- [72] J. K. Chen, J. E. Beraun, *Numer. Heat. Tr. A-Appl.* **40**, 1, 1-20, (2001).
- [73] B. Koopmans, “Laser Induced Magnetization Dynamics.” (Eds.): B. Hillebrands, K. Ounadjela. *Spin Dynamics in Confined Magnetic Structures II*, Topics Appl. Phys. **87**, 253-320. Springer, (2003).
- [74] M. v. Kampen, C. Jozsa, J.T. Kohlhepp, P. LeClair, L. Lagae, W.J.M. de Jonge, and B. Koopmans. *Phys. Rev. Lett.*, **88**, 22 (2002).
- [75] B.E.A. Saleh and M.C Teich, *Fundamentals of Photonics*, Wiley-Interscience (2007).
- [76] S.L. Chin, *Fundamentals of Laser Optoelectronics*, World Scientific (1989)
- [77] P. Argyres, *Phys. Rev.*, **97**, 2 (1955).
- [78] H. R. Hulme, *Proc. Roy. Soc.* **A135**, 237 (1932).

- [79] K. Shinagawa. *Faraday and Kerr effects in Ferromagnets*. (Eds.): S. Sugano, N. Kojima. Magneto-Optics. Springer Series in Solid-State Sciences, **128**, Springer, Berlin, Heidelberg (2000).
- [80] C.Y. You and S.C. Shin *Appl. Phys. Lett.* **69** (9), (1996).
- [81] Z.Q. Qui, and S. D. Bader, *Rev. Sci. Instrum.*, **71**, 3, (2000).
- [82] S.N. Savenkov. Jones and Mueller Matrices: Structure, symmetry relations and information content. (Eds): A.A. Kokhanovsky. Light Scattering Reviews 4. Springer Praxis Books. Springer, Berlin, Heidelberg (2009).
- [83] Y. Acremann, C. H. Back, M. Buess, O. Portmann, A. Vaterlaus, D. Pescia, H. Melchior, *Science*, **290**, 5491 (2000).
- [84] E. Jiménez, N. Mikuszeit, J. L. F. Cuñado, P. Perna, J. Pedrosa, D. Maccariello, C. Rodrigo, M. A. Niño, A. Bollero, J. Camarero, and R. Miranda, *Rev. Sci. Instrum.*, **85**, 053904 (2014).
- [85] S. Mizukami, E. P. Sajitha, D. Watanabe, F. Wu, T. Miyazaki, H. Naganuma, M. Oogane, and Y. Ando, *Appl. Phys. Lett.*, **96**, 152502 (2010).
- [86] F.R. Verdun, C. Giancaspro, and A. G. Marshall, *Appl. Spectrosc.* **42**, 5 (1988).
- [87] C. Berk, F. Ganss, M. Jaris, M. Albrecht, and H. Schmidt, *Appl. Phys. Lett.* **112**, 052401 (2018).
- [88] T. Hasegawa, et al., *J. Appl. Phys.*, **99**, 053505 (2006).
- [89] D. Weller, et. al., *J. Vac. Sci. Technol. B.*, **34**, 060801 (2016).
- [90] M.N. Baibich, J.M. Broto, A. Fert, F. Nguyen Van Dau, and F. Petroff, P. Etienne, G. Creuzet, A. Friederich, and J. Chazelas, *Phys Rev Lett.* **61**, 2472 (1988).
- [91] A. Barthélémy, A. Fert, F. Petroff, K.H.J. Buschow (Ed.), *Handbook of Magnetic Materials*, Vol.12, Elsevier, Amsterdam 1-96 (1999).
- [92] J. Zhang, Y. Liu, F. Wang, J. Zhang, R. Zhang, Z. Wang, and X. Xu, *J. Appl. Phys.* **111**, 073910 (2012).
- [93] J. Lindner, and K. Baberschke. *J. Phys. Condens. Matter.* **15**, R193-R232 (2003).

- [94] C. Kittel, *Phys. Rev.* **73**, 155 (1948).
- [95] S. M. Rezende, C. Chesman, M. A. Lucena, A. Azevedo, F. M. de Aguiar, and S. S. P. Parkin, *J. Appl. Phys.* **84**, 958 (1998).
- [96] Z. Li, R. Skomski, S.H. Liou, S. Michalski, M. Chipara, and R.D. Kirby, *J. Appl. Phys.* **109**, 07C113 (2011).
- [97] B. Kuanr, *J. Appl. Phys.* **93**, 7232 (2003).
- [98] S. Pal, S. Barman, O. Hellwig, and A. Barman, *J. Appl. Phys.* **115**, 17D105 (2014).
- [99] A. Layadi and J.O Artman, *Ferromagnetic Resonance in a Coupled Two-Layer System*, *J. Magn. Magn. Mat.*, **92**, 143-154, (1990).
- [100] J.K. Chen, J.E. Beraun, “Numerical Study of Ultrashort Laser Pulse Interactions with Metal Films”, in *Numerical Heat Transfer, Part A: applications: An international Journal of Computation and Methodology*, 40:1, 1-20 (2001).
- [101] S.M. Zhou, and L. Sun, *J. Magn and Magn Matt.* **292**, 65-71 (2005).
- [102] Y. Endo, O. Kitakami, and Y. Shimada, *IEEE Trans. Magn.* **34**, 4 (1998).
- [103] J.-W. Kim, M. Vomir & J.-Y. Bigot, *Sci. Rep.* **5**, 8511 (2015).
- [104] F. Hansteen, A. Kimel, A. Kirilyuk, and T. Rasing, *Phys. Rev. B*, **73**, 014421 (2006).
- [105] B. Koopmans, “Laser-Induced Magnetization Dynamics”, B. Hillebrands, K. Ounadjela (Eds.): *Spin Dynamics in Confined Magnetic Structures II*, *Topics Appl. Phys.* **87**, 253–320 (2003).
- [106] F. Hellman et. al, *Rev. Mod. Phys.* **89**, 025006 (2017).
- [107] A. Brataas, A.D. Kent, and H. Ohno, *Nat. Mater.* **11**, 3311 (2012).
- [108] A.J. Schellekens, K.C. Kuiper, R.R.J.C. de Wit, and B. Koopmans, *Nat. Commun.* **5**, 4333 (2014).
- [109] B. Dieny and M. Chshiev, *Rev. Mod. Phys.* **89**, 025008 (2017).

- [110] S. Mangin, M. Gottwald, C-H. Lambert, D. Steil, V. Uhlír, L. Pang, M. Hehn, S. Alebrand, M. Cinchetti, G. Malinowski, Y. Fainman, M. Aeschlimann and E. E. Fullerton, *Nat. Mater*, **13**, 3864 (2014).
- [111] M. C. Weber, H. Nembach, and J. Fassbender, *J. Appl. Phys*, **95**, 11 (2004).
- [112] M. van Kampen, C. Jozsa, J. T. Kohlhepp, P. LeClair, L. Lagae, W. J. M. de Jonge, and B. Koopmans, *Phys. Rev. Lett*, **88**, 22 (2002).
- [113] G. P. Zhang, and W. Hubner, *Phys. Rev. Lett*, **85**, 14 (2000).
- [114] C. Kittel, *Phys Rev.*, **73**, 2 (1947).
- [115] V. Kambersky, *Can. J. Phys.*, **48**, 2906 (1970).
- [116] H. Nembach, J. Shaw, C. Boone, and T. J. Silva, *Phys. Rev. Lett.* **110**, 117201 (2013).
- [117] C. Berk, F. Ganss, M. Jaris, M. Albrecht, and H. Schmidt, *IEEE J Sel. Top. Quantum Electron*, **25**, 4 (2019).
- [118] R. Sbiaa, H. Meng, and S. N. Piramanayagam, *Phys. Status Solidi RRL* **5**, 12, 413–419 (2011).
- [119] C. Berk, F. Ganss, M. Jaris, M. Albrecht, and H. Schmidt, *Appl. Phys. Lett.* **112**, 052401 (2018).
- [120] Z. Diao, Z. Li, S. Wang, Y. Ding, A. Panchula, E. Chen, L-C. Wang, and Y. Huai, *J. Phys: Cond. Matt.* **19**, 16 (2007).
- [121] Y. Tserkovnyak and A. Brataas, *Phys. Rev. Lett*, **88**, 11 (2002).
- [122] B. Heinrich, Y. Tserkovnyak, G. Woltersdorf, A. Brataas, R. Urban, and G.E.W. Bauer, *Phys. Rev. Lett.*, **90**, 18 (2003).
- [123] G. Woltersdorf, O. Mosendz, B. Heinrich, and C.H. Back, *Phys. Rev. Lett*, **99**, 246603 (2007).
- [124] J. Walowski, M. Kaufmann, B. Lenk, C. Hamann, J. McCord and M. Munzenberg, *J. Phys. D: Appl. Phys.* **41**, 164016 (2008).
- [125] Y. Tserkovnyak, A. Brataas, and G. Bauer, *Phys. Rev. Lett.* **88**, 11 (2002).

- [126] J. Z. Sun, *Phys. Rev. B* **62**, 570 (2000).
- [127] M. Bauer, J. Fassbender, B. Hillebrands, and R. L. Stamps, *Phys. Rev. B.*, **61**, 3410 (2000).
- [128] P.W. Huang and R. H. Victora, *J. Appl. Phys.*, **115**, 17B710 (2014).
- [129] M. Oogane, T. Wakitani, S. Yakata, R. Yilgin, Y. Ando, A. Sakumaand, and T. Miyazaki, *Jpn. J. Appl. Phys.* **45**, 3889 (2006).
- [130] J. Walowski, M. Djordjevic Kaufmann, B. Lenk, C. Hamann, J. McCord and M Munzenberg, *J. Phys. D: Appl. Phys.*, **41** 164016 (2008).
- [131] A. Barman, S. Wang, J. Maas, A. R. Hawkins, S. Kwon, J. Bokor, A. Liddle, and H. Schmidt, *Appl. Phys. Lett.*, **90**, 202504 (2007).
- [132] A. Barman, S. Wang, J.D. Maas, A. Hawkins, S. Kwon, A. Liddle, J. Boker, H. Schmidt, *Nano Lett.*, **6**, 2939, (2006).
- [133] A. J. Schellekens, L. Deen, D. Wang, J. T. Kohlhepp, H. J. M. Swagten, B. Koopmans, *Appl. Phys. Lett.* **102**, 082405 (2013).
- [134] A. Brataas, Y. Tserkovnyak, and G. E. W. Bauer, *Phys. Rev. Lett.*, **101**, 037207 (2008).
- [135] M.C. Hickey, and J.S. Modera *Phys. Rev. Lett.*, **102**, 137601 (2009).
- [136] D. Steiauf, and M. Fahnle, *Phys. Rev.B.*, **79**, 140401 (2009).
- [137] V. Kambersky. *Can. J. Phys.*, **48**, 2906 (1970).
- [138] R. J. Elliot, *Phys. Rev.* **96**, 2 (1954).
- [139] V. Kambersky, *Can. J. Phys.*, **48**, 2906 (1970).
- [140] J. Kunes, and V. Kambersky, *Phys. Rev. B.*, **65**, 212411 (2002).
- [141] J M Wesselinowa *J. Phys. C: Solid State Phys.*, **20** 4639 (1987).
- [142] S. Mizukami, D. Watanabe, T. Kubota, X. Zhang, H. Naganuma, M. Oogane, Y. Ando, and T.Miyazaki, *Appl. Phys. Express*, **3**, 123001 (2010).

- [143] M. Jaris, Y. Yahagi, B. K. Mahato, S. Dhuey, S. Cabrini, V. Nikitin, J. Stout, A. R. Hawkins, and H. Schmidt, *Appl. Phys. Lett.*, **109**, 202403 (2016).
- [144] A. Capua, S-H. Yang, T. Phung, and S. S. P. Parkin, *Phys. Rev. B.*, **92**, 224402 (2015).
- [145] J. Dubowik, K. Załeski, H. Głowinski, and I. Goscińska, *Phys. Rev. B.*, **84**, 184438 (2011).
- [146] A. Barman, and J. Sinha, *Spin Dynamics and Damping in Ferromagnetic Thin Films and Nanostructures*. Springer, 13-24 (2018).
- [147] A. Barman, S. Wang, J. D. Maas, A. R. Hawkins, S. Kwon, A. Liddle, J. Bokor, and H. Schmidt, *Nano Lett.* **6**, 2939 (2006).
- [148] A. Scherbakov et al, *Phys. Rev. Lett.* **105**, 117204 (2010).
- [149] B. Koopmans, “Laser-Induced Magnetization Dynamics”, in *Spin Dynamics in Confined Magnetic Structures II*. Berlin: Springer, 253-320 (2003).
- [150] J.F. Robillard, A. Devos, and I. Roch-Jeune, *Phys. Rev. B* **76**, 092301 (2007).
- [151] Graczykowski, S. Mielcarek, A Trzaskowska, J. Sarkar, P. Harkonen and B. Mroz, *Phys. Rev. B.* **86**, 085426 (2012).
- [152] M. Kostylev, P. Schrader, R. L. Stamps, G. Gubbiotti, G. Carlotti, A. O. Adeyeye, S Goolaup and N. Singh, *Appl. Phys. Lett.* **92**, 132504 (2008).
- [153] G. Gubbiotti, S. Tacchi, M. Madami, G. Carlotti, A.O. Adeyeye and M. Kostylev, *J. Phys. D: Appl. Phys.* **42**, 264003 (2010).
- [154] Y. Yahagi, B. Harteneck, S. Cabrini, and H. Schmidt, *Phys. Rev. B* **90**, 140405 (2014).
- [155] Z. Liu, R. Brandt, Y. Yahagi, B. Hansen, B. Harteneck, J. Bokor, A. R. Hawkins, and H. Schmidt, *Appl. Phys. Lett.* **98**, 052502 (2011).
- [156] C. Berk, Y. Yahagi, S. Dhuey, S. Cabrini and H. Schmidt, *J. Magn. Magn. Mater.*, **426**, 239-244 (2017).

- [157] T. Saito, O. Matsuda, M. Tomoda, and O. B. Wright, *J. Opt. Soc. Am. B*, **27**, 2632 (2010).
- [158] H. Ulrichs, D. Meyer, M. Muller, S. Wittrock, M. Mansurova, J. Walowski and M Munzenberg, *J. Appl. Phys.* **120**, 142116 (2016).
- [159] J. Walowski, M. Djordjevic Kaufmann, B. Lenk, C. Hamann, J. McCord and M Munzenberg, *J. Phys. D: Appl. Phys.* **41**, 164016 (2008).
- [160] A. J. Schellekens, L. Deen, D. Wang, J. T. Kohlhepp, H. J. M. Swagten, B. Koopmans, *Appl. Phys. Lett.* **102**, 082405 (2013).
- [161] Amir Capua, See-hun Yang, Timothy Phung, and Stuart S. P. Parkin, *Phys. Rev. B*, **92**, 224402 (2015).
- [162] Y Yahagi, C. Berk, B. Hebler, S. Dhuey, S. Cabrini, M. Albrechy and H. Schmidt, *J. Phys. D: Appl. Phys.* **50** 17LT01 (2017).
- [163] M. Weiler, L. Dreher, C. Heer, H. Heubl, R. Gross, M.S. Brandt, and S.T.B. Goennenwein, *Phys. Rev. Lett.*, **106**, 117601 (2011).
- [164] L. Dreher, M. Weiler, M. Pernpeintner, H. Heubl, R. Gross, M.S. Brandt, and S.T.B. Goennenwein, *Phys. Rev. B* **86**, 134415 (2012).
- [165] A. G. Gurevich and G. A. Melkov, *Magnetization Oscillations and Waves* (CRC Press, New York, 1996), pp. 10–20.
- [166] Y. Yahagi, Ph.D. thesis, “Nanomagnet Dynamics with Magnetostatic and Magnetoelastic Interelement Coupling,” University of California Santa Cruz (2015).
- [167] Y. Ren, Y. L. Zuo, M. S. Si, Z. Z. Zhang, Q. Y. Jin, and S. M. Zhou, *IEEE Trans. Magn.* **49**, 3159 (2013).
- [168] H.-S. Song, K.-D. Lee, J.-W. Sohn, S.-H. Yang, S. S. P. Parkin, C.-Y. You, and S.-C. Shin, *Appl. Phys. Lett.* **102**, 102401 (2013).
- [169] A. V. Chumak, V.I. Vasyuchka, A.A. Serga and B. Hillebrands, *Nat. Phys.* **11**, 453-561 (2015).
- [170] A. Biswas, S. Bandyopadhyay, and J. Atulasimha, *Appl. Phys. Lett.* **103**, 232401 (2013).

- [171] V. Sampath, N. D'Souza, D. Bhattacharaya, G.M. Atkinson, S. Bandyopadhyay, and J. Atulasimha, *Nano Lett.* **16**, 5681–5687 (2016).
- [172] P.G. Gowtham, D. Labanowski, and S. Salahuddin, *Phys. Rev. B.* **94**, 014436 (2016).
- [173] V.G. Baryakhtar, and A.G. Danilevich, *Low.Temp. Phys.* **43**, 351 (2017).
- [174] M. Weiler, L. Dreher, C. Heeg, H. Huebl, R. Gross, M.S. Brandt, and S.T.B. Goennenwein, *Phys. Rev. Lett.* **106**, 117601 (2011).
- [175] L. Thevenard, C. Gourdon, J. Y. Prieur, H. J. con Bardeleben, S. Vincent. L. Becerra, L. Largeau, and J. Y. Duquesne, *Phys Rev. B.* **90**, 094401 (2014).
- [176] C.Berk, Y. Yahagi, S. Dhuey, S. Cabrini, and H. Schmidt, *J. Magn. Magn. Mater.* **426**, 239-244 (2017).
- [177] Y. Yahagi, C. Berk, B. Hebler, S. Dhuey, S. Cabrini, M. Albrecht, and H. Schmidt, *J. Phys. D: Appl. Phys.* **50**, 17LT01 (2017).
- [178] L. Novotny, *Am. J. Phys.* **78**, 1199 (2010).
- [179] S. R-K. Rodriguez, *Eur. J. Phys.* **37**, 025802 (2016).
- [180] L. Dreher, M. Weiler, M. Pernpeintner, H. Huebl, R. Gross, M. S. Brandt, and S. T. B. Goennenwein, *Phys. Rev. B.* **86**, 134415 (2012).
- [181] C.C Tannaoudji, B. Diu, and F. Laloe, *Quantum Mechanics (Vol. 1)*, (1992).
- [182] D.T. Ha, D.T. Thuy, V.T. Hoa, T.T.T. Van, and N.A. Viet, *J. Phys.: Conf. Ser.* **865**, 012007 (2017).
- [183] Z. Jacob, *Nat. Mater.* **13**, 1081-1083 (2014).
- [184] H. Huebl, C. W. Zollitsch, J. Lotze, F.Hocke, M. Greifenstein, A. Marx, R. Gross, and S.T. B. Goennenwein, *Phys. Rev. Lett.* **111**, 127003 (2003).
- [185] J. Restrepo, C. Ciuti, and I. Favero, *Phys. Rev. Lett.* **112**, 013601 (2014).

- [186] J. Oh, M. D. Le1, H.H. Nahm, H. Sim, J. Jeong1, T.G. Perring, H. Woo, K. Nakajima, S. Ohira-Kawamura, Zahra Yamani, Y. Yoshida, H. Eisaki, S.W. Cheong, A.L. Chernyshev & J.G. Park, *Nat. Commun.* **7**, 13146 (2016).
- [187] M. Levinson, *Journal of Sound and Vibration.* **98**, 289-298 (1985).
- [188] D. Wang, W. Liu, and H. Zhang, *Comput. Methods Appl. Mech. Engrg.* **286**, 230–267 (2015).
- [189] B. Lautrup *Physics of Continuous Matter: Exotic and Everyday Phenomena in the Macroscopic World.* (CRC, 2011).
- [190] H. M. Ledbetter, and R. P. Reed, *Journal of Physical and Chemical Reference Data.* **2**, 531 (1973).
- [191] B. Hillebrands, K. Ounadjela (Eds.): Spin Dynamics in Confined Magnetic Structures II, *Topics Appl. Phys.* **87**, 253–320 (2003).
- [192] J. K. Chen, J. E. Beraun, *Numer. Heat. Tr. A-Appl.* **40**, 1, 1-20, (2001)
- [193] Y. Yahagi, B. Harteneck, S. Cabrini, and H. Schmidt, *Phys. Rev. B*, **90**, 140405 (2014).
- [194] J.F. Robillard, A. Devos, and I. Roch-Jeune, *Phys. Rev. B* **76**, 092301 (2007).
- [195] Y. Yahagi, Ph.D. thesis, “Nanomagnet Dynamics with Magnetostatic and Magnetoelastic Interelement Coupling,” University of California Santa Cruz (2015).
- [196] R Grossinger, R.S. Turtelli and N. Mehmood, *IOP Conf. Ser.: Mater. Sci. Eng.* **60**, 012002 (2014).
- [197] R. Gontarz, H. Ratajczak, and P. Suda, *Phys. Stat. Sol.* **6**, 909 (1964).
- [198] F. R. Verdun, C. Giancaspro, and A. G. Marshall, *Appl. Spectrosc.* **42**, 5 (1988).
- [199] A. Capua, *Phys. Rev. B.* **92**, 224402 (2015).
- [200] S. Groblacher, K. Hammerer, M.R. Vanner, and M. Aspelmeyer, *Nat. Lett.* **460**, 6 (2009).

- [201] C. M Bender, *PT Symmetry: In Quantum and Classical Physics*, World Scientific (2018).
- [202] M. Vogel, A.V. Chumak, E. H. Waller, Thomas Langner, V.I. Vasyuchka, B. Hillebrands, and G. von Freymann, *Nat. Phys.* **11**, 487-491 (2015).
- [203] M. Krawczyk, and D. Grundler, *J. Phys.: Condens. Matter.* **26**, 123202 (2014).